Dissertation

submitted to the
Combined Faculties for the Natural Sciences and for Mathematics
of the Ruperto-Carola University of Heidelberg, Germany
for the degree of
Doctor of Natural Sciences

Put forward by
Johannes Frohnmayer, M. Sc.
Born in: Filderstadt, Germany

Oral examination: April 27th, 2017

Bottom-Up Assembly of Synthetic Model Systems for Cellular Adhesion

Referees:
Prof. Joachim P. Spatz
Prof. Ulrich Schwarz

Zusammenfassung:

Aus dem zweiten Gesetz der Thermodynamik folgt, dass jede Zelle durch eine Grenzfläche von ihrer Umwelt abgetrennt sein muss. Deshalb sind alle Zellen von einer Lipidmembran ummantelt. Erst dadurch wird der hohe Grad an Organisation möglich. Damit jedoch Nährstoffe und Informationen diese Barriere passieren können, sind diverse Transmembranproteine nötig. Diese Voraussetzungen muss auch die Synthetische Biologie bei der Erschaffung künstlicher Zellen berücksichtigen. In dieser Doktorarbeit wurde ein simples und leicht beeinflussbares Modellsystem für Zelladhäsion entwickelt. Zunächst wurde die Adhäsion von sogenannten "Small Unilamellar Vesicles", Proteoliposomen mit Thrombozyten-Integrin, auf eine mit extrazellulären Matrixproteinen funktionalisierte Oberflächen mit einer Quarzkristall-Mikrowaage untersucht. Des Weiteren wurde, wegen der geringen Stabilität von "Giant Unilamellar Vesicles" (GUVs), ein neues Kompartimentsystem entwickelt, das "droplet-stabilized Giant Unilamellar Vesicle" (dsGUV). Hierfür wurde die Vielseitigkeit und Stabilität von Tröpfchenmikrofluidik mit der Biokompatibilität von Lipidmembranen kombiniert. Durch die Verwendung von mikrofluidischer Pico-Injektionstechnologie ist es möglich Komponenten nacheinander in ein Modellkompartiment einzuführen. Dies öffnet den Weg zu komplexeren und vielfältigeren Modellsystemen. In dieser Arbeit wird als Beispiel die Rekonstitution von Thrombozyten-Integrin in dsGUV gezeigt. Darüber hinaus wird ein Verfahren gezeigt, mit dem GUV aus dsGUV herausgeholt werden können.

Abstract:

The second law of thermodynamics requires life processes to be separated by a boundary from their environment. Therefore, all cells are encapsulated by a lipid membrane. This enables life's great degree of organization. To allow nutrients and information to pass this barrier, cells use various transmembrane proteins for material and signal transduction. When creating artificial cells, synthetic biology has to account for these facts. This thesis presents the development of such a stable and easy-to-manipulate protocell model for cellular adhesion experiments. First adhesion of small unilamellar vesicles containing reconstituted blood-platelet integrin to functionalized surfaces were studied using quartz crystal microbalance. Due to restrictions of giant unilamellar vesicles (GUV), a novel compartment system, named droplet-stabilized giant unilamellar vesicles (dsGUV), was created combining the versatility of microfluidics, the stability of surfactant-stabilized water-in-oil droplets, with the high level of bio-mimicry of lipid membranes. Through the use of microfluidic pico-injection technology, components can be sequentially added to the compartment, pathing the way for more complex and diverse model systems. In this work, reconstitution of integrin into dsGUVs is presented. The system was characterized using different methods. Finally the recovery of GUVs from dsGUVs to a physiological environment is presented.

Contents

Acronyms

AC	Alternating Current
AFM	Atomic Force Microscopy
ATTO488	4-(2-(3,6-diamino-4,5-disulfo-3H-xanthen-9-yl) - N-methylbenzamido) Butanoic Acid
BSA	Bovine Serum Albumin
CAD	Computer Aided Design
CAM	Cell Adhesion Molecule
CMC	Critical Micelle Concentration
DARPin	Designed Ankyrin Repeat Protein
DC	Direct Current
DLS	Dynamic Light Scattering
DMF	Dimethylformamide
dsGUV	Droplet-stabilized GUV
ECM	Extracellular Matrix
EDTA	Ethylenediaminetetraacetic Acid
ELISA	Enzyme-linked Immunosorbent Assay
FA	Focal Adhesion
F-actin	Filamentous Actin
FAK	Focal Adhesion Kinase
FCS	Fluorescence Correlation Spectroscopy
FEM	Finite Element Method
FRAP	Fluorescence Recovery After Photobleaching
GFP	Green Fluorescent Protein
GNP	Gold Nano Particle
GRGDSP	Gly-Arg-Gly-Asp-Ser-Pro
GUV	Giant Unilamellar Vesicle
His6	Hexa Histidine-tag
HLB	Hydrophilic-lipophilic Balance
ITO	Indium Tin Oxide
LUV	Large Unilamellar Vesicle
MD	Molecular Dynamics
MLV	Multilamellar Vesicle
MS	Mass Spectroscopy
NMR	Nuclear Magnetic Resonance
NTA	Nitrilotriacetic Acid
OD	Optical Density
PBS	Phosphate-buffered Saline

PDMS	Polydimethylsiloxane
PEG	Poly(ethylene Glycol)
PFO-MEG	Perfluoroctanyl-ethylen Glycol
PFO-TEG	Perfluoroctanyl-triethylen Glycol
PFPE	Perfluorinated Polyether
PIP2	Phosphatidylinositol 4,5-bisphosphate
PP	Packing Parameter
PSMF	Phenylmethane Sulfonyl Fluoride
PTFE	Polytetrafluorethylen
QCM-D	Quartz Crystal Microbalance With Dissipation Monitoring
RGD	Arginine-glycine-aspartic Acid
SB	Synthetic Biology
SDS-PAGE	Sodium Dodecyl Sulfate-polyacrylamide Gel Electrophoresis
SEM	Scanning Electron Microscopy
SLB	Supported Lipid Bilayer
SUV	Small Unilamellar Vesicle
TAMRA	5-(and-6)-Carboxytetramethylrhodamine
TEM	Transmission Electron Microscopy
THF	Tetrahydrofuran
TRI2500	PFPE($2500\,g/mol$)-PEG($600\,g/mol$)-PFPE($2500\,g/mol$)
TRI7000	PFPE($7000\,g/mol$)-PEG($1400\,g/mol$)-PFPE($7000\,g/mol$)
UV	Ultraviolet

Lipids

DGS-NTA	1,2-dioleoyl-sn-glycero-3- [(N-(5-amino-1-carboxypentyl) Iminodiacetic Acid) Succinyl]
DOPC	1,2-dioleoyl-sn-glycerol-3-phosphocholine
DOPE	1,2-dioleoyl-sn-glycero-3-phosphoethanolamine
DOPS	1,2-dioleoyl-sn-glycero-3-phospho-L-serine
egg PC	L-α-phosphatidylcholine
egg PG	L-α-phosphatidylglycerol
PC	Phosphatidylcholine
POPC	1-palmitoyl-2-oleoyl-sn-glycero-3-phosphocholine

Part I.

Introduction

1. Cell Structure

The cell is the basic biological, functional, structural and self-replicating unit of all organisms from bacteria to complex multicellular life forms. Eukariotic cells consist of a plasma membrane, which encloses the cytoplasm, the cytoskeleton and a range of organelles, such as the nucleus, as depicted in figure 1.1.[1] The plasma membrane is a selectively permeable barrier separating the cell's interior from the extracellular environment. It is composed of a phospholipid bilayer of approximately 5 nm thickness with embedded proteins.[1, 2] Endo- / exocytosis and transmembrane proteins such as ion channels allow the cell to establish and maintain gradients of ions, nutrients and metabolites across the membrane.[3, 4] Cell membranes with the embedded proteins are involved in a variety of cellular processes such as cell adhesion and signalling and serve as the attachment surface for several extracellular structures, including the glycocalyx and the intracellular cytoskeleton.[5–9]

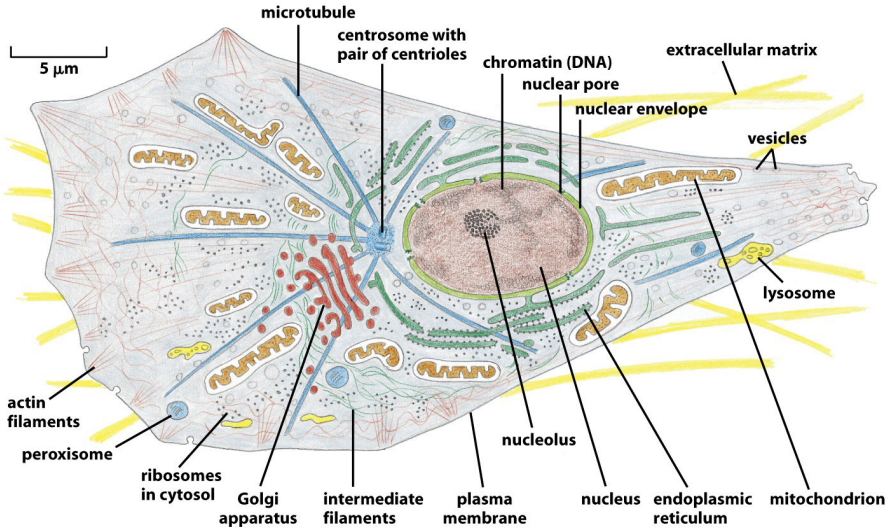

Figure 1.1.: A schematic representation of a typical animal cell, showing its compartmentalization into many different organelles. Reprinted from Alberts et al. [1].

The cytoskeleton is a network of interlinked filaments that extends throughout the cytoplasm thereby maintaining the overall shape and mechanical resistance to deformation.[10] In multicellular organisms the cytoskeleton stabilizes the entire

tissues through association with extracellular connective tissue and other cells.[1, 11] The cytoskeleton is a highly dynamic structure composed of three main proteins (figure 1.2) – filamentous actin (F-actin), intermediate filaments and microtubules – which are capable of rapid growth or disassembly dependent on the cell's processes at a certain period of time.[12] Both actin filaments and microtubules assemble from globular monomers, G-actin and tubulin, respectively allowing for the high dynamics of their structures. In contrast, intermediate filaments are made up from fibrous subunits forming a coiled-coil. By actively contracting and relaxing the cytoskeleton facilitates cellular morphogenesis and motility.[13]

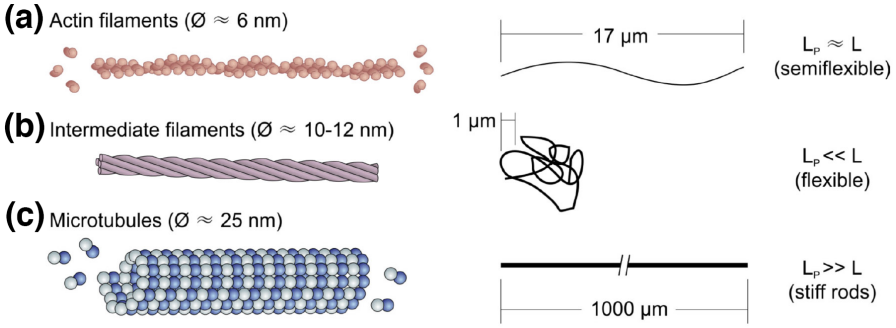

Figure 1.2.: Eucariotic cells are stabilized by a highly dynamic and adaptive cytoskeletal system consisting of three types of filaments. Actin filaments (F-actin) form from globular monomers (G-actin). They determine the morphology of the cell's surface and play an important role in cell locomotion. Intermediate filaments provide mechanical strength to cells and whole tissues. Microtubules are long hollow cylinders that form from α and β heterodimers and are usually attached at one end to a microtubule-organizing center or centrosome. They play an important role in intracellular transport and determine the positions of the organelles. The scale bars indicate the persistence length L_p of the different fibers in comparison to an average filament length L. Reproduced from Martin Deibler. [14].

Cells sense and interact with their environment in many different ways. One of these processes, cell adhesion, is the ability of cellular membrane proteins to attach to surfaces such as the extracellular matrix (ECM) and other cells. Together with biochemical sensing,[15, 16] mechanosensing is essential for a cell to adjust internal mechanisms to its surrounding.[17, 18] Hence, it is fundamental for regulating motility, differentiation, apoptosis, as well as the development of complex multicellular organisms. Cell adhesion is mediated through the action of transmembrane glycoproteins, called cell adhesion molecules, like cadherins, integrins, selectins and syndecans.[1] In section 1.2 cell adhesion in general and especially integrins will be discussed in more detail.

1.1. Cell Adhesion

The ability of cells to adhere to surfaces of other cells, or to the ECM is crucial for the structure and development of tissue, but also to cell mobility in general. This process is governed by a complex interplay between the ECM, cell junctions, adhesion mechanisms and the cytoskeleton.[19] The binding of cell adhesion molecules (CAMs), mainly transmembrane proteins, to molecules on adjacent cells or the ECM is specific and follows the key-lock principle. The specificity arises from a complementary geometrical shape and charge. The binding sites are shaped to maximize electrostatic interactions between oppositely charged amino acid side chains of CAM and ligand and to maximize the number of hydrogen bonds between both proteins.[20] Four different functions of cell adhesion can be distinguished, as presented in figure 1.3, each with a different molecular basis:[1]

(a) Anchoring junctions: These cell-cell or cell-matrix adhesions transmit stress and are tethered to the cytoskeleton. Cell-Matrix adhesions can stabilize tissue through binding to the ECM. In epithelial cells, cell-cell adhesion junctions form a stable sheet by directly linking the cytoskeleton of neighbouring cells.

(b) Occluding junctions: Common in epithelial cells, they seal gaps between cells to create an impermeable sheet.

(c) Channel-forming junctions: By creating channels they link the cytoplasm of adjacent cells.

(d) Signal-relaying junctions: Important for synapses these junctions allow for signal molecules to be relayed between connected cells.

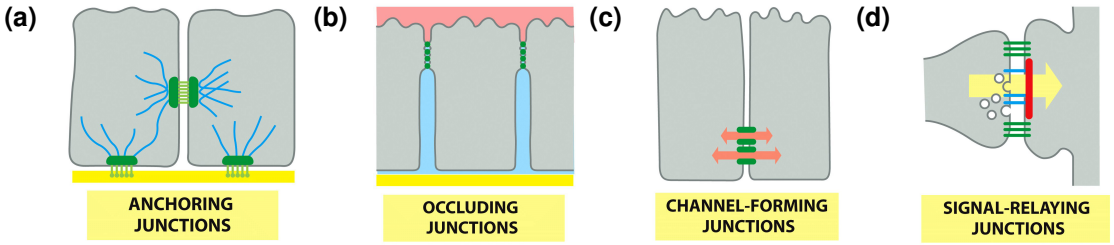

Figure 1.3.: Schematic representation of the four different functional classes of cell junctions. (a) Through anchoring junctions cells are either linked to other cells, typically via cadherins, or to the ECM, typically via integrin. (b) Epithelial cells form occluding junctions to form a sealed layer. (c) To transfer small molecules and ions between each other, cells form passageways called channel-forming junctions. (d) Common in nerve synapses, signal-relaying junctions are complex structures, consisting of anchorage and signaling proteins. Reproduced from Alberts et al. [1].

CAMs are organized into four protein superfamilies; selectins, integrins, syndecans and cadherins. Commonly they consist of a large extracellular domain, a helical transmembrane domain and an intracellular domain. The later is often connected to the cytoskeleton.[1, 21]

1.2. Focal Adhesions

Focal adhesions (FAs) are large macromolecular assemblies, shown in figure 1.4, through which actomyosin-driven contractile forces and regulatory signals are transmitted between the ECM and an interacting cell. These sub-cellular structures mediate the regulatory effects of cells in response to cell-ECM adhesion.[18, 22] The pivotal elements of FAs are the transmembrane receptor proteins of the integrin family, which will be discussed in more detail in section 1.3.[6] Integrins bind to different ligands of the ECM and are mechanically linked to actin fibers by complex multi-protein structures. This network of proteins is collectively referred to as the "adhesome" containing >100 different components with multiple interactions.[23–26] It can be differentiated into several functional "subnets". Each of these signalling pathways switches different molecular interactions within the whole network, consequently regulating cell adhesion.[6] FAs assemble, grow and disassemble in time scales of minutes. The pseudo steady state of a focal adhesion is maintained by rapid exchange of material with the cytosol. The large number of proteins involved in a FA complex suggests a considerable functional diversity. It has been shown, that signals transmitted from FAs to other parts of the cell, relate to a wide range of cellular processes from cell motility to cell fate decisions.[27, 28]

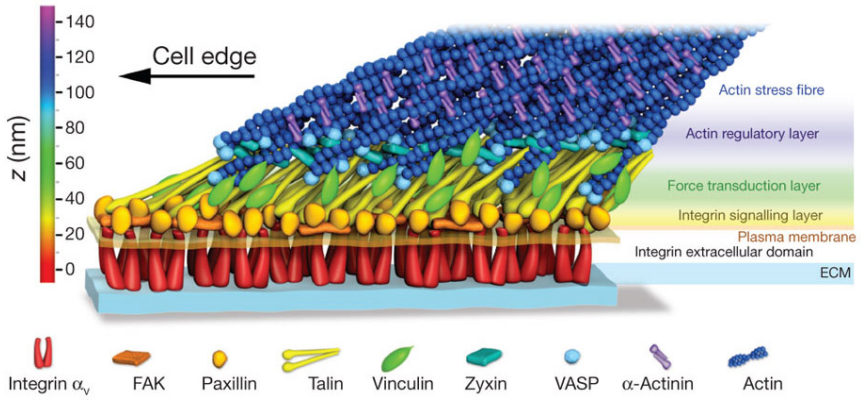

Figure 1.4.: Schematic model of the proteins constituting FAs. The sketch depicts experimentally determined protein interactions and the vertical positioning of the components. Note that the model does not depict protein stoichiometry. Taken from Kanchanawong et al.[29].

During cell migration cell-matrix adhesion sites assemble dynamically in a sequential cascade of compositional changes.[27, 30] Integrins spontaneously diffuse and aggregate in the plasma membrane.[31] Through association of talin to their cytoplasmic tails, integrins get activated and show increased binding affinity to the ECM.[32] Integrin-talin pairs can bind to the ECM, resulting in their immobilization. Engagement to the ECM promotes recruitment of adapter protein paxilin to the integrin clusters. This in turn recruits additional integrins to enlarge the clusters and they mature to nascent adhesions.[31, 33–35] The majority of these nascent adhesions disassemble within minutes, while a subpopulation mature into focal complexes.[36] This development is promoted by the recruitment of the actin-bundling protein α-actinin. Together with talin, α-actinin established a link between the ECM-bound integrins and the actin cytoskeleton.[37, 38] The transition of nascent adhesions to focal complexes is facilitated by mechanical tension caused by the polymerization of actin.[39–42] Larger forces induced by actomyosin contractility further promote the maturation of focal complexes to FAs, by mechanical stretching of focal complexes (e.g. talin, cas) and them exposing binding sites.[43–45]

1.3. Integrins

Integrins are heterodimeric transmembrane proteins which are important for cell-cell and cell-ECM interactions. An integrin receptor is composed of one of 18 known α-subunits noncovalently bound to one of 8 β-subunit assembling into 24 different pairing combinations.[46] Both subunits cross the cell membrane, with short intracellular C-terminals and large extracellular N-terminal domains at their respective ends, see figure 1.5. The intracellular domains are linked to the cytoskeleton through a complex of proteins called adhesome, as described in section 1.2. The extracellular parts of integrin bind to specific binding sites of ECM proteins such as collagen or fibronectin. Integrin not only senses environmental cues and transfers the information into the cell, but also the conformation of integrin can be actively altered upon intracellular signals thereby actively regulating adhesion.[47]. Both mechanisms depend on transmission of forces across the membrane and conversion into electrochemical activity – a process called mechanotransduction.[48, 49] As these dual function receptors are wired to other signaling pathways, integrin-mediated cell anchorage can affect cytoskeletal organization and cell motility as well as differentiation and apoptosis.[50]

A characteristic feature of most integrin receptors is their ability to bind a variety of ligands on other cells or more often in the ECM. Moreover, many ECM and cell surface adhesion proteins bind to multiple integrin receptors.[52] One of this binding sites is the short amino-acid sequence arginine-glycine-aspartic acid

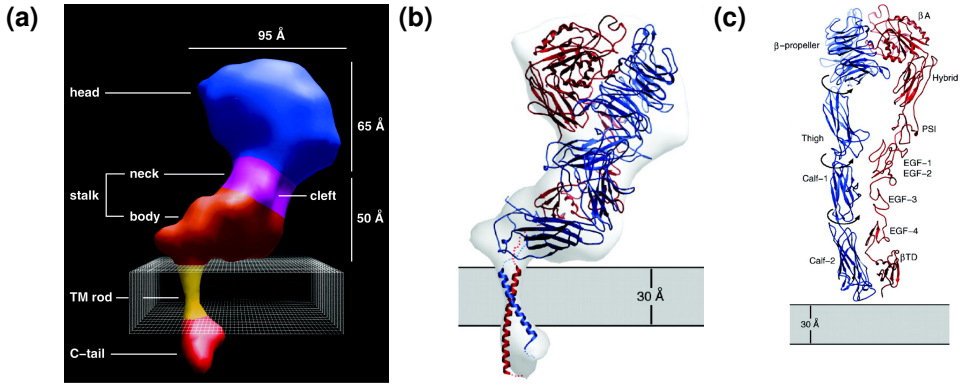

Figure 1.5.: Structure of integrin $\alpha_{IIb}\beta_3$ obtained through X-ray crystallography, small angle neutron scattering and cryo TEM measurements. (a) Surface-shaded 3D density map of the integrin $\alpha_{IIb}\beta_3$ heterodimer at $20\,\mathring{A}$ resolution. The dimensions and domains are indicated. Ribbon models depicting integrin $\alpha_{IIb}\beta_3$ in the (b) low-affinity state, which can transform to the (c) active state (only the extracellular parts are shown). Reproduced from Adair and Yaeger. Copyright (2002) National Academy of Sciences, U.S.A.[51]

(RGD), which is exposed in many ECM proteins like fibrinogen and fibronectin. Integrins selectively recognizes differently structured biomimetic RGD-containing peptides.[53] One type of integrin, that binds specifically to RGD, is integrin $\alpha_{IIb}\beta_3$.[54, 55] This type of integrin is an abundant membrane protein in blood platelets and epithelial cells.[50, 56] The vascular localization places this integrin in a strategic position to provide adhesive functions necessary for hemostasis, wound healing and angiogenesis. As a protocol for purifying integrin $\alpha_{IIb}\beta_3$ from blood platelets was well established within our group and thrombocyte concentrate is readily available, it was a preferable choice to continue working with this type of integrin for synthetic biology (SB) applications.[57]

The structure of integrin and its function were reconstructed using different analysis methods such a X-ray protein cristallography, small angle neutron scattering or cryo electron microscopy in combination with molecular dynamics (MD) simulations, shown in figure 1.5.[51, 61, 63–67] The mechanism by which integrin receptors are triggered to change their confirmation to activate or deactivate adhesion has long been controversial.[68] There are three conformational states of integrins on cell surfaces (figure 1.6) – two inactive, bent closed (figure 1.5a and 1.5b) and extended-closed as well as one active, extended-open (figure 1.5c).[62] According to one model, the deadbolt model,[69] integrin can be activated despite of a bent head domain through binding of a ligand and a consequent conformation change. This claim is supported by a range of experiments, that indicate no change in height of the extracellular domains after incubation liposomes containing reconstituted integrin in Mn^{2+},[69, 70] although it had previously been shown that addition of Mn^{2+} results in the activation of integrin.[46] On the other side a

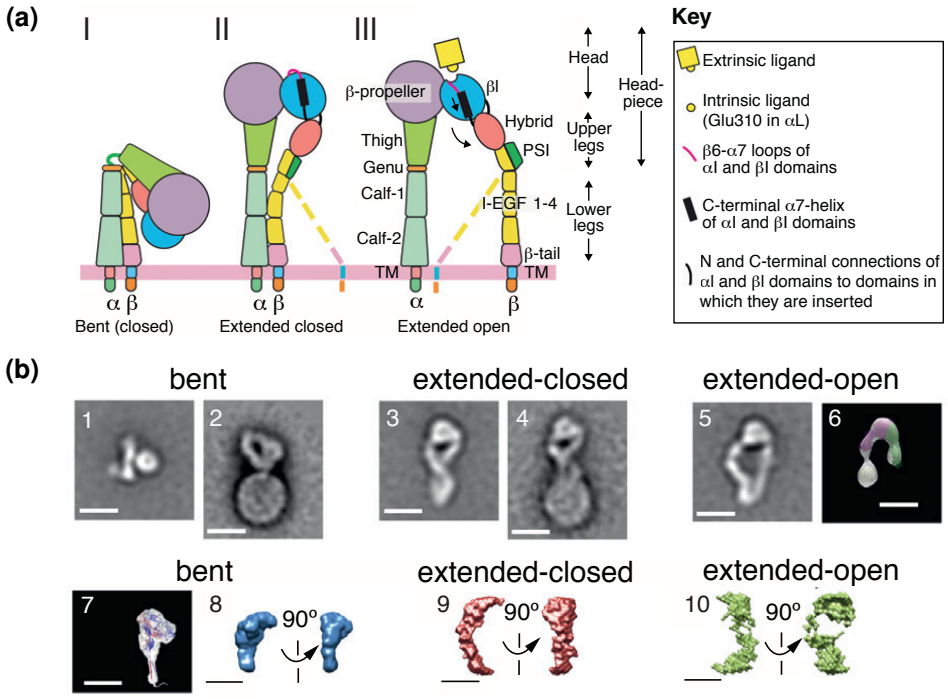

Figure 1.6.: The three overall integrin conformational states. (a) The bent conformation has a (I) closed headpiece and a low binding affinity. Extension at the α-knee and β-knee releases an interface between the headpiece and lower legs and yields an (II) extended-closed conformation also with low binding affinity. Swing-out of the hybrid domain at its interface results in the (III) extended-open conformation with an increase of the binding affinity by three orders. Image of (b) Integrin $\alpha_{IIb}\beta_3$ in detergent (1, 3 and 5 [58] and 6 [59]) and embedded in lipoprotein nanodisks (2, 4 [60]), with no additives (1 and 2), Mn^{2+} (3), talin head domain (4) and RGD peptides (5, 6). Negative stain electron tomography class average (6). Three-dimensional molecular envelopes of purified, detergent-soluble native integrin $\alpha_{IIb}\beta_3$ in solution determined by small-angle neutron scattering (7)[61] or X-ray scattering (8-10)[58] with no additions (7 and 8), Mn^{2+} (9), or Mn^{2+} and RGD mimetic (10). Adapted from Rpinger at al.[62].

switchblade model was proposed, where the integrin is first brought to its active confirmation before binding a ligand.[71] More recent results suggest that cytoplasmic regulators, such as talin and kindlin, mediate the conformational change of integrin and thus, activation is likely triggered from inside the cell, not through binding of a ligand.[50, 62] Therefore, the switchblade model is the more probable description of the integrin activation mechanism.

2. Synthetic Biology

SB is an emerging, complementary approach to traditional "classical" biology that applies engineering principles to design and assemble biological components.[72–74] Traditional cell-biologists apply the so called "top-down" approach, where genetic engineering is used to manipulate cellular processes and observe the effect. SB is an alternative approach, often referred to as "bottom-up", since the studied system is commonly build from the ground up, e.g. single proteins. SB can be broadly categorized into two branches. One uses mostly natural molecules to re-engineer emergent behaviors from natural biology, with the goal to understand the design principles of its functional moduls.[75, 76] The other seeks to design and construct new bio-inspired components such as enzymes, genetic circuits, or artificial cells.[75, 77]

2.1. Model Systems

The chemistry of life takes place in the microscopic, enclosed volume of cells. Its picoliter volume is even further subdivided into even smaller compartments by cellular organelles and vesicles. To understand processes at these small scales it can be beneficial to recreate compartments of the same dimensions to perform controlled experiments in such confined spaces.[78] This strategy constitutes the so called "bottum-up" approach, where the experimenter attempts to build up the observed system freed from the enormous complexity exhibited by cells. The three different complementary techniques for forming microscopic compartments are sketched in figure 2.1.

2.1.1. Lipid Vesicles

A common compartment used in SB are vesicles consisting of lipids, which have the advantage of mimicking the structure and dynamics of a cell membrane to a high degree.[79] This approach has been employed mostly in the first half of the research presented in this thesis and will be described in more detail in section 4.2.

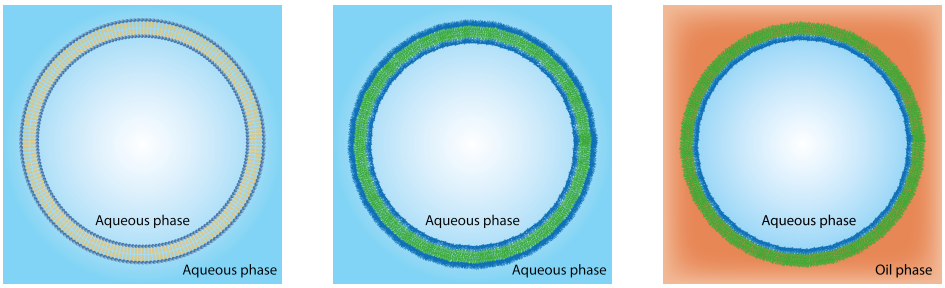

(a) Liposome **(b)** Polymersome **(c)** Water-in-Oil Droplet

Figure 2.1.: Schematic representations of three different SB compartment model systems. (a) Spheres consisting of a lipid bilayer, so called vesicles or liposomes, are the most traditional model system in SB. They mimic biological systems to a high grade. (b) Polymersomes replace the lipid bilayer by triblock polymers. These polymers can be modified to have special chemical or mechanical properties. (c) Technically water-in-oil polymer-stabilized droplets are also polymersomes. To avoid confusion and to distinguish them from older water-in-water polymersomes they are usually referred to as water-in-oil droplets.

2.1.2. Polymersomes

A parallel approach employs block-polymers instead of lipids for the self-assembly of cell-like confinements, so called polymersomes. These vesicles are made of amphiphilic copolymers that provide the compartments a higher stability, rigidity and longer lifetime than lipid vesicles.[80, 81] The use of artificial polymers allows to finely tune the properties of the interface, such as thickness, bending and stretching moduli and the permeability of the membrane. Polymers can also be tweaked to allow the incooperation of (transmembrane) proteins with controlled orientation via tethering to functional groups or antibodies.[82, 83] Currently, the most common method to prepare cell-sized polymersomes are electroformation and double emulsion techniques.[84, 85]

2.1.3. Droplets

An alternative approach, which experiences growing popularity since the beginning of the millennium, is the use of fluidic chips with channels and chamber in the order of micrometers, hence called microfluidics. This technology will be introduced in section 3. A method combining both polymersomes and microfluidics is droplet-based microfluidics. Here microfluidic chips are used to form self-assembled droplets at a flow junction between at least one hydrophobic and one hydrophilic phase. Similar to polymersomes, the droplet interface properties can be finely tuned using different block-copolymer surfactant molecules. The second half of the research presented in this thesis was based on this approach, it will be discussed in more detail in section 3.2.

2.1.4. Cellular Adhesion as a Model System

Since SB has come to prominence around the year 2000,[86, 87] the introduced compartment systems have been used for various applications. Due to its complexity, cellular adhesion (section 1.1) is a promising model system to be examined with the methods of SB. Moreover, to the best of my knowledge, there have so far only been a few studies reported in this field.[28, 88, 89] Probably the main cause that has constrained developments in this field is the low stability of lipid compartment systems.[90] Commonly in experiments with large vesicles surfaces are passivated, to prevent attractive forces, such as Van der Waals forces causing rupture of the lipid membrane. However, modelling of adhesion requires a protocell binding to a functionalized surface. Here, either the compartment can be strengthened, e.g. by adding a cytoskeleton, or the interaction can be tuned, e.g. by controlling ligand spacing, or adding a space such as a glycocalyx.

In the first part of this thesis the adhesion properties of traditional lipid vesicles with reconstituted integrin were studied. Due to the mechanical and chemical instabilities of lipid vesicles a further expansion of this approach was restricted. Therefore, the development of a new model system combining droplet-based microfluidics with a phospholipid bilayer is presented in the second part. However, first microfluidics will be introduced in chapter 3 followed by an overview on lipid model systems in chapter 4. This arrangement is due to contentual reasons, as microfluidics is a common method to form lipid vesicles and is therefore part of both chapters.

3. Microfluidics

With the development of soft-lithography technologies, the production of fluidic chips with micrometer scale structures in large quantities and at a low cost became widely available. Therefore, microfluidics experienced a wide adoption and an acceleration of its developmet.[91, 92] With growing access to this method to produce chips containing complex but microscopic fluidic structures, this technology was poised to advance a broad range of chemical and biological research. By way on miniaturization and parallelization microfluidics allows for the integration of multiple experiments into one single micro-fabricated chip. The picoliter-scale analysis coupled with the high integration of functionality results in a substantial leap in throughput.[93] Figure 3.1 gives a good example of these advantages. This technology has seen tremendous development over the last years, resulting in the adaptation into commercial products such as DNA microarrays.[94] The technology offers wide opportunities for biological,[95–97] chemical[97–99] and medical[100–103] research and applications, but only a fraction of its potential is yet unraveled.[104] With an ever growing palette of functional units in microfluidics, e.g. the integration of valves, which can also function as pumps,[105] electronics,[106, 107] and even logical elements [108, 109], single devices can now generate, handle and analyze samples with minimal user intervention.[93, 110]

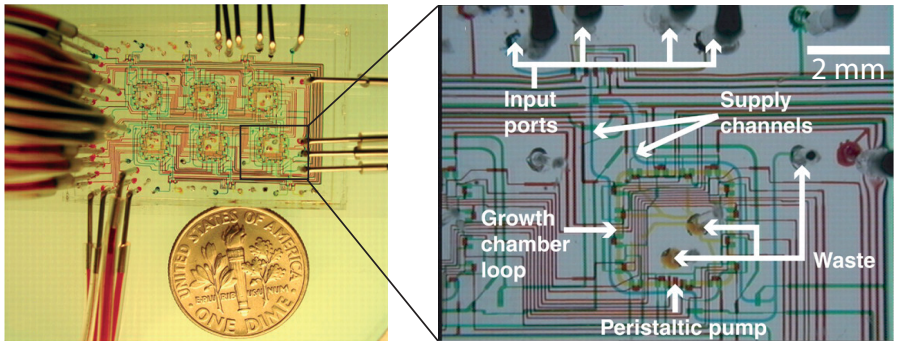

Figure 3.1.: Microfluidics allows the downscaling of many laboratory functions. The micrographs show six microchemostats that operate in parallel on a single chip. Various inputs have been loaded with food dyes to visualize channels and sub-elements of the microchemostats. On the left the whole structure is shown with a coin of $18\,mm$ in diameter as comparison. The optical micrograph on the right shows a single microchemostat and its main components. Adapted from from Balagaddé et al. [111].

The major aim of the research was to combine the high grade of biomimetic properties of liposomes, see section 4.2, with the advantages of droplet-based microfluidics, see section 3.2. Therefore, a new compartment assembly was developed overcoming restrictions of previous model systems. This novel system merges lipid vesicles with the high production rate of microfluidic droplets. This includes the possibility to sequentially add biomolecules via pico-injection droplet-based microfluidic technology.[106] Section 3.2 will discuss droplet-based microfluidics in more detail.

3.1. Fluid Dynamics of Microfluidics

A basic understanding of fluid dynamics, especially at small scales, is crucial to understand and design microfluidic chips. In our daily life, we experience nearly exclusively turbulent flows, e.g. a stone in a river will drag eddies behind itself, a vortex will form after the removal of the plug from in a bathtub. At these dimensions inertial forces dominate the dynamics of flows. But when scaling down to the level of cells and of course microfluidics viscous forces start to dominate. In these regimes the behavior of fluids changes quite drastically. This observation is quantified by the Reynolds number.

3.1.1. Reynolds Number

The concept of the Reynolds number was first introduced by Sir George Stokes in 1851,[112] but was later popularized and named after Osborne Reynolds in 1883.[113, 114] The dynamics of a fluid element are driven by the hydraulic pressure acting to accelerate it by overcoming its inertia and friction, given by its viscosity. The Reynolds number Re is defined as the ratio of these inertial forces to viscous forces acting on the element and consequently quantifies the relative importance of these two types of forces for given flow conditions.[113, 115] Mathematically this relation is quantified as

$$Re = \frac{\rho U L}{\mu}, \tag{3.1}$$

where μ is the dynamic viscosity, U is the mean velocity of the liquid, ρ is the density and L is a characteristic linear dimension of the system. The Reynolds number is a dimensionless parameter characterizing the flow regime. It is not a property of a fluid but rather a combination of fluid properties (ρ and μ) with geometric properties and flow velocity.[115] At high Reynolds numbers ($Re > 4000$) flows tend to be turbulent where viscous effects are mainly important in

narrow boundary layers. In a microfluidic context, the characteristic dimension L is considered to equal the hydraulic diameter of a channel,

$$D_H = \frac{4A}{P}, \tag{3.2}$$

where A is the cross sectional area and P the wetted perimeter of the channel. Inserting equation 3.2 in equation 3.1, results in

$$Re = \frac{4\rho_c AU_c}{P\mu_c}, \tag{3.3}$$

here the index c marks that these are properties of the carrier fluid. Due to the length scale and velocities this is the flow regime where cellular processes and microfluidics take place.[116]

As an example of the flow regimes in which microfluidics operates, the Reynolds number for the most common microchannels used in this research will be calculated. The properties of the carrier fluid, FC-40, are $\rho_c = 1855\,kg/m^3$ and $\mu_c = 4.1\,mPa\,s = 4.1 \cdot 10^{-3} kg/(m\,s)$, the channel has a rectangular cross-section with $L = 30\,\mu m$ side length and the volumetric flow is usually $500\,\mu l/h = 1.389 \cdot 10^{-10} m^3/s$. By inserting these values into equation 3.3, results in a Reynolds number for common microfluidic structures is in the range of

$$Re_{mf} = \frac{4\rho_c\, L^2\, Q/L^2}{4\, L\, \mu_c} = \frac{1.855 \cdot 10^3\, \frac{kg}{m^3} \cdot 1.389 \cdot 10^{-10}\, \frac{m^3}{s}}{3 \cdot 10^{-5}\, m \cdot 4.1 \cdot 10^{-3}\, \frac{kg}{m\,s}} = 2.095 \tag{3.4}$$

The consequences of low Reynolds number on the fluid dynamics will be addressed in the next section.

3.1.2. Laminar Flow

The general condition for laminar flow is a Reynolds number below $Re < 2000$ – a condition met by all microfluidic chips. Here that fluid flows in parallel layers, so called laminae[1], with adjacent layers sliding past each other without disruption.[113] In this flow regime there are neither cross-currents perpendicular to the direction of flow, nor eddies or swirls of fluids. Despite the laminae moving in parallel lines, they do not move at uniform velocities. If the mean flow speed along a tube is u, the layer in the centre is moving at approximately 2u, while the layers in touch with the wall are almost stationary due to the no slip boundary condition.[115]

[1]Latin: lamina, n. pl. laminae, a thin plate, sheet, or layer

In many microfluidic experiments a further condition for the flow regime is met – at Reynolds numbers below $Re \ll 1$ Stokes flow or creeping motion occurs.[117] In this extreme case of laminar flow viscous forces predominate over comparable small advective inertial forces.[118] Furthermore, the differential equations describing Stokes flow are reduced to a linearization of the Navier-Stokes equation.[118] Therefore, two interesting conclusions about the properties of stokes flow can be drawn:

> **Instantaneity:** A stokes flow is only time dependent if time dependent boundary conditions exist. In other words, there is no history dependence.
>
> **Time-reversibility:** An immediate consequence of linearization, time-reversibility means that a time-reversed Stokes flow solves the same equations as the original Stokes flow. This also means that is very difficult to mix fluids in this flow regime.[2]

These principles have to be taken into account when designing microfluidic chips. However, these can be used to the microfluidic engineers advantage: having parallel streams with little mixing or to create finely tuned gradients.[119] With this the theoretical considerations on fluid behavior can be concluded. In the following, practical guidelines for microfluidic chip design will be introduced.

3.1.3. Elementary Principles for Fluidic Networks

In high school physic teachers tend to explain electric circuits with the flow of water along ducts. Many microfluidic textbooks use the analogy of electric circuits to explain their fluid analog.[115] In actual fact, by replacing electric properties with their fluidic counterparts, the laws of electronic circuits can be transformed into fluidic ones. The following considerations are only valid for single phase flow. Ohm's law,

$$\Delta V = IR, \tag{3.5}$$

where ΔV is the change in electric potential, I the current and R the resistance, translates to

$$\Delta p = QR_H, \tag{3.6}$$

where Δp is the pressure drop, Q the volumetric flow rate and R_H the hydraulic resistance. A summary of further equivalent laws is shown in table 3.1. Most commonly, in microfluidics we are interested in the pressure cost of a structural unit at a certain volume flow. Continuing the electric circuit analogy, if N microfluidic

[2] There is still mixing due to diffusion.

structures are connected in series, the effective hydraulic resistance $R_{H,eff}$ equals the sum of all N hydraulic resistances $R_{H,n}$,

$$R_{H,eff} = \sum_{n=1}^{N} R_{H,n}, \tag{3.7}$$

as the same volumetric flow has to pass through all of them. This is not the case when structural units are placed in parallel. As the stream splits up the volumetric flow through each element is decreased. Again, the equation describing the effective hydraulic resistance $R_{H,eff}$ should be familiar from high school physics,

$$\frac{1}{R_{H,eff}} = \frac{1}{\sum_{n=1}^{N} R_{H,n}}. \tag{3.8}$$

As the hydraulic resistance can increase drastically for very thin channels, the design of a structure, as described in section 3.2.4, relied heavily on the principle described by equation 3.8.

Electrical relation	Fluid mechanical relation
$\Delta V = IR$	$\Delta p = QR_H$
$\sum_{n=1}^{N} I_n = 0$	$\sum_{n=1}^{N} Q_n = 0$
$P = I\Delta V = I^2R$	$P = Q\Delta p = Q^{2R_H}$
$R = \frac{L}{\sigma\pi a^2}$	$R_H = \frac{8\,\mu L}{\pi a^4}$

Table 3.1.: A list of electrical laws and their fluid analogs. For electrical systems, ΔV is the potential difference, I is the current, R is the resistance and σ is the conductivity of the material. With single phase non-compressible laminar flows, Δp is the pressure difference, Q is the volumetric flow rate, R_H is the hydraulic resistance, k is the permeability (k is related to the cross-sectional shape of the channel) and μ is the dynamic viscosity. In the last row of the table we compare the electrical and hydraulic resistance of a rod with a circular cross-section with radius a. [115]

3.1.4. Hydraulic Resistance of Common Ducts

Since it is useful to know the results of hydraulic resistance to estimate flows, shear forces, or the effect of a change in geometry, the solution for two common geometries will be presented, but largely without derivation. Many of the early microfluidic devices were fabricated using glass capillaries. For a tube of circular cross-section the Navier-Stokes equation can be easily solved. For the more

common channel geometry in microfluidics, the rectangular cross section, the hydraulic resistance is considerably more difficult to derive. Generally the hydraulic resistance of microfluidic chips can be found for any channel geometry by solving the Navier-Stokes equations for uniform, incompressible Newtonian fluids,

$$\rho\frac{\partial \mathbf{u}}{\partial t} = -\rho\mathbf{u}\nabla\mathbf{u} - \nabla p + \mu\triangle\mathbf{u} \tag{3.9}$$

where $\mathbf{u}$ is the velocity field, ρ is the density, μ the dynamic viscosity and p is the pressure. As it was shown in section 3.1.1, microfluidic flows are "nearly" instantaneous. Thus, in case of a a constant flow, it is sufficient to derive the solution for a fully developed ($\partial\mathbf{u}/\partial_z = 0$, where $\mathbf{u}_z$ is the direction of flow) and steady flow ($\partial_t\mathbf{u} = 0$). Focusing on laminar flows in a uniformly shaped ducts, there are no swirls and orthogonal flows ($u_x = u_y = 0$). In a circular tube the flow is also axisymmetric. Applying these conditions to equation 3.9 simplifies to

$$\nabla p = \mu\triangle\mathbf{u}. \tag{3.10}$$

The no slip boundary condition at the pipe wall requires that the speed of the fluid is 0 at the duct wall, $\mathbf{u}_{wall} \equiv 0$. Thus the solution for the velocity field for a tube of circular cross-section in cylindrical coordinates, also called Hagen-Poiseuille's law,[118] is

$$u(r) = \frac{1}{4\mu}\left|\frac{\mathrm{d}p}{\mathrm{d}z}\right|\left(a^2 - r^2\right), \tag{3.11}$$

where $\frac{\mathrm{d}p}{\mathrm{d}z}$ is the pressure gradient along the flow axis, which can be assumed constant for most microfluidic flows. The Poiseuille flow is characterized by a parabolic velocity profile. From equation 3.11 the volumetric flow rate,

$$Q = 2\pi\int_0^a u(r)rdr = \frac{\pi a^4}{8\mu}\left|\frac{\mathrm{d}p}{\mathrm{d}z}\right|, \tag{3.12}$$

can be derived. Hence the flow rate depends on the fourth power of the radius a. The moral here is that even small changes to channel diameters have a high impact on flow rates or pressure within the system. Note, here the analogy to an electric circuit breaks, as the electro-osmotic flow displays a flat velocity profile across a conductor and the resistance is only dependent on the cross sectional area. Since for most microfluidic devices a linear pressure gradient along each channel can be assumed, $\left|\frac{\mathrm{d}p}{\mathrm{d}z}\right|$ is often replaced by $\frac{\Delta p}{L}$. Therefore equation 3.12 can be simplified to a more practical form for microfluidics,

$$Q = \frac{\Delta p}{R_H}, \tag{3.13}$$

where the hydraulic resistance of a cylindrical duct is defined as

$$R_H = \frac{8\mu}{\pi a^4} L. \tag{3.14}$$

In general, this equation can be used as an approximation for non-circular channels, by replacing the radius a with the hydraulic radius $r_h = \frac{2A}{P}$, where A is the cross-sectional area and P the wetted perimeter.

Recalling the Reynolds number, see section 3.1.1 and especially equation 3.1, the average velocity U can be of interest,

$$U = \frac{Q}{\pi a^2} = \frac{a^2}{8\mu} \left| \frac{\mathrm{d}p}{\mathrm{d}z} \right|. \tag{3.15}$$

Combining equations 3.1 and 3.15, we see that the Reynolds number is proportional to the third power of the radius, $Re \propto a^3$.

As most microfluidic chips are produced using photolithography, the most common channel structure these days is rectangular. Deriving the exact solution for this problem is quite complicated. The commonly used approach is a Fourier series expansion of the channel cross-section, where the hydraulic resistance is given by [115, 120]

$$R_H = \frac{12\mu L}{wh^3} \cdot \psi^{-1} \quad \text{with} \tag{3.16}$$

$$\psi = 1 - \left[\frac{192h}{w\pi^5} \sum_{n=1,3}^{\infty} \frac{1}{n^5} \tanh\left(\frac{n\pi w}{2h}\right) \right]. \tag{3.17}$$

Usually it is sufficient to truncate the Fourier series in equation 3.17 after the first harmonics, since the error is below 1% for $h/w < 1$,

$$R_H = \frac{12\mu L}{wh^3} \left[1 - \frac{192h}{\pi^5 w} \tanh\left(\frac{\pi w}{2h}\right) \right]^{-1}. \tag{3.18}$$

This concludes the summary of basic principles concerning the fluid dynamics necessary for the design of microfluidic chips.

3.2. Droplet-Based Microfluidics

Forming compartments as reactors for biological and chemical reactions is obviously one key element for many chemical and biological experiments, especially for SB purposes. Through two-phase microfluidic devices aqueous droplets[3] can be generated for stable separation of chemicals, biomolecules and even cells.[121] Despite the fact that the potential of water-in-oil micro-emulsion droplets was already described in 1954 by Joshua Lederberg,[122] the first devices for the microfluidic generation of droplets using capillary systems were published in 2000 by Vyawahare et al. and Umbanhowar et al.[121, 123] Today most droplet-based microfluidic devices are made of polydimethylsiloxane (PDMS) using standard and soft-lithography methods.[92, 124]

Droplets are generated either in a hydrodynamic flow-focusing junction, where the aqueous flow is cut by the immiscible phase from two opposing orthogonal channels (cross-junction or flow focusing junction, figure 3.2a), or injecting an aqueous phase orthogonally into a flow of the immiscible phase (the T junction, figure 3.2b).[125–128] Daisy-chaining cross-junctions allows the formation of multiphase droplets.[129–131] In this work only cross-junctions were used. In both cases the aqueous flow is cut into distinct droplets. Encapsulated chemicals mix within milliseconds through chaotic convection and are not subject to diffusion or dispersion.[128, 132] Microfluidic chips allow for the generation of highly mono-disperse droplets, $< 1\%$ in diameter or $< 3\%$ in volume, [133] at a wide band of frequencies up to megahertz rates.[93, 121]

Beside the droplet formation units, there is a wide palette of functional units available to the microfluidic circuit engineer, see figure 3.3. There are various possibilities to manipulate formed droplets, for example to pico-inject additional aqueous solution into the droplet (see section 3.2.3) or to split them into daughter droplets (see section 3.2.4). Additionally, several methods have been proposed to sort droplets passively by size through channel geometry,[135] pillar arrays,[136] or Dean flows [137, 138] and actively through dielectrophoretic forces.[108, 109, 139]. The use of two layer devices also allows the implementation of gates and peristaltic pumps.[140] These are a few examples from a long list of functional units that can be integrated and combined in microfluidic chips.

[3] Like many other terms, the word "droplet" was first coined by William Shakespeare in his play "Timon of Athens".

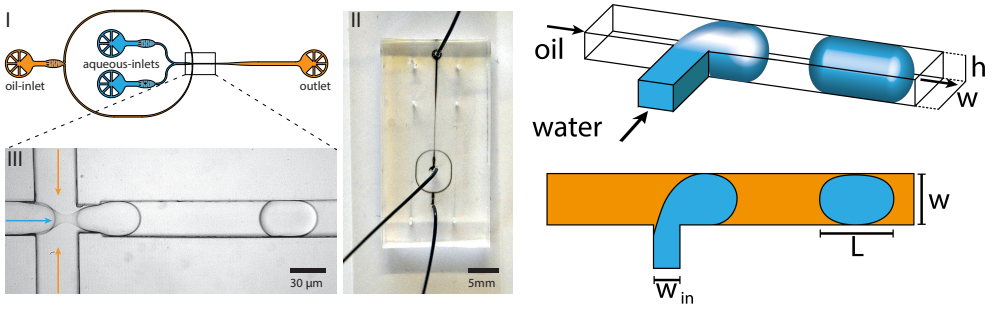

(a) Cross-junction **(b)** T-junction

Figure 3.2.: Two microfluidic junction geometries for droplet production. (a) Presentation of a microfluidic chip containing a flow-focusing junction used to generate droplets. I) A 2-D sketch of the chip as drawn in the CAD software. There are three inlets, one oil and two aqueous, in the left half and one outlet on the right side. Orange indicates channels carrying oil (pure or as continuous phase) and blue indicates the solely aqueous channels. II) Photograph of a microfluidic chip for droplet production. (The channels are filled with ink to provide contrast.) III) Droplets being generated in a flow-focusing junction. Adapted from Frohnmayer et al.[134] (b) Sketches showing a T-junction design.

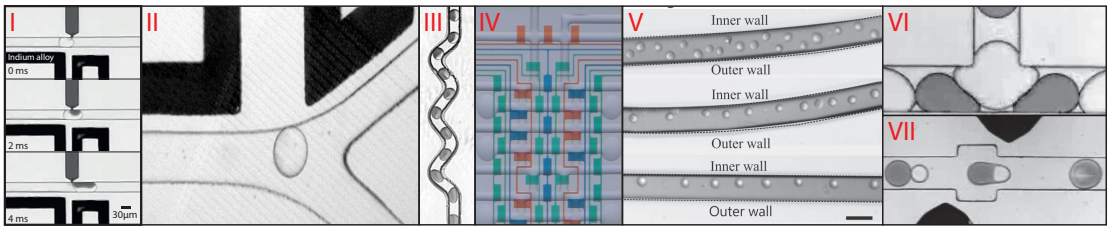

Figure 3.3.: Presentative microscopic pictures of common droplet-based microfluidic functional units. These include **I** pico-injection,[106] **II** droplet-sorting by changing the droplet trajectory through dielectrophoretic forces,[108, 109, 141] **III** droplet-content mixing through bending, **IV** two layer network of microfluidic channels (the colored control lines manipulate valves that function as gates and pumps),[142] **V** cell separation using Dean-flow in spirals,[143] **VI** dropsplitting in reverse-T-junctions,[120, 144] and **VII** droplet-fusion by electrophoresis .[145, 146] Figures IV and V have been reproduced from Squires et al.,[142] and Kemna et al., respectively. Figures VI and VII have been adapted from Baret et al. `http://sms.crpp-bordeaux.cnrs.fr/movies`.

3.2.1. Droplet Formation in two Phase Flows

Thus far, only the fluid dynamics of single phase flows were discussed. One of the important principles in the low Reynolds numbers regime is the laminarity of flows. That that posts the basic question, why do droplets form in the first place. Between immiscible fluids surface tension γ increases the free energy of the interface between the fluids and the dynamics are drawn towards reducing the interfacial area.[142] If there was no interfacial tension between water and oil, the streams would just flow parallel to each other in laminar sheets. As an example, a thin water stream breaks into droplets due to the Plateau-Rayleigh instability.[147–149] In 1873, Joseph Plateau determined experimentally that a vertically falling stream of water will break up into droplets if the column length is greater than about 3. 13 to 3. 18 times its diameter; later a more precise value of 3.143 ± 0.004 was obtained.[150] The theoretical value of π for this multiple was derived by John William Strutt, 3$^{\text{rd}}$ Baron Rayleigh.[147] Competing stresses drive the interface: Surface tension acts to reduce the interfacial area, while viscous forces act to extend and drag the interface in the direction of flow.[151, 152] These stresses destabilize the interface and tiny perturbations in the flow grow and cause droplets of radius r_d to form, thus reducing the free energy.[149] The resulting droplet size can be estimated by balancing the two stresses on the interface, Laplace pressure γ/r_d on one side, viscous stresses $\mu U/a$ on the other side:

$$r_d \approx \frac{\gamma}{\mu U} d = \frac{d}{Ca}, \tag{3.19}$$

where U is the flow speed, μ the dynamic viscosity and d the channel width (see section 3.1.4). Here we also introduced the capillary number

$$Ca = \frac{\gamma}{\mu U}, \tag{3.20}$$

a dimensionless parameter found whenever interfacial stresses competes with viscous stresses.[142, 152]

In the most common droplet formation structure, with a flow-focusing cross-junction, the calculation of droplet size is complicated due to the flow of the second phase and the channel geometry. Experiments showed that only slight variations in the channel geometry[153] and fluid viscosity[154] influenced the droplet size strongly. There are different flow regimes in a cross junction depending on the flow ratio $Q = \frac{Q_d}{Q_c}$ between the absolute volumetric flows of the dispersed Q_d and the continuous phases Q_c. These range from viscous displacement at low flow rates and high Q to jetting at high absolute volumetric flows, jetting mono-dispersed for small Q and jetting-plug for high Q.[155] The following droplet size estimations

are only valid for values of Q where mono-dispersed droplets are formed.

The earliest proposed solution by Ward et al. included only the flow rates of the dispersed Q_d and the continuous phases Q_c,[156]

$$\frac{l}{d} = \alpha \left(\frac{Q_d}{Q_c} \right)^{0.25}, \tag{3.21}$$

where α is a geometry and fluid property dependent coefficient.[156] Since the droplet is deformed through geometry constraints by the channel, not the radius r_d of an undeformed droplet, but the length l to width d ratio is given. Equation 3.21 fits well with experimental data for capillary numbers from 0.1 to 1. The model was further improved by including the capillary number explicitly,[157]

$$\frac{l}{d} = \alpha \left(\frac{Q_d}{Q_c} \right)^{0.2} Ca^{-0.2}. \tag{3.22}$$

More recently, the model was expanded based on theoretical considerations in combination with numerical results,

$$\frac{l}{d} = \left(\alpha_1 + \alpha_2 \frac{Q_d}{Q_c} \right) Ca^{-m}, \tag{3.23}$$

where $\alpha_{1,2}$ and m are fitting parameter.[158] The model was later confirmed by numeric simulations and expanded by viscoelastic models to predict the conditions for the onset of jetting.[159] Many microfluidic experimenter rely on experience when designing and operating a device. But especially for corner cases, knowledge of theory can prevent some tedious steps of trial and error.

3.2.2. Surfactants

Amphiphilic molecules called surfactants[4], short for "surface active agents", may act as detergents, wetting agents, emulsifiers, foaming agents and dispersants. These usually organic compounds stabilized the first vessels of life[160, 161] and to this day, in the form of lipids, they form the membrane which separates the cells of all known organisms from their environment.[1] Without this barrier, life would be thermodynamically impossible.[162] Moreover, with an annual world production of 15 $Mtons$ artificial surfactants, half of which are soaps, are also a major industrial product.[163]

[4]The word surfactant is often used synonymously for the pulmonary surfactant. However, in this work the term will be used solely for the chemical class of molecule.

Surfactants consist of both a hydrophilic (head) and one or two hydrophobic groups (tails). The latter usually consist of branched, linear, or aromatic hydrocarbon or perfluorinated chains. Surfactants are usually classified as non-, cat-, an-, or zwitterionic by the net charge of their polar heads, where zwitterionic heads contain two oppositely charged groups. Due to their amphiphilic structure, surfactants preferentially aggregate at the interface between two immiscible phases. This lowers the surface free energy by reducing the surface tension and removing the hydrophobic part from the water. The decrease of surface tension depends directly on the amount of molecules accumulated at the interface, as given by the Gibbs adsorption isotherm for dilute solutions,

$$\Gamma = -\frac{c}{RT}\frac{d\gamma}{dc_b}, \tag{3.24}$$

where Γ is the surface concentration, R is the gas constant, T is temperature, c_b the surfactant bulk concentration and γ the surface tension.[164] As surfactants aggregate at the interface between two phases, it rigidifies through the so called Maragoni effect.[165, 166]

Upon reaching the critical micelle concentration (CMC) the surfactants start forming aggregates, such as micelles, thus again decreasing the system's free energy by decreasing the contact area of hydrophobic parts of the surfactant with water.[167] The formation of micelles strongly depends on the CMC, which represents the lowest concentration at which excess surfactants form micelles.[168] The concentration of free surfactants stays constant. Other types of aggregates can also be formed, such as spherical or cylindrical micelles or bilayers, depending on their hydrophobic to hydrophilic ratio and overall structure. Below this concentration surfactants dissolve as monomers. A widespread definition of the CMC is

$$0 = \left(\frac{d^3\phi}{dc_t^3}\right)_{c_t \stackrel{!}{=} CMC} \tag{3.25}$$

$$\phi = a[micelle] + b[monomer] \tag{3.26}$$

where ϕ is the function of the tenside solution, c_t is the total concentration and a, and b are proportional coefficients.[169]

In emulsions, surfactants have the elementary role of preventing droplet coalescence – a requirement critical for droplet based-microfluidics.[170] Adding surfactants provides an energy barrier and by reducing the surface tension of the unfavourable large interfacial area, it lowers the overall energy level of the system, thus stabilizing the metastable state of a dispersion.[170, 171]

A wide variety of head groups, polar and non polar groups, have been tested.[172] The most commonly used head groups for biological applications are poly(ethylene glycol) (PEG) chains. PEG molecules passivate the droplet's inner interface and therefore minimize unspecific adhesion of proteins and other biologic compounds.[172, 173] Special synthesized surfactants that present specific binding sites on the inner surface of the droplet have been synthesized to functionalize the droplet's interface.[174]

The hydrophobic tail, usually consisting of hydrocarbon or perluorinated chains, is selected according to the chemical properties of the used oil. Generally, fluoro-based surfactants are considered to be more effective in stabilizing droplets and content retention compared to hydrocarbon-based surfactants of the same chain length and with the same hydrophilic head.[175, 176] This can be attributed to the difference in energy required to transfer a CF_2 group from bulk into micellar state in comparison to a CH_2 group.[175] The surfactant layer also functions as a steric barrier shielding the droplets from coalescence. The ability of a surfactant to stabilize droplets is mainly determined by the structure, length and chemical composition of the hydrophobic part and is quantitatively described as the hydrophilic-lipophilic balance (HLB),

$$HLB = 20\frac{H_w}{H_w + L_w}, \tag{3.27}$$

where H_w and L_w are the molecular weights of the hydrophilic and hydrophobic parts, respectively.[168, 177] HLB values range from 0 for a hydrophobic and 20 for a hydrophilic molecule.[176] For the stabilization of water-in-oil emulsions surfactants require a HLB value in the range on 1 to 10.[175]

The number of hydrophobic tail chains also influences the CMC of surfactants. Polymeric surfactants with a single tail chain are referred to as di-block, double-chained surfactants are called tri-block. Other factors are the hydrophilic and hydrophobic moieties, the nature of the solvent and the temperature. A high droplet stability can be achieved using surfactants with long hydrophobic fluorocarbon chains. They form a dense layer of 10 to 50 nm thickness.[173] However, surfactants exceeding a molecular weight of 20,000 DA are subject to slow diffusion and thus aggregation.[173] To prevent droplet coalescence it is vital to account for surfactant diffusion rates and adjust production rates and chip design accordingly. Furthermore, surfactants are vital for the retention of molecules within droplets, especially for molecules with a hydrophilicity in the range $0 > \log(D) > -7$.[178]

Here D is the ratio of the sums of the experimentally measured concentrations of the ionized and un-ionized forms of the compound in each of the phases,[179, 180]

$$D = \frac{[solute]_{oil}^{ionized} + [solute]_{oil}^{un-ionized}}{[solute]_{water}^{ionized} + [solute]_{water}^{un-ionized}}. \tag{3.28}$$

3.2.3. The Microfluidic Pico-Injector

A critical challenge for the adoption of droplet-based microfluidics for SB research was the development of a method to carry out multi-step reactions with precise and sequential addition of reagents to the droplets.[128] Omitting surfactants, this could be achieved by a simple T-junction.[181, 182] However, since the surfactants prevent reagents from entering the droplets, this method cannot be used with stable emulsions. This is a significant limitation, because stability is essential to ensure that droplets in contact do not merge and their contents remain isolated.[106] One approach is the controlled fusion of pairs of droplets either passively through channel geometry or actively through electrocoalescence, whereby an electric field destabilizes the droplet interfaces.[183–186] Since for each fusion two streams of droplets need to be perfectly aligned, it is a challenge to perform multiple additions and reagents will be strongly diluted with each step. To overcome these limitations Abate et al. developed the pico-injector, see figure 3.4.[106]

Towards this end, first, a spacer junction, a T-junction with oil phase flowing from the orthogonal channel, aligns preformed droplets with an even, adjustable distance. The space between the droplets was necessary to prevent neighboring droplets to coalesce. Second, the pico-injector consists of a pair of electrodes and a pressurized injection channel – commonly with these elements on opposing sides of the main channel. The injection channel narrows to a small slit, resulting in a high curvature between the aqueous solution and the oil in the main channel. This creates a high pressure differential between the channel, which is approximately determined by the Laplace pressure

$$P_{in} - P_{out} = 2\gamma/r, \tag{3.29}$$

where P_{in} is the pressure of the injection fluid, P_{out} the pressure in the flow channel, γ the water/oil surface tension and r the radius of curvature of the interface in the slit.

Abate et al. originally proposed to energize one electrode with a negative and one electrode with a positive potential, each time a droplet passes.[106] Today, usually the upstream electrode is used as a ground/shield electrode while a high frequency potential is applied to the downstream electrode.[107, 187] The surfactant layer at

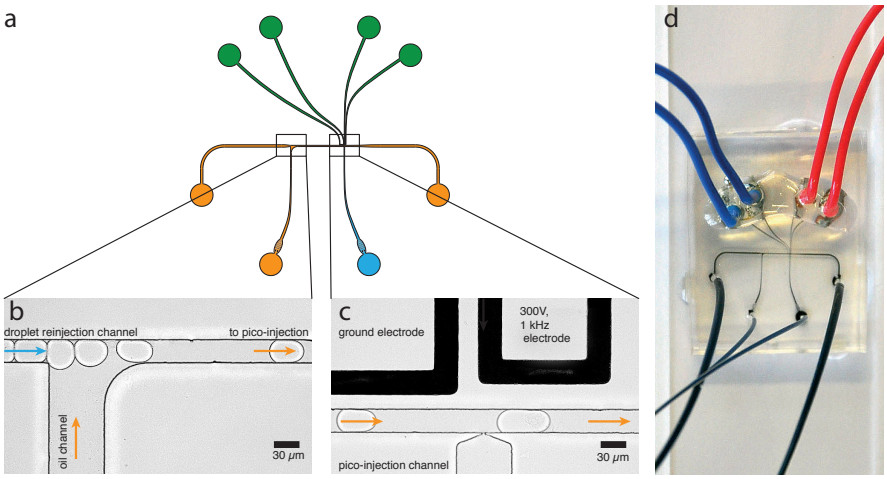

Figure 3.4.: (a) Structure of a droplet-based pico-injection device. (b,c) Bright-field images of the major features in a pico-injection device. Pico-injection technology allows the controlled injection of aqueous solutions into surfactant-stabilized droplets. (b) The spacing between the droplets is controlled through addition of oil via the second oil channel. (c) An electric field reduces the stability (poration) of the surfactant layer at the droplet interface and allows for injection of an aqueous solution containing reagants from the pico-injection channel. The injection process can be visualized by comparing the droplet size before and after the injection. (d) Shows an image of a microfluidic chip for pico-injection. The channels are filled with ink to provide contrast. Adapted from [134].

the water-oil interface ruptures due to an electrically induced thin-film instability, allowing the reagent from the injection channel to flow into the droplet.[184, 188] As the droplet progresses along the channel, it remains connected to the orifice of the injection channel by a narrow bridge of fluid until the surface tension is broken.

By placing several pico-injectors in a row, multiple reagents can be added sequentially, as shown in figure 3.5. Triggering the electrodes separately also allows combinatorial injections. [106, 190] The electrode material, commonly an expansive indium alloy with a low melting temperature, can also be replaced by salt water.[107] By adding electrolytes to the injection solution, electrodes can be ommited.[191]

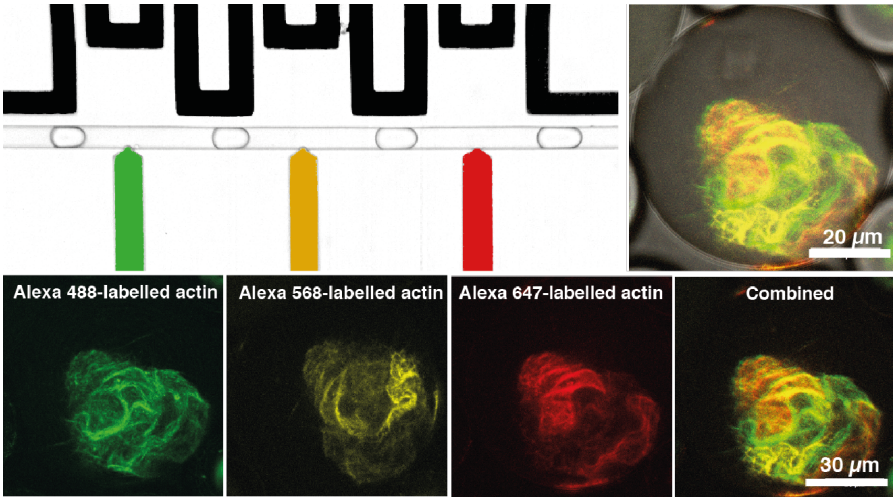

Figure 3.5.: A triple-pico-injector injecting G-actin labeled with different fluorescent dyes into droplets. The bottom row displays the actin networks generated through this pico-injection device. Picoinjectors could also be used in combination for serial and combinatorial injection. Adapted from Janiesch.[189].

3.2.4. The Dropsplitter

One of the challenges of this research was the generation of small droplets ($2\,\mu m$ diameter), for cryo TEM observation. This challenge requires the use of very narrow channel. In section 3.1.4 it was described that the hydraulic resistance of a $3\,\mu m$ rectangular channel is four orders, $\mathcal{O}(4)$, higher than of a $30\,\mu m$ rectangular channel. The obvious consequence is that downscaling of well known structures would not work. Therefore, a different approach was required.

To overcome the limitations associated with very narrow channels a droplet splitter, as designed by Link et al. in 2004[144] and improved by Abate et al. in 2009,[120] was adapted. The original idea consisted of a reverse T-junction, where a flow is split along two rectangular channels. Once a critical capillary number C_{cr} is reached, viscous and pressure forces break up the droplets into two daughter droplets. The critical capillary number depends on flow conditions, channel dimensions and the interfacial tension between the fluids (see equation 3.20). Below the critical capillary number, the droplets will randomly choose one path and remain intact. The critical capillary number was derived as

$$C_{cr} = \alpha\,\varepsilon_0(1/\varepsilon_0^{2/3} - 1)^2, \tag{3.30}$$

where α is a dimensionless coefficient, depending on the viscosity difference of the two fluids and the geometry and the initial droplet elongation $\varepsilon_0 = l/\pi d$. By adjusting the ratio of hydraulic resistances between the two forks, the flow rate and

consequently the relative size of the daughter droplets can adjusted, see section 3.1.3.

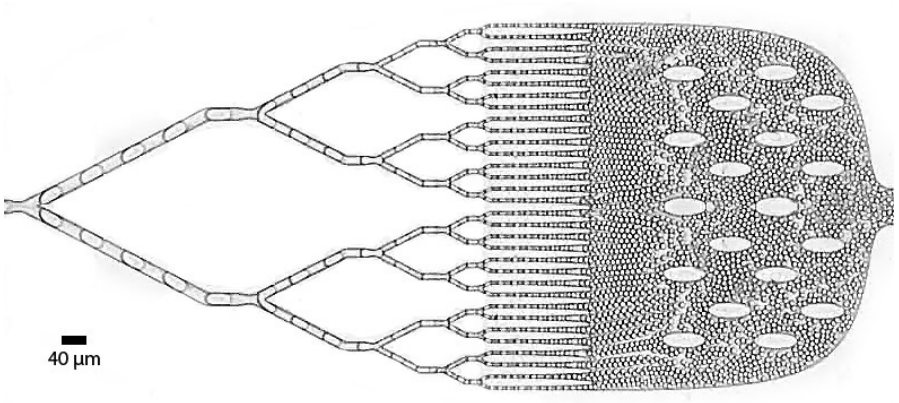

Figure 3.6.: Representative bright-field image of droplet-splitting array for production of monodisperse droplets at high throughput and small diameter. In this device droplets are split five times with the smallest channels only $3\mu m$ in diameter. A device with maximum six level of splitting units (splitting every droplet into 64 daughter droplets) with the smallest channels only measuring $2\mu m$ in width was developed in this research.

Additional splits can be added to break down the original droplets in two even smaller fractions, see figure 3.6. Each split halves the volume, so that every three divisions halve the diameter. However, the original design kept the channel dimensions constant and as the fluid is divided into an increasing number of channels, the flow velocity drops. Eventually, the capillary number falls below C_{cr} and splitting fails.[120, 192] This can be to some degree delayed, by increasing the initial flow rates. Abate et al. proposed the simple solution of decreasing the channel cross-section after each split, optimally by 50%. Thus keeping the capillary number constant. Here microfluidic engineer has to balance the increasing hydraulic resistance of each single channel (equation 3.18) and the reduced effective resistance R_{eff} (equation 3.8) of the splitting array.

An interesting implementation of the droplet splitting design was proposed, where a small arbitrarily angled side channel is used to collect a small volume droplet from the larger mother droplet.[193] This could be used to take probes of reactions within droplets, without destroying the overall integrity of the droplet.

4. Lipid Model Systems

Lipid membranes are an important structural unit of cells, as described in section 1. A lipid membrane confines a compartment that is the physical barriers of all cells. In the case of eucariotic cells further lipid membranes shape the subcompartments and form the various organelles. The thickness of lipid bilayers is estimated to be as thin as $4\,nm$. Moreover, small lipid vesicles with diameter of $50\,nm$ to $100\,nm$ are used by the cells for transport of different bio-reagents for necessary metabolism..[1, 194] Furthermore lipid membranes are the home of 27% of the human proteome – the transmembrane proteins.[195] Therefore, lipid bilayer is an obvious choice for protocell systems.

Lipids with a concentration above the critical CMC values (see section 3.2.2) in aqueous environments spontaneously form bilayers due to the amphiphilic nature of the molecules. The CMC for common lipids such as phosphatidylcholine (PC) can vary strongly from $0.46\,nM$ for 16:0 PC to $90\,mM$ for 5:0 PC[1] depending on their acyl composition.[196] Studies have found a significant and substantial allometric decline with increasing body mass in different species.[197, 198]

The most abundant types of lipids composing cellular membranes are phospholipids, sphingolipids and cholesterol.[199] Phospholipid molecules generally consist of a tail, two hydrophobic fatty acids, bound together by a glycerol molecule, the headgroup. Phospholipids are classified depending on the residue bound to the phosphate. Many headgroups have a residual negative charge under physiological conditions. Saturated lipid molecules have no multiple bonds between in their tail chains.

As the number of tails can vary from one to four, lipids differ greatly in shape. The molecular geometry of lipids strongly influences assembly into micelles, membrane structure, curvature and permeability as well as membrane-protein interactions.[2, 200, 201] The so called packing parameter (PP),

$$PP = v_m/a_0 \cdot l_C, \tag{4.1}$$

describes the relation between the molecular chain volume v_m, the optimal headgroup area a_0 and the maximal possible extension of the acyl chains. Phospho-

[1] Values taken from `avantilipids.com/tech-support/physical-properties/cmcs/`

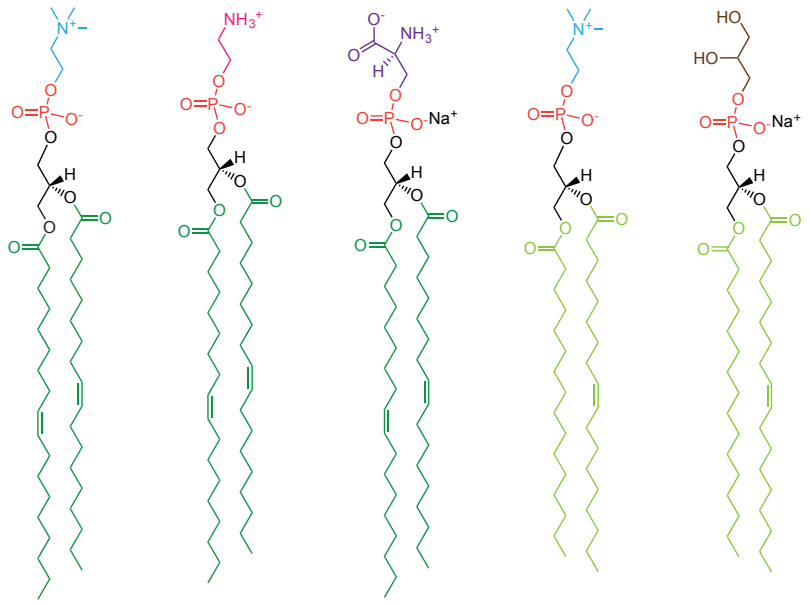

(a) DOPC **(b)** DOPE **(c)** DOPS **(d)** egg PC **(e)** egg PG

Figure 4.1.: Chemical structures of the most used lipids in this work: (a) 1,2-dioleoyl-sn-glycerol-3-phosphocholine (DOPC), (b) 1,2-dioleoyl-sn-glycero-3-phosphoethanolamine (DOPE), (c) 1,2-dioleoyl-sn-glycero-3-phospho-L-serine (DOPS), (d) L-α-phosphatidylcholine (egg PC) and (e) L-α-phosphatidylglycerol (egg PG). The two different fatty acid tails are colored green, the glycerol backbone in black, the phosphate group in red, the choline headgroup in light blue, the amine headgroup in pink, the serine headgroup in violet, an the glycerol headgroup in brown. Structures are taken from `https://avantilipids.com/` and were drawn with ChemDraw 15 (Perkin Elmer, USA).

lipids and sphingolipids have cylindrical shape ($PP \approx 1$). These self-assemble into a bilayer exposing their hydrophilic headgroups, shielding the hydrophobic tails from the surrounding aqueous phase. Cone shaped lipids, such as isyophospholipids and polyphosphoinositides, ($PP < 0.5$) normally form micellar aggregates with the hydrophobic lipid tails being located at the micelle core while the hydrophilic headgroups are exposed towards the aqueous bulk solution. Truncated cone-shaped lipids ($PP > 1$) form reverse micelles with the lipid tails directed towards the continuous phase and the hydrophilic heads at the micellar core enclosing small volumes of aqueous solution.[200] Biological membranes of living cells are in constant flux, consisting out of several hundred of different lipids and proteins.

Due to differences in phase transition temperatures, interactions between lipids and miscibility limitations, lipids composing a membrane can laterally demix forming rafts of different phase.[202, 203] In the fluid phase lipid molecules can diffuse

freely in the two dimensional membrane, while in the gel phase their position is fixed, resulting in a higher rigidity of the membrane. The longer the fatty acid chains are, the higher is the phase transition temperature due to increased Van-der-Waals interactions between the tails.

4.1. Supported Lipid Bilayer

Supported lipid bilayers (SLBs) are planar membranes formed on a rigid hydrophilic support such as glass or silica.[204, 205] Common methods for SLB formation are vesicle fusion, Langmuir-Blodgett deposition and the surfactant depletion method. When vesicles are exposed to a polar surface, such as oxygen plasma treated glass, they initially adhere and rupture to form planar bilayer patches.[206–208] Electrostatic interactions are an important factor for this process. However, Van-der-Waals and steric forces also play a role.[209, 210] Since all of these factors are influenced by surface properties and lipid composition, they are considered crucial elements for bilayer formation.[211] Neutrally or positively charged lipids – the latter are not existing in nature at physiological conditions – are more prone to the formation of SLB. For negatively charged lipids a concentration of bivalent cations, especially Mg^{2+} and Ca^{2+}, of $1\,mM$ or higher can be required to induce rupture.[206, 207] Recent findings suggest, that bilayer formation is not triggered by reaching a critical concentration,[212] instead single ruptured liposomes appear to form patches, which grow and merge until full coverage is reached.[204, 213] The growth of a SLB is shown in figure 4.2. Bearing this in mind, the possibility of an incomplete or patchy SLB if the reservoir of liposome is insufficient for full coverage exists.

4.2. Lipid Vesicles

A key factor of living cells is compartmentalization. A standard method in SB to encapsulate small volumes is the creation of lipid vesicles, so called protocells. These are spontaneously formed when dried lipids are exposed to water.[214] These spontaneously formed vesicles are typically multilamellar (many-walled, multilamellar vesicle, MLV) and of a wide range of sizes from tens of nanometers to several micrometers.[215] Methods such as sonication or extrusion through a membrane break these initial vesicles into single-walled vesicles of uniform diameter known as small unilamellar vesicles (SUVs), smaller than 100 nm and large unilamellar vesicles (LUVs), between 100 nm and a few micrometers. For cell size compartments, GUVs, usually several tens of micrometers, were developed. In comparison to SUVs and LUVs, GUVs can be observed with standard microcopy

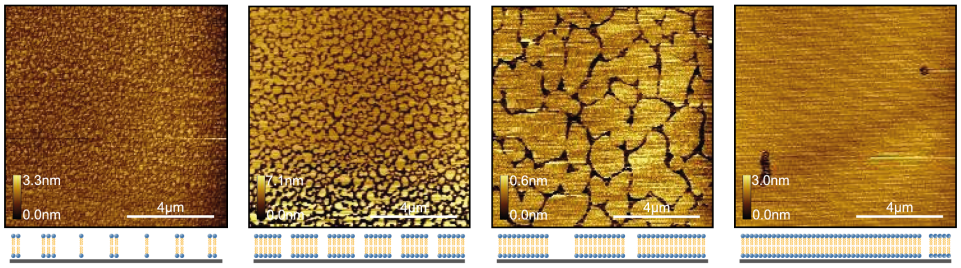

(a) after $5\,min$ **(b)** after $10\,min$ **(c)** after $17\,min$ **(d)** after $20\,min$

Figure 4.2.: Time series of a DOPC supported lipid bilayer formation acquired with AFM. Four separate samples of DOPC supported lipid bilayer on mica that were incubated for (a) $5\,min$, (b) $10\,min$, (c) $17\,min$ and (d) $20\,min$. Below each image is a sketch of the state of the lipid coverage on the the mica surface. The time series shows that an incomplete coverage with SLB patches is possible. These images were taken in pure water at room temperature. Adapted from Attwood et al. licensed under CC BY 3.0 / Lipid bilayer design has been harmonized with other figures.[213]

techniques. However, GUVs are mechanically and chemically unstable. Therefore their production is time consuming and at low yield compared to SUVs/LUVs.[216] A general note, a vesicle is not a state of thermodynamic equilibrium, but rather a kinetically trapped state.[215, 217]

4.2.1. Small and Large Unilamellar Vesicles

SUVs and LUVs have been hugely popular in research for a long time with applications ranging from drug delivery to SB.[218–221] SUVs/LUVs can easily be produced at a high yield by common methods such as sonication, which has been used since the 1950s,[222] extrusion,[223] and detergent removal. The latter allows for reconstitution of transmembrane proteins.[224, 225] These methods are sketched in figure 4.3.

Most protocols start by mixing the desired composition and amount of lipids solved in chloroform within a tainted glass vial. The solvent is then completely evaporated under a gentle stream of an inert gas. Afterwards, the lipid residue is rehydrated with the desired buffer at target concentration. At this point the protocols of the three different production techniques, presented here, diverge. In case of sonication and extrusion the solution is given time to allow the lipids to swell and form MLVs. Sonication with either a tip or a bath sonicator leads to SUVs of around $30\,nm$ in size depending on the lipid composition and sonication, as shown in figure 4.3a.[226] The main complications of this approach are lipid degradation caused by the high energy input and contamination with metal chips from the sonicator tip.

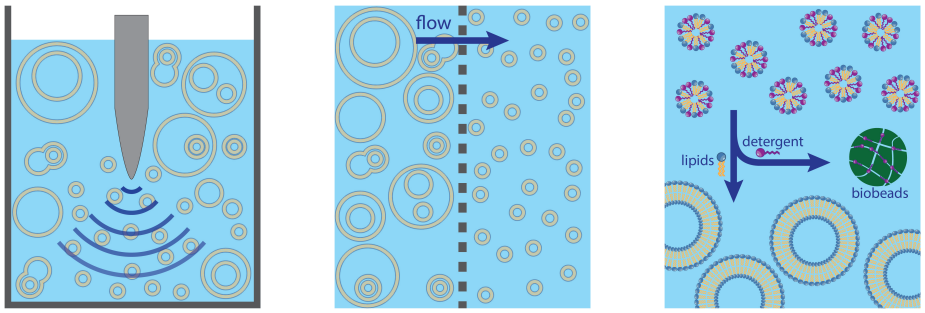

(a) Sonication **(b)** Extrusion **(c)** Detergent Removal

Figure 4.3.: Different methods of SUV/LUV preparation. MLVs are broken down into SUVs or LUVs through (a) sonication with a tip sonicator or (b) by extrusion through a porous membrane. (c) SUVs/LUVs formation by detergent removal, through porous polysterene beads that adsorb detergend molecules. Adapted from [57].

Alternatively the solution containing MLVs can also be extruded several times through a porous polycarbonate or anodized aluminium membrane yielding SUVs/ LUV, see figure 4.3b. The vesicle diameter can be finely tuned by choice of the pore diameter. Noting that the resulting vesicle diameter is relative to the pore diameter but generally considerably larger. With good quality membranes very monodispers vesicles can be produced. Normally around 9 passes through the membrane are sufficient to form unilamellar vesicles.[227] This method results in no detectable lipid degradation.[223]

In contrast to the two previously introduced methods, the detergent removal approach was introduced in the 70s to allow the reconstitution of transmembrane protein.[228, 229] Here the dried lipids are dissolved in a buffer containing a detergent and if required a transmembrane protein. The detergent shields the hydrophobic part of the transmembrane protein preventing denaturation. After incubation of the solution, the detergent is subsequently removed by either dialysis,[230, 231] gel filtration,[232] or by the addition of polystyrene beads.[233] The latter method is presented in figure 4.3c. Through the removal of detergent, the liposomes self-assemble with the transmembrane protein reconstituted into their lipid bilayer. These liposomes are normally referred to as proteoliposomes.

As SUVs/LUVs are to small to be observed with most optical microscopy techniques, their size distribution has to be measured with techniques like dynamic light scattering (DLS).[234–236]. Common method to analyze SUVs/LUVs are AFM and quartz crystal microbalance with dissipation monitoring (QCM-D), see section 7.

4.2.2. Giant Unilamellar Vesicles

GUVs are a widely used as protocells and, additionally they also used to study lipid membrane behavior because they closely resemble the basic membrane structure of biological cells.[237–239] Compared to SLBs, GUVs present better biological environment as there is no interaction with a nearby solid surface to induce friction defects or denature proteins.[240] Due to such advantages a variety of techniques to form GUVs have been developed. In the following sections some of these techniques will be described. These techniques are shown in figure 4.4.

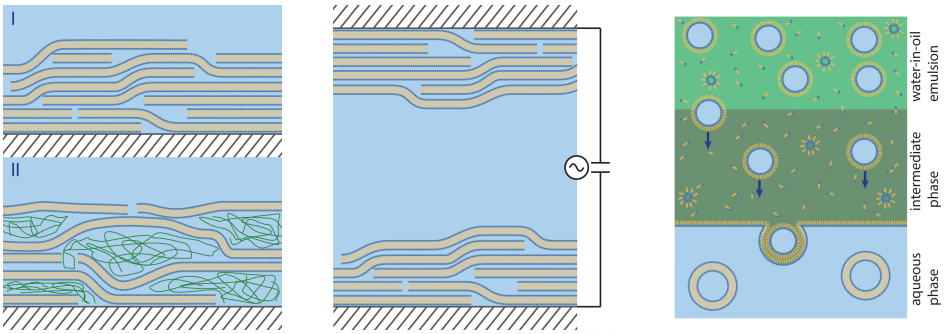

Figure 4.4.: Schematic representation of different methods for GUVs preparation. (aI) Gentle hydration of dried lipid layers. (aII) Modofoed gentle hydration method. In this method agarose or hydrogels are incorporated between the lipids. This method improves the encapsulation of molecules. (b) Electroformation: Under optimal conditions electroformation can form homogeneous GUVs and also allows the formation of GUVs with reconstituted transmembrane proteins. (c) Double emulsion based-methods: In this method leaflets of GUVs are formed separately. First a water-in-oil emulsion is created and then the water droplets are passed through a second lipid leaflet to an aqueous phase forming a complete GUV.

4.2.2.1. Spontaneous Swelling

Proposed in 1969 by Reeves and Dowben, this is the first published method for GUV formation.[241] Lipids are dried as for the formation of SUVs/LUVs (see section 4.2.1). They are then gently hydrated in purified water. Subsequently, the vial is left undisturbed for a period, generally a few hours, of time to allow swelling. The initial swelling conditions are depicted in figure 4.4aI. However, this method stands as a good example for the challenges faced when producing GUVs. If the flask containing the hydrated lipids is subject to shaking, the lipid layer ruptures and MLVs form.[242–244] Deposition of layers containing to many lipids has a similar effect.[245, 246] With this approach it is also impossible to grow large liposomes in a physiological buffer unless $10 - 20\,\%$ of negatively charged lipids are part of the composition.[247] However, when the buffer contains the

critical concentrations of cations, Mg^{2+} and Ca^{2+}, there is no GUV growth with mixtures containing negatively charged lipids. Instead, enhanced formation was observed with solely neutral lipid compositions.[248] Similarly, GUV formation can be achieved from lipid compositions containing pegylated lipids, i.e. lipids with a PEG-functionalized headgroup.[249] The PEG chains protrude from the membrane into the surrounding medium. This increases the repulsive force between the layers and promotes the growth of GUVs. It also has a stabilizing effect on the formed GUVs. Other factors like nanostructured surfaces,[250] temperature[251] and other additives, e.g. nonelectrolytic monosaccarides (glucose, mannose and fructose), can also play a role.[248]

4.2.2.2. Electroformation

In 1986 Angelova and Dimitrov proposed a method to improve GUV formation from thin films by applying an electric potential on the hydrated lipid layers.[252–254] The method is sketched in figure 4.4b. Under optimal conditions this method, known as electroformation or electroswelling, can lead to rather homogeneous GUVs.[255] Commonly the lipids are deposited on conducting surfaces, such as indium tin oxide-coated (ITO-coated) glasses, or platinum wires . TheGUVs are produced using direct current (DC) or alternating current (AC) potentials. Concerns that lipids, in particularly polyunsaturated lipids, might oxidate through contact with the electrodes, have been voiced. Therefore, a method applying an externally applied field has been shown to work.[256] For ion concentrations below $10\,mM$ frequencies of around $10\,Hz$ are used. It was long thought impossible to grow GUVs at higher salt concentrations. However, recent studies showed that GUVs can be prepared at physiological conditions unsig an AC field with a frequency of $500\,Hz$.[238, 257, 258]

Similar to spontaneous swelling the surface structure, e.g. micropatterns,[259] and chemistry[260] have an impact on vesicle growth. Moreover, lipid layer preparation method may also influence the GUVs generation. For example, homogeneous deposition of lipid films through spincoating results in twice bigger GUVs even with lipid compositions that do not work with standard electroswelling.[261] In contrast to spontaneous swelling, if the lipid composition contains too many charged lipids ($\sim 10\,\%$), growth of GUVs fails using standard electroformation.[262] The technique is not limited to lipids solved in chloroform. Aqueous solutions containing preformed SUVs or LUV can be used instead.[258] In this case, the lipid film was not completely dried after deposition, incidentally making the method more stable to high salt concentrations. The use of proteoliposomes allows the growth of GUVs preserving reconstituted transmembrane protein.[263]

The electroformation approach was adapted to grow GUVs in flow chambers[264] or microfluidic channels,[265] through which it was subsequently possible to replace the medium inside and outside of the grown GUVs.[266] This indicates a quite permeable bilayer, supporting the concerns that lipids might oxidize. It was shown that macromolecules could be entrapped during vesicle growth by a subsequent replacement of the outside buffer.[264] This intake appears to occur through lipid tubules interconnecting the vesicles.[266, 267] Generally with some reported exceptions,[264, 266, 268] both, the spontaneous swelling and the electroformation method, do not allow efficient encapsulation of large water-soluable molecules or charged compounds, as these molecules have to permeate the lipid film. An alternative approach is microinjection, puncturing individual vesicles with micro needles, into preformed GUVs.[269–271]

4.2.2.3. Gel-Assisted Formation

For many SB applications encapsulation of large molecules, such as proteins, is crucial. As discussed in the previous sections, both, spontaneous swelling as well as electroformation, provide partial solutions to encapsulation related issues and microinjection into preformed GUV has a low yield. For this purpose an interesting variation on the spontaneous swelling method using hydrogels can be employed. Here the lipid precursor is applied on a dry hydrogel, such as agarose,[272, 273] polyvinyl alcohol[274] and dextran(ethylene glycol).[275] The process is sketched in figure 4.4aII. Modulation of the degree of hydrogel network cross-linkage tunes the vesicle size distribution.[275] However, hydrogen polymers, especially agarose, can be encapsulated into the GUVs and can change their mechanical properties and reduce their stability.[276] MD simulations indicate that the encapsulation efficiency is dominated by the interaction of the proteins with the membrane, while no significant dependence on the size of the encapsulated molecule nor on the speed of the vesicle formation was found.[277] Gel-assisted formation works for many different lipid mixtures, covering a wide range of lipids with headgroups of zwitterionic, cationic or anionic nature.[274]

4.2.2.4. Emulsion-Based Methods

Emulsion-based techniques step away from spontaneous bilayer assembly. Instead by using emulsions the layers of the bilayer membrane, often referred to as leaflets, are formed separately.[273] Figure 4.4c sketches this two-step process. These methods commonly start by creating water-in-oil droplets. Lipids, which are solved in the oil, aggregate in a monolayer at the oil water interface and thus stabilize the droplets. To form complete GUVs, these droplets have to be enveloped by a second leaflet. The primary disadvantage of emulsion based techniques is that residual oil might be trapped in the final lipid bilayer, which might alter the rheological

properties of the membrane.[278, 279] However, on the other hand these methods can reach an encapsulation efficiency of 100 %.[273] Various techniques have been developed, to achieve this goal. Here we will discuss inverted emulsions and microfluidic formation as examples.

Inverted Emulsions The inverted emulsion technique starts by creating stable water-in-oil emulsions in lipid saturated oil. The water droplets are surrounded by a monolayer of lipids.[280, 281] The emulsion is then transferred to a tube containing two layered phases, on top lipid saturated oil (for example dodecane, squalene,[280] or mineral oil[281]) containing lipids and at the bottom aqueous phase. If the two phase system is incubated prior to the addition of the stable emulsion, a monolayer of lipids forms at the interface. Due to the density difference between water and oil, the droplets are pulled by gravity towards and across the interface. The planar monolayer at the interface wraps around the droplet moving across it, forming a complete GUV. The process can be accelerated by centrifugation[280] or addition of sucrose to the internal content of the droplets and equiosmotic glucose solution to the aqueous bulk phase.[282, 283] The separate formation of the two bilayers allows the preparation of GUVs with asymmetric transbilayer lipid compositions between the inner and out leaflet.[282, 284] This enables the tweaking of mechanical and dynamical properties of the membrane.[284–286] The production of inverted emulsion droplets with microfluidic techniques narrows their size distribution (see section 3).[281, 287]

Microfluidic Formation Microfluidic techniques are not limited to produce monodisperse water-in-oil droplets, but also water-oil-water double emulsions (see section 3).[278, 288–290] In double emulsion droplets an inner water droplet is surrounded by a thin oil shell, which in turn is surrounded by water – each of these interfaces are stabilized by a lipid monolayer. If the oil phase is thin enough it can shrink to an oil pocket, in an otherwise completely defect free GUV.[278, 291] By replacing the junction forming the second emulsion with a phase separation structure the inverted emulsion approach can be remolded.[292] Another approach is the replacement of oil by a non-water miscible volatile organic solvent, e.g. mixtures of toluene and chloroform.[289, 290]

This concludes the selection of techniques for the formation of GUVs. The full list of published methods is quite extensive, but many of the omitted approaches, such as microfluidic jetting,[293], or vesicle fusion are variations of the introduced methods, or difficult to implement, respectively.[294–297]

4.3. Reconstitution of Membrane Proteins

In principle, all methods for the formation of unilamellar vesicles, as presented in sections 4.2.1 and 4.2.2, can be modified to prepare proteoliposomes. However, for each method there are pros and cons that have to be taken into account.[298–301] Nevertheless, as illustrated, some of these techniques are fit better than others.

Organic solvents or high energy exposure may lead to denaturation. Therefore, detergents are a key ingredient for the extraction of membrane proteins from natural membranes,[57] it is obvious that detergent removal is currently the method of choice for the production of proteoliposomes. The detergent and the way to remove it, may differ between protocols and proteins, but the principle is preserved. The starting point of this approach is mixing and incubation of detergent, lipids and solubilized protein, which leads to the formation of lipid-detergent-protein and lipid-detergent micelles.[229, 233] The gradual removal of the detergent by different methods like dilution, dialysis, gel filtration, or adsorption into polystyrene beads promotes the growth of proteoliposomes.

In the detergent removal method, the critical element is to bring the detergent concentration below the CMC (see 3.2.2). The simplest way to achieve this is dilution, obviously. But there are some drawbacks, such as decreased concentration and the detergent removal limitations. Dialysis faces a similar challenge, it only works well with detergents with a high CMC. The method relies on the selective retention of a semipermeable dialysis membrane. This size exclusive penetrability only allows the passage of single detergent molecules. The rate is driven by gradient of the detergent concentration. Even if the outside buffer is exchanged regularly this method is still time consuming. Gel filtration in contrast is quite fast. Depending on the sample volume it takes minutes to hours.[302] Due to the rapidity of the removal, proteins may be reconstituted incompletely and inhomogeneously. Therefore, gel chromatography has largely gone out of fashion. The currently most widely used method is detergent removal via adsorption through porous, hydrophobic polystyrene beads, synonymously referred to by their commercial name “Bio-Beads”.[303–306] The main drawback of this method is concomitant adsorption of lipids. However, the capacity to adsorb lipids is two orders smaller than for detergents. This high difference in capacity could be related to the small pores of the polystyrene beads measuring only $9\,nm$ in diameter. Only minuscule molecules are able to penetrate into these channels. Where, the total surface area of the pores is four orders bigger than the outer surface of the bead. Nonetheless, adsorption capacity of the beads is an important factor that has to be taken in account.[233]

Girard et al. formalized a general strategy that combined detergent removal followed by electroformation to produce GUVs with reconstituted proteins.[57] Variations of the protocol were applied for the hydrophobic proteins such as bacteriorhodopsin, ATPase,[263] and SNARE[307] using gel filtration and voltage-gated potassium channel protein using polystyrene beads.[308, 309] Furthermore, electroformation was succesfully applied to natural membrane extracts.[239, 257, 310] As some proteins require high ion concentrations to preserve their conformation and/or functionality, it is important to mention that more recent developments have overcome the low salt restriction by using AC electric field frequencies of $500\,Hz$ (see section 4.2.2.2).[238, 257, 258]

Some proteins, e.g. OmpF[311] and the bacterial mechanosensitive ion channel proteins MscS (Small conductance mechanosensitive channel) and MscL (Large conductance mechanosensitive channel)[312], can be directly reconstituted into detergent destabilized GUVs. Another reported approach is the reconstitution of membrane protein into GUVs via peptide-induced fusion. Here proteoliposomes functionalized with the fusogenic peptide WAE (N-Trp-Ala-Glu-Ser-Leu-Gly-Glu-Ala-Leu-Glu-Cys) were fused into preformed GUV.[313] This method was further improved by the proposal of fusogenic (proteo-)liposomes – usually by charged mediated fusion.[314, 315] For SB cell model system it could be interesting to combine one of these techniques with a technique that allows effective encapsulation.

5. Motivation

Physics is the search for the underlying principle. From Newton's apple to gravitational wave detectors physicists have strived to find the basic rules governing the observed. At the heart of many complex processes are simple sets of laws. Newton's laws of motion stand as a good example.[316] Three simple laws are sufficient to describe the relation between force, matter and movement. Yet if we look at the world around, its complexity often diverts from seeing these fundamental principles. Something as simple as the outcome of a coin toss, can prove impossible to predict. Thus many experiments have been designed to isolate and reveal these underlying principles and describe them as the laws and theories of physics.

The subject of my study as a biophysicist has been life in its many facets. In itself life is one of the most elaborate processes. Even the basic building block of life, the cell, is overwhelming in its complexity. Applying the methods of traditional cell biology it can be a delicate to connect cause and effect in the multi-branched labyrinths of cellular signaling pathways. In the pursuit of finding these basic mechanisms that control these processes a complementary approach was developed, synthetic biology (SB). SB is the attempt of rebuilding functional units of biology isolated from the complexity of their original surrounding. The goal of these simplified model system is to keep the experiment as simple while controlling as many parameters as possible.

Excited by this approach, my research was focused on the development of a model system to study focal adhesions (FAs). FAs are complex sub-cellular macromolecular assemblies, consisting of a large number of proteins. Through them mechanical force and regulatory signals are transmitted between the extracellular matrix (ECM) and an interacting cell.[52] Currently 156 different components and 690 interactions with an average of 8.66 interactions per component have been identified.[6] The vision was to develop a FA model system that reduces the complexity to the minimal but still functional number of components. Moreover, the system should be adapted to technology allowing subsequent and sequential addition of components and to permit evaluation their exact function within the larger machinery. The basis of this system would be the cell-like compartment and the transmembrane glycoprotein integrin, which is the link between the cell interior and its surrounding.

As a cell can't exist without the lipid membrane enclosing it, the same is true for most SB model systems. For this purpose many approaches use lipid-based vesicles – so called protocells – as a compartment of choice. The obvious advantage of using a lipid compartment are the cell-membrane-like properties such as controlled structure, permeability, stiffness and diffusion.[161] However, as it became apparent during my initial research and literature a solely lipid-based compartment system poses many limitations that don't support my vision. Mainly due to the low mechanical and chemical stability of lipid vesicles,[90] it is very difficult to manipulate them after their creation and especially inject additional components into the protocell. As a conclusion I needed to develop a novel compartment system that will be more stable, yet preserved the biophysical properties of known protocells.

The sparking idea, the combination of water-in-oilemulsion droplets produced by microfluidic technology with lipid vesicles. Droplet-Based microfluidics offers impressive features such as kHz production rates of mono-disperse, stable polymer-stabilized emulsion droplets. Moreover, it offers a pico-injection method to inject a controlled amount reagents into preformed droplets at high-throughput.[106] Due to such advantages my motivation was to merge this technology with lipid vesicles. More specifically the major goals of my research were: 1) To use polymer-stabilized droplets as a stabilizing scaffold for lipid vesicles; 2) to implement pico-injection for subsequent and precise delivery of biological components – the basis concept of bottom-up assembly; 3) to reconstitute functional transmembrane proteins; 4) and if all of these would be achieved to recover the assembled protocells to a physiological environment.

Part II.

Materials and Methods

6. Proteins

Proteins are the chief actors within cells, their vast array of functions includes structural stabilization, catalyzing metabolic reactions, transporting molecules and vesicles and replicating, transcoding and repairing DNA. There is a plethora of different protein with various different shapes.[1] Many proteins, like a Swiss army knife, perform multiple functions.[317, 318] In fact, proteins are present in such abundance, that they make up for up to half the dry mass of a cell.[319] Therefore, to mimic functional units of cells any model system in SB requires high quality, functional proteins (or artificial alternatives). Due to the quality and purity of self-purified proteins being often superior to these commercially available – if available at all – the facilities to purify part of the proteins used in this work were established. An endeavour made largely possible by Christine Mollenhauer and Christian Eberhard. In the following sections the steps necessary to purify integrin $\alpha_{IIb}\beta_3$, section 6.2 and fibronectin, section 6.4 will be described.

Protein purification requires a set of common procedures from protein biochemistry, such as sodium dodecyl sulfate-polyacrylamide gel electrophoresis (SDS-PAGE), enzyme-linked immunosorbent assay (ELISA), ultracentrifugation and purification over specific gel filtration columns respectively affinity columns. As these methods are standard and can be found in any appropriate textbook, they will not be explained in this thesis.[320, 321]

6.1. Buffers

Buffers used for protein purification and reconstitution were prepared with ultrapure water ($\geq 18\,M\Omega/cm$, Millipore) and stored at $4°C$. The pH-values were adjusted with HCl solution. The following buffers were used:

Platelet washing buffer: $20\,mM$ Tris-HCl, pH 7.4, $150\,mM$ NaCl, $1\,mM$ EDTA, $0.01\,\%$ (w/v) acetylsalicylic acid

Platelet lysis buffer 1: $50\,mM$ Tris-HCl, pH 7.4, $1\,mM$ $CaCl_2$, $1\,mM$ $MgCl_2$

Platelet lysis buffer 2: $0.1\,\%$ (w/v) Triton X-100 dissolved in platelet lysis buffer 1

Elution buffer: 20 mM Tris-HCl, pH 7.4, 100 mM NaCl, 1 mM $CaCl_2$, 1 mM $MgCl_2$, 0.1 % (w/v) Triton X-100, 0.02 % (w/v) NaN_3

Column buffer: 20 mM Tris-HCl, pH 7.4, 150 mM NaCl, 1 mM $CaCl_2$, 1 mM $MgCl_2$, 0.1 % (w/v) Triton X-100, 0.02 % (w/v) NaN_3, 2 mg/l Aprotinin

Reconstitution buffer: 20 mM Tris-HCl, pH 7.4, 50 mM NaCl, 1 mM $CaCl_2$, 0.1 % (w/v)

6.2. Integrin Purification

The integrin $\alpha_{IIb}\beta_3$ purification protocol was adapted from Kai Peter[322] and established in our lab by Christian Eberhard and Christine Mollenhauer.[57] The purification process spans over three days. Normally, integrin $\alpha_{IIb}\beta_3$ was purified from $\sim 2\,l$ of outdated human blood platelet concentrate (within 14 *days* of venipuncture, Katharinenhospital Stuttgart, Germany).

Day 1: As the first step, contamination through other, mainly larger cells like erythrocytes and leukocytes were removed through differential centrifugation for 20 *minutes* at 1400 *rpm* ($\sim 300\,g$) at room temperature with a Sorvall RC6 centrifuge using an SLA 3000 rotor (both Thermo Scientific, USA). After the platelets were pelleted at 4000 *rpm* ($\sim 2700\,g$) for 30 *minutes*, the supernatant was replaced by platelet washing buffer and the pellet was resuspended. This washing step was repeated three times. The washed platelet pellet was resuspended in 100 ml platelet lysis buffer 1 and placed on ice. Platelets were broken with a Turrax homogenizer (IKA, Germany) in two 20 *seconds* intervals, adding two tablets of cOmplete protease inhibitor (Roche, Switzerland) during the first and one tablet during the second run. A sample to monitor the process with SDS-PAGE was taken. The lysis solution was then centrifuged with an Optima L-80 XP ultracentrifuge (Beckman Coulter, USA) for 30 *minutes* at 39,000 *rpm* ($\sim$ 120,000 g) at 4°C using a Beckman 45 Ti rotor (Beckman Coulter,USA). The platelet was then resuspended in 150 ml of platelet lysis buffer 2 and kept on ice. The platelets were further broken down during two 20 *seconds* intervals processing with the Turrax, adding one cOmplete protease inhibitor during each step. The solution was then rotated slowly at 4°C for one hour. A second sample was taken to monitor the process with SDS-PAGE. The solution was centrifuged using the ultracentrifuge for 15 *minutes* at 4°C at 19,000 *rpm*. The pellet was disposed and 1 ml of the supernatant was kept as third sample for documentation. The supernatant was loaded for affinity chromatography onto an equilibrated Concanavalin A column (GE Healthcare Life Sciences, USA) using an ÄKTA protein purification system

(GE Healthcare Life Sciences, USA) at $0.5\,ml/min$. The column was subsequently washed overnight at $0.2\,ml/min$.

Day 2: Elution buffer for the ConA column was prepared by adding $100\,mM$ mannose to the equilibration buffer and used to elude bound glycoproteins from the ConA column with a flow rate of $0.5\,ml/min$. The elution was collected in $5\,ml$ fractions. The fractions around the peak of ultraviolet (UV) detection were checked on their integrin content through SDS-PAGE. Fractions containing integrin were pooled, the rest was discarded. Next the pooled solution was applied to an equilibrated heparin column (GE Healthcare Life Sciences, USA) at $0.5\,ml/min$ for heparin affinity chromatography and the direct flow-through was collected in fractions. The fractions around the peak of UV detection were checked by SDS-PAGE for their integrin concentration. Again integrin-containing fractions were pooled, the rest was discarded. The pooled solution was concentrated to less than $5\,ml$ by ultrafiltration (Amicon Ultra-15, $50\,kDa$ MWCO, Merck, Germany). The concentrate was loaded to a Superdex 200 column (GE Healthcare Life Sciences, USA) and eluded overnight with elution buffer at a flow rate of $1\,ml/min$ and collected in $10\,ml$ fractions.

Day 3: Once again UV peak fractions were analysed by SDS-PAGE. The fractions of the highest concentrations and purity of integrin $\alpha_{IIb}\beta_3$ were filtered through a hidrophilic $0.22\,\mu m$ membrane and aliquoted. The purified protein was stored at $-80°C$. Biological activity of the purified integrin was determined by ELISA using AB1967 anti-integrin α_{IIb} antibodies (Merck, Germany).

6.3. Integrin Labeling

The protocol for integrin labeling with fluorescent dyes has been adapted from Kai Peter.[322] If necessary, integrin $\alpha_{IIb}\beta_3$ was concentrated by ultrafiltration (Amicon Ultra-15, $50\,kDa$ MWCO, Merck, Germany) to a concentration of $\geq 1mg/ml$ in column buffer. $10\,mg/ml$ 5-(and-6)-Carboxytetramethylrhodamine (TAMRA), succinimidyl ester (C1171, Thermo Fisher Scientific, USA) was dissolved in anhydrous dimethylformamide (DMF). Immediately, followed by the dropwise addition of $50\,\mu l$ of dye solution to $1\,ml$ of integrin solution, while swirling the container lightly. The solution was kept in the dark while being rotated at room temperature for one hour. The protein was separated from unbound dye via an equilibrated PD-10 desalting column (GE Healthcare Life Sciences, USA). The dye/protein ratio was determined through the molecular dye extinction ($\varepsilon_{555} = 92{,}000 M^{-1}cm^{-1}$ [322]) and protein extinction coefficient ($\varepsilon_{280} = 1.18 ml/(mgcm)$ [323]). Biological activity of the labeled integrin was determined by ELISA using AB1967 anti-integrin α_{IIb} antibodies (Merck, Germany).

6.4. Fibronectin Purification

Fibronectin, a glycoprotein, is most abundant in the blood plasma, in this case human blood plasma. The purification protocol relies on its specific, high-affinity binding to denatured collagen.[324] The following steps were performed at room temperature. First, the plasma was centrifuged at 10,000 g for 30 $minutes$ to remove erythrocytes or other particles by differential centrifugation. After phenylmethane sulfonyl fluoride (PSMF) and ethylenediaminetetraacetic acid (EDTA) were added to a final concentration of 100 mM and 10 mM, respectively, the supernatant was filtered by an equilibrated Sepharose CL-4B column (GE Healthcare Life Sciences, USA) to remove contaminants, e.g. fibrinogen. The flow-through was directly loaded to a Gelatin Sepharose column (GE Healthcare Life Sciences, USA), where the fibronectin bound to the gelatin. The process was monitored by UV detection at 280 nm. The column was washed with phosphate-buffered saline (PBS) buffer, pH 7. 4, until the optical density (OD) level returned the level of pure buffer. Bound fibronectin was eluded with 6 M urea in PBS, pH 7. 4, with a flow rate of 2 ml/min and collected in 2 ml fractions. The fractions corresponding to peak of UV detection were assessed by SDS-PAGE. The appropriate fractions were pooled and the final concentration was measured by absorbance at UV 280 nm. Fibronectin was sterile filtrated and stored by −80°C in PBS with 6M Urea. For use as a binding agent, fibronectin was dialysed against PBS, pH 7. 4. and subsequently stored at −20°C for about 4 weeks with no apparent deterioration.

6.5. Integrin reconstitution into Liposomes

Liposomes containing reconstituted integrin $\alpha_{IIb}\beta_3$ were prepared by adapting a protocol proposed by Erb and Engel.[325, 326] In brief, 50 $mol\%$ of egg PC and egg PG respectively were dried under a gentle stream of nitrogen and kept in vacuum overnight. Subsequently, the dried lipids were dissolved in reconstitution buffer and integrin $\alpha_{IIb}\beta_3$ at a 1:1000 integrin-lipid ratio was added. The solution was incubated at 37°C for 2 $hours$ in a shaker at 600 rpm. Triton X-100 was removed in two subsequent washing steps of 3. 5 $hours$ using 50 mg/ml SM-2 Biobeads. The size distribution of liposomes and integrin-liposomes was measured by DLS in a Malvern Zetasizer Nano ZS setup (Malvern, UK).

6.6. Peptides

Two peptides, named SN528 and SN529, were kindly provided by Prof. Horst Kesslers group at the technical university of Munich. Both contain the same RGD binding site. The peptides were designed for high binding affinity for integrin $\alpha_{IIb}\beta_3$. Their structures are shown in figure 6.1. In difference to SN529, SN528 contains a thiol group for immobilization on gold surfaces. SN529 was used for QCM-D experiments and SN528 was used to functionalize gold-linked surfactants.

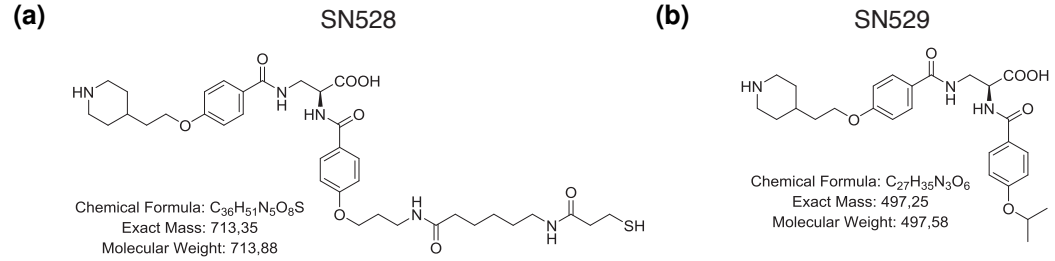

Figure 6.1.: Chemical structures of mimetic peptides SN529 and SN529. These compounds are tuned for high binding affinity to integrin $\alpha_{IIb}\beta_3$ and contain a binding site similar to the RGD motif. (a) A version of the molecule with a thiol end-group. This peptide was used to functionalizie gold nanoparticles on the inner interface of microfluidic water-in-oil emulsion droplets. (b) This version lacks the thiol group and was used in QCM-D experiments as a competitive binding site.

In addition to these custom highly specific peptides a commercially available RGD-ligand peptide was acquired. The chemical structure of Gly-Arg-Gly-Asp-Ser-Pro (GRGDSP, Sigma-Aldrich, USA) is shown in figure 6.2. The compound's molecular weight of 587 Da makes it 18% heavier than SN529. The peptide was used as a commercial comparison to the newly synthesized counterparts.

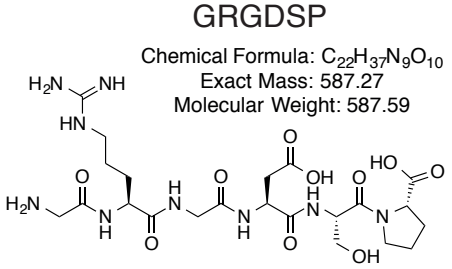

Figure 6.2.: Chemical structure of mimetic peptide GRGDSP. This compound contains a RGD binding site for integrin $\alpha_{IIb}\beta_3$.

7. QCM-D

Quartz crystal microbalance with dissipation monitoring (QCM-D) is a powerful method to study adhesion of lipid vesicles. The immobilization of intact liposomes on various crystal coatings has been extensively studied over the past years.[327–332] QCM-D experiments were also used for detailed analysis of the mechanisms of vesicle rupture and their transformation into SLBs in more detail. When a critical surface coverage of intact vesicles is reached on planar substrates, such as gold or SiO_2, they rupture and a SLB spreads out on the surface.[211, 333] The underlying kinetics of this process depend on many parameters including vesicle size,[327, 334] surface chemistry,[327] temperature,[327, 335] lipid charge,[207] osmotic pressure,[327, 336] membrane fluidity,[329] electrostatic interactions and the presence of bivalent cations.[337]

Quantifying the specific binding of proteoliposomes containing reconstituted integrin $\alpha_{IIb}\beta_3$ to ECM proteins by QCM-D analysis, gives an important insight into their potential as a model system for FA. To investigate the interaction between these protocells with biointerfaces, SiO_2 crystals were coated with different ECM proteins. Fibrinogen (purified from human plasma, Calbiochem, USA) and fibronectin (see section 6.4) were chosen because they are natural ligands of integrin $\alpha_{IIb}\beta_3$ and contain a RGD binding site. Collagen type I (calf skin, Sigma Aldrich, Germany) was chosen as a negative control to exclude unspecific interactions.[52] Furthermore, the controllability of integrin-mediated adhesion on fibrinogen coated crystals was studied by the effect of various free RGD-peptides in solution on adhered proteoliposomes and pure integrin. The results will be discussed in chapter 13.

7.1. Buffers

Buffers used for QCM-D experiments were prepared with ultra-pure water ($\geq 18\,M\Omega/cm$, Millipore) and stored at $4°C$. The pH-values were adjusted with HCl solution. The following buffers were used:

Standard buffer: $20\,mM$ Tris-HCl, pH 7. 4, $50\,mM$ NaCl, $1\,mM$ $CaCl_2$

Activation buffer: dissolve $1\,mM$ $MgCl_2$ and $1\,mM$ $MnCl_2$ in standard buffer

Protein coating	Protein binding	
	Frequency change $[Hz]$	Dissipation change $[10^{-6}]$
Fibrinogen	-98.9 ± 2.2	3.46 ± 0.06
Fibronectin	-74.3 ± 2.2	3.04 ± 0.07
Collagen	-151 ± 4	34 ± 1

Table 7.1.: Frequency and dissipation shifts as monitored by QCM-D after $2.5\,hours$ of coating SiO_2 crystals with different ECM proteins and an additional $30\,minutes$ washing step. Frequency decreases and increases in dissipation indicate successful ECM protein binding.

7.2. QCM-D Experimental Protocol

QCM-D (E4, Q-Sense AB, Sweden) was used to investigate the adhesion of pure liposomes and integrin-liposomes.The signals measured by the piezoelectric quartz crystal sensor were the frequency shift ΔF and the change in energy dissipation ΔD. SiO_2 coated sensor crystals (QSX 303, Q-Sense AB, Sweden) were cleaned with a 2 % Hellmanex III solution (Hellma, Germany) followed by oxygen plasma treatment at $150\,W$ with $0.4\,mbar$ for $30\,minutes$ (Gigabatch, PVA TePla Ag., Germany). A constant flow of $25\,\mu l/min$ through the measurement chamber was preserved through each experiment. The sample solution was continuously fed to the crystal chamber by a peristaltic pump (Ismatec IPC, IDEX, Germany) and the working temperature was retained at $21°C$. The resonance frequency and dissipation were measured at 6 harmonics (15, 25, ..., $65\,MHz$) simultaneously. The operating frequency analyzed for the results and reported here is the 7^{th} overtone ($35\,MHz$) and was normalized by the order of the overtone.

After equilibrating the system with activation buffer for $40\,minutes$ (step I), the crystals were coated with either fibronectin, fibrinogen or collagen diluted in activation buffer at a concentration of $50\,\mu g/ml$ (stepII). During the adhesion of the different ECM proteins over a periode of $2.5\,hours$ the frequency decreased and the dissipation increased accordingly. The absolute changes are listed in table 7.1 and shown in figure 13.3(b) to (d).

Binding of fibrinogen for $2.5\,hours$ and a consequent $30\,minuntes$ washing step (step III) with activation buffer led to a reduction from the initial resonance frequency by $\Delta F_{Fg} = (-98.8 \pm 2.2)Hz$ and an increase in dissipation by $\Delta D_{Fg} = (3.46 \pm 0.06) \cdot 10^{-6}$. For fibronectin the frequency and dissipation were shifted by $\Delta F_{Fn} = (-74.3 \pm 2.2)Hz$ and $\Delta D_{Fn} = (3.04 \pm 0.07) \cdot 10^{-6}$, respectively. Collagen binding led to a resonance frequency decrease of $\Delta F_{Fn} = (-151 \pm 4)Hz$ and a

dissipation increase of $\Delta D_{Fn} = (34 \pm 1) \cdot 10^{-6}$. After the washing step liposomes, integrin-liposomes or integrin were loaded into the flow system (step IV). Finally, in a fifth step the crystals were washed for 4 or more hours with activation buffer.

	Fibrinogen		Fibronectin		Collagen	
density	Voigt	Sauerbrey	Voigt	Sauerbrey	Voigt	Sauerbrey
1.150	16.1 ± 1.6	15.1 ± 0.3	17.4 ± 0.4	11.0 ± 0.6	56 ± 12	20.4 ± 0.5
1.300	14.3 ± 1.5	13.3 ± 0.3	15.0 ± 0.4	9.7 ± 0.5	54 ± 8	18.0 ± 0.5

Table 7.2.: Thickness estimates of the three different ECM protein films on SiO_2 crystals. The software QTools from Q-Sense was used to calculate the film thicknesses with the Voigt and the Sauerbrey model.[338, 339] The density of he protein layers was estimated using comparable values in both models.[340] The densities are given in $[g/cm]$ and the thickness is given in $[nm]$.

The thickness of the three different ECM protein layers on the quartz crystals was estimated according to the Voigt and the Sauerbrey model.[338, 339] The Sauerbrey model, a model for thin rigid films, provides a lower limit of the thickness for these viscoelastic protein layers. The Voigt model also takes the viscoelasticity of the film into account, thus yielding more accurate results. As densities of the protein coatings comparable values from literature in both models were used.[340] The fits were carried out using the software QTools (Q-Sense, Sweden) and are listed in table 7.2. The results estimate all protein layers to exceed $10\,nm$ in thickness. This indicates that the protein coatings form a closed layer and should prevent any direct interaction between the crystals and the samples.

7.3. Adhesion Kinectics

Here, it might be appropriate to add some theoretical considerations on the kinetics of adhesion. In the previously described experiments proteins or liposomes were flown from a reservoir over a quartz crystal coated with different protein. Some of the specimen bind with a given probability λ_1 to the functionalized surface. But the binding isn't an irreversible process as some of the adhered specimen dissociate with a given probability λ_2. This can be written as

$$n_u \underset{\lambda_2}{\overset{\lambda_1}{\rightleftharpoons}} n_b. \tag{7.1}$$

where n_u is the number of unbound vesicles in solution and n_b is the number of bound vesicles. Since the surface is small and we constantly renew the supply of vesicles we can assume that n_u is a constant,

$$\frac{\partial n_u}{\partial t} \equiv 0. \tag{7.2}$$

From equation 7.1 we derive the following function for n_b:

$$\frac{\partial n_b}{\partial t} = \underbrace{\lambda_1 n_u}_{x_1} \underbrace{(bs - n_b)}_{x_2} - \underbrace{\lambda_2 n_b}_{x_3}. \tag{7.3}$$

x_1: The binding of vesicles from solution to the surface with rate λ_1.

x_2: As the surface area is limited we have to introduce a restricting factor for the total amount of possible bound vesicles. Here bs is the number of possible binding spots and is defined as total area divided by the area available to each vesicle at the maximal packing density. Also a monolayer is assumed.

x_3: Vesicles unbinding from the surface depending on both the dissociation rate λ_2 and the number of bound vesicles n_b.

Integration of equation 7.3 yields an exponential recovery curve,

$$n_b(t) = \frac{\lambda_1 bs\ n_u - n_{b,0} \exp\left[-(\lambda_1 n_u + \lambda_2)(t + const.)\right]}{\lambda_1 n_u + \lambda_2}. \tag{7.4}$$

For many experiments the equilibrium or fixed point of this system can be of interest,

$$\frac{\partial n_b}{\partial t} \equiv 0. \tag{7.5}$$

Combining equatiosn 7.3 and 7.5 gives

$$0 \equiv \lambda_1 n_u (bs - n_b) - \lambda_2 n_b. \tag{7.6}$$

Rearanging equation 7.6 and abbreviating $\lambda \equiv \lambda_1/\lambda_2$ yields

$$n_b = \frac{\lambda_1 n_u bs}{\lambda_1 n_u + \lambda_2} \equiv \frac{\lambda n_u bs}{\lambda n_u + 1}, \tag{7.7}$$

which is also called Langmuir isotherm.[341] Following this calculation, an exponential saturation can be expected from the results. Whereby, the measured signal should converge against the Langmuir isotherm.

7.4. Plotting of QCM-D Data

The data collected during QCM-D experiments, was exported from a proprietary, binary format to a text file using QTools 3.1.21.593 (Q-Sense, Sweden). The data was plotted using the open-source software Gnuplot 4.6 (`http://gnuplot.sourceforge.net/`). The script plotting the data points acquired for frequency and dissipation against time is attached in the appendix II.1. The script also adds vertical lines indicating when a new reagent reached the analysis chamber.

Due to the complexity of adhesion dynamics, two further scripts were written. The first of these scripts plots the dissipation at given time point against the corresponding frequency. To indicate the progression of time, data points are color coded. Through this method changes in the conformation of adhering reagents can be made visible. The script is reproduced in the appendix II.2. The second script comprises of a function computing the shift between neighboring data sets and thus computing the first derivative of the measured data. As this method is highly susceptible to noise, the processing of the data included averaging over 5 or 10 (corresponding to 1 *second* or 2 *seconds* of measurement time, respectively) data points. The code computing this manipulation is added to the appendix II.3.

8. Droplet-Based Microfluidics Methods

The following chapter summarizes the materials and methods used for the microfluidic experiments in this work. This includes all the surfactants synthesis protocols, a step-by-step guide for the production of designs and clean room protocols. Finally, the design of the observation chambers used to image droplets with a microscope is presented.

8.1. Surfactant Synthesis

The essential factor for the stability of water-in-oil emulsion droplets are the surfactants aggregating at their interfaces as described in section 3.2.2. Nonionic fluorosurfactants consisting of perfluorinated polyether (PFPE) hydrophobic blocks provide their long-term stability by preventing coalescence, whereas PEG hydrophilic blocks serve as a biocompatible, inert droplet interface.[173] Optionally, to provide active sites for biochemical interactions within the droplets, surfactants that were covalently linked to gold nano particles (GNPs), with a diameter of $\sim 5nm$ can be added.[174] Mixed with gold-free surfactants at molar ratios ranging from 1:1000 to 1:2000, stable droplets with a inner surface, that can easily functionalized via thiol chemistry, can be formed. Most of the synthesis protocols were established by Jan-Willi Janiesch and he also performed most of the syntheses of most surfactants used during this research.

8.1.1. Triblock

The synthesis of the PFPE-PEG-PFPE triblock-copolymer surfactants was based on a protocol reported earlier,[173] but with several modifications.[174] The surfactants were synthesized using perfluorinated polyether (PFPE, Krytox FSH, Chemours, USA), with a molecular weights of $2500\,g/mol$ and $7000\,g/mol$ and poly(ethylene glycol) (PEG, Fluka, Germany) with molecular weights of $600\,g/mol$ and $1400\,g/mol$. Two different versions were synthesized, TRI2500 consisting of PFPE($2500\,g/mol$)-PEG($600\,g/mol$)-PFPE($2500\,g/mol$) and TRI7000 consisting of PFPE($7000\,g/mol$)-PEG($1400\,g/mol$)-PFPE($7000\,g/mol$).

All solvents (ultra dry) used for the synthesis were supplied by Sigma-Aldrich (Germany) and stored with a molecular sieve under nitrogen or argon atmosphere. The synthesis was carried out under argon atmosphere in dry tetrahydrofuran (THF)

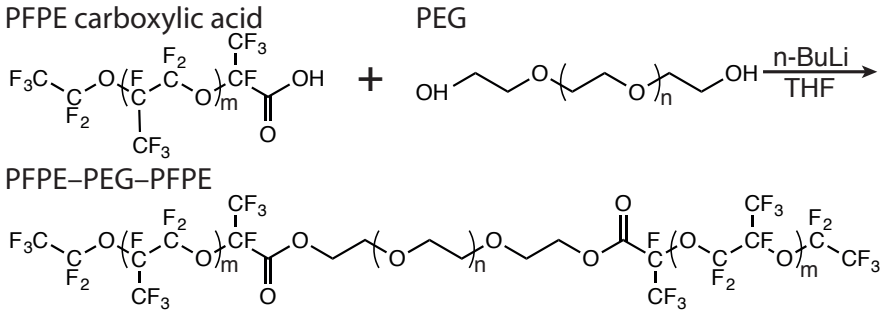

Figure 8.1.: Sketch of PFPE-PEG-PFPE triblock-copolymer surfactant synthesis. Taken from Frohnmayer et al.[134]

solvent in a tempered Schlenk-flask. In brief, $1\,mmol$ PEG was dissolved in $90\,ml$ of dry THF and cooled to -78°C. N-butyl lithium ($1.25\,ml$ of a $1.6\,M$ solved in hexane equaling $2\,mmol$) was added drop wise over a period of $60\,minutes$ to the PEG solution and stirred for additional $30\,minutes$ at -78°C. Thereafter, under continued stirring, the reaction is gradually brought to room temperature. Upon reaching room temperature $2\,mmol$ PFPE-carboxylic acid was added drop wise over a period of $30\,minutes$ and stirred for additional $2\,hours$. The THF was removed together with unreacted PEG using a separatory funnel. The product of the reaction was dissolved in 99.8% methanol to separate it from insoluble, unreacted PFPE-carboxylic acid. The PFPE-PEG-PFPE triblock polymers, which are soluble in methanol, were transferred to a clean flask and dried with a rotary evaporator at 40°C. The product was a clear and viscous liquid. The synthesized triblock surfactants were analyzed with nuclear magnetic resonance (NMR) spectroscopy and mass spectroscopy (MS).

8.1.2. Gold-linked Surfactant

Gold-linked diblock-copolymer PFPE($7000\,g/mol$)-PEG($350\,g/mol$)-Au surfactants were synthesized in a one-step process.[174] PFPE($7000\,g/mol$)-carboxylic acid ($9.3\,mg$, $1.3\,\mu mol$) and KOH ($10\,\mu l$ of a $5\,M$ solution) were added to $5\,ml$ functionalized GNP solution (11-Mercaptoundecyl)tetra(ethylene glycol), 2% w/w, nanoparticle diameter $\sim 5\,nm$ (Sigma Aldrich, Germany) and stirred for $1\,hour$ to achieve flocculation of the PFPE-PEG-Au product and of unreacted PFPE. Subsequently, the water was removed by freeze-drying the solution for $24\,hours$. The PFPE($7000\,g/mol$)-PEG($350\,g/mol$)-Au surfactants were dissolved in $1\,ml$ of fluorinated oil, FC-40 (3M, USA) and filtered with a hydrophobic filter (PTFE $0.2\,\mu m$) to remove unreacted, hydrophilic (11-Mercaptoundecyl)-tetra-(ethylene glycol)-functionalized GNPs.

Polymer	Full name	PEG moiety	PFPE moieties
TRI2500	PFPE(2500 $\frac{g}{mol}$)-PEG(600 $\frac{g}{mol}$)-PFPE(2500 $\frac{g}{mol}$)	$Mw = 600\ \frac{g}{mol}$ $\overline{n} = 12$	$Mw = 2500\ \frac{g}{mol}$ $\overline{m} = 17$
TRI7000	PFPE(7000 $\frac{g}{mol}$)-PEG(600 $\frac{g}{mol}$)-PFPE(2500 $\frac{g}{mol}$)	$Mw = 1400\ \frac{g}{mol}$ $\overline{n} = 30$	$Mw = 7000\ \frac{g}{mol}$ $\overline{m} = 48$
PFPE-PEG-Au	PFPE(7000 $\frac{g}{mol}$)-PEG(350 $\frac{g}{mol}$)-Au	$Mw = 350\ \frac{g}{mol}$ $\overline{n} = 4$	$Mw = 7000\ \frac{g}{mol}$ $\overline{m} = 48$

Table 8.1.: Molecular characteristics of the synthesized copolymers employed for droplet stabilization and functionalization. The structures of the triblock polymers are shown in figure 8.1 and the structure of the gold-linked diblock polymer is shown in figure 8.2.

8.1.3. Functionalization of Gold-linked Surfactant

To provide adhesion sites for integrin on the surface of gold-nanostructured droplets, see section 8.1.2, a two-step protocol was devised to functionalize the GNPs with a RGD-peptide, SN528 (see section 6.6), via thiol chemistry. The RGD peptide used in the experiments was designed and synthesized for maximum binding affinity for integrin $\alpha_{IIb}\beta_3$ by Dr. Stefanie Neubauer at Prof. Horst Kesslers group at the technical university of Munich.[342] The structure is presented in section 6.6.

Freeze-dried PFPE-PEG-Au diblock-copolymer surfactants were dissolved in $100\mu l$ of fluorinated oil FC-40 at a concentration of $25\mu M$. An aqueous solution containing the RGD peptides ($50\mu M$, $100\mu l$) was added and the emulsion was stirred for $1\,hour$. To remove unbound RGD peptides, the emulsion was centrifuged, sedimenting the heavier oil. Subsequently, the supernatant was discarded and the

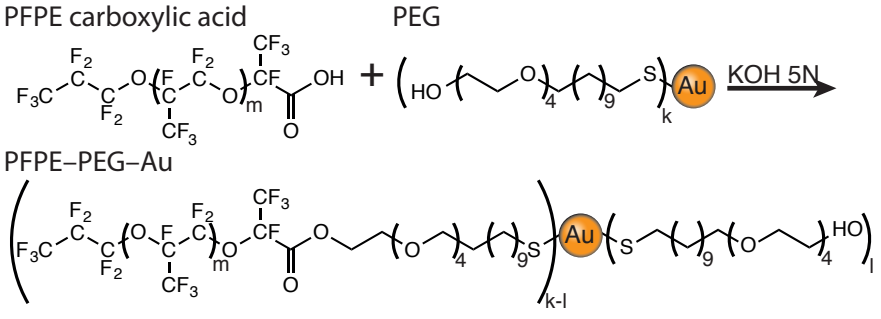

Figure 8.2.: Sketch of the synthesis PFPE-PEG-Au diblock-copolymer surfactants. Taken from Frohnmayer et al.[134]

precipitant was freeze-dried for 24*hours* to remove any remaining water. Finally, the product was dissolved in 1 ml of (the oil) FC-40 and filtered with a hydrophobic filter (PTFE $0.2\mu m$), removing traces of unreacted peptide.

8.1.4. Destabilizing Surfactants

Droplet-based microfluidics is often used to manipulate the content of the droplets. Therefore, it can be of interest to recover or extract the content of the droplets after processing them. The common approach to achieve this target has thus far been a bulk demulsification of droplets. By adding an additional aqueous layer followed by a demulsification reagent to a viol containing the to be broken up droplets.[174, 343, 344] In this work two different demulsification reagents were used 1H,1H,2H,2H-perfluoro-1-octanol or perfluoroctanyl-ethylen glycol (PFO-MEG) (Sigma-Aldrich, USA),[343, 344] and 2-(2-(2-Hydroxyethoxy)ethoxy)-ethyl 2,2,3,3,4,4,5,5,6,6,7,7,8,8,8- penta- decafluorooctanoate or perfluoroctanyl-triethylen glycol (PFO-TEG).[174] The chemical structures of both demulsifiers are shown in figure 8.3.

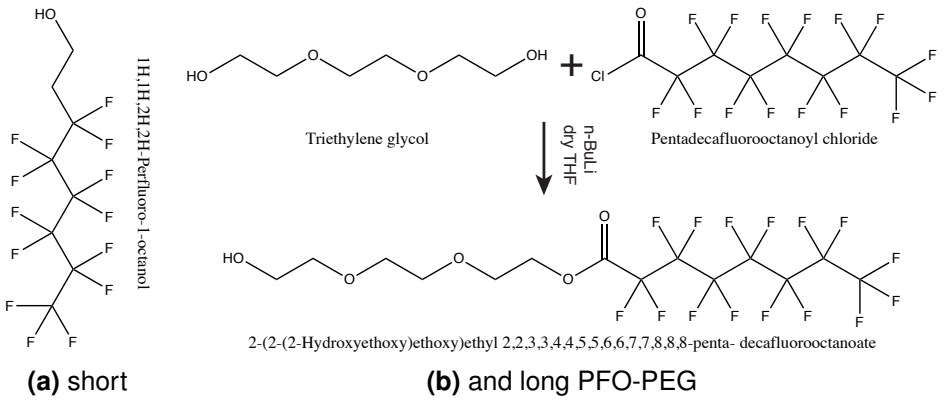

(a) short **(b)** and long PFO-PEG

Figure 8.3.: Chemical structures of demulsifying (destabilizing) surfactants. (a) 1H,1H,2H,2H-perfluoro-1-octanol acquired from Sigma-Aldrich (USA) and (b) 2-(2-(2-Hydroxyethoxy)ethoxy)ethyl 2,2,3,3,4,4,5,5,6,6,7,7,8,8,8-penta- decafluorooctanoate was synthesized in the group. Figure (b) was adapted from Platzman et al.[174]

PFO-TEG was synthesised under Argon atmosphere in a tempered Schlenk-flask. $6.36\,g$ of triethylene glycol ($MW = 208.5\,g/mol$, Sigma-Aldrich, Germany) were dissolved in $200\,ml$ dry THF and cooled to $-78°C$. $18.5\,ml$ of an $1.6\,M$ solution of N-butyl lithium dissolved in hexane was added drop wise over the course of $1\,hour$ and subsequently stirred for $30\,minutes$. Under continued stirring the solution was brought to room temperature and stirred for an additional $30\,minutes$. $12.7\,g$ of pentadecafluorooctaoyl chloride ($MW = 432.51\,g/mol$, Sigma-Aldrich,

Germany) was added drop wise over the course of 30 $minutes$ and stirred for an additional 4 $hours$. Thereafter, the THF and unreacted triethylene glycol were removed through a separatory funnel. The crude product was washed with 10 ml of pure water to remove the lithiumchloride. Following the washing step the crude product was dried in vacuum and purified using column chromatography. The column was filled with a silica gel and a 2:1 petroleum ether (60/40) and THF mixture was used as mobile phase. The PFO-TEG was analyzed with NMR spectroscopy and MS.

8.2. Oil-Phase

For droplet-based microfluidics the surfactant concentration should be in the range between 1 and 20 mM. In general, lager droplets require a lower surfactant concentration than small droplets. A lower surfactant concentration reduces droplet stability.[345] A high concentration causes an incomplete cut-off during droplet creation and the formation of small intermediary droplets. Additionally, at high surfactant concentration diffusion biomolecules into the oil phase is enhanced due to small surfactant micelles.[178] For most experiments, following synthesis, TRI7000 and TRI2500 surfactants were mixed separately with gold-linked surfactants and were dissolved in FC-40 (3M, USA) to final concentrations of 2.5 mM and 3 μM for triblock and gold-linked surfactants, respectively. These mixtures were used as oil phases in the droplet-based microfluidic experiments in this work.

8.3. Device Production

The overall design of microfluidic devices has evolved drastically since the onset of the technology. Whereas the first generation microfluidic chips were mostly based on glass capillaries, the majority of modern chip designs have adapted photo- and soft-lithography methods in their production. These technologies have boosted new developments by allowing complicated geometries including steps in hight or even multi-layer devices. There might be a new revolution dawning on the horizon with the emerging of micrometer scale 3D printers such as the nanoscribe.[346, 347] However, as the focus of this work lies on application, Ockham's razor[1] was applied to all designs in this thesis. As the emphasis was not on the possible, but rather on how much could be achieved with simple means, only the basic soft-lithography techniques were necessary. The following subsections and figure 8.4 summarize the steps necessary to produce a microfluidic device.

[1] Ockham's razor or lex parsimoniae is a problem-solving principle that states among competing hypotheses, the one with the fewest assumptions should be selected.

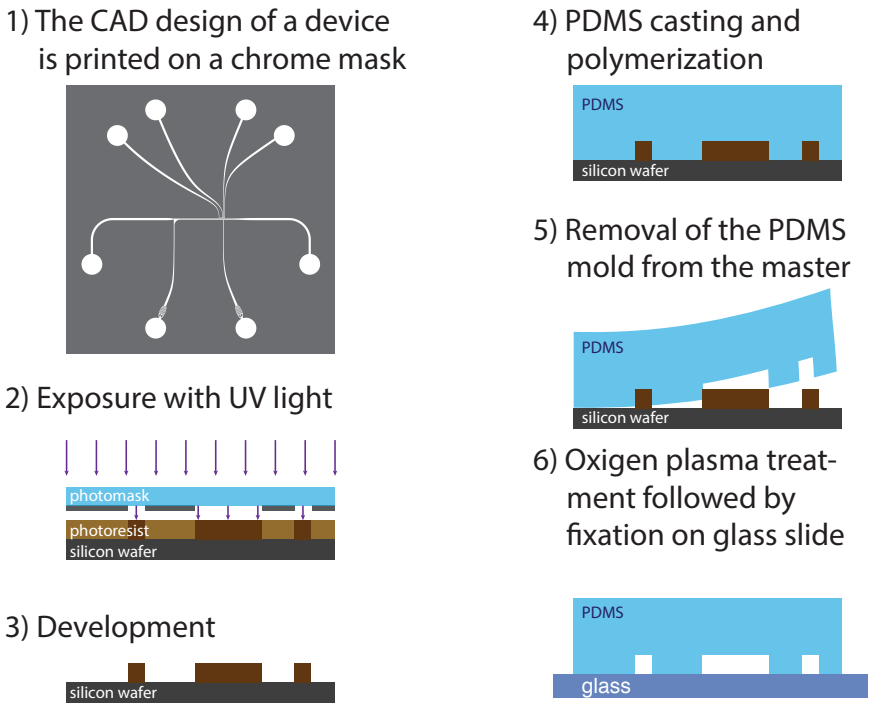

Figure 8.4.: Schematic representation of the steps to produce a microfluidic device. Step 1: The structure is drawn using CAD software and printed on a chrome coated soda lime glass via ion-etching. Step 2: A silicon wafer coated with negative SU8 photoresist is then exposed with UV light through the mask. The UV radiation triggers polymerization of the photoresist. Step 3: The unpolymerized photoresist is washed away with developer. Step 4: PDMS is poured on the the silicon wafer containing the master. Step 5: The cured PDMS cast is removed from the master. Step 6: A glass slide and the PDMS were briefly exposed to an oxygen plasma and then pressed against each other to guaranty fixation. Adapted from Frohnmayer et al.[134]

8.3.1. Design of Microfluidic Structures

A two-dimensional design of the desired device structures was drawn with the computer aided design (CAD) software QCAD-pro (version 3.15.4, Ribbonsoft, Switzerland). A negative of the structure, the channels transparent with the rest opaque, was printed on a chrome coated soda lime glass via ion-etching (JD PHOTO DATA, UK).

8.3.2. Photolithography

The mask was used for standard contact photolithography to obtain a positive relief on a silicon wafer. Different viscosities of SU8[2] negative photoresis (MicroChem, USA) were used to achieve structure heights ranging from $5\,\mu m$ to $80\,\mu m$ on silicon wafers. The process sheets provided by MicroChem were a reasonable starting point, but some alteration and additions were necessary to achieve an optimal result.

photoresist type	3005	3025	2075
structure height	$5-6\,\mu m$	$30\,\mu m$	$80\,\mu m$
prespin $10\,s$	$500\,rpm$	$500\,rpm$	$500\,rpm$
spin $30\,s$	$2750\,rpm$	$2750\,rpm$	$2750\,rpm$
softbake at 65°C	–	$2\,min$	(temperature-
softbake at 95°C	$3\,min$	$5\,min$	parabola)
exposure	$16\,s$	$7\,s$	$12\,s$
hardbake at 65°C	–	$2\,min$	(temperature-
hardbake at 95°C	$3\,min$	$5\,min$	parabola)
developping	$20\,s$	$2\,min$	$10\,min$

Table 8.2.: Summary of the photolithography experimental settings relevant for the structures in this work. As microfluidic chips with three different structure heights were used, the protocol needed to be adapted for three different types of SU8 negative photoresist. The roughly linear relation between structure height and exposure time apparently breaks at very fine structures, $\sim 2\mu m$, these only developed properly at long exposure times. For thick coating, especially when larger areas were cured, the photoresist tended to detach from the SiO_2 wafer if a classical two step hardtbake was used. Therefore, a gradual temperature parabola starting from $65\,$℃ heating to $95\,$℃ and cooling back to $65\,$℃ using the hotplates thermal inertia, reduced stressed to to rapid temperature changes and greatly improved the attachment.

Photolithography was done in a class 100 cleanroom with special UV-light free illumination to guaranty optimal conditions. Silicon wafers (Prime CZ-Si wafer $2inch$ or $4\,inch$, p-type (Boron), $1-10\,\Omega/cm$, MicroChemicals, Germany) were backed at 200°C before use to remove any moisture. Wavers were fixated on a spin

[2]The different types of SU8 can be distinguished by number consisting of up to four digits. The first two number denote the generation of the photoresist, 20 for 2nd and 3rd generation, the first generation lacking these digits. The last two digits indicates the approximal intended structure height.

coater and dust was removed with a nitrogen gun. $1\,ml$ of SU8 photoresist per inch wafer diameter was applied using a $10\,ml$ pipette. The orifice of the pipet tip was widened by removing part of the tip with a scalpel for SU8-2075 due to the high viscosity of the photoresist. The wafers were spin-coated with settings according to table 8.2. The bulge of photoresist at the edge of the wafers was scraped of with a razor blade. The spincoated wafers were then softbaked in two temperature steps, 65°C and 95°C to remove solvent from the photoresist. Following exposure to UV-light at hard contact mode in an MJB4 mask aligner (Süss MichroTec, Germany) , they were directly placed on a hotplate for the hardbake at 65°C and 95°C. Unexposed photoresist was removed with mr-DEV 600 developer (MircoChemicals, Germany). Structures were checked using reflected light microscopy and structure height was confirmed through profilometry (Dektak 8, Veeco, USA).

8.3.3. PDMS Molds

Polydimethylsiloxane (PDMS, Sylgard 184, Dow Corning, USA) was prepared by mixing the polymerization reagent with the oligomer in a $1:9$ (w/w) ratio. Following mixing the polymer was degassed in a centrifuge. To generate a replica PDMS was poured onto a wafer containing the master. Before curing at 65°C in an oven for $2\,hours$ or longer, the PDMS was again degassed in a desiccator. A square of the PDMS containing the replica of the structure was cut out using disposable scalpels (Cutfix 11, B. Braun, Germany). Following the incision 70% ethanol was sprayed on the PDMS cutting edges to reduce sticking. The cutout was then carefully removed. The wafer containing the master was cleaned with 70% ethanol, dried and reused. Inlet and outlet holes ($0.5\,mm$ and $0.75\,mm$ were punched through the PDMS with biopsy punchers (Harris Uni-Core, Ted Pella, USA). Finally, the PDMS cutouts were cleaned with 70% ethanol.

8.3.4. PDMS Device

Cover slides ($24 \times 60\,mm$, #1,5) were cleaned by sonicating them for $15\,minutes$ at 60°C in 20% Extran MA01 (Merck Millipore, Germany) solution and twice with pure water. The PDMS molds and the cover slides underwent a short oxygen plasma (PVA TePla 100, PVA TePla, Germany) at $200\,W$ and $0.45\,mbar$ for $20\,seconds$ treatment to achieve better bonding between them. Directly after the plasma treatment, the PDMS cutouts were placed onto the glass cover slides and pressed together to remove enclosed air bubbles and increase contact. Removing dust from PDMS and cover slides with a nitrogen gun after removing them from the plasma oven and before sticking them together greatly improved results. The devices were placed in a 65°C oven for two hours to improve sealing stability. For hydrophobic coating of the channels SigmaCote (chlorinated

organopolysiloxane solved in heptane, Sigma-Aldrich, Germany) or Ombrello (unknown substance, Motono, Germany) was filtered trough a hydrophobic polytetrafluorethylen (PTFE) filter and directly used to passivate the microfluidic channels in the cured chips with a hydrophobic layer. After around one minute incubation the channels were filled with FC-40 oil and sealed with adhesive tape to prevent contamination with dust.

Pico-injection devices were additionally equipped with electrodes. The devices were placed on a hotplate heated to 60°C. Indalloy 19 (51% indium, 32.5% bismuth, 16.5% tin, Indium Cooperation, USA) was carefully pushed into the inlets of the electrode microchannels. When touching the heated glass, the indium alloy melted and filled the channel. After completely filling the channels striped wire tips (MC6A-1, Farnell, UK) were pushed in the electrode inlets. The wires were fixed to the device with Loctite 352 (Henkel, Germany). The glue was then cured by exposing it with UV light.

8.4. Droplet Formation

As described in section 3.2 microfluidics allows the creation of mono-disperse water-in-oil emulsion droplets. In this work three different classes of devices were used for droplet production: The standard forming droplets with diameters in the range of $30\,\mu m$ to $40\,\mu m$, a larger counterpart covering $100\,\mu m$ to $120\,\mu m$ and special structures for droplets below $10\,\mu m$. The flow rates were controlled with Standard Infuse/Withdraw Pump 11 Pico Plus Elite syringe pumps (Harvard Apparatus, USA). For larger volumes $1\,ml$ Luer syringes with a low dead-volume (613-2794, Henke Sass Wolf, Germany) and for small volumes $0.3\,ml$ or $0.5\,ml$ insulin syringes (BD Micro-fine Demi, "Becton, Dickson and Company", USA) were used. PTFE-tubing ($\varnothing_{in} = 0.3\,mm$, $\varnothing_{out} = 0.6\,mm$, Bola, Germany) was pulled on Sterican 20 syringe needles (B Braun, Germany) and used to connect the syringes to the devices.

The standard oil phase consisted of $2.5\,mM$ TRI7000 dissolved in FC-40 oil. If necessary $3\,\mu M$ of gold-linked surfactant was added to the solution. Flow ratios were kept in the range of 2:3 to 1:2 aqueous to oil phase. With absolute flow rates of $200\,\mu l/hour$ aqueous and $300\,\mu l/hour$ oil phase for standard $30\,\mu m$ droplets and $1800\,\mu l/hour$ and $3200\,\mu l/hour$ for large $100\,\mu m$ droplets, respectively. The process of droplet self-assembly in the flow focusing junction is discussed in more detail in section 3.2.1. Following production, droplets were collected at the outlet by transferring via an additional PTFE-tube to an Eppendorf tube (Eppendorf, Germany) or a micro tube (Sarstedt, Germany).

8.5. Pico-Injection

To allow precise delivery of various biological components into preformed droplets, microfluidic chips can be integrated with small and compact electrodes to apply electric fields across micro-channels. These electric fields induce a thin film destability of the surfactant leaflet and facilitate controlled injection of aqueous phase into the droplets. The technology behind was introduced in more detail in section 3.2.3.

Building and refinement of this set-up was a major task during this Ph.D. The design of our droplet-based pico-injection unit was adapted from Abate et al.[106] A microfluidic flow control system (MFCS-EZ, Fluigent, France) was used to control the pressure on all inlet channels. Preformed droplets were injected into the pico-injection unit via a designated inlet. The spacing between the droplets was controlled through addition of oil with $2.5\,mM$ surfactants via the second oil channel. The pressure on the injection and spacing channels had to be slightly readjusted for each experiment, but was around $200\,mbar$ and $220\,mbar$, respectively. Following the separation step, isolated droplets passed an electric AC field (frequency of $1kHz$, voltage of $250V$) generated by a HM 8150 signal generator (HAMEG, Germany) and amplified by a 623B-H-CE linear amplifier (TREK, USA) attached to two electrodes made of Indalloy 19 (51% indium, 32.5% bismuth, 16.5% tin, Indium Cooperation, USA). The induced thin film instability allows injection of reagents via a pressurized injection channel on the opposite site of the electrodes. The pressure applied to the injection channel was set between $100\,mbar$ and $120\,mbar$ depending on intended injection volume and viscosity of the injection solution. The injection volume was controlled precisely between $1\,pl$ to $100\,pl$ dependent on the applied pressure in the injection channel.

8.6. Droplet Observation

Following production or manipulation (e.g. pico-injection), the droplets were collected at the outlet of the microfluidic device and transferred to an analysis chamber, as sketched in figure 8.5(a). The following observation chamber design was used in this work. A small coverslip ($18\,mm \times 18\,mm$) coverslides was placed on a large coverslip ($24\,mm \times 60\,mm$) with a spacer in between. Commonly glass shards form cover slips (thicknesses $\#0 \approx 130\,\mu m$, $\#1 \approx 150\,\mu m$ and $\#1.5 \approx 170\,\mu m$) or two strips of double-sided adhesive tape (thickness $\approx 80\,\mu m$, Tesa, Germany) were used for the spacing.

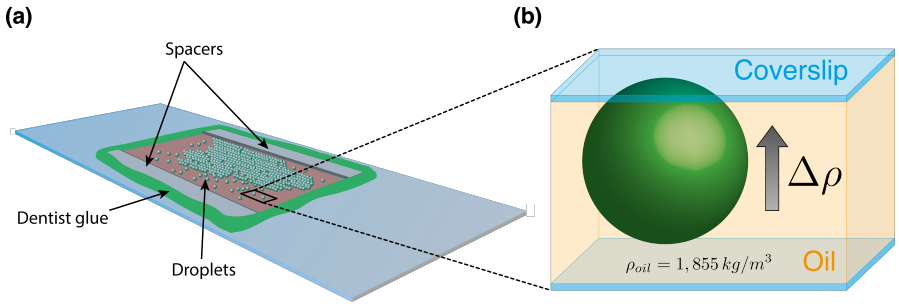

Figure 8.5.: (a) Schematic Illustration of an analysis chamber to store droplets for analysis and characterization. Spacers were chosen according to droplet diameter. (b) Cross section through an observation chamber.

First the spacers were placed on the large cover slide. Subsequently, roughly $5\,\mu m$ of droplet emulsion were pipetted in the center of the slide.[3] The smaller cover slide was then placed on top of the spacers. The volume below the small cover slide is filled with additional FC-40 oil containing the same surfactants as used for droplet production. After the space between the cover slides was filled, the chamber was sealed with two-component Twinsil glue (Picodent, Germany).

Due to the density difference, $1{,}000 kg/m^3$ compared to. $1{,}855\,kg/m^3$, the droplets ascend towards the upper cover slide of the observation chamber, as shown in figure 8.5(b). As the objective used in most observations, a HCX PL APO 63x/1.40-0.60 (Leica, Germany), has a very short working distance, a #0 cover slide was used to allow focusing through the whole droplet.

8.7. Femtoliter Droplets

Cryo-scanning electron microscopy (cryo-SEM) in combination with freeze-fracture are well established methods to observe the content of droplets.[174, 189] However, some specimen, such as lipid bilayer, require even higher resolutions as possible with SEM. An alternative, offering the necessary resolution, is cryo-transmission electron microscopy (cryo-TEM).[348] However, sample preparation protocols for cryo-TEM are mainly adapted for observing cell or tissue samples.[349] As droplets are surrounded by a continuous oil phase, these protocols can't be applied. Nevertheless, a collaborator agreed to try measure microfluidic droplets with a cryo-TEM microscope, if they were as small as $2\,\mu m$. Creating droplets in these dimensions requires a special approach, due to the increased hydrodynamic resistance of small channel (see section 3.1.4). Therefore the dropsplitter design, introduced in sec-

[3]The amount of droplets should not exceed a monolayer in the finished chamber – less is preferable.

tion 3.2.4, was adapted for these requirements. The final device is shown in figure 8.6. The concept of the published designs were adjusted to the requirements to produce minuscule droplets. The author is not aware of any publication presenting microfluidic droplets with these small dimensions.

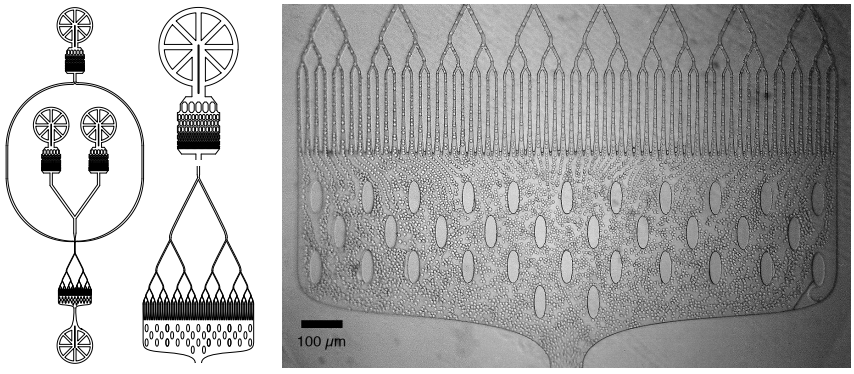

Figure 8.6.: Dropsplitter design with six bifurcations. (a) Drawing of the structure with the main features enlarged. (b) Brightfield Image of the dropsplitter in action.

To produce droplets in these dimensions the cross-section of the channels has to be reduced accordingly. Therefore, a photolithography protocol for a structure height of $5 - 6\,\mu m$ was devised. Reducing the structure height any further, causes problems in the soft-lithography process. Because the molds are made of the soft polymer PDMS (see section 8.3.4), the ceiling of channels with a low width to height radio tends to collapse and bond to the glass slide. This effect can be partially compensated with pillar structures, as present in figure 8.6a. Yet at the same time, the channel width should be as large as possible to reduce hydraulic resistance.

Moreover, due to the elastic nature of the PDMS channels within the mold can be considerably finer, than PDMS pillars. Small pillars with high aspect ratios often snap loose when the mold is removed from the master. A fact that led to the development of the filter structure used in this device. The design was crucial to preserve functionality of the device during droplet production. The filter structure's finest pores are $2\,\mu m$ in diameter. The pillars in between measure $20\,\mu m$ in their smallest dimension. The lowest width found to work. The same design principle was applied to the splitting structure, which uses identical dimensions.

9. dsGUV

Due to the limitations of GUVs as a protocell model system, a keystone of this thesis was the development of a novel combined stable lipid-droplet model system, that combines many of the advantages of droplet-based microfluidics with the high grade of biocompatibility of lipid membranes. The following sections will provide the requirements necessary to create a dsGUV within the droplets. Towards this goal two distinct pathways were developed. The formation of dsGUVs starts by encapsulating aqueous solution containing liposomes within droplets. A schematic representation of dsGUVs is shown in figure 9.1. The key factors for the efficient formation of SLBs were adapted to mediate the creation of a lipid bilayer at the droplet interface. As the droplet volume only offers a finite reservoir, considerations about the necessary lipid concentrations in encapsulated solution are described in section 9.1.1. Knowing the right concentration, SUVs and GUVs can be formed, as described in sections 9.1.2 and 9.1.3, respectively.

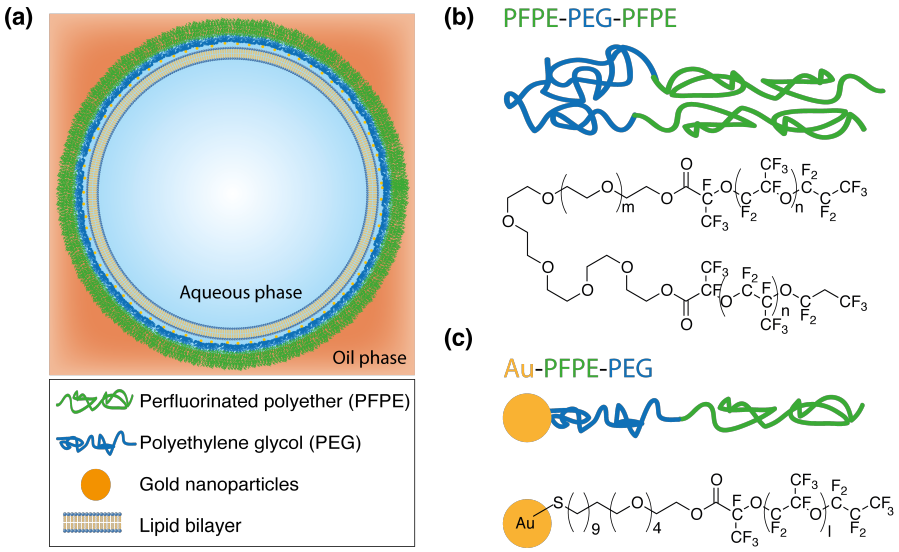

Figure 9.1.: (a) Schematic representation of a dsGUVs. Water-in-oil droplets are stabilized in a continuous oil phase by a triblock-copolymer in hairpin conformation. Optionally diblock-copolymer-linked gold nanoparticles can be added to allow functionalization of the droplet interface. A lipid bilayer is supported by the polymer leaflet at the oil-water-interface. (b) and (c) present chemical structures of PFPE-PEG-PFPE triblock-copolymer and PFPE-PEG-Gold diblock-copolymer surfactants, respectively. Taken from [134]

9.1. Lipid Vesicle Preparation

The start of every dsGUV experiment is the preparation of lipids. Depending on the intended droplet size, the right concentration has to be chosen. The theoretical concentration will be derived in section 9.1.1. For most experiments SUVs prepared according to section 9.1.2 were used. But in some experiments also relied on the formation of GUVs as described in section 9.1.3.

9.1.1. Lipid Concentration

Droplet-based microfluidics allows a high-throughput generation of mono-disperse droplets (diameter variance $< 1\%$) with precise volume and surface area.[126] Therefore, it is possible to estimate the necessary amount of lipid required for formation of continuous lipid bilayer at the droplet surface. Because droplets are spherical, simple arithmetic gives for the necessary lipid concentration needed to cover the droplet by a bilayer

$$C_{lip} = \frac{6}{(rN_A A_{lip})} \tag{9.1}$$

where r is the droplet radius, A_{lip} is the area per lipid in lipid membrane and N_A is the Avogadro constant. The difference in the radii of the inner and outer membrane leaflet was ignored because the radius of a droplet is two orders of magnitude larger than the thickness of a lipid layer. Therefore, the error is negligible. The surface area of common phospholipids in a membrane, e.g. DOPC, is $A_{lip} \approx 0.7nm^2$.[350] Applying this value in equation 9.1, the following lipid concentrations for different droplet dimensions cane be derived: $C_{lip}(r = 20\mu m) = 712\mu M$; $C_{lip}(r = 50\mu m) = 285\mu M$ and; $C_{lip}(r = 75\mu m) = 190\mu M$. These concentrations are essential when preparing dsGUVs to assure full bilayer coverage.

Working with concentrations lower than the critical value will result in a partial lipid bilayer formation (see section 4.1). Concentrations higher than the threshold will lead to accumulation of liposomes in the aqueous phase and eventual diffusion into the oil phase.[178] For lipid concentrations as high as the surfactant concentrations lipids will compete to accumulate at the droplet interface after droplet formation and delay the accretion of the stabilizing surfactant layer. Therefore, special droplet production devices were designed to prevent coalescence – by keeping the droplets spaced in single file in a long and thin channel, surfactants were given sufficient time to aggregate at the interface.

9.1.2. Extruding Liposomes

Extrutsion is a standard method to produce monodisperse vesciles in short time (see section 4.2.1). For this work SUVs were created according to protocols reported earlier.[351, 352] In brief, lipids were dissolved in pure chloroform, mixed at desired composition and concentration and dried under a gentle stream of nitrogen. To remove traces of the solvent, lipids were kept in vacuum for roughly $1\,hour$. The dried lipids were then hydrated by adding the desired buffer and suspended by pipetting them up and down. The solution was vortexed for one hour. Note, often it was more practical to dissolve a multiple of the target concentration in pure water and combine it with a concentrated buffer for each experiment.

SUVs size was homogenized and multilamellar vesicles were broken up by extruding the solution $9\times$ times through a polycarbonate filter (Whatman, Germany) with a pore size of $50\,nm$ using an extruder (Avanti Polar Lipids, USA). The mean SUVs diameter distribution was determined to be $100 \pm 10\,nm$ using DLS. Solutions containing SUVs were stored at 4°C for not longer than $48\,hours$ or used immediately after production.

Following is a list of lipid compositions used for SUV creation in this thesis:

1. DOPC:DOPE:DOPS 8:1:1, including 1% 4-(2-(3,6-diamino-4,5-disulfo-3H-xanthen-9-yl) - N-methylbenzamido) butanoic acid (ATTO488)-DOPE,
2. DOPC:DOPE:DOPS 8:1:1, including 1% rhodamine B-labeled DOPE,
3. egg PC:egg PG 1:1, including 1% rhodamine B-labeled DOPE,
4. egg PC:egg PG, including 1% ATTO488-DOPE,
5. DOPC:DOPS 9:1, including 1% ATTO488-DOPE.
6. DOPC:1,2-dioleoyl-sn-glycero-3- [(N-(5-amino-1-carboxypentyl) iminodiacetic acid) succinyl] (DGS-NTA)(Ni), 9:1.
7. DOPC, 1-palmitoyl-2-oleoyl-sn-glycero-3-phosphocholine (POPC) and cholesterol, 4:4:2, including 1% ATTO488-DOPE.

9.1.3. Electroformation of GUVs

Electroformation is one of the standard techniques used to form lipid vesicles in the size of cells (see section 4.2.2). For this work GUVs were formed using the protocol as described by Herold et al.[353] The steps are sketched in figure 9.2.

In brief, lipid mixtures at the desired concentration (from $1\,mM$ to $5\,mM$) were dissolved in pure chloroform and $10\,\mu l$ to $20\,\mu l$ of solution was spread onto the cunducting surface of two ITO coated glasses (Sigma-Aldrich, Germany). Following chloroform evaporation, the electroformation cell was assembled. Therefore, the two ITO coated glasses were placed facing each other with their respective conductive sides. To avoid direct contact two Teflon spacers ($1\,mm$ thickness) were used. Copper tape (3M, USA) was used to connect the conducting indium alloy layer to a signal generator (RS Components, Germany). Subsequently, the chamber was filled with Milli-Q water (Millipore filtered) and sealed with two-component glue (Twinsil Picodent GmbH, Germany). An alternating electrical potential of $10\,Hz$ at $1\,V$ amplitude was applied for $2\,hours$ to form GUVs. Finally the GUVs were collected using a syringe, stored at 4°C and used for further experiments within $48\,hours$.

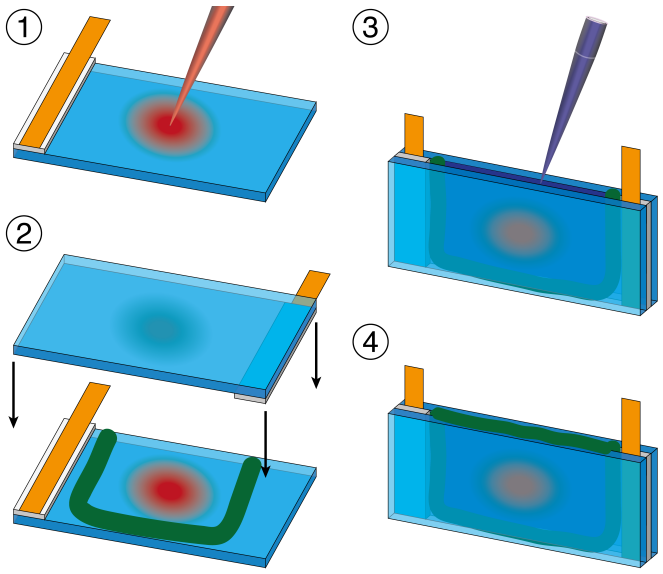

Figure 9.2.: Electroformation assembly for the formation of GUVs. (1) A Teflon spacer and copper tape is attached to two ITO-coated glass slides. The lipid-chloroform solution is applied and spread with the flat side of the pipet tip. (2) A two-component glue is applied in a U-shape to one of the glass slides. Both glass slides are pressed against each other. (3) The cavity is filled with pure water. (4) The chamber is sealed with two-component glue and an alternating current with f $10\,Hz$ at $1\,V$ is applied for $2\,hours$.

9.2. GFP-labeling of Gold-linked Surfactants and DGS-NTA Lipids

As there were no fluorescently-labeled microfluidic surfactants available when this project was started, the gold linked surfactant was functionalized with green fluorescent protein (GFP). hexa histidine-tagged (His6-tagged) GFP was a gift from S. Gardia (Addgene, plasmid #29663). The Protein was expressed in *Escherichia coli* using standard protocols and purified by Ni-Nitrilotriacetic acid (NTA) chromatography. His6-tagged GFP was bound to gold-linked surfactants via Ni-NTA-thiol according to the protocol of Platzman et al. with the exception that purified Milli-Q water (Millipore filtered) was used as aqueous phase instead of PBS buffer.[174]

To achieve a comparable system His6-tagged GFP was also linked to the lipid bilayer of dsGUVs Therefore $NiCl_2$ ($9\,\mu l$, $100\,mM$, Fluka, Germany) was mixed with water solution of DGS-NTA lipids ($300\,\mu l$, $1\,mM$) and stirred for $20\,minutes$. SUVs were produced according to the protocol in section 9.1.2 of DOPC:DGS-NTA(Ni), 9:1 ($300\,\mu M$) were encapsulated into microfluidic droplets ($100\mu m$ diameter). Following encapsulation, water solution containing His6-tagged GFP ($10\,\mu M$) and $MgCl_2$ ($10\,mM$) was pico-injected into these droplets in order to form GFP-functionalized dsGUVs.

9.3. Fluorescence Intensity Analysis of dsGUVs

A key question, that arose during the characterization of dsGUVs, was related to the structure of the lipid layer (partial lipid bilayer, as describe in section 4.1, a lipid bilayer, or a lipid multilayer). Therefore, an important set of experiments was investigating the dependency of the encapsulated concentration of lipids with the fluorescence intensity of the resulting dsGUVs. Here the lipid concentration was varied from a theoretical undersaturation to an oversaturation (see section 9.1.1). The former only allowed the formation of a partial lipid bilayer, the latter of a multilayer.

Moreover, the fluorescence intensity of dsGUVs formed with the theoretically correct concentration of encapsulated lipids was compared to the fluorescence intensity of freestandin GUVs. To keep parameters as comparable as possible, GUVs were encapsulated into droplets before the measurement.

However, the refractive index difference between the aqueous droplets and the oil environment causes refraction and diffraction. Which in turn raises some concerns regarding the values derived from such microscope observations. To compare the membrane fluorescence intensity of encapsulated GUVs to that of dsGUVs of the

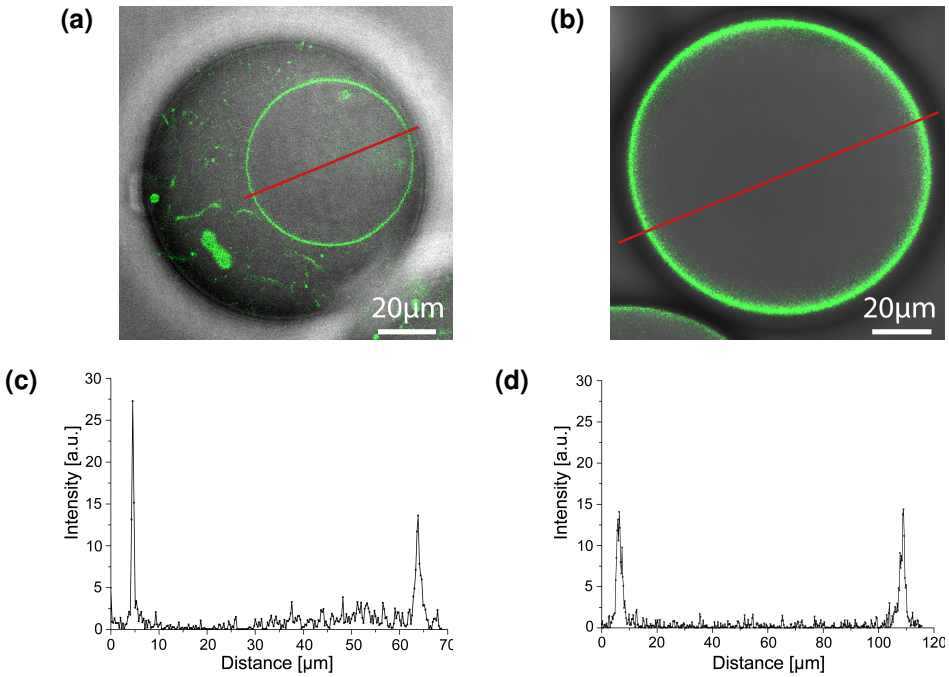

Figure 9.3.: (a) and (b) Composite of phase-contrast and fluorescence images of encapsulated GUVs and dsGUVs (egg PC:egg PG, 9:1, 0.5 % ATTO488-DOPE), respectively. (c) and (d) Fluorescence intensity profiles along the indicated lines as presented in (a) and (b), respectively. Adapted from Frohnmayer et al.[134]

same lipid composition (egg PC:egg PG, 9:1, including 0.5 % ATTO488-DOPE), GUVs were encapsulated into the droplets and dsGUVs were produced. Both types of droplets were evaluated back-to-back preserving identical settings with a Leica SP5 confocal microscope (Leica, Germany) equipped with an argon laser as well as a white-light laser, using a 63x oil objective (HCX PL APO 63x/1.40-0.60, Leica, Germany), ATTO488 was exited at 488 nm, with the argon laser and the detection window was set to $498 - 540nm$. The pinhole for data acquisition was set to 1 Airy unit, which corresponds to the diameter of the Airy disk of 96 nm and 0.9 nm thickness of the optical section. More then twenty intensity profiles were extracted for each droplet type using Fiji/ImageJ.

From both, microscope images as well as evaluated data in figure 9.3, a light blur in the fluorescence from GUVs close to the droplet interface can be observed. This is caused by refraction and diffraction at the water-oil interface due to a difference in the refractive indices of water (1.333) and FC-40 oil (1.290). This effect causes a widening of the intensity profile as shown in figure 9.3 and a reduction of the fluorescence intensity amplitude of the GUV part close to the droplet interface. Therefore, to compare fluorescence intensities, a Gaussian function with a background correction was fitted to the intensity profiles using a nonlinear least-square fit (MATLAB R2015a SP1, MathWorks, USA). The MATLAB script used for evaluation is attached in the appendix I.3.

10. FRAP

For the understanding of any biological system, diffusion is a crucial factor.[354–356] Here it is investigated to derive information about the conformation of the lipid layer and other molecules confined to the droplet interface.[357] A layer of intact liposomes adhered to the interface or lipid interwoven with the microfluidic surfactant would have a significantly lower diffusion speed, than lipids within a lipid bilayer. Towards this goal, the mobility of fluorescently labelled lipids and other molecules confined to the interface of the nano-structured droplets were investigated.

fluorescence recovery after photobleaching (FRAP) was chosen as technique for these measurements as the method is well established. Data was collected using a Leica SP5 confocal microscope (Leica, Germany) equipped with an argon laser as well as a white-light laser. Images were recorded at a constant temperature of 25°C using a 63x oil objective (HCX PL APO 63x/1.40-0.60, Leica, Germany). The pinhole for data acquisition was set to 1 Airy unit, which corresponds to the diameter of the Airy disk of $96\,nm$ and $0.9\,nm$ thickness of the optical section. The focus was set on the lower droplet base as shown in figure 10.1.

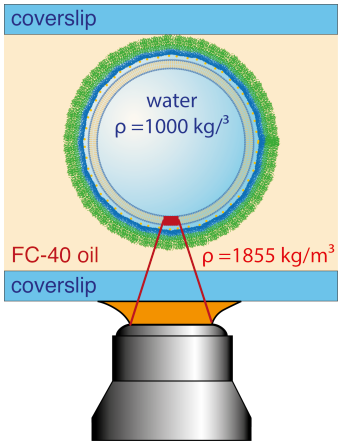

Figure 10.1.: Schematical representation of the experimental FRAP setup. As the density of the droplets content($\rho_{\mathrm{H_2O}} = 1000 kg/m^3$) is substantially lower than the density of the surrounding FC-40 oil ($\rho_{FC-40} = 1855 kg/m^3$) the droplets aggregate at the upper cover slide of the observation chamber (see section 8.6). The focus was adjusted to the bottom of the droplets to exclude any interactions with the glass surface.

A circular spot with a diameter of $5\mu m$ was selected as the bleaching spot. The chronological sequence in each FRAP experiment consisted of 10 pre-bleaching images, followed by 2 to 10 bleach pulses at the bleaching most of the fluorescent signal and finally 50 to 200 post-bleaching images to record the fluorescence recovery at various time intervals. The time intervals and frame number were chosen matching the recovery to near convergence of the observed sample. Figure 10.2 shows the recovery for three different samples. FRAP analysis followed a protocol proposed by Axelrod et al. (1976) and Soumpasis (1983).[358, 359]

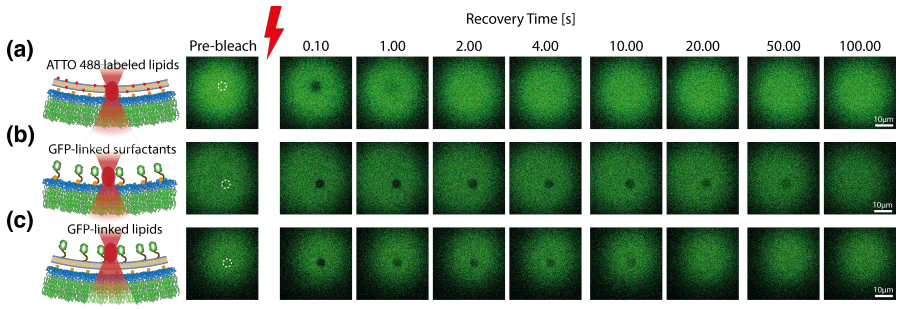

Figure 10.2.: Example images from FRAP experiments of the mobility of different interface components of droplets/dsGUVs. FRAP was performed on (a) fluorescently labeled lipids (b) droplets containing GFP-linked surfactants and (c) GFP linked lipids. The bleached area is circled in the pre-bleached frame and the recovery time (seconds after bleaching completion) is indicated to the top of the fluorescence recovery frames. Adapted from Frohnmayer et al.[134]

To correct for background noise I_{bg}, the average fluorescence background signal was measured in the oil phase using the same settings as for FRAP measurements. The derived value of I_{bg} was subtracted from all measured values. Mean intensity values for the bleaching spot $I(t)$ and the whole droplet base $T(t)$ were extracted. A sample set of raw data is shown in figure 10.3a. $I(t)$ and $T(t)$ were normalized by the averages of the prebleaching values, I_{pb} and T_{pb}. To correct for photofading, the intensities of the bleached spot were multiplied with the reciprocal, normalized intensities of the droplet base, $T(t)$. Thus, the normalized and corrected intensities, I_{nor}, were calculated according to function

$$I_{nor}(t) = \frac{I(t) - I_{bg}}{I_{pb} - I_{bg}} \cdot \frac{T_{pb} - I_{bg}}{T(t) - I_{bg}}. \tag{10.1}$$

To evaluate the kinetics of the fluorescence recovery through diffusion, aa exponential recovery function

$$f(t) = a(1 - \exp(\lambda t)), \tag{10.2}$$

was fitted using a robust nonlinear least-square method to the corrected data I_{nor} using MATLAB R2015a SP1 (MathWorks, USA). Figure 10.3b shows a sample set

of normalized data including the fitted curve. The resulting values of the coefficient λ were then used to calculate the half-recovery time $\tau_{1/2}$ for each bleaching experiment,

$$\tau_{1/2} = -\frac{\log(0.5)}{\lambda}. \tag{10.3}$$

The diffusion coefficient D is related to the half-recovery time $\tau_{1/2}$ via the square radius of the bleaching spot, assuming a Gaussian bleaching profile and a numerically derived correction factor 0.32 for the Gaussian shape of the bleaching spot[1],[358, 359]

$$D = 0.32\frac{r^2}{\tau_{1/2}}. \tag{10.4}$$

The average diffusion coefficient for each experiment and its standard error were calculated from at least 20 measurements measured on different droplets. The MATLAB script used for this analysis is attached in the appendix, see I.1.

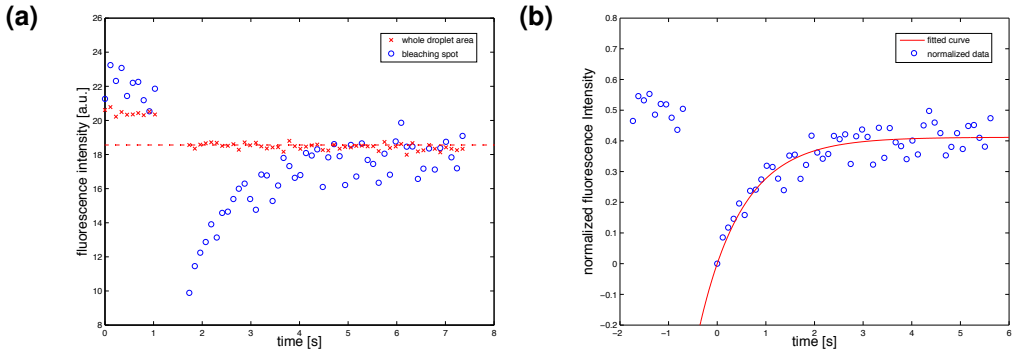

Figure 10.3.: Sample FRAP data of ATTO488-DOPE set with evaluation. (a) Here the average fluorescence intensity extracted from different spots of a FRAP experiment is plotted. The blue dots show the fluorescence intensity at the bleaching spot and the red crosses the average fluorescence intensity of the whole droplet area in focus. Before analysis the data points were corrected for background. Furthermore the recovery data is corrected for photofading with the reciprocal normalized intensity of the corresponding datapoint from the whole droplet. The fluorophore in this experiment, ATTO488, is very stable against photobleaching. A red line at the hight of the first post-bleaching datapoint is given as a reference. (b) The corrected and normalized data points are presented with the corresponding fit.

The quality of the absolute diffusion coefficients can be further improved by taking the diffusion during the bleaching into account.[360–362] Therefore an intensity profile across the bleaching spot was taken from the first post-bleaching image.

[1]The Gaussian shape of the bleaching spot is caused by diffusion during the bleaching process. The correction factor for a perfect shaped rectangular bleaching spot would be 0.25, which nicely matches equation 10.5 for $r_n = r_e$

By fitting a Gaussian distribution an effective radius r_e can be computed. The corrected version of equation 10.4 is defined as

$$D_{cor} = \frac{r_n^2 + r_e^2}{8\tau_{1/2}}, \tag{10.5}$$

where r_n is the nominal radius of the bleaching spot. A MATLAB script to derive the effective radius for a set of measurements is provided in the Appendix I.2.

11. Approaches for Recovery of GUVs from dsGUV

The greatly improved stability and manipulability of dsGUVs over GUVs comes at the cost of confining the lipid vesicle to a microfluidic droplet. Although there is the possibility to functionalize the inner surfactant interface of the droplet, the result a major restrictions to study protocell-surface interactions. Therefore, it was investigated if dsGUVs could be recovered from the droplets encapsulating them.

In literature multiple methods have been proposed to recover the content of microfluidic droplets. The content is usually cells or products from reactions performed within the droplets. Methods using electrocoalescence[363, 364] were excluded from this search, as strong electrical fields not only destabilize microfluidic surfactant sheets but also lipid bilayers. Therefore, these methods are unfit for GUV recovery. Another common approach to recover the content of droplets is the use of destabilizing surfactants to break the emulsion.[174, 343, 344] This more gentle method was adapted and optimized for the recovery of GUVs. The resulting methods are described in more details in section 11.1 for bulk recovery and section 11.2 for a microfluidic approach.

First, a bulk approach which allows recovery of large numbers in short time will be described in section 11.1. However the bulk approach makes monitoring of intermediate steps difficult and is mainly restricted to viewing the end result. Therefore, a microfluidic chip was designed to allow observation of recovery one droplet at a time. This is immensly important as all proofs of lipid bilayer formation in dsGUV thus far have been indirect. Here, recording recovery in real time additionally provides a more sound basis for the claims made in this thesis concerning the nature of dsGUVs. The design and function of the newly designed chip will be explained in section 11.2.

Additionally, due to the shear forces acting on the GUV during recovery, not all lipid compositions forming dsGUVs were persistent enough to survive the process. Hence, a set of different lipids compositions were investigated fit to survive the recovery process. An overview of working compositions will be given in section 11.4.

The results presented here are were achieved in collaboration with Marian Weiss and Lucia Benk. They represent an early stage development. Presented here is a proof of concept. Therefore, at this point applicability of the method can be proven. Follow-on projects will focus on the optimization of this approach.

11.1. Bulk Recovery

Bulk deemulsification is probably the most intuitive approach to recover the content of droplets. As surfactants are required to prevent droplets from coalescing (see section 3.2.2), exchanging long surfactants with short surfactants reverses this effect. In this thesis two such surfactants were used, PFO-MEG,[343, 344] and PFO-TEG.[343, 344] Their chemical structure is provided in further detail in section 8.1.4. The steps to achieve bulk recovery are sketched in figure 11.1.

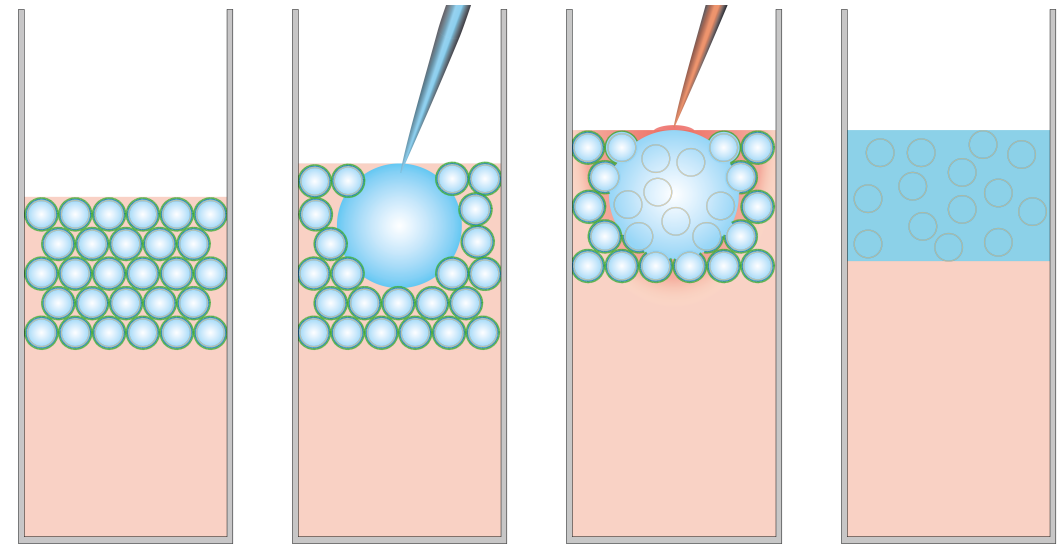

Figure 11.1.: Sketch of the experimental steps of bulk recovery of GUV from dsGUV. (a) Droplets are stored in a reaction tube after production. Due to the lower density of the aqueous medium compared to FC-40 oil the droplets float on top. (b) $100\,\mu l$ of buffer is added to the droplet layer. The encapsulated and added buffer should either be the same or matched for osmotic balance, otherwise the stability of recovered GUV might be reduced.[216, 365–367] (c) $100\,\mu l$ of deemulsifying surfactant solution are dropwise dripped on the buffer droplet. (d) After a few minutes the destabilizing surfactant has deemulsified the mixture, resulting in an aqueous phase containing in GUV on top and oil at the bottom. Centrifugation at low velocities improves the separation of the two phases.

First, droplets are generated and collected in a reaction tube. Due to the density difference between oil and aqueous medium the droplets float to the top of the vial and form a dense layer. A drop of 100 μl of buffer is placed in one large drop in the center of the droplet layer. It is preferable to use the identical aqueous buffer as used in droplet production to reduce osmotic pressure. It should also be possible to match osmotic concentrations.[216, 365–367]

Next, a 20 $vol\%$ solution of PFO-MEG disolved in FC-40 is gently dripped on top of the buffer drop. The solution should slowly trickle down on the interface between the drop and the droplet solution. Tilting the tube to increase the interface area and slowing rotating it about it's longitudinal axis improves the results. The whole process of deemulsification takes less then five minutes. Residual oil drops in the aqueous phase can be centrifuged down by briefly spinning the tube at low speed. The aqueous solution containing GUV can be carefully removed with a pipet and immediately used for observation or experiments.

11.2. The Droplet-Recovery-Chip

To proof that dsGUVs contain a fully formed GUV, recovery of the latter is a credible approach, especially, if the extraction process can be observed. Additionally, it opens up a viable way to optimize the parameters necessary to get a high recovery yield. Findings acquired with this device can in turn be used to improve bulk recovery. The microfluidic chip designed for this purpose combines functional taken from other designs and arranges them to fit this new purpose. The design and the functional units are shown in figure 11.2. The design was developed by Marian Weiss.

Using a microfluidic flow control system (MFCS-EZ, Fluigent, France) flows in the chips were controlled by adjusting the pressure on all inlet channels. As stress on the droplets, e.g. shear forces, were to be kept at a minimum, all pressures were chosen below 20 $mbar$ with minor corrections for individual chips and experimental runs. Additionally, the channels were produced to exceed the droplet hight with 45 μm.

After reinjecting preformed droplets into the recovery chip, they passed a droplet seperation T-junction, figure 11.2b. This T-junction is identical to the structure used in pico-injection devices as described in section 3.2.3.[106] In difference to the pico-injection device, here the TRI7000 is replaced by destabilizing PFO-MEG, or PFO-TEG surfactants in the spacing oil. At similar pressure on both channels the spacing channel displaces roughly 80 % to 90 % of the oil from the droplet channel.

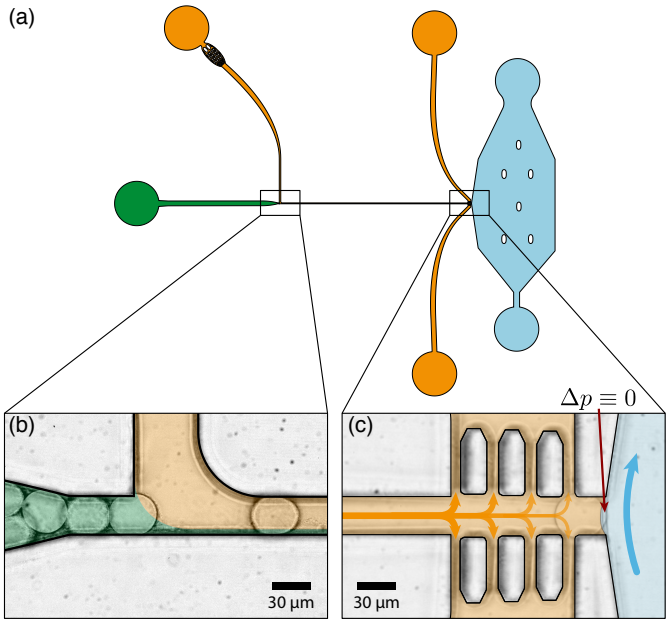

Figure 11.2.: Microfluidic device for recovery of droplet content and its functional units. (a) The whole design of the device with the droplet injection channel marked green, the channel containing oil with the destabilizing surfactant in orange and the aqueous channel in blue. (b) Microscope image of the spacing T-junction. The displacement of each phase without droplets is indicated in a colored overlay – orange for oil containing the destabilizing surfactant and green for oil from the reinjection channel. (c) Two microscope images of the droplet trapping and recovery area merged. Pictures were taken $5\,ms$ appart and show a droplet right before and after fusion. Pillars above and below the droplet carrying channel prevent droplets from entering the adjecent channels. In absence of droplets in the trapping area, pressure on the aqueous channel is adjusted, that there is no pressure gradient at the interface between oil and aqueous channels.

The low flow speed along the channel carrying the droplets to the next functional unit, gives the destabilizing surfactants time to replace their stable counterparts. The droplet carrying channel ends in a trapping structure inspired by previously published structures.[186, 368–371] This subunit is shown in figure 11.2c. Here four small slits on both sides connect the main channel with two adjacent channels. The width of these slits were chosen to prevent droplets from entering due to the Laplace pressure.[372, 373] Thus allowing only the oil phase to flow to the side channels. Finally the droplet carrying channel ends in a wide orthogonal channel carrying aqueous solution. The pressure on the aqueous channel is adjusted so the pressure difference at the interface to the oil channel is zero, $\Delta p \equiv 0$, when no droplet is in the trapping zone. Therefore, with no droplet blocking the slits there is no net flow between these oil and aqueous channel.

When a droplet enters the trapping zone, it blocks the slits on both sides. Thus, reducing the channel total cross section connecting the main and adjacent oil channels. According to Hagen-Poiseuille equation, this increases the pressure (see section 3.1). As the droplet traverses along the trapping area, it passes pairs of slits, opening them up again for oil flow. With each open pair of slits the channel cross section for the oil to flow to the adjacent channels increases, subsequently decreasing pressure pushing the droplet along the channel. The droplet decelerates as it approaches the oil-water interface. Provided a sufficient concentration of destabilizing surfactant, the residual surfactant layer peels of the droplet at contact with the water phase and its content is ejected into the water phase.

11.3. Observation of recovered GUVs

Recovered GUV, especially those extracted through bulk recovery, can be observed in chambers constructed as described in section 8.6. GUVs are mechanically unstable in comparison to droplets and tend to rupture when brought into contact with bare glass surfaces. Therefore, the glass slides were passivated with bovine serum albumin (BSA), before assembling the chamber.

A dense surface coating was achieved by incubating oxigen plasma-cleaned glass slides for $2\,hours$ in $10\,mg/ml$ BSA (SERVA, Germany) dissolved in PBS (Gibco, USA) on a see-saw rocker. Next, the glass slides were rinsed twice with PBS and washed in PBS for $5\,minutes$. The washing process was repeated with H_2O. Finally the glass slides were blow-dried with nitrogen.

11.4. Lipid Compositions for Recovery

Not all lipid compositions forming dsGUV appear to form lipid bilayers durable enough to survive the forces during the recovery process. Follow-on Projects will further investigate the necessary conditions and improve the yield of recovered GUV. Lipid compositions were screened by Lucia Benk.

At this point a few general trends for the stability of lipid bilayers have been identified. In accordance with published observations,[374–376] $10\,mol\%$ to $20\,mol\%$ cholesterol (C8667, Sigma-Aldrich, USA) improve the stability of membranes. GUV consisting of lipid compositions exceeding net $10\,mol\%$ of negatively charged lipids could not be recovered. There are also indications that using part POPC instead of DOPC enhances membrane durability.

The main lipid composition for the experiments presented in this work a molar ratio of 4:4:2 of DOPC, POPC (both Avanti Polar Lipids, USA) and cholesterol. For recovery experiments $1\,mM$ of SUVs were prepared through extrusion, according to the protocol described in section 9.1.2.

11.5. Recovery of Integrin-GUVs

For the purpose of recovering GUVs containing reconstituted integrin $\alpha_{IIb}\beta_3$, the protocol for detergent removal presented in section 6.5 was modified. Instead of a $50\,mol\% : 50\,mol\%$ of egg PC and egg PG lipid mixture, pure egg PC was used. Note, the major constituent in egg PC is POPC.[1] Thus omitting lipids with a negative net charge completely. The rest of the protocol was kept as described earlier.

A second solution of liposomes was produced through extrusion as described in section 9.1.2 with a total concentration of $1.8\,\mu M$. The lipid composition for recovery listed in section 11.4 was changed to a molar ratio of 4:3:2 of DOPC, POPC and cholesterol.

For droplet production both liposome solutions were mixed in a 9:1 ratio with a total concentration of $1\,mM$ in activation buffer (7.1) resulting in dsGUV consisting of lipid composition with a molar ratio of 4:4:2 of DOPC, POPC/egg PC and cholesterol, closely resembling the composition described in section 11.4. The buffer used was the activation buffer (see section 7.1). The same buffer was also used for the QCM-D experiments.

[1] For more information see: `https://avantilipids.com/product/840051/`

12. Finite Element Simulations

Finite element method (FEM) is considered as a well established and convenient technique for solving complex problems in science and technology. It allows to approximate boundary value problems of differential equations which are otherwise extremely complicated to solve or generally unsolvable. The first step of the FEM is the discretization of the continuous domain of the problem into small subdomains, so called "finite" elements, interconnected at points, nodes, common to two or more subdomains. Several approaches can be used to transform the physical formulation of the problem to its finite element discrete analogue. For a physical problem described by a differential equation the most popular method of its finite element formulation is the Galerkin method. If the physical problem is a minimization of a functional then variational formulation of the finite element equations should be used. Direct and iterative methods can be used for solution. The FEM solves values for these nodal points, values inside the elements are interpolated using the nodal points. Many FEM programs also include a post processing system, which interpolates values to display the solution graphically and derive additional parameters.

12.1. Model Design

COMSOL Multiphysics 5.2 (COMSOL AB, Sweden) was used for numerical computations in this thesis. A model to approximate the electric fields generated in a pico-injection device was set up. First the structures from 2D vector files were reduced to the relevant parts (see section 8.3.1) and imported into COMSOL. There they were placed on a work plane and extruded to the height of the corresponding photolithography process (see section 8.3.2). The geometry was complemented by adding structures of the glass cover slides, the PDMS mold and a surrounding air sphere and is shown in figure 12.1a. Values for the relative permittivity $\varepsilon_r = \varepsilon/\varepsilon_0$ for boronsilicate $\varepsilon_r = 4.6$ (Schott, Germany), PDMS $\varepsilon_r = 2.75$ (Corning, USA) and FC-40 $\varepsilon_r = 1.9$ (3M, USA) were taken from the official product information. Droplets of different volumes were modeled to fit the volume of a spherical droplet $V(d = 40\,\mu) = 33.5pl$, or $V(d = 100\,\mu) = 524pl$ depending on the structure. Their relative permittivity was set to an adjustable parameter, with a standard value of $\varepsilon_r = 80.1$ (H_2O at $20°C$).

The meshing setting was set to "physics controlled" and an extremely fine grid. The mesh of the most important structures is shown in figure 12.1b. In the physical model, the upstream electrode was defined to be a ground and the downstream electrode was defined to be the terminal. The voltage on the potential was set to $1\,V$ in all models. As the electric field is linearly depending on the potential, field strength for other voltages can thus be easily calculated. All plots of electric fields show the normalized electric field in SI units V/m. For electroporation experiments the values are often given in kV/cm.[377] So for comparison a correction factor of $1\,V/m = 10^{-5}\,kV/cm$ has to be applied. After completing the setup of the model the electrostatic field was computed. The capacitance of the system and the droplet volume were derived from the simulated results. A parametric sweep of the radius of the air sphere was performed to find the optimal boundary conditions and minimize errors due to meshing.

12.1.1. Radius of the Air Sphere and Boundary Conditions

As electric charges cause wide ranging fields, the size of the modeled volume and the boundary conditions are important for the quality of a FEM simulation of these fields. However, as the FEM approach quantifies the volume into finite elements, the meshing of these nodes also influences the solution. As the number of nodes is limited by the computing power, the simulated volume can't be extended indefinitely or nodes won't be able to render the geometry. If the mesh goes below a minimal domain size, one charge might be split over two nodes, what causes artifacts of auto-repulsion. Modern meshing algorithms take many of these effects into account. However, errors still occur.

Therefore, the same geometry was simulated over a range of different radii of the air sphere. Two parameters derived from the model were compared for the results, the volume of the droplet and the global capacitance of the system. The results are shown in figure 12.1.

Both charge and volume show inconsistencies below a radius of $225\,mm$. To keep the mesh of the important structures as fine as possible, the radius of the air sphere was set to $250\,mm$. The boundary condition for the air sphere surface was tested with floating potential and zero charge. Simulations yielded the same results for the capacitance independently of the setting. The boundary condition was then set to zero charge.

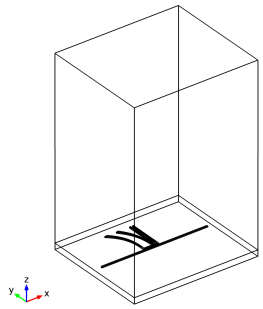

(a) Rendering of the geometry

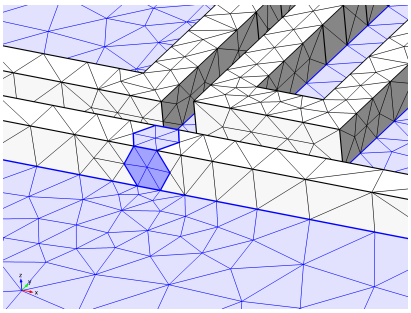

(b) Mesh of the droplet

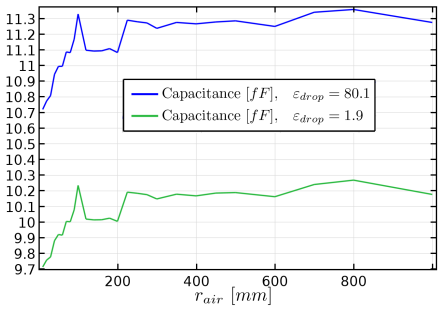

(c) Global capacitance vs radius of air sphere

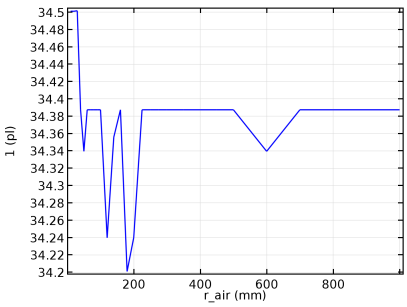

(d) Droplet volume vs radius of air sphere

Figure 12.1.: Setup of the FEM model to compute electric fields in microfluidic devices. (a) shows a rendering of the overall geometry and (b) the mesh of the central structure. The graphs show (c) the capacitance of the simulated geometry plotted against the radius of the air sphere and (d) the volume of the droplet plotted against the radius of the air sphere.

12.1.2. Electrode Design

During the design of the pico-injection structure and following projects the question of the ideal electrode design was raised. The field should be as homogeneously as possible, while keeping the production of the chip simple. Publications containing microfluidic chips with electrodes show a variety of different designs.[106, 108] Moreover, there is also a variety of techniques used to manufacture the electrodes.[107, 139, 378, 379] The technique of choice in this study is filling channels with a low melting temperature indium alloy (see section 8.5). This was done with little effort, but requires a distance of minimum 10 μm between electrode and fluidic channels, that depends on structure height.

Different designs of electrodes were sketched and imported into the model. The electric field was computed for a each structure. The field distribution was extracted from a droplet in the center of the electrodes.

12.2. Electric Field Exposure

The microfluidic droplets are not only used in the field of SB, the technology is also used for experiments with living cells.[137, 143, 380] It has been shown that cells can be cultured in microfluidic droplets for multiple days.[174, 381] However, the exposure to electric fields, such as required in a pico-injection device could potentially harm cells.[377] At the same time this technology can be used for transfection of the cells.[380, 382–384]

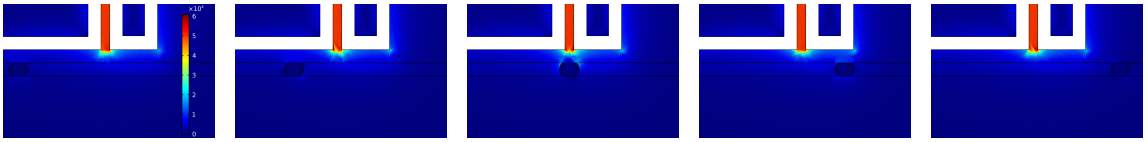

(a) $-200\,\mu m$ **(b)** $-100\,\mu m$ **(c)** $0\,\mu m$ **(d)** $100\,\mu m$ **(e)** $200\,\mu m$

Figure 12.2.: Electric field in the x-y plane at the half the channel height simulated for droplets in various positions, ranging from $-200\,\mu m$ to $200\,\mu m$ in $100\,\mu m$ steps.

To asses the exposure of cells to electric field, the droplet position was parametrized. The electric field was computed for droplet positions from $-200\,\mu m$ to $+240\,\mu m$ in $5\,\mu m$ steps in relation to the center of the electrodes. For each position the electric field strength along the main axes of the droplets were exported. In connection with the flow speed, derived from recorded high speed camera footage, this can be used to estimate the exposure to the electric field.

12.3. Electric Droplet Sensing

Previous studies have presented methods to distinguish the content of droplets through by determining the relative permittivity with capacitor in proximity to the channels.[139, 378, 379] Therefore, it was interesting if it could also be possible to detect if a droplet contained a cell. Maybe if it would even be possible to distinguish the number of cells. Here it should be noted, that the electric permittivity of cells is a complex, nonlinear problem.[385–387] Moreover, the electric coefficient of cells is highly frequency dependent. However, the model currently does an electrostatic computation. Furthermore, the ion concentration, which is part of every cell medium, is currently not accounted for in this model. The premise was, to get an idea if the change in capacitance was strong enough to be measurable. Here, the capacitive reactance X_C of the capacitor in the AC current is important,

$$X_C = \frac{1}{2\,\pi\,f\,C}, \tag{12.1}$$

where f is the frequency of the electric potential and C is the capacitance. With both increasing frequency and capacitance the electric resistance of the circuit decreases in a reciprocal dependency. Therefore, a change in the content of a droplet can have a measurable effect on the electric current. This simulation was run to estimate if a setup using the current electrode type could be sensitive enough to be used as a sensor.

Part III.

Results and Discussion

13. “Classical” Liposomes

This chapter will sumarize the results obtained when studying cellular adhesion with a traditional liposome model system. The SUV were produced using detergent removal. This method allowed the reconstitution of integrin $\alpha_{IIb}\beta_3$ into liposomes. Binding kinetics were measured with the label free QCM-D method. In section 13.1 the stability of liposomes with and without reconstituted integrin $\alpha_{IIb}\beta_3$ due to unspecifical binding to uncoated SiO_2 crystals is studied. This is essential as the stability of liposomes was an ongoing topic throughout this work. Section 13.2 covers the binding of integrin-liposomes, liposomes and integrin to the ECM protein covered QCM-D crystals. In comparison to previously reported adhesion model systems using biotin-straptavidin interactions, this is a step towards closer mimicry of biological systems.[328, 388, 389] Section 13.3 discusses two methods of controlling adhesion. First, RGD containing peptides were used to mediate unbinding (subsection 13.3.1). Secondly, various integrin concentrations were used to tweak the binding affinity of integrin-liposomes (subsection 13.3.2).The relevance of these findings will be discussed in section 13.4. Buffers used in this chapter are listed in materials and methods, section 7.1.

13.1. Binding on uncoated SiO_2 Crystals

Pevious studies observed formation of SLB upon the binding of liposomes to uncoated quartz crystals by rupture of the liposomes. This indicates a mechanical instability of the liposomes.[328, 337] Integrins, like many other proteins and lipids, were also found to unspecifically bind to quartz crystals.[207, 337, 390–392] Therefore, the interaction of integrin-liposomes and pure liposomes with uncoated SiO_2 crystals were studied over $5\,hours$ and $40\,minutes$ to analyze unspecific binding effects and the respective liposome stability as shown in figure 13.1.

Directly after injection both, liposomes and integrin-liposomes, showed a strong binding affinity to the uncoated crystals as indicated by the frequency decrease and dissipation increase directly after introducing the samples to the measurement chamber. After approximately $30\,minutes$ the resonance frequency drop of the pure liposome channel reached a minimum of $\Delta F_{max} = -56.5\,Hz$ increased again and converged to a stable value of $\Delta F_{conv} = -27 \pm 3\,Hz$ as listed in table 13.1. The dissipation signal showed a similar but less pronounced response of opposite sign, $\Delta D_{max} = 3.48 \cdot 10^{-6}$ and $\Delta D_{conv} = (0.49 \pm 0.09) \cdot 10^{-6}$. These signal changes are

an indicator for rupture of the pure liposomes and formation of a SLB as sketched in figure 13.1a. In contrast, the binding of integrin-liposomes on uncoated SiO_2 crystals resulted in a continuous frequency drop by $\Delta F_{max} = -125.1 \pm 0.4\,Hz$ $3.5\,hours$ after injection. The corresponding dissipation steadily increased at the same time by $\Delta D_{max} = (35.89 \pm 0.11) \cdot 10^{-6}$. From this observation it can be concluded that the integrin-liposomes stayed intact when adhering to uncoated SiO_2 crystals. In the subsequent washing step the frequency increased again by $\Delta F_{final} = 136\,Hz$ and the dissipation declined by $\Delta D_{final} = 31.0 \cdot 10^{-6}$. This suggests that the adhered integrin-liposomes only bound weakly and thus adhered unspecifically to the SiO_2 surfaces. Contrary, the lipid-bilayer as formed on the glass by liposome rupture could not be removed from the surface by washing with buffer

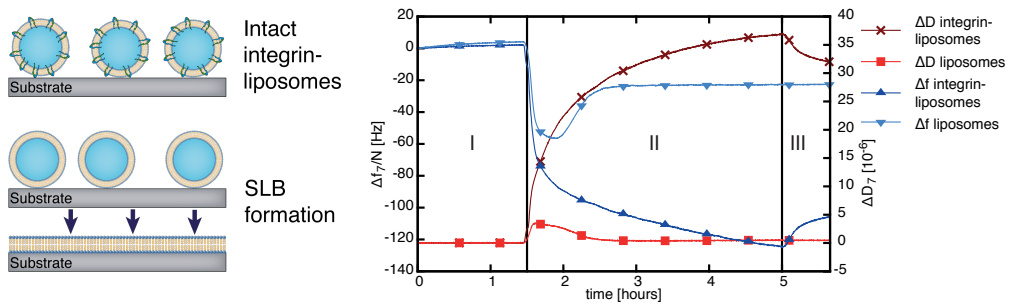

(a) Schematic representation **(b)** QCM-D results

Figure 13.1.: (a) Schematic drawing of intact integrin-vesicles and the formation of a SLB from pure liposomes. It may well be that there are oppositely oriented integrins reconstituted in the liposomes. Since these do not contribute to adhesion they are not drawn in the schemes throughout the manuscript. (b) Frequency and dissipation recordings for liposomes on untreated SiO_2 crystals. After a $1\,hour\,30\,minutes$ washing step (step I), liposomes and integrin-liposomes were loaded onto the crystals for $3\,hours\,30\,minutes$ (step II), followed by another $30\,minutes$ washing step (step III). At the beginning of step II liposomes and integrin-liposomes showed strong binding to the uncoated crystals. After $30\,minutes$ the resonance frequency for the pure liposome channel reached a minimum of $\Delta F_{max} = -56.5\,Hz$, increased again and finally converged to a stable value of $\Delta F_{cv} = -27\,Hz$, thus indicating the formation of a SLB. The dissipation curve showed a corresponding increase and then declined again. In contrast, integrin-liposomes showed a pronounced frequency decrease and a corresponding dissipation increase, which is comparable to the binding experiments on ECM proteins. Hence, integrin-liposomes were stable on uncoated SiO_2 crystals and did not rupture. Adapted from Frohnmayer et al.[342]

Protein coating	Protein binding	
	Frequency change $[Hz]$	Dissipation change $[10^{-6}]$
Liposomes	-27 ± 3	0.49 ± 0.09
Integrin-Liposomes	-125.1 ± 0.4	35.89 ± 0.11

Table 13.1.: Binding of different ECM proteins and liposomes to SiO_2 crystals as monitored by QCM-D: Pure liposomes yielded frequency and dissipation signals, which were characteristic of SLB formation. Integrin-liposomes led to a frequency decrease and a large dissipation change, which shows that these vesicles stayed intact and did not form SLBs on the SiO_2 crystals.

To further analyze the binding of the two different types of liposomes, a different approach for data visualization reveals additional insights into the binding kinetics. According to Sauerbrey's model for the adhesion of rigid thin layers to quartz crystals, there is a linear relationship between the frequency decrease $(-\Delta F)$ and the mass increase per unit area $(\Delta m/A)$.[338] As this model was not developed for soft organic films, it may only be seen as an approximation for our synthetic cell model of (integrin-)liposomes, which enclose an aqueous medium. However, as Tellechea et al. reported, plotting the dissipation against frequency can be used to identify changes in the conformation of the adhering layer.[393]

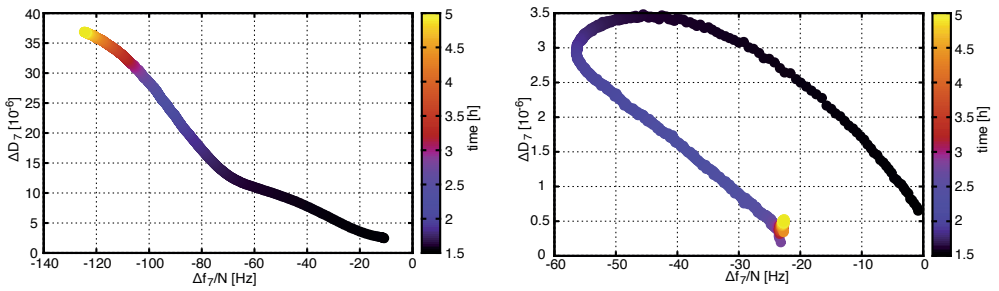

(a) integrin liposome **(b)** pure lipoisome

Figure 13.2.: Analysis of dissipation versus frequency for (a) binding of integrin-liposomes and (b) pure liposomes. Graph (a) displays a monotonically decreasing frequency, which indicates that the integrin-liposomes stayed intact. In graph (b) the trajectory reverses due to the rupture of the pure liposomes and formation of an SLB. Adapted from Frohnmayer et al.[342]

Figure 13.2a and (b) show the corresponding values of ΔD against ΔF analysis for integrin-liposomes and pure liposomes bound to uncoated quartz crystals. In figure 13.2b, the $\Delta D/\Delta F$ analysis for the adhesion of integrin-liposomes yielded an almost linear relationship after the equilibration period, which indicates that the liposomes did not rupture on the SiO_2 crystals. In contrast, for pure liposomes the

kinetic showed a reversal $\Delta D/\Delta F$ trajectory, which clearly shows that the vesicles ruptured to form a SLB. Hence, it can be concluded that the reconstitution of integrin into liposomes has a mechanically stabilizing effect on the liposome durability as compared to the observed rupturing of pure liposomes on SiO_2. One hypothesis is that the increase of durability is caused by a reduction of van der Waals forces due to steric hindrance of the integrin.[394] Integrin protrudes $\sim 160\,\mathring{A}$ in active and,[46] and $\sim 115\,\mathring{A}$ in inactive conformation from the membrane.[51] The lipid membrane itself could also be strengthened by the incorporation of the larger transmembrane protein.

13.2. Binding on ECM Protein Coated Interfaces

The general tendency of frequency and dissipation shifts in QCM-D measurements was recorded to study the binding of integrin-liposomes, pure liposomes and pure integrin to different ECM protein coatings over 11 *hours* and 40 *minutes* as shown in figure (b) to d and listed in table 13.2. The experimental setup is schematically shown in figure 13.3a. DLS revealed that pure liposomes and integrin-liposomes used in these experiments had an average diameter of 100 nm to 200 nm (see section 6.5). In the following QCM-D analysis the binding of integrin-liposomes, pure liposomes and soluble integrin to fibrinogen- and fibronectin-coated quartz crystals was studied. The frequency and dissipation shifts were determined by subtracting the average over the last five minutes of the buffer wash before addition of the samples (step III) and of the final buffer wash in step V. The errors are the sum of both standard deviations.

protein	Pure Integrin		Liposomes		Int-Lipo	
coating	ΔF $[Hz]$	ΔD $[10^{-6}]$	ΔF $[Hz]$	ΔD $[10^{-6}]$	ΔF $[Hz]$	ΔD $[10^{-6}]$
Fg	-73.6 ± 0.1	6.78 ± 0.04	4.93 ± 0.15	0.14 ± 0.04	-153.34 ± 0.09	23.20 ± 0.04
Fn	-38.84 ± 0.14	4.52 ± 0.03	-0.02 ± 0.08	0.17 ± 0.03	-60.79 ± 0.15	19.69 ± 0.04
Col	–5.1 ± 0.2	0.32 ± 0.09	-4.9 ± 0.2	0.23 ± 0.07	-4.5 ± 0.2	-0.41 ± 0.08

Table 13.2.: Summary of maximal frequency and dissipation shifts during integrin-mediated adhesion on fibrinogen-coated crystals upon addition of RGD-peptides as monitored by QCM-D. Addition of the RGD-peptides SN529 and GRGDSP to adhered integrin-liposomes and integrin led to detachment of both samples, indicated by respective frequency increases and dissipation decreases. The unit of frequency shifts is Hz and the unit of dissipation shifts is -10^{-6}.

For fibrinogen coatings pure liposomes yielded a small increase in frequency and a very stable dissipation. Integrin binding led to a final reduction of the resonance frequency by over $\Delta F_{final} = -73.6 \pm 0.1\,Hz$ and an increase in dissipation of $\Delta D_{final} = (6.78 \pm 0.004) \cdot 10^{-6}$. For integrin-liposomes a shift of $\Delta F_{final} = -153.34 \pm 0.09\,Hz$ and an increase of dissipation by $\Delta D_{final} = (23.2 \pm 0.004) \cdot 10^{-6}$ was measured.

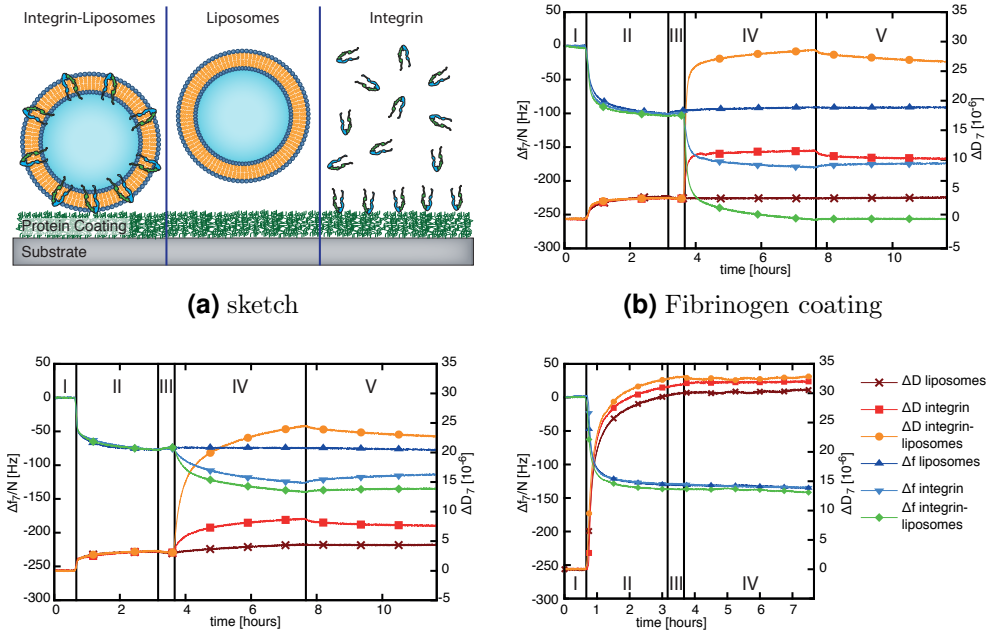

(a) sketch

(b) Fibrinogen coating

(c) Fibronectin coating

(d) Collagen coating

Figure 13.3.: (a) Schematic representation of integrin-liposomes being flushed over protein-coated crystals in the QCM-D chamber. (b) to (d) Frequency and dissipation shifts for binding of liposomes, integrin $\alpha_{IIb}\beta_3$ and integrin-liposomes on three different ECM protein coatings. For the first $40\,minutes$ activation buffer was flown over the crystals (step I). In the following $2\,hours\ 30\,minutes$ a solution containing $50\,\mu g/ml$ of (b) fibrinogen, (c) fibronectin and (d) collagen was loaded into the QCM chamber (step II). After a second $30\,minutes$ washing step with activation buffer (step III) three different samples were added to one QCM-D sensor, respectively. We added pure liposomes to one sensor, $50\,\mu g/ml$ of activated integrin $\alpha_{IIb}\beta_3$ to another crystal and liposomes containing reconstituted integrin to a third sensor. Pure liposomes were found to show no interaction with any of the ECM protein coatings. Pure integrin and integrin-liposomes adhered to fibrinogen and fibronectin surfaces and did not bind to collagen coatings. Adapted from Frohnmayer et al.[342]

The addition of pure liposomes to fibronectin-coated surfaces only caused small changes of the frequency and dissipation signals. Binding of integrin to these surfaces resulted in a decrease of the resonance frequency by $\Delta F_{final} = -38.84 \pm 0.14\,Hz$ and a dissipation increase of $\Delta D_{final} = (4.53 \pm 0.03) \cdot 10^{-6}$. The binding of integrin-liposomes lowered the frequency by $\Delta F_{final} = -60.79 \pm 0.15\,Hz$ and increased the dissipation by $\Delta D_{final} = (19.69 \pm 0.004) \cdot 10^{-6}$.

These results indicate that integrin-liposomes and pure integrin bound to fibrinogen and fibronectin while no binding effects were observed for pure liposomes. In comparison to fibronectin and fibrinogen, collagen has no binding sites for integrin integrin $\alpha_{IIb}\beta_3$. Thus, binding of integrin and integrin-liposomes to this ECM protein was not expected. As shown in figure 13.3d there was only a small shift in the resonance frequency and dissipation signal when pure integrin ($\Delta F_{final} = -5.2 \pm 0.2\,Hz$ and $\Delta D_{final} = (0.32 \pm 0.09) \cdot 10^{-6}$) or integrin-liposomes ($\Delta F_{final} = -4.5 \pm 0.2\,Hz$ and $\Delta D_{final} = (-0.41 \pm 0.008) \cdot 10^{-6}$) were loaded onto collagen-coated crystals. This observation differs only slightly from the previous results for pure liposomes on fibrinogen- and fibronectin-coated crystals and confirms our assumption that integrin-liposomes or pure integrin did not specifically bind to collagen.

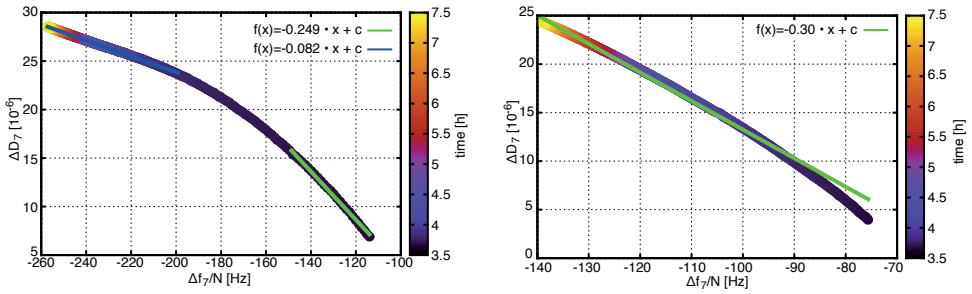

(a) Fibrinogen **(b)** Fibronectin

Figure 13.4.: Analysis of dissipation versus resonance frequency shifts for the binding of integrin-liposomes on (a) fibrinogen- and (b) fibronectin-coated SiO_2 crystals. Both graphs show a nearly linear relationship between the measured values, which indicates that the liposomes were stable and did not rupture to form a SLB. Adapted from Frohnmayer et al.[342]

The specific binding of integrin-liposomes to fibrinogen- and fibronectin-coated crystals was further characterized by analysis of the corresponding $\Delta D/\Delta F$ plots in figure 13.4. For both protein coatings a linear relationship was obtained. In case of fibrinogen the linear fit was split into two portions as a change in dynamics was observed (see figure 13.4a). During the first 6 *minutes* of integrin-liposome adhesion a $\Delta D/\Delta F$ gradient of $-2.49 \cdot 10^{-8}\,Hz^{-1}$ was obtained, which

indicates a fast kinetics (green line). After the initial 6 *minutes* of integrin-liposome adhesion the dynamics change into a slower regime. Here the linear fit for a time period of 3 *hours* and 30 *minutes* (blue line) has a gradient of $-0.82 \cdot 10^{-8}\, Hz^{-1}$. The observed linear relationship between bound mass and dissipation after the equilibration period indicates that the liposomes did not rupture or form a SLB on the fibrinogen surface and thus confirmed our previous observation. When integrin-lipsomes adhered to fibronectin-coated crystals the gradient $\Delta D/\Delta F$ reached $-3.0 \cdot 10^{-8}\, Hz^{-1}$ (figure 13.4b). As the frequency and dissipation shifts reach higher values on fibrinogen as on fibronectin, a denser packing of integrin-liposomes on the surfaces can be assumed. This could cause a rearrangement and deformation of the vesicles, which would account for the change in the $\delta D/\Delta F$ regime on fibronectin.

A rough estimate places the number of integrins per liposome at around 130 for a diameter of 120 *nm*. However the orientation of the integrin is unknown. Due to the spontaneous nature of their reconstitution, the distribution is likely 50 : 50 in either direction.[394] Although, membrane curvature could have an effect on their orientation. Additionally, transmembrane protein are not static in a membrane.[202, 395] Temporally binding to ligands reduces the integrin diffusion speed, effectively increasing the concentration in the binding area.[396] Therefore, the mobile integrins migrate into the contact zone between the vesicle and the ECM-coated crystal producing more bonds and a larger spreading pressure.[89, 397] If the ligand density is sufficiently high, the spreading pressure could lead to a deformation of the liposomes.

13.3. Controlling Synthetic Adhesion

Quantifying the specific binding of integrin-liposomes to ECM proteins by QCM-D analysis gives important insight into the interaction of synthetic cells with various biointerfaces. Therefore, the controllability of integrin-mediated adhesion on fibrinogen-coated crystals was further analyzed. The effect of two RGD-peptides in solution on specific adhered integrin-liposomes and integrin was also studied. Additionally, different lipid to integrin rations were used to form integrin-liposomes, to examine the concentration dependency on the integrin-mediated specific adhesion to fibrinogen-coated crystals.

13.3.1. Competative Binding

In this series of experiments the effect of free RGD-peptides on the binding of specifically adhered integrin-liposomes and pure integrin was analyzed. Therefore, analog to previous experiments integrin-liposomes and integrins were bound to

fibrinogen-coated crystals as shown in figure 13.5, step I. Subsequently, in step II $500\,\mu M$ of peptide GRGDSP, or $500\,\mu M$ of peptide SN529 solved in activation buffer (for buffers see section 7.1) were introduced to measurement chambers, respectively (step II). Signal changes were recorded for 11 $hours$. A reference chamber was washed with pure activation buffers, which did not contain any RGD-peptides. In step III all channels were switched to the pure activation buffer. The frequency and dissipation shifts from the end of sample binding to the end of our final washing step are listed in table 13.3 and were determined as described in section 13.2.

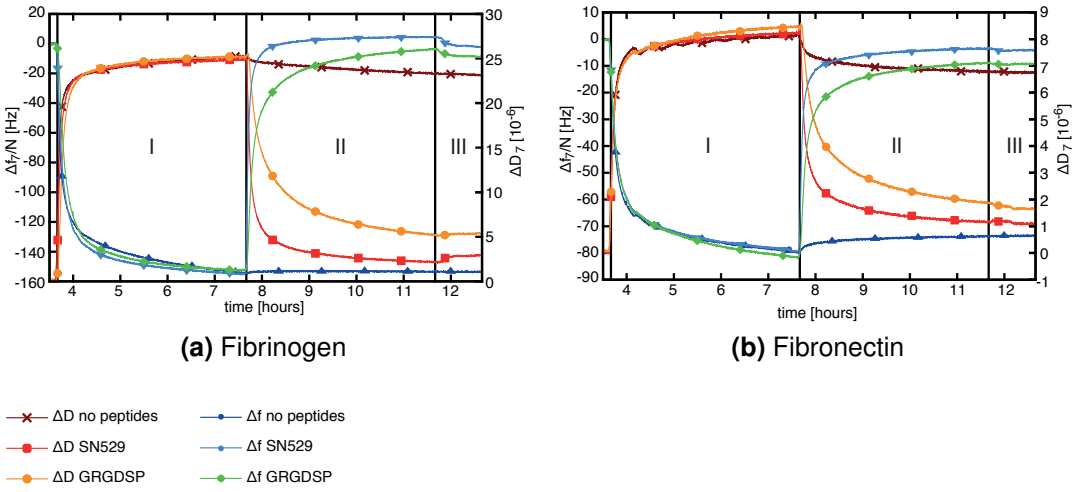

Figure 13.5.: Comparison of frequency and dissipation shifts for the competitive vs. uncompetitive unbinding of (a) integrin-liposomes and (b) integrin $\alpha_{IIb}\beta_3$ on fibrinogen. Integrin-liposomes and $50\,\mu g/ml$ of pure integrin $\alpha_{IIb}\beta_3$ were added to two fibrinogen-coated SiO_2 crystals each (step I). In step II activation buffer was added to all crystals. For integrin-liposomes and pure integrin $500\,\mu M$ of the RGD-peptides GRGDSP and SN529 was added in one channel each, respectively. A very strong increase in resonance frequency and a strong decrease in dissipation during this step indicated an unbinding of integrin-liposomes and pure integrin in the channels where SN529 was added. Addition of GRGDSP resulted in a less pronounced unbinding of integrin-liposomes and pure integrin, which was indicated by smaller signal changes than for SN529. When only activation buffer was loaded into the system no unbinding of integrin-liposomes or integrin was observed. Adapted from Frohnmayer et al.[342]

For integrin-liposomes the addition of SN529 yielded a frequency increase of $\Delta F^{lip}_{SN529} = 135 \pm 13\,Hz$ and a dissipation decrease of $\Delta D^{lip}_{SN529} = (-26.9 \pm 1.1) \cdot 10^{-6}$. In the activation buffer the frequency and dissipation only recovered by $\Delta F^{lip}_{act} = 0.68 \pm 0.15\,Hz$ and $\Delta D^{lip}_{act} = (-2.10 \pm 0.05) \cdot 10^{-6}$, respectively. These signal changes indicated a strong unbinding of the integrin-liposomes from the fibrinogen-coated crystals. When the peptide GRGDSP was added to ad-

hered integrin-liposomes the corresponding signal changes were less pronounced, $\Delta F^{lip}_{GRGDSP} = 129 \pm 18\,Hz$ and $\Delta D^{lip}_{GRGDSP} = (-23.2 \pm 1.9) \cdot 10^{-6}$, so that a weaker unbinding effect from the fibrinogen surfaces was observed with this peptide, which has a larger molecular weight than SN529.

Addition of SN529 to pure integrin yielded a frequency increase of $\Delta F^{int}_{SN529} = 77 \pm 11\,Hz$ and a dissipation decrease of $\Delta D^{int}_{SN529} = (-7.2 \pm 0.6) \cdot 10^{-6}$. With GRGDSP the frequency only increased by $\Delta F^{int}_{GRGDSP} = 74 \pm 13\,Hz$ and the dissipation was lowered by $\Delta D^{int}_{GRGDSP} = (-6.9 \pm 0.7) \cdot 10^{-6}$. In the activation buffer the frequency and dissipation only recovered by $\Delta F^{lip}_{act} = 6.1 \pm 0.1\,Hz$ and $\Delta D^{lip}_{act} = (-1.39 \pm 0.04) \cdot 10^{-6}$, respectively.

	Activation buffer		SN529		GRGDSP	
	int-lipo	integrin	int-lipo	integrin	int-lipo	integrin
ΔF	0.68 ± 0.15	6.1 ± 0.1	135 ± 13	77 ± 11	129 ± 18	74 ± 13
ΔD	-2.10 $\pm$ 0.05	-1.39 $\pm$ 0.04	-26.9 $\pm$ 1.1	-7.2 $\pm$ 0.6	-23.2 $\pm$ 1.9	-6.9 $\pm$ 0.7

Table 13.3.: Summary of maximal frequency and dissipation shifts during integrin-mediated adhesion on fibrinogen-coated crystals upon addition of RGD-peptides as monitored by QCM-D. Addition of the RGD-peptides SN529 and GRGDSP to adhered integrin-liposomes and integrin led to detachment of both samples, indicated by respective frequency increases and dissipation decreases. The unit of frequency shifts is Hz and the unit of dissipation shifts is 10^{-6}.

These signal changes indicate that pure integrin was also unbound by both RGD-peptides with SN529 resulting in a stronger unbinding effect than GRGDSP due to the difference in molecular weight. With the peptide SN529 both, integrin-liposomes and pure integrins, were almost completely removed from the fibrinogen surfaces as can be seen by the corresponding frequency changes, which re-approach the pre-sample value after 11 $hours$. The unbinding of integrin-liposomes and integrins mediated by the peptide GRGDSP was less complete, as the frequency signals did not reach the initial value after 12 $hours$ 40 $minutes$. The chambers, into which activation buffer without any RGD-peptides was injected, did not show any frequency or dissipation changes during step II. Hence, the observed unbinding was caused by the presence of the different free RGD-peptides in the flow system.

These differences between the two peptides are even more pronounced in the first derivative of the measured data in step II as shown in figure 13.6. The dynamics quickly increase to a peak and as the amount of bound sample decreases steadily converges to zero. The first phase could be attributed to a Michaelis-Menten like substrate-enzyme binding phase.[398] While the latter slow down is, referencing

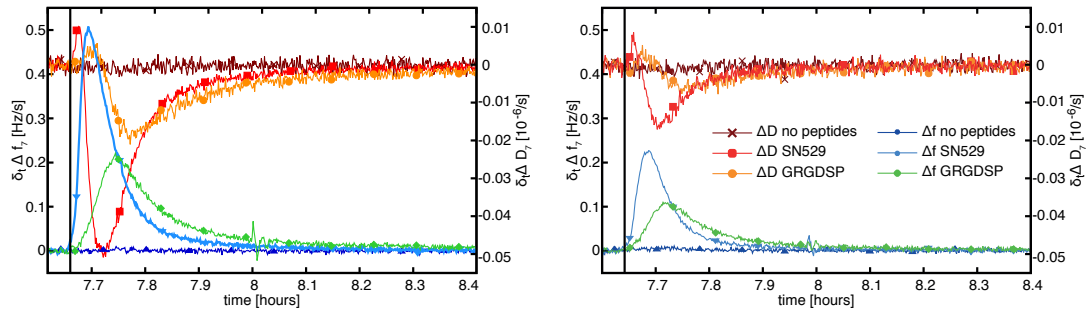

(a) Integrin-Liposomes **(b)** Integrin

Figure 13.6.: First derivative of competitive unbinding of (a) integrin-liposomes and (b) integrin from ECM proteins coated SiO_2 QCM-D sensors. As the computing the first derivative from QCM-D data is very susceptible to noise, all plotted derivative data points were averaged in a rolling mode over five consecutive measurement points, which accounts for $1\,second$ of measurement time.

figure 13.5, due to a depletion of substrate. Overall the dynamics are comparable faster and more pronounced for SN529 in comparison to GRGDSP. A possible explanation is the slower diffusion and permeation of the sample layer, due to the lager molecule size.

13.3.2. Dependence on Integrin-Concentration

Next the binding affinity of this model system for cellular adhesion was more thoroughly studied by measuring liposomes with different molar densities of reconstituted integrin. Therefore, integrin-liposomes with molar ratios of integrin lipid of 1 : 1000, 1 : 3000 and 1 : 4000 were prepared. The average size of these samples was determined by DLS to be on average $111 \pm 2\,nm$. The narrow size distribution is important, as generally an influence of liposome size on the recorded signals was observed. This effect was not further investigated quantitatively, since there is currently no method of controlling the liposome size using the detergent removal method. The general tendency in the $100nm - 200\,nm$ size range used in these experiments seems to be a decreased frequency shift and an increased dissipation shift with increasing size.

The specific adhesion of the different integrin-liposomes was studied on fibrinogen-coated crystals for $11\,hours$ and $40\,minutes$. The results are shown in figure 13.7 and table 13.4. The frequency shifts were determined as described in section 13.2. The acquired values were $\Delta F_{1:1000} = -153.34 \pm 0{,}13\,Hz$, $\Delta F_{1:3000} = -82.8 \pm 0.3\,Hz$ and $\Delta F_{1:4000} - 54.71 \pm 0.15\,Hz$. The dissipation signals were found to be $\Delta D_{1:1000} = (23.20 \pm 0.03) \cdot 10^{-6}$, $\Delta D_{1:3000} = (19.84 \pm 0.004) \cdot 10^{-6}$ and $\Delta D_{1:4000} = (16.90 \pm 0.03) \cdot 10^{-6}$. These results indicate that the frequency and

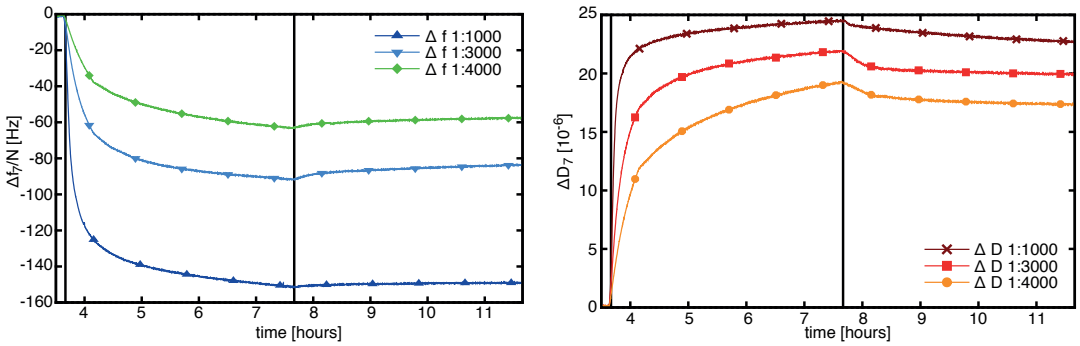

(a) Frequency **(b)** Dissipation

Figure 13.7.: Adhesion of integrin-liposomes with different integrin concentrations to fibrinogen-coated SiO_2 crystals. The molar ratio of lipids to proteins were $1:1000$, $1:3000$ and $1:4000$: The (a) frequency and (b) dissipation changes indicate a strong relation between the integrin concentration and the binding affinity of integrin-liposomes to fibrinogen-coated crystals. Adapted from Frohnmayer et al.[342]

dissipation changes depend on the integrin:lipid ratio, which is used to initiate the reconstitution of integrins into lipid vesicles by detergent-mediated self-assembly. The reconstitution of different integrin concentrations into lipid vesicles was found to be a valuable tool to tune different adhesion strengths in synthetic model cells, i.e. reduced integrin concentrations resulted in less adhesion strength.

	Different integrin concentrations		
	1:1000	1:3000	1:4000
Frequency change $[Hz]$	-153.34 $\pm$ 0.13	-82.8 $\pm$ 0.3	-54.71 $\pm$ 0.15
Dissipation change $[10^{-6}]$	23.20 $\pm$ 0.03	19.84 $\pm$ 0.04	16.9 $\pm$ 0.03

Table 13.4.: Adhesion of integrin-liposomes with varying integrin concentration to fibrinogen surfaces as monitored by QCM-D. The signal changes clearly correlated with the integrin concentration: For decreasing integrin concentration in the liposomes the frequency and dissipation shifts were less pronounced, thus leading to reduced binding to the fibrinogen-coated crystals.

13.4. Discussion

The research presented here was done in order to investigate the integrin-mediated adhesion of a minimal synthetic cell systems on naturally occurring ECM proteins using QCM-D analysis. Previously, biotin-functionalized liposomes have been used on avidin-coated surfaces to mimic the molecular recognition processes involved in cell adhesion.[332] In this study a model system was used, which was less biorelevant since receptor-ligand pairs are not naturally occurring in cells as it is the case for integrins.[6] This model system has now overcome these limitations by reconstituting functionally active integrins into lipid vesicles and studying their adhesion on ECM proteins like fibrinogen, fibronectin and collagen.

When pure liposomes were loaded onto uncoated quartz crystals a strong unspecific binding affinity was observed, which resulted in liposome rupture and the formation of SLBs as it had previously been reported.[336, 399] In contrast, integrin-liposomes, which were loaded onto uncoated quartz crystals, did not rupture to form bilayers. This finding leads to the conclusion that reconstituted integrin stabilizes the liposomes. This effect could either be a steric repulsion or due to an increased mechanical stability. Although integrin-liposomes appear to be more stable, this experiment points on the general issue of liposome stability. Based on these results the adhesive behavior of integrin-liposomes as a simplified cellular model system on different ECM proteins was studied.

On the RGD-containing ECM proteins fibrinogen and fibronectin specific integrin-mediated adhesion of integrin-liposomes in the presence of bivalent ions was observed. On collagen, which does not contain any RGD binding sites, no adhesion affinity of integrin-liposomes, liposomes or pure integrin on was measured. Neither was binding of pure liposomes to any of the crystal coating detected. These reference measurements confirmed that the observed interaction between integrin-liposomes or pure integrin and fibronectin as well as fibrinogen was caused by the specific binding of integrin to the RGD sequence. From these results it can be concluded, that the ECM proteins used in this study formed confluent layers on the SiO_2 surface. Most notably because pure liposomes did neither bind nor rupture. Pure integrin was found to specifically bind to fibrinogen and fibronectin with frequency changes comparable to the binding of integrin-liposomes on both RGD-containing ECM proteins. Nevertheless, the dissipation shifts of pure integrin binding to fibrinogen and fibronectin were less pronounced than for integrin-liposomes. This observation indicates that pure integrin formed a tight monolayer on the protein-coated crystals. In comparison, liposomes move a volume of the enclosed and surrounding liquid when oscillating. This movement results in a major damping effect, which is responsible for the observed strong dissipation shifts when integrin-liposomes bind to fibrinogen or fibronectin. Therefore, for the

first time, a cell model system with reconstituted integrins in lipid vesicles was established. It mimics integrin-mediated cell adhesion on RGD containing ECM proteins.

Furthermore, the synthetic adhesion of this model system on fibrinogen surfaces was reversed by addition of two RGD-peptides with different molecular parameters. Here, the binding sites of fibrinogen competed with the binding sites of free RGD-peptides in solution, which was added in a higher concentration than the RGD binding sites available on the fibrinogen-coated crystals. In this experiment integrin-liposomes were found to detach from the fibrinogen surfaces even faster than pure integrins. This more pronounced unbinding of integrin-liposomes might have occurred because pure integrins formed a tight molecular layer on the fibrinogen-coated crystals and were less accessible for the free RGD-peptides than the spherical integrin-liposomes, which protruded into the surrounding peptide-loaded buffer with an average diameter of $100\,nm$ to $200\,nm$. In comparison, the peptide SN529 resulted in a complete unbinding of integrin-liposomes and integrins whereas GRGDSP peptides did not detach the adhered integrin-liposomes and integrins completely and as quickly. This different competitive unbinding behavior is related to the different molecular structures and molecular weights of the RGD peptides: with $587\,Da$ the peptide GRGDSP is approximately 1.2 fold larger than the peptide SN529, which only weighs $498\,Da$. As a result of this size and structural difference the smaller peptide SN529 might be more mobile in solution and accessible for the integrin binding pocket as well as the molecular structure results in higher affinity binding than peptide GRGDSP. In summary, yielding a more pronounced unbinding of integrin-liposomes and integrins.

Additionally, by reconstituting different integrin concentrations into lipid vesicles it was also possible to control the adhesion strength of integrin-liposomes on fibrinogen surfaces even further. With decreasing integrin concentration in the synthetic cells the adhesion on fibrinogen was reduced proportionally. In future studies on integrin-mediated adhesion this result will promote the development of a minimal cell model system with tailored synthetic adhesion. The next step towards synthetic cells, which mimic and control adhesion, will be the reconstitution of integrins into cell-sized giant unilamellar lipid vesicles. Thereby, reconstituted integrins might even help to overcome the limitations of current model cells due to the fragile nature of giant lipid vesicles.

14. Charaterization of dsGUV

The formation of compartments enclosed by a lipid membrane, is one of the distinguishing features of eukaryotic cells. As a key step in the development of life, the evolution of these compartments allowed spatial and temporal control over biological processes.[400, 401] Approaches in SB to remodel cell-like compartments based on lipids have fundamental limitations. In part, this is due to the mechanical and chemical instability of lipid vesicles,[90] and lack of technical means available for their manipulation. The hybrid droplet and lipid compartment system developed in this thesis, the droplet-stabilized GUV (dsGUV), overcomes many of these restrictions. The droplet-microfluidic basis of this technique allows the sequential loading of such compartments with reagents through pico-injection. The characterization presented in this thesis focused on the transmembrane protein integrin $\alpha_{IIb}\beta_3$. A proof of concept of the dsGUV system was developed in collaboration with Jan-Willi Janiesch. The characterization of this new model system was done in close collaboration with Marian Weiss. A submitted publication additionally includes work done by collaborators analysing a second transmembrane protein, F_0F_1-ATP synthase and formation of tubulin (both Marian Weiss) and actomyosin complexes (Jan-Willi Janiesch and Barabara Haller) within dsGUVs.

Several characterization techniques were employed in order to investigate, if the inner droplet interface is covered by an intact and continuous lipid layer. As a straight forward experiment the fluorescence intensity of dsGUVs produced with a lipid composition containing a percentage of fluorescently labeled lipids was measured and compared to intensities of GUVs conisting of the same lipid composition. First, the total concentration of lipids in the aqueous solution was varied from values below the theoretical coverage to an over saturation. Thus, the dependency from concentration to fluorescence intensity was derived. Second, droplets formed with the theoretical correct amount were compared to GUVs formed with the same lipid composition.

To exclude a combined lipid-surfactant layer the diffusion kinetics of the lipid bilayer as well as other molecule confined to the droplet interface was studied using FRAP (see chapter 10). These values were compared to values measured for SLBs and values taken from literature. This allowed an interesting overview regarding the dynamics of the interface and additionally indicates future possibilities of the dsGUV model system.

To conclude the characterization of dsGUVs, the possibility to recover the GUV from droplets was investigated. Although this method is in an early developmental stage, the results were highly promising and a proof of concept will be presented. Of all the characterization methods presented in this thesis, will provide the most conclusive answer about the nature of the lipid bilayer in the dsGUVs.

14.1. dsGUV Formation

There are two experimental approaches to form dsGUV. Both methods start by encapsulating SUVs/LUVs, or GUVs dissolved in MilliQ water into water-in-oil droplets during droplet production. Similar to the formation of planar SLBs the presence of bivalent cations was identified as a crucial factor for dsGUVs formation.[402, 403] Omitting bivalent ions no transfer of the encapsulated liposomes to the droplet interface in the form of lipid bilayer was observed. In these cases, for SUVs/LUVs a homogeneous distribution of the fluorescence signal was observed through the whole volume of the droplet and GUVs stayed intact. Therefore, following optimization the formation of dsGUV requires bivalent cations. A concentration of $10mM$ $MgCl_2$ in the aqueous phase has shown the best results as shown in figure 14.1a. An observation that is supported by studies on the formation of planar SLBs, Mg^{2+} ions are known to be the most efficient mediators of lipid vesicle rupturing due to promotion of adhesion to the substrate.[403, 404] The addition of other bivalent ions, such as Ca^{2+} ($10mM$) or Mn^{2+} led to slower or partial bilayer formation as presented in figure 14.1b. If bivalent ions were introduced into preformed droplets containing either LUVs or GUVs through pico-injection, dsGUV formation was also observed.

The standard way for dsGUV formation was a one-step experimental approach. Here, both types of lipid vesicles (SUVs and GUVs) were mixed with bivalent ions and encapsulated within the droplets during the droplets production. This method allowed a very high production rate in the kHz range. Alternatively, a two-step approach, where liposomes and bivalent ions are introduced separately, was chosen for some experiments. In that case the bivalent ions were pico-injected into SUV, or GUV-caontaining droplets. Both experimental approaches are depicted in figure 14.2.

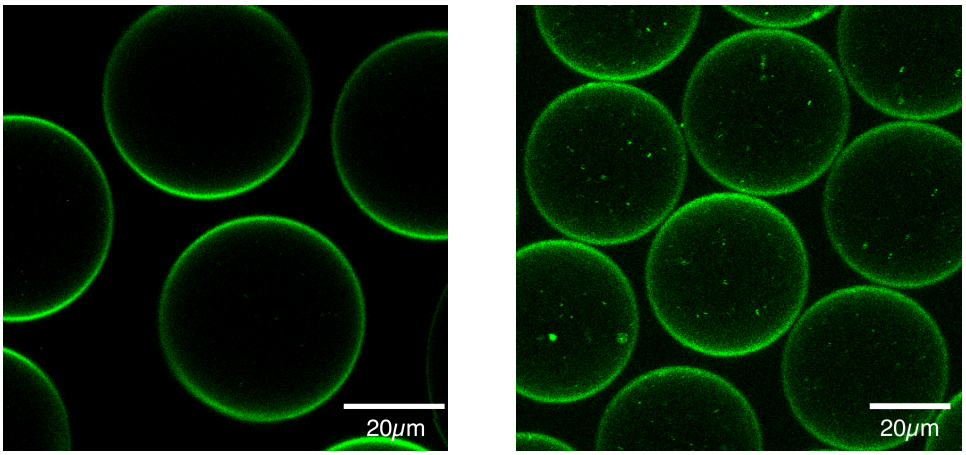

(a) $10\,mM$ Mg^{2+} **(b)** $10\,mM$ Ca^{2+}

Figure 14.1.: Fluorescence cross-section images of the lipid distribution (with the LUV composition DOPC:DOPE:DOPS 8:1:1 including 1% ATTO488-DOPE) within the droplets containing (a) $10\,mM$ Ca^{2+} and (b) $10\,mM$ Ca^{2+}, measured $1\,hour$ after formation. Adapted from Frohnmayer et al. [134]

14.2. Intensity Analysis

As described in section 9.3 the intensity signal observed from a lipid membrane in proximity to the interface of a droplet is distorted by refraction and defraction due to the oil-water interface (see figure 9.3). This complication was resolved by fitting a gaussian curve at the intensity profiles and integrating the area under the curve as described in section 9.3. Therefore in the following sections, 14.2.1 and 14.2.2, the units given will be an arbitrary unit $(a.u.)$, as measured by the microscopes photomultiplier, times the dimension integrated over in micrometers μm.

14.2.1. Concentration Dependency

By varying the lipid concentration in the encapsulated volume in combination with the narrow size distribution of microfluidic droplets, the relationship between the available amount of lipids and the resulting fluorescence intensity could be determined. A plot of the measured data is shown in figure 14.3. This analysis provides answers to the following key questions. Are the theoretical considerations concerning the necessary lipid concentration presented in section 9.1.1 credible? Is there a partial lipid bilayer (section 4.1) below the threshold?

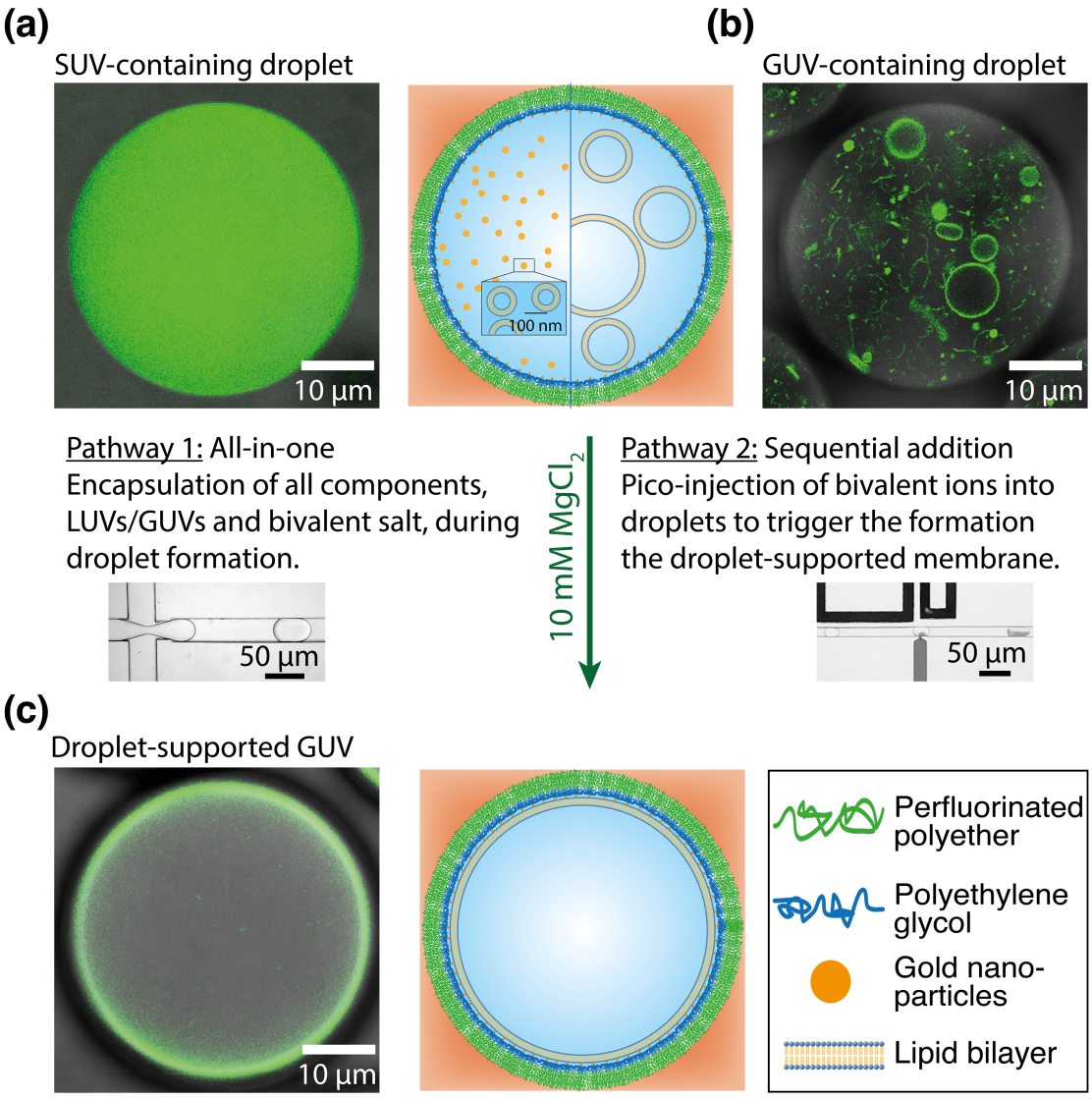

Figure 14.2.: Schematic representation of two experimental approaches for dsGUVs formation. The production of dsGUVs starts by forming (a) SUVs/LUVs or (b) GUVs and encapsulating them into water-in-oil droplets. In an All-in-one: approach (pathway 1) $10\,mM$ Mg^{2+} are encapsulated with the liposomes. Alternatively, Mg^{2+} can also be pico-injected into preformed droplets containing liposomes (pathway 2). (c) The bivalent ions cause the liposomes to form a supported lipid bilayer on the droplet interface. Fluorescence signal comes from ATTO488-DOPE, which making up 0.5% of the lipids mixture consisting of 8:1:1 DOPC:DOPE:DOPS. Adapted from Frohnmayer et al. [134].

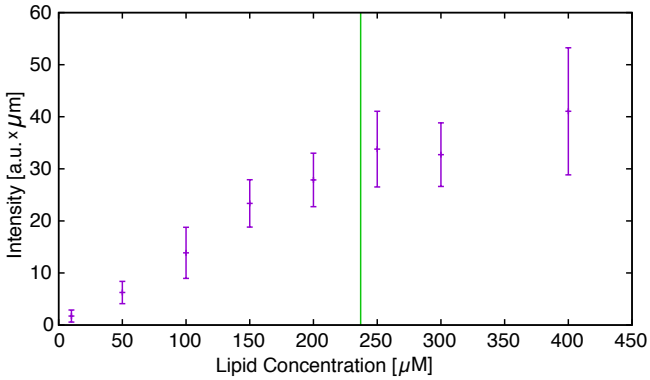

Figure 14.3.: Intensity analysis of dsGUV with a diameter of $120\,nm$ produced with different lipid concentrations. The theoretical sufficient amount is indicated by a green vertical bar at $237\,\mu M$. The data points up until this point are approximately linear, which matches the expected behavior. Above an excess amount of lipids is expected. Here liposomes form aggregates at the interface, which makes intensity analysis difficult. This effect is visible in the increased standard deviation at the $400\,\mu M$ data point.

Considering the diameter of $120\,\mu m$ of the droplets used in this experiment, a calculated concentration of $237\,\mu M$ lipids is required for full bilayer coverage. As can be observed in figure 14.3, the intensity values are increasing approximately linear up to the theoretical estimated concentration. At elevated concentration the intensity reaches a plateau. It should be noted that at higher concentrations the excess lipids form aggregates of liposomes at the interface, thus making it more difficult to measure credible intensity values. This effect is showing a higher deveation for the data point at $500\,\mu M$.

14.2.2. Intensity Comparison of dsGUVs and GUVs

The intensity of dsGUVs was compared to the intensity of GUV encapsulated into droplets. The GUVs were encapsulated into droplets to keep results as comparable as possible. The fitting of the measured intensity profiles revealed similar integrated intensity values of $42 \pm 8\,a.u. \times \mu m$ and $44 \pm 4\,a.u. \times \mu m$ for dsGUV and the encapsulated GUVs, respectively. These findings suggest that freely suspended GUVs and dsGUV consist of the same density of fluorescently labeled lipids. This concludes the analysis on the intensities of the lipid bilayers.

14.3. FRAP Analysis

Intensity analysis revealed information regarding the density of fluorescently labeled lipids. But the information about the conformation of these lipids is limited. Moreover, the possibility of a mixed surfactant lipid layer had to be excluded. It can be predicted, that the diffusion coeficient of TRI7000 surfactants ($MW \sim 15{,}400\,g/mol$) will be smaller than the diffusion coefficient of lipids ($MW = 760 - 800\,g/mol$) not only due to higher molecular weight,[405, 406] but also due to polymeric spaghetti-like structure.[407, 408] Additionally, in a mixed layer the diffusion of the lipids would also decrease, as they would need to diffuse around the larger molecules.[409, 410] Therefore, measuring the diffusion of different molecules confined to the interface gave insight into its structure. A detailed explanation of the evaluation is provided in section 10.

14.3.1. GFP-labeled GNP-Surfactants

Due to the lack of fluorescently labeled surfactants, the diffusion of the surfactants could not be measured directly. Therefore, gold-linked surfactants (see section 8.1.2) were labeled fluorescently using GFP.[174] FRAP analysis of this probe revealed diffusion coefficients of $0.21 \pm 0.05\,\mu m$ and $0.20 \pm 0.05\,\mu m^2/s$ when mixed with TRI7000 and TRI2500, respectively. These values are slightly lower than literature values obtained for water-in-water polymersomes.[411] A possible explanation for the lower diffusion coefficients of water-in-oil droplets is the viscosity of the surrounding oil, FC-40, which is $3.8\times$ times higher than the viscosity of water. Oil viscosity might be also a potential reason for the similar diffusion coefficients, independent of the surfactant molecular weight. It is worth mentioning here that different GFP and the surfactant concentrations in the range between $1\,\mu M$ and $10\,\mu M$ and $1\,mM$ and $10\,mM$, respectively, did not affect the surfactant mobility.

14.3.2. GFP-labeled Lipids

It can be observed that the fluorescent signal of GFP is localized at the membrane (figure 14.4c) of the DGS-NTA(Ni)-containing dsGUVs in comparison to an equally distributed fluorescent signal (figure 14.4d) within the droplets containing no functionalized lipids. It has to be noted here, that this diffusion coefficient is one order of magnitude higher in comparison to GFP-labeled surfactants. FRAP measurements of the GFP-functionalized dsGUVs revealed a diffusion coefficient of $1.22 \pm 0.03\,\mu m^2/s$. Successful functionalization of the dsGUVs with His6-GFP is particularly important, since the NTA-thiol chemistry behind the immobilization of these proteins is the same as required for immobilization of proteins such as actin and tubulin.

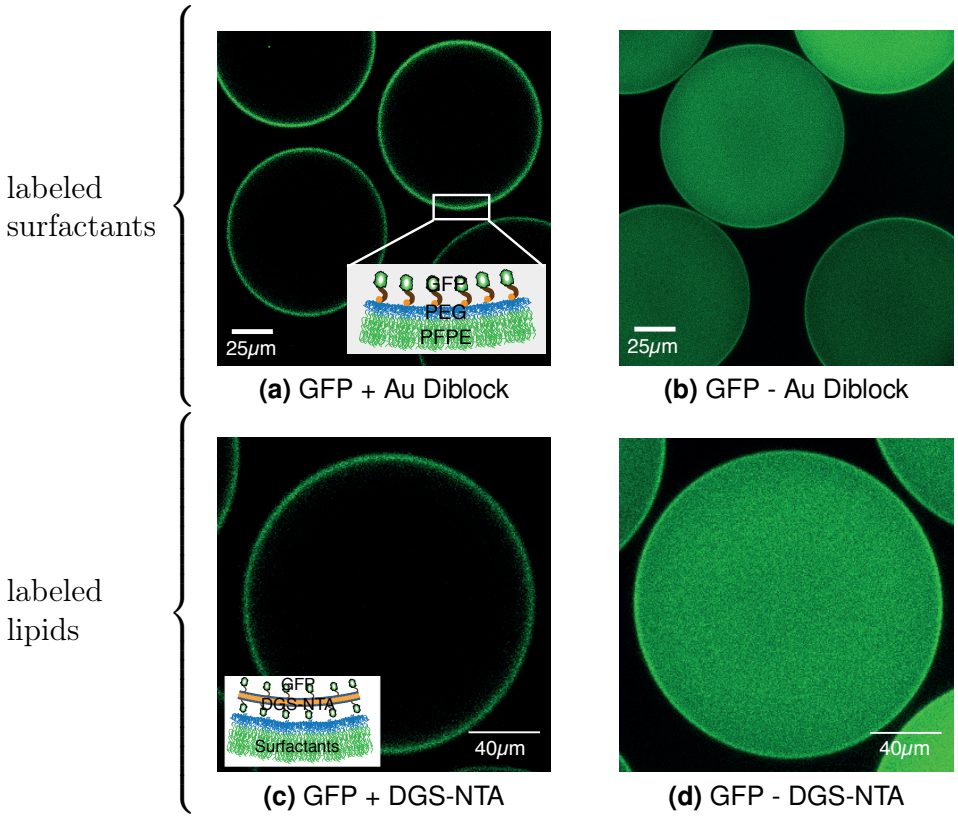

(a) GFP + Au Diblock **(b)** GFP - Au Diblock

(c) GFP + DGS-NTA **(d)** GFP - DGS-NTA

Figure 14.4.: Cross-section confocal images of (a) gold-nanostructured and (b) gold-free polymer-stabilized droplets formed with aqueous solution of His6-GFP-NTA-thiol measured 1 day after formation. (c) A fluorescence cross-section image of His6-GFP linked to DGS-NTA(Ni)-containing dsGUV. (d) In contrast to the dsGUV containing NTA-lipids, the fluorescence intensity in the dsGUV containing DOPC only is distributed equally. Adapted from Frohnmayer et al.

14.3.3. Lipid Diffusion

As an incorporated layer of lipids and surfactans would result in a decreased lipid diffusion, FRAP measurements were performed to compare the lipid diffusion coefficients in encapsulated GUVs and dsGUVs. The results derived for various lipid composition and fluorophore types are presented in table 14.1.

Lipid composition	Diffusion Coefficient $[\mu m^2/s]$	
	Encapsulated GUVs	dsGUVs
DOPC:DOPE:DOPS (8:1:1), 1% ATTO488-DOPE	3.52 ± 0.26	3.31 ± 0.77
egg PC:egg PG (1:1), 1% ATTO488-DOPE	3.96 ± 0.51	2.88 ± 0.06
DOPE, 1% Rhb-DOPE	4.42 ± 0.65	4.11 ± 0.59

Table 14.1.: Summary of the diffusion coefficients obtained for different lipid compositions in dsGUV by FRAP measurements.

The data shows a minor reduction of lipid diffusion in dsGUVs. FRAP and fluorescence correlation spectroscopy (FCS) measurements performed in previous studies with similar lipid compositions revealed diffusion coefficients in the same range as well as a similar tendency to lower values in the case of SLB.[357, 404] In SLBs this can be related to the fact that lipid membrane is subject to friction with the supporting material. A comparable effect should be caused by the polymer shell of the droplet, whose mobility is estimated an order of magnitude lower (see section 14.3.1). Moreover, it is known that bivalent ions bind to phosphatidylcholine membranes and lead to a decrease in the self-diffusion of lipids in the membrane.[412–414]

14.3.4. Electron Microscopy

In addition to the characterization methods shown here, cryo-SEM and cryo-TEM were employed to gain additional information about the nature of the lipid bilayer. However, cryo-SEM ambiguous results, while cryo-TEM yielded no results at all. Figures show cryo-SEM micrographs of freeze-fractured droplets 14.5a without and 14.5b a dsGUV.

Figure 14.5c shows dsGUVs of less than $4\,\mu m$ diameter. These droplets were produced with the microfluidic chip presented in section 8.7. The intent was to evaluate if droplets could be observed with a cryo-TEM. Most current cryo-TEM sample preparation methods, are designed for microscoping cells or tissue.[349] The oil surrounding the droplet could interfere with these methods or require major adjustments. However, a collaborator kindly agreed to try, if we were able to produce droplets with around $2\,\mu m$ diameter. However, our collaborator was not able to measure the droplets with a sufficient resolution.

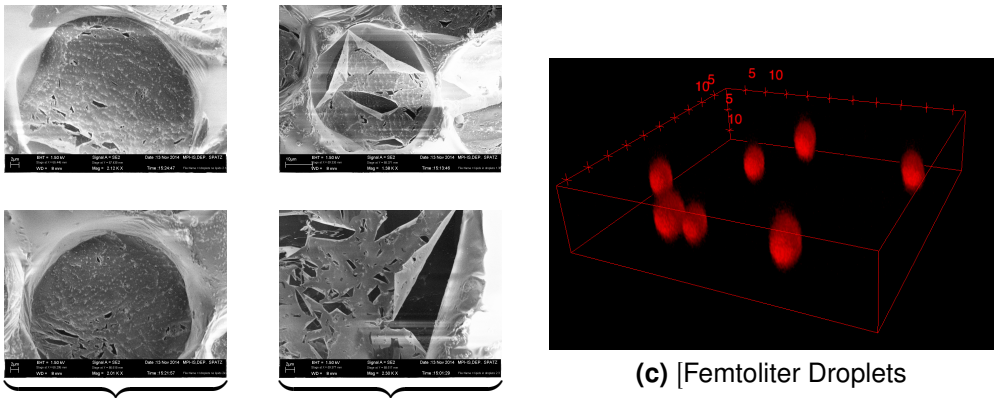

(a) without lipids **(b)** with lipids **(c)** [Femtoliter Droplets

Figure 14.5.: SEM micrographs of freeze-fractured droplets (a) without and (b) with a dsGUV. It is not possible to derive a credible conclusion from these micrographs. There is a thin film, peeling of the interface, visible in the right column of SEM images. However, it is not possible to determine if this is a lipid bilayer. (c) Fluorescence images of femtoliter droplets containing a dsGUV with ATTO488-DOPE.

14.4. Pico-Injection of Protein into dsGUV

With most current SB methods, as described in SB chapter 4, it is a tedious task to reconstitute or encapsulate proteins into GUVs. Applying the currently available methods, reconstitution and incapsulation of proteins into the freestanding GUVs is very complicated due to mechanical and chemical instabilities. A major driving force in the development of dsGUVs was the intend to overcome this restriction. In fact dsGUVs allow a sequential addition of multiple reagents as they are based on droplet-based microfluidic technology. The following section will cover the experimental steps of bottom-up assembly of a cell model system.

A key advantage of this novel protocell system is the possibility to manipulate preformed dsGUVs and thus allow sequential loading of additional components when building up a model system. Preformed dsGUVs, see section 14.1, were introduced into a pico-injection device, for subsequent pico-injection of various bioreagents. As this work was originally focused on modeling integrin-mediated adhesion, integrin $\alpha_{IIb}\beta_3$ was used as an example to showcase the advantages of the compartment system. The process is schematically depicted in figure 14.6. Pico-injection of integrin $\alpha_{IIb}\beta_3$-containing proteoliposomes into preformed dsGUVs lead to fusion of proteoliposomes and reconstitution of integrin into the dsGUVs. The correct reconstitution of the transmembrane protein was shown using diffusion measurements.

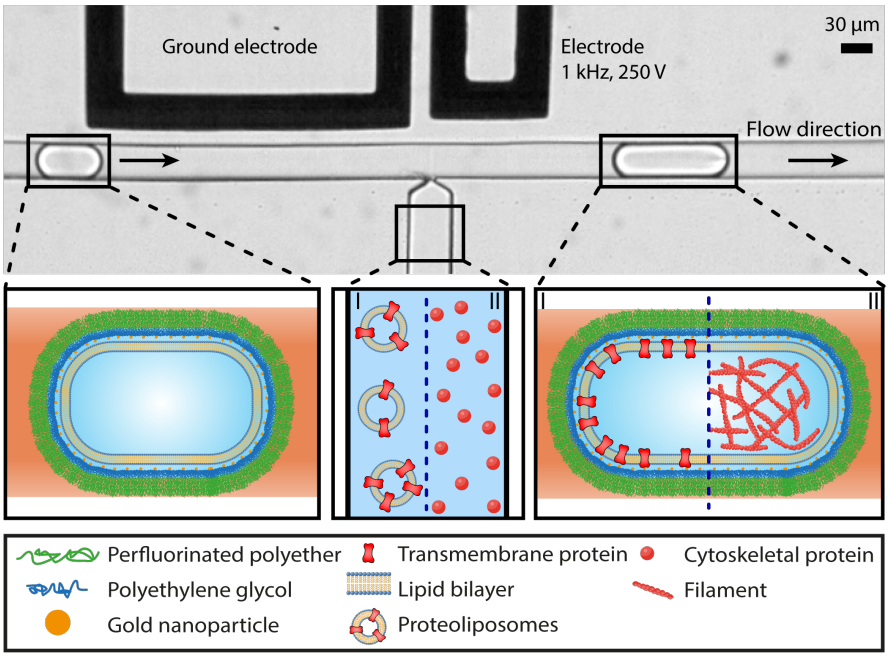

Figure 14.6.: Schematic representation of subsequent protein injection into dsGUVs via microfluidic pico-injection technology pico-injection. This can either be done in the (I) form of proteoliposomes, which allows to incorporate the transmembrane proteins into the dsGUVs' lipid bilayer, or (II) in form of free proteins, e.g. to observe cytoskeletal formation.

Lipid Composition	Object	D_{lip} $[\mu m^2/s]$	D_{pro} $[\mu m^2/s]$
None	GFP	NA	0.20 ± 0.05
DOPS:DGS-NTA (9:1)	GFP	NA	1.22 ± 0.03
DOPC:DOPE:DOPS (8:1:1), 1% ATTO488-DOPE	Integrin (Liposomes)	2.17 ± 0.07	0.67 ± 0.10
DOPC:DOPE:DOPS (8:1:1), 1% ATTO488-DOPE	Integrin (pure)	2.27 ± 0.22	0.70 ± 0.06
DOPC:DOPE:DOPS (8:1:1), 1% ATTO488-DOPE	Integrin (pure) + SN528	2.27 ± 0.16	0.13 ± 0.03

Table 14.2.: Summary of the diffusion coefficients of lipids and proteins reconstituted in dsGUVs obtained by FRAP measurements.

FRAP measurements were performed to investigate the mobility of transmembrane proteins incorporated in the membrane of dsGUV with a diameter of $150\,\mu m$. Table 14.2 presents a summary of diffusion coefficients of both, the lipids D_{lip} in dsGUVs and of the corresponding reconstituted proteins D_{pro}. In all cases, the measured D_{lip} values were lower in comparison to the diffusion coefficients of the dsGUVs containing no proteins listed in table 14.1. Lower diffusion coefficient values can be attributed to the fact that the lipid lateral diffusion is a subject to steric and charge-related perturbations from the incorporated proteins.[415]

The results for the diffusion coefficients measured for the reconstituted integrin $\alpha_{IIb}\beta_3$ of $D_{pro} \approx 0.7\,\mu m^2/s$ were consistent, independently on whether they were introduced as solubilized protein or reconstituted into proteoliposomes. These values are in good agreement with previously published studies on integrin $\alpha_{IIb}\beta_3$ lateral mobility in planar supported lipid bilayers or in the cellular membranes as obtained by FRAP,[325, 326, 394] and FCS measurements.[416]

To asses the functionality of the incorporated integrin, GNP-nanostructured droplets (section 8.1.2) functionalized with peptide SN528 (section 6.6) were used to provide binding sites for integrin adhesion. In this case the diffusion coefficient of integrin dropped significantly ($D_{pro} = 0.13\,\mu m^2/s$) to values closely resembling the mobility of the surfactant layer. This observation indicates a successful establishment of a linkage between the integrin and a functionalized droplet interface. Therefore, it is likely that part of the integrin is oriented correctly and remains functional within dsGUVs.

14.5. Advances in GUV Recovery from dsGUV

The following results represent early stages of the development of the recovery process. Nonetheless, they not only give insight into the structure of the dsGUV, but additionally hint at the future potential of the compartment system. Two approaches were devised to retrieve GUVs from droplets, a microfluidic approach, that allowed observation of single recovery events and an easy to apply bulk recovery. The former was crucial for a key insight on destabilizing surfactant choice and will be elemental to the further development of the method. The latter will very likely be the method of choice in future to recover large quantities of GUVs. The recovery process was developed in collaboration with Marian Weiss and Lucia Benk.

14.5.1. Effects of Destabilizing Surfactants

Although PFO-MEG and PFO-TEG have similar chemical structures as presented in section 8.1.4, their effects on surfactants and lipid membranes differ strongly. Both have been used in published work to deemulsify surfactant stabilized water-in-oil droplets to retrieve their content.[174, 343, 344]

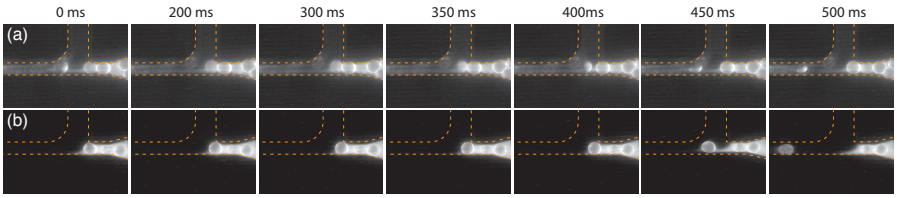

Figure 14.7.: The effects of (a) PFO-TEG and (b) PFO-MEG destabilizing surfactants on dsGUV observed in fluorescence in the ATTO488-DOPE fluorescence channel. The fluorescence signal shows that PFO-TEG starts to distort the lipid bilayer after $300\,ms$ of being in contact with a dsGUV. After $500\,ms$ the lipid bilayer appears to have crumpled in one part of the droplet. In contrast when using PFO-MEG the lipid bilayer appears to remain intact.

A general observation is the difference in latency between the droplets coming in contact with the destabilizing surfactant and coalescence of the droplets. At the same concentration the effect of PFO-TEG is more immediate. In the microfluidic recovery device concentrations comparable to the regular stabilizing surfactant of $2.5\,mM$ to $10\,mM$ were sufficient. For the same experiment $30\,vol.\,\%$ to $50\,vol.\,\%$ of PFO-MEG were required. In bulk the effects of PFO-TEG are more immediate, but in case of low concentration of PFO-TEG the deemulsification process slows down and eventually stops. Given time even at low concentration PFO-MEG completely deemulsifies droplets.

The usage of an extremely light sensitive Phantom v2511 high-speed camera (Vision Research, USA) allowed recording fluorescence at 1,000 fps and above. This enabled a crucial insight into the usability of the destabilizing surfactants. Although PFO-TEG appears to be the reagent of choice, due to its more immediate effect, there is a show-stopper. As shown in figure 14.7 PFO-TEG not only seems to interact with the microfluidic surfactants, but also with the lipid layer. Roughly $500\,ms$ after coming in contact with the reagent, the lipid membrane did completely collapse. In contrast, PFO-MEG does not appear to have any effect on the membrane and its stability. Therefore, PFO-MEG was used for GUV recovery experiments following this discovery.

14.5.2. Recovery in a Microfluidic Chip

The recovery device used in this thesis was designed by Marian Weiss with the fast acting PFO-TEG in mind, so channel length was adjusted accordingly. Early experiments with simple water-in-oil droplets and GUVs encapsulated in droplets showed promising results. An example of the latter is shown in figure 14.8. Here a droplet immediately breaks up upon coming in contact with the water phase and ejects its content, ATTO488-DOPE-containing GUVs. The high concentration of GUVs in the aqueous phase shows that this process can run stable for a long time. The concentration is reached even with a flow constantly removing recovered GUVs. Interestingly, as opposed to the observations described in section 14.5.1 the GUVs do not appear to be affected by the PFO-TEG.

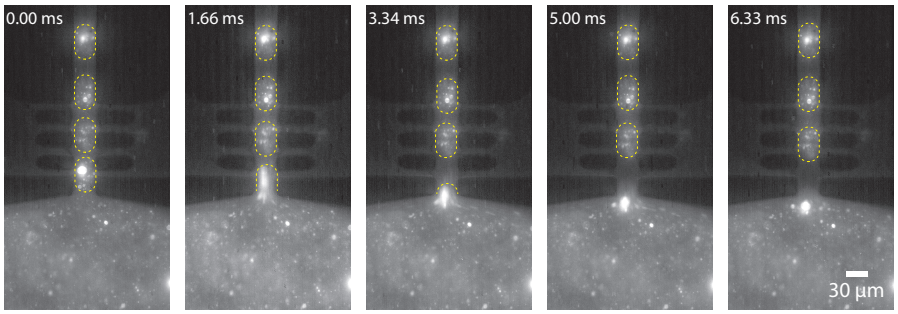

Figure 14.8.: Recovery of encapsulated GUVs in a microfluidic device. The outline are indicated by dotted yellow lines.

Recovery of dsGUVs in a microfluidic device using PFO-MEG is shown in figure 14.9. 14.9a shows brightfield images of ATTO488-DOPE and (b) a fluorescent image taken seconds apart. GUVs are not visible in brightfield images under these conditions. Clearly visible in the brightfield images are oil drops sticking to the walls. In the fluorescent image these oil drops are covered by fluorescent layer and not distinguishable from GUVs, or dsGUVs. As PFO-MEG breaks the surfactant layer only slowly, oil is pushed into the aqueous channel along with the droplets. Figures 14.9c and (d) also show a backlog due to the slow breakup process. This increases the probability of two droplets fusing with each other instead of with the water interface. An event that, in all observed incidents, led to unsuccessful recovery of the dsGUVs.

There is a variety of challenges this approach of recovery currently faces. For once, recovered GUVs don't seperate from the oil-water interface and tend to stick to the interface. The probability of GUVs to be recovered intact decreases above $30\,\mu m$.

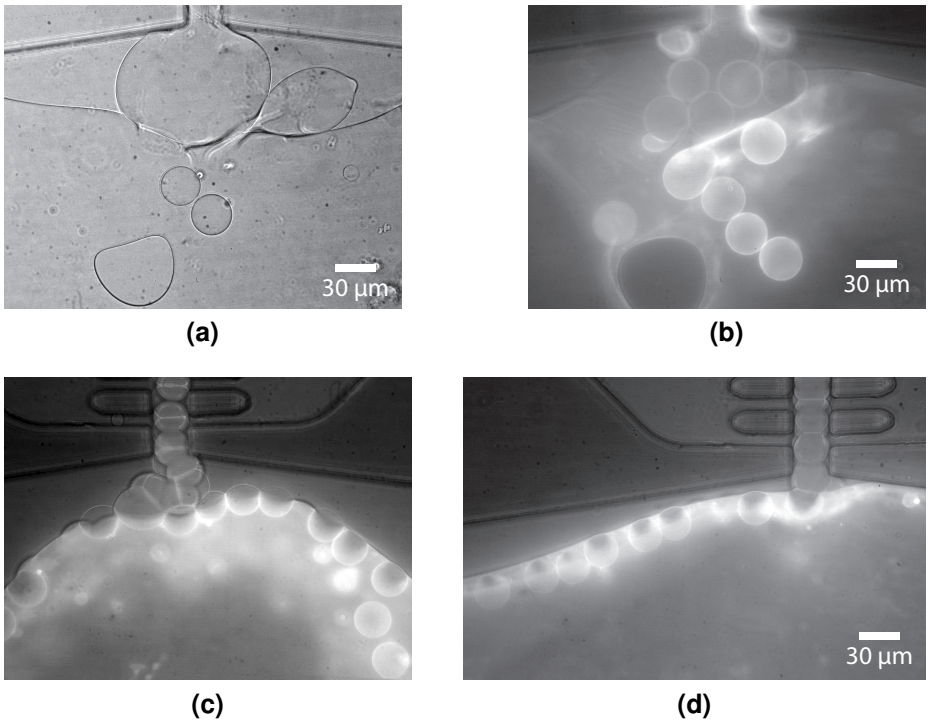

Figure 14.9.: Microscope pictures of GUVs being recovered in a microfluidic device in (a) brightfield illumination and (b)–(d) fluorescence illumination. (b) GUV are practically invisible in brightfield illumination with the low contrast range of the high speed camera used. In contrast to the oil droplets which show a stronger contrast. When comparing this image to a fluorescent image (b) taken seconds apart, previously invisible GUVs can be seen. However, oil drops visible in the brightfield image, can't be istinguished from GUVs in the fluorescence observation. These images were kindly provided by Lucia Benk.

14.5.3. Integrin-containing GUV Recovery

One of the fundamental constraints of current methods of GUV formation in SB is their restriction to either incorporate transmembrane proteins or to promote enclosure of cytosolic protein. Something where dsGUV are able to shine. But to really find adoption as a novel model system, recovery of protein containing GUV will be necessary. Here recovery of vesicles containing integrin $\alpha_{IIb}\beta_3$ is shown as an example of a transmembrane protein.

Figure 14.10 shows a recovered GUV with integrin $\alpha_{IIb}\beta_3$ embeded in its membrane. In the surrounding volume fragments of broken GUV are visible. Quantification of the survival rate is difficult, but is likely around 1% at the current developmental stage of the method. Considering the high production rate in the kHz range, this is still a productive approach. Functionality of the integrin after recovery was not yet confirmed.

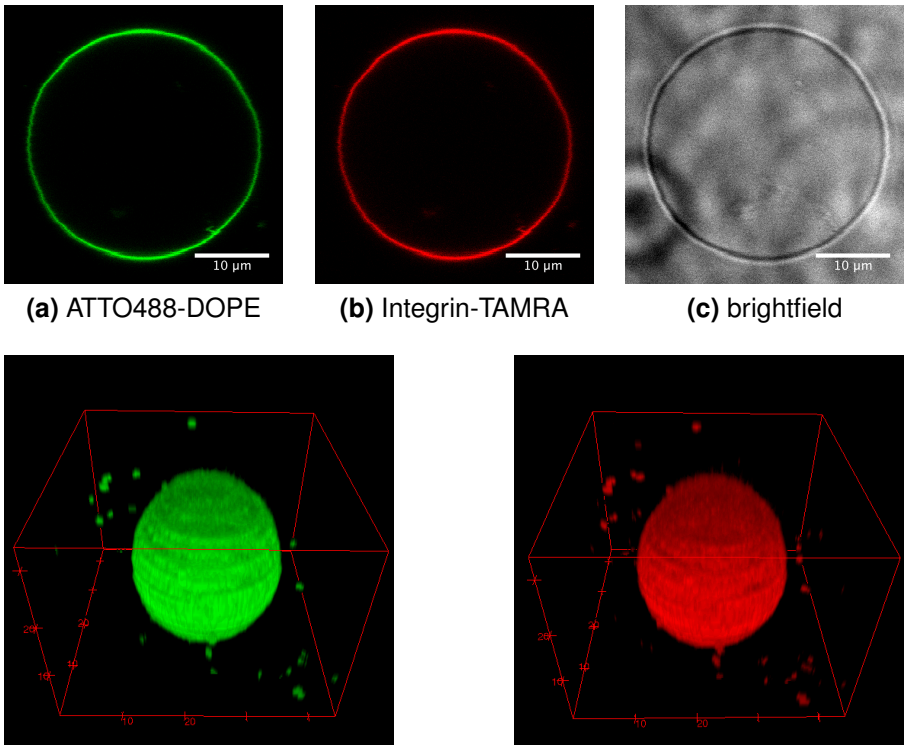

(a) ATTO488-DOPE **(b)** Integrin-TAMRA **(c)** brightfield

(d) ATTO488-DOPE **(e)** Integrin-TAMRA

Figure 14.10.: Microscope images of GUVs containing reconstituted integrin $\alpha_{IIb}\beta_3$ recovered from dsGUV, (a) ATTO488-DOPE, (b) integrin $\alpha_{IIb}\beta_3$ labeled with TAMRA and (c) a brightfield picture. Volume renderings were genereted from Z-stacks recorded for (d) ATTO488-DOPE and (e) TAMRA-labeled integrin $\alpha_{IIb}\beta_3$ with FIJI/ImageJ. The GUVs shown here preserved the size, $30\,\mu m$, of the droplets they were recovered from. In the volume projection fragments of broken GUVs are visible around the intact GUV. Due to the mechanical stress during recovery a majority of GUVs did not survive the process. Considering the high production rates of microfluidic droplet formation, even in the current early stages of development, the yield exceeds many other approaches.

14.6. Discussion

In conclusion, the developed technology overcomes fundamental limitations associated with the formation and manipulation of lipid based compartments in SB. This will enable the construction of more complex and sophisticated synthetic cells. Assembling such protocells with distinct functionality requires the combination of different proteins, molecules and buffer conditions. Moreover, many experiments require substances to be added subsequently to prevent unwanted interactions. A task impossible with most currently available technologies, where all components are encapsulated at once.

The formation of dsGUVs enables the generation of mechanically and chemically stable compartments which can be sequentially loaded by pico-injection technology with different proteins and other molecules. It allows for the combination of molecules and molecular organizations which naturally would not exist. These system properties will enable the realization of a real bottom-up assembly of complex combinations and functions within synthetic compartments in the future. It is worthwhile to mention that the formation of synthetic cells by this technology is a high-throughput method which enables the generation of up to 10^4 functional compartments per second. Therefore, it generates a vast number of protocells of unique precision which may be applied for follow-up scientific and technological applications.

At the beginning of this work concerns about the nature of the lipid bilayer were raised. To proof formation of an intact lipid bilayer various characterization techniques were used to investigate the nature of the lipid bilayer. Fluorescence intensity measurements showed comparable values as measured for GUVs under the same conditions. Analysis of the diffusion kinetics using FRAP yielded similar results for the lipid diffusion coefficient as reported in SLB. In comparison, diffusion coefficients measured for surfactants were one order lower. Especially, considering the positive recovery results an intact lipid bilayer can be assumed.

The potential of the new compartment for SB has been presented in this thesis using the transmembrane protein integrin $\alpha_{IIb}\beta_3$. Within living cells integrin is part of a large protein complex called focal adhesion. Any model system mimicking this cellular adhesion system will require a variety of proteins to function. Diffusion measurements for integrin yielded similar results as reported in other studies for GUVs and SLBs. The activity of integrin was shown by functionalizing gold-linked surfactants with a RGD-peptide. In this case, diffusion droped to values in good agreement with the diffusion of the surfactants. Applying the pico-injection method it will be possible to sequentially add more proteins, such as talin or vinculin and expand this model system.

A submitted publication will additionally expand the scope of model systems building on the dsGUVs approach. Collaborator Marian Weiss reconstituted functional F_0F_1-ATP synthase into dsGUVs. Driven by a pH gradient created by the addition of a special oil, conversion of adenosine diphosphate to adenosine triphosphate could be shown. Aditionally, two cytoskeletal complexes were created within dsGUVs. Collaborators Jan-Willi Janiesch and Barbara Haller were able to form actomysin complexes within the droplets and lin the filaments via His6-tags to the lipid bilayer. Marian Weiss used the dsGUV as a compartment to form tubulin complexes. In these experiments the lipid layer was important, as tubulin showed unspecific interaction with the microfluidic surfactant in absence of the lipid layer.

These examples show some of the possible applications the novel compartment system offers.

However, the microfluidic droplet stabilizing the dsGUV is a blessing and a curse at the same time. While providing increased stability and the means to apply microfluidic techniques such as pico-injection, it limits the scope of possible protocell-surface interactions. Therefore, the possibility to recover GUVs from dsGUVs was investigated. Although this technology is still in an early stage, promising results were achieved. Towards this goal, a microfluidic as well as a bulk method were developed. The former allowed observation of individual GUVs being recovered from dsGUVs. While the latter allows to expand this process for a large number in a short period of time. The recent progresses in recovery show, that the dsGUVs compartment system could also be an intermediate step. Complex model systems could be assembled within microfluidic chips and later be recovered to perform experiments, that were previously impossible. This opens up a broad range of future applications.

15. In Silico Microfluidics

The development of increasingly sophisticated functional units in microfluidics entails a growing complexity in the overall structure of the devices. Therefore, the design tools have to be updated to keep pace with the evolution of the microfluidic chips. Previous studies have taken steps into this direction, simulating droplet formation,[417, 418] and sonic waves in microfluidic chips.s However, an extensive literature search yielded no results regarding electric fields in microfluidic chips. For many applications, it might be sufficient to tune up the electric field until the desired effect occurs.

15.1. Field Strength in standard Pico-Injector

The setup and use of a system for microfluidic pico-injection was a major task during this thesis. However, during the development and application of the system questions about the strength an distribution of the electric field arose. Therefore, a FEM model was set up to settle this question. The simulation was computed for two sizes of droplets, used for pico-injection experiments in this work and the corresponding pico-injection structures. The droplets had a diameter of $40\,\mu m$ ($34.388\,pl$) and $120\,\mu m$ ($105.72\,pl$). Channel width and height of the droplet carrying channels for the former were $30\,\mu m$ and for the latter $80\,\mu m$. The results are shown in figure 15.1.

As explained in section 12.1, in all simulations presented here, the potential was set to $1\,V$. As the normalized electric field is linearily dependent on the electric potential, this allows the easy calculation for fields caused by different potentials. For example the electric field computed in the center of a small droplet had a strength of $E_{1V} = 777\,V/m$. In most experiments a peak voltage of $250\,V$ was applied, hence the peak electric field was $E_{250V} = 194\,kV/m$. This is in the range most electroporation experiments use.[377] In the center of a $80\,\mu m$ droplet the field is $28\,\%$ ($557V/m$) weaker than in a $30\,\mu m$ device. This could be compensated by increasing the potential.

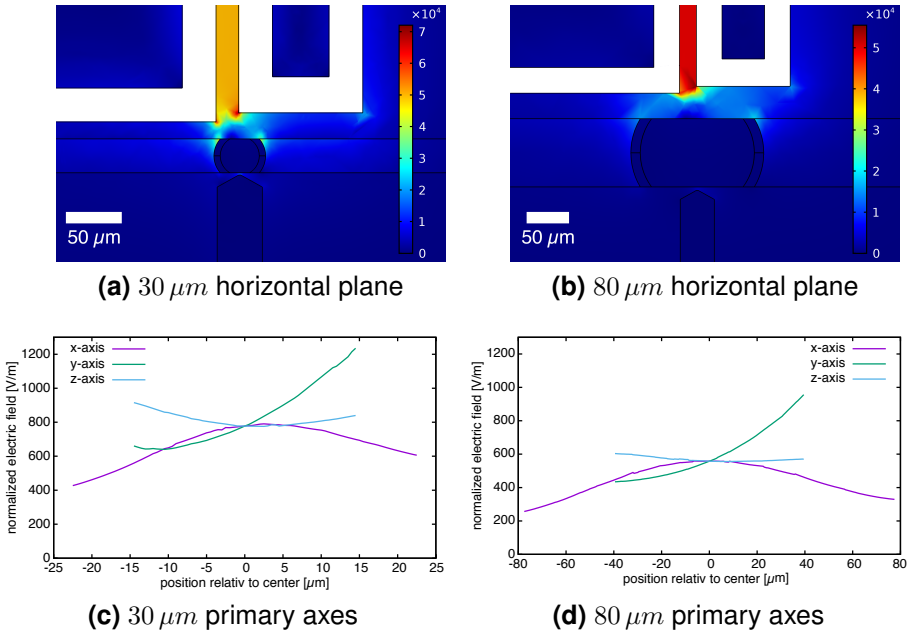

(a) $30\,\mu m$ horizontal plane **(b)** $80\,\mu m$ horizontal plane

(c) $30\,\mu m$ primary axes **(d)** $80\,\mu m$ primary axes

Figure 15.1.: Normalized electric field in two pico-injection designs. (a) and (b) show the normalized field in horizontal plane at half the channel height for $30\,\mu m$ and $80\,\mu m$ structures, respectively. (c) and (d) the normalized electric field along the main axes of a small and large droplet, respectively. The data points along the y-axis start at the interface to the injection channel, where the field strength is $681\,V/m$ and $434\,V/m$ for the $30\,\mu m$ and the $80\,\mu m$ structure, respectively. Considering the distance to the electrodes is $50\,\mu m$ greater, the increased height of the electrodes partially compensates the larger dimensions of the device.

Probably the most crucial point for pico-injection experiments is the interface to the injection channel. Here the difference in field strength is considerably greater, $434\,V/m$ ($80\,\mu m$) in comparison to $681\,V/m$ ($30\,\mu m$). This $36\,\%$ difference is due to the increased dimensions of the channel and the resulting longer distance between electrodes and the injection orifice. However, the increased distance between electrodes and injectors is partially compensated by the increased structure height of the electrodes.

15.2. Field vs Droplet Position

Until this point, only static droplets were considered. However, in microfluidic experiments droplets pass a functional unit within milliseconds. This information can be important, when working with cells. Either to determine if the exposure to an electric field might damage a cell. Moreover, this information could be used to determine if the field exposure would be sufficient for electroporation.

Therefore the electric field was simulated for various droplet positions. The normalized electric field was extracted from all simulations along the main axes of the droplet, analogue as presented before in figures 15.1c and 15.1d. These cuts were then aligned according to droplet position and the resulting kymographs are shown in figure 15.2.

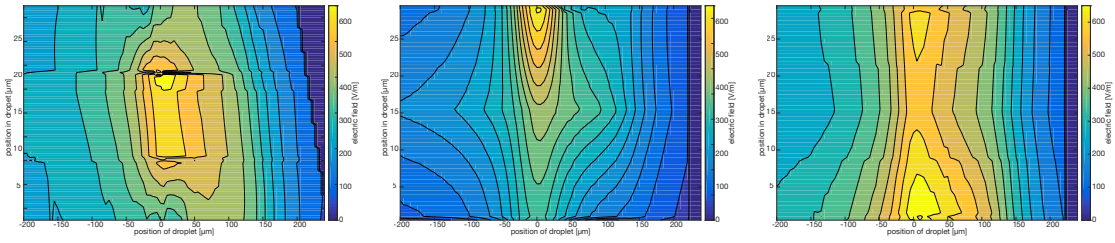

(a) x-axis **(b)** y-axis **(c)** z-axis

Figure 15.2.: Kymograph of the normalized electrical field along the main axes of a droplet as it traverses past two electrodes. The electric field was simulated for droplets moving in $5\,\mu m$ steps along the channel from $-200\,\mu m$ to $240\,\mu m$ in relation to the center of the electrodes. The normalized electrical field along the droplets primary axes was extracted from each simulation results and is printed as a kymograph for (a) the x-axis, (b) the y-axis and (c) the z-axis. In connection with the flow velocity of a droplet, this can be used to estimate the field exposure.

From high-speed camera footage, the velocity of a droplet in a pico-injection channel was determined in the range of $10\,mm/s$ to $15\,mm/s$. Referencing this information with the simulated field strength, it can be estimated that that a cell at the center of a droplet would be exposed to a field greater than $500\,V/m$ for $6.7\,ms$ to $10\,ms$. A value in good agreement with common electroporation protocols.[377]

15.3. Electrode Geometry

For most experiments it is preferable to have a homogeneous field distribution. However, when fabricating microfluidic chips, the design of the electrode can have a major impact on the yield of functional chips. The walls between electrodes and channels often lead to bulging of, or leaking through the separating wall. Furthermore, as the technique, used in this thesis to incorporate electrodes to the devices (see section 8.3.4), requires two inlets, addition of electrodes requires costly space on the chips. Therefore, a range of electrode designs, mostly inspired by publications, were simulated.[106, 108] The results are shown in figure 15.3.

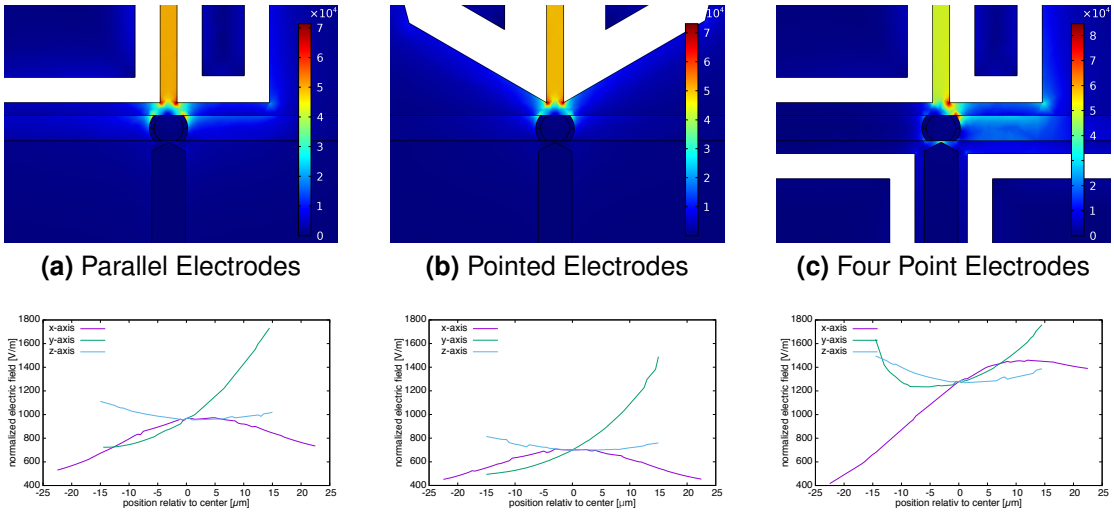

Figure 15.3.: Electric field created by different electrode designs. The upper row shows the electric field strength in the x-y-plane through the middle channel height. The lower row consists of graphs showing the electric field distributions along the main axes of the droplet. The electrodes in panels (a) and (d) are placed in the same distance to the channel (in the standard pico-injection design used in this work, the phase electrode is set back by $8\,\mu m$.), (b) and (e) are pointed towards the channel and (c) and (f) represent a more elaborate design.

The first design, shown in figure 15.3a, moves the phase electrode in the same distance to the channel as the ground electrode then the standard design (see section 15.1). This $8\,\mu m$ shift strengthens the generated electric field by about 25 %. However, the overall shape and distribution is very similar.

The pointy design shown in figure 15.3b) is used by Baret et al.,[108]. The retracting electrodes results in field weaker than the parallel design, although the distance to the channel is identical. This is an interesting observation, because it shows that the electric field is not only shaped by the two electrodes, but also by the droplet with a high dielectric constant.

The more elaborate design featuring three ground electrodes 15.3c produces a higher and more homogeneous field in comparison to the simpler designs. Both upstream electrodes were set to ground, to shield the spacing structure (see section 8.5) from electrical fields. Otherwise coalescence in the reinjection channel has been observed.

15.4. Sensitivity of a Capacitor

A range of publications have presented methods to determine the content of a droplet by measuring the difference in capacitance when the droplet passed a pair of electrodes.[139, 378, 379] They report that it is possible to estimate the ratio of water to ethanol within the droplets due to the change in capacitance.[378] Currently, there are techniques available to sort droplets containing cells, through a fluorescent signal.[108] Therefore, it was considered if it would be possible to sort droplets by the change in capacity of a pair of electrodes? Does a cell alter the capacitance enough to be able to determine of a droplet contained any cell or even to count them?

However, in these works different techniques to fabricate the electrodes were used which allowed electrodes in direct contact with the channel. This raised the question if indium-alloy electrodes could also be employed for this purpose. Therefore a simple capacitor was sketched an the capacitance was computed for two different droplet sizes and various values of the relative permittivity $varepsilon_r$. The model is shown in figure 15.4 and the results are presented in table 15.1.

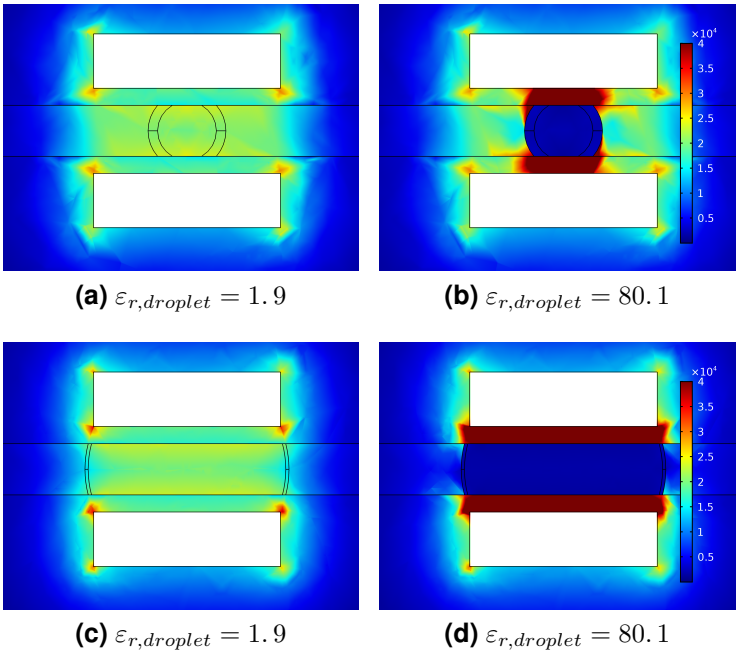

(a) $\varepsilon_{r,droplet} = 1.9$ **(b)** $\varepsilon_{r,droplet} = 80.1$

(c) $\varepsilon_{r,droplet} = 1.9$ **(d)** $\varepsilon_{r,droplet} = 80.1$

Figure 15.4.: Simulation of the electric field in droplets in a simple capacitor design.

radius (volume)	$\varepsilon_{r,droplet}$			
	80.1^{a}	74.22^{b}	25.3^{c}	1.9^{d}
$22.895\,\mu m$ ($34.388\,pl$)	$11.0745\,pF$	$11.0637\,pF$	$10.8358\,pF$	$9.9978\,pF$
$60\,\mu m$ ($105.72\,pl$)	$12.8508\,pF$	$12.8221\,pF$	$12.2170\,pF$	$9.9371\,pF$

Table 15.1.: Capacitance ofa microfluidic capacitor containing droplets with different relative permittivity. As values for the relative permittivities ε_r for H_2O at a) $20°C$ and b) $37°C$, c) ethanol and d) FC-40. Capacitance was calculated for two droplet sizes (see figure 15.4).

As presented in section 12.3 the capacitance influences the capacitative reactance. For example at $600\,Hz$ a capacitor of $11.0745\,pF$ is equivalent to $23.952\,M\Omega$, $11.0637\,pF$ to $23.976\,M\Omega$, $10.8358\,pF$ to $24.480\,M\Omega$ and $9.9978\,pF$ to $26.532\,M\Omega$.

Here, a first step towards a more complex question is taken. It showcases both the potential and the shortcomings of the current state of the model. On one side the capacitance for a range of dielectric constants was computed. This information could be applied to estimate which conditions are to be expected within an actual experiment. At the same time, the simulation does not yet include AC current or the effects of ions in the medium. Moreover, it doers not contain the most important object the cell. Prodan et al. have shown that the latter is a quite complex problem.[387]

15.5. Discussion

Results from numerical simulations should always be taken addito salis grano[1]. There is of curse the element of numerical errors and artifacts caused by the the model. Moreover, a simulation only computed the model defined. However, the actual problem might be more complex and involve physical properties excluded from the simulation. In case of the model presented here, only electrostatic computation is provided. A more complete model should surely dive into the realms of electrodynamics. Furthermore, the model could be expanded to model the ion concentration in the buffers. The current state represent the groundwork and show what has been possible in the given time. A follow-on project can build on what is provided here and expand it.

But there are interesting results from the work done so far. First of all, the field distribution and strength for a droplet containing pure H_2O in a pico-injector was computed. This fills a gap, that many publications working with electric field in microfluidics have left open. The results show that the fields generated for injection are comparable to what is used for cell transfection. Moreover, the electric field distributions for a range of droplet positions was simulated, which could be of help for future applications including cells.

With the growth of the microfluidic group and the diversification of requirements, various electrode designs were proposed. A model was established that allows easy loading of new structures and the computation of the field generated within them. With this information future designs can be improved. Again, this information can be used for other applications such as cell transfection.

In future, more complex questions such as dielectrophoretic forces will have to be tackled. At this point a first step to in silico microfluidics was taken and basic FEM simulations were produced.

[1] "With a pinch of salt/wit", idiom likely coined by Pliny the Elder, that something should be viewed with skepticism, or to not take it literally.

Part IV.

Summary and Outlook

16. Summary

In many respects the development of protocell model systems has been stagnant over the last decade. The application of cell-sized lipid vesicles in SB is partially restricted by the low chemical and mechanical stability of GUVs.[90] High ion concentrations, especially bivalent cations,[419] and low pH values[420] cause lipid membrane fusion. Moreover, the manipulation of GUVs, specifically the injection of reagents, is very tedious. Therefore, at the beginning of this research to develop a lipid-based model system for cellular adhesion, SUVs were used due to their higher stability in comparison to GUVs. Finally, as a result of the gained knowledge a leap to a completely new approach was taken. Combining the lipid-compartment approach with water-in-oil droplet-based microfluidics led to the development of a novel compartment system, the dsGUV. The novel approach has great potential to break some of the shackles holding back development of cellular model systems.

In the first part of this thesis a minimal synthetic cell system with lipid vesicles in the range of $100\,nm$ to $200\,nm$ to study integrin-mediated adhesion on various ECM proteins and two different RGD peptides was established. This model system was investigated by means of QCM-D. The analysis of the frequency and dissipation recordings clearly indicate that integrin $\alpha_{IIb}\beta_3$ was functionally reconstituted into the lipid vesicles. Specific bindings to fibrinogen- and fibronectin-coated crystals were observed when integrin was activated with bivalent ions. The integrin-mediated adhesion of this cell model system could be controlled by adjusting the concentration of reconstituted integrin. Moreover, the addition of dissolved RGD-peptides to specifically adhered integrin-liposomes yielded controlled detachment of the protocells. The differences in affinity of the two RGD-peptides for integrin binding could be assessed by the QCM-D data. These results show that integrin-liposomes are a good model system to mimic cell adhesion. Moreover, this model system allows adhesion quantitification on different binding ligands. Integrin-liposomes will also be ideal candidates for encapsulation and investigation of intracellular adhesion-asociated proteins, for instance talin or focal adhesion kinase. However, it is very difficult to scale up this approach to cell size, as a consequence of the low stability of GUVs. Therefore, as this research progressed, it became more and more apparent, that a different approach had to be developed.

16. Summary

The electric light did not come from
continuous improvement of candles.

(Oren Harari)

As a result of this knowledge, a new approach that merges lipid vesicles and water-in-oil copolymer-stabilized droplets to generate mechanically and chemically stable cell-like compartments, called droplet-stabilized GUV (dsGUV), was developed. Combining the advantages of microfluidic technology (e.g. stability and high-throughput generation and manipulation) with the biophysical properties of lipid membranes (e.g. lipid bilayer structure and diffusion) the dsGUVs provides this system with superior features in comparison to previously reported synthetic bio-compartments. Moreover, due to the enhanced stability, dsGUV can be sequentially loaded with biomolecules using microfluidic pico-injection[106] and offers optimal conditions for bottom-up assembly of complex synthetic cells.[174, 178, 421, 422] In the following paragraphs a summary of the major steps towards dsGUVs formation and analysis are described. At the final stage of the research, methods to recover GUVs from droplets were investigated and a proof of concept is presented. By replacing stabilizing surfactant with destabilizing surfactants the polymer shell of the droplet can be removed and the content recovered to an aqueous phase. Conditions, e.g. lipid compositions, for successful GUVs recovery have been identified.

First, the necessary amount of lipids required for a continuous bilayer formation was calculated according to the mono-disperse size of the droplets. Next, to initiate rupture of the encapsulated liposomes and formation of a SLB at the droplet inner interface, it has been shown that bivalent cations are required. $10\,mM$ Mg^{2+} ions proved to be the most efficient mediator of vesicle rupture.[403, 404] To confirm lipid bilayer formation in the dsGUVs and to assess its dynamics, fluorescence intensity analyses and FRAP measurements were performed and compared to encapsulate free-standing GUVs, consisting of the same lipid compositions. The measurements revealed similar intensity values for dsGUVs and encapsulated GUVs, respectively. These findings indicate similar lipid composition for dsGUVs and GUVs. FRAP measurements revealed similar lipid mobility in dsGUVs as in encapsulated free-standing GUVs. Slightly lower diffusion coefficient values in the case of dsGUVs are attributed to the fact that the supported lipid membrane is subject to friction from the copolymer-stabilized droplet inner interface. Similar and even stronger tendency towards lower values of the diffusion coefficient were reported for planar supported lipid membranes compared to free-swimming GUVs.[240, 357] Moreover, the diffusion coefficient of the surfactants was measured and determined to be one order lower than the diffusion coefficient of the lipid membrane. Therefore, a mixed lipid-surfactant layer can be excluded. Moreover, dsGUVs containing DGS-NTA were successfully functionalized with His6-GFP,

showing the potential of the system for various synthetic biology applications. Furthermore, to prove the formation of an intact GUV within a dsGUV, recovery of the former from the supporting droplets was achieved.

To construct complex cellular machineries by means of bottom-up assembly, automated microfluidic pico-injection technology was adapted to allow for the sequential loading of various sub-cellular functional units into the dsGUVs. Following the formation of dsGUVs, the pico-injection system[106] was used to fuse proteoliposomes, i.e. liposomes containing TAMRA-labeled integrin $\alpha_{IIb}\beta_3$ integrin, with the dsGUVs. Co-localization of integrin and lipid fluorescence signals were observed, indicating successful fusion of proteoliposomes with the dsGUVs.

FRAP measurements of transmembrane proteins reconstituted into dsGUVs revealed diffusion coefficients in good agreement with the previously published studies on integrin $\alpha_{IIb}\beta_3$ mobility in planar supported lipid bilayers or in cellular membranes.[326, 394, 416] Moreover, to test integrin activity RGD peptides anchored to gold-linked surfactants [174, 342] were used to provide binding sites for the reconstituted integrin. In that case, the diffusion coefficient of integrin closely matched the mobility of the copolymer surfactant layer which stabilizes the droplet. This observation indicates a successful binding between the integrin and the RGD on the droplet interface and functional incorporation of integrin in the lipid bilayer of the dsGUVs. It also reveals that at least some of the integrin were oriented correctly, i.e. that the extracellular part points towards the copolymer-stabilized droplet inner interface.

The developed technology overcomes fundamental limitations associated with the formation and manipulation of currently existing protocells or polymersoms for the design of complex synthetic cells. The assembly of a cell-like compartment with distinct functionality requires the combination of different proteins, molecules and buffer conditions which are incompatible when applied in the same spatial confinement at once. The formation of dsGUVs enables the generation of mechanically and chemically stable compartments which can be sequentially loaded by pico-injection technology with different proteins and molecules. It allows for the combination of biochemical which would be impossible by simply mixing the reagents. The properties of the system will enable the realization of a real bottom-up assembly of rather complex combinations and functions within synthetic compartments in the future. It is worthwhile to mention that the formation of synthetic cells by this technology is a high-throughput method which enables the generation of up to 10^4 functional compartments per second. Therefore, it generates a vast number of synthetic cells of unique precision which may be applied for follow-up scientific and technological applications.

In addition to the experimental work, a first step into the simulation of electric fields in microfluidic steps were undertaken. There is still a lot that needs to be done, but already some valuable results were achieved. For the first time the field in pico-injection devices were computed and found to be similar to these used for cell transfection. Moreover, steps were taken to improve the electrode design in future microfluidic chips.

17. Outlook

In this section two pathways of possible future experiments will be discussed. First of all, there is the further development of a model system for cellular adhesion. In this thesis, a major obstacle barring future progress has been overcome by the development of dsGUVs and exciting mile-stones are in reach. Moreover, a method to recover GUVs from droplets has been presented and this process will be further refined in the future. By now, this technique already allows the production of large numbers of GUVs containing reconstituted integrin. The recovered protocells could be used to study GUV-surface interactions. However, due to the low stability of large vesicles, this would require to finely control the affinity of the surface, e.g. by soft polymer cushions.[19, 395, 423] Interference reflection microscopy, sometimes referred to as reflection (interference) contrast microscopy, could be used to investigate the adhesion behavior of the vesicles.[19, 88, 89, 397, 424] Similar GUV-surface interaction experiments would also be possible with one of the many other CAMs.

In follow-on experiments this model system could be expanded by integrin-linked action filaments and myosin. Therefore, I would reccomend to combine the advantages of dsGUVs and the recovery of protocells with the achivements of my colleagues, Jan-Willi Janiesch and Barabara Haller. In their research they made great progress in mimicking the actomyosin complex within microfluidic droplets.[189, 425, 426] With the novel dsGUV compartment system and the surrounding microfluidic technologies it has become feasible to start converging these projects. The result would be a much more complete model of FAs.[23, 27] The planned model is sketched in figure 17.1, right inlet. By connecting the integrin to the actomyosin complex forces can be transduced between the protocell and its environment. This could for example be done in a microfluidic chip that dynamically changes the shape of the droplet.

However, an important linker to connect these two systems is still missing – talin.[427–431] Talin is known to bind and activate integrin, while simultaneously anchoring actin filaments.[432–435] As some time past between the heyday of work with purified talin in the eighties and early nineties,[436, 437] attempts to retrieve detailed protocols were unsuccessful. Some progress has already been made to fill in the blanks in the available publications and the protein was purified within the group. However, the activity of the newly purified has not yet been determined.

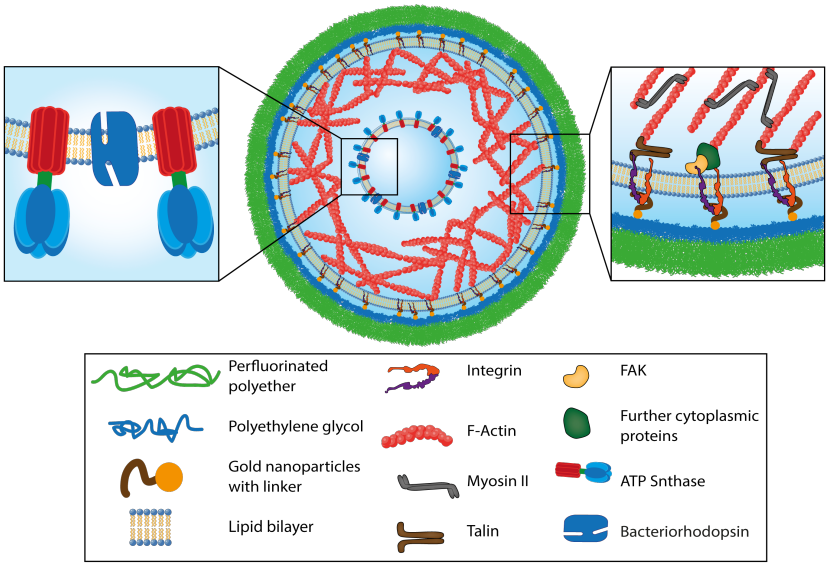

Figure 17.1.: Schematic representation of a complex minimal synthetical cell that could be realized with the dsGUV approach. Here many important components of a FA are present, as well as an energy supply. An actomyosin complex is bound via talin or alternative linkers to membrane embedded integrin. The integrin in turn adheres to gold nanoparticles functionalized via thiol chemistry with peptides containing an RGD binding site. Additionally there is GUVs encapsulated within the droplet, containing reconstituted F_0F_1-ATP synthase and bacteriorhodopsin. These encapsulated GUVs could provide a light triggered power supply. Such a sophisticated, bio-inspired protocell requires many different components. This complexity is enabled by the use of microfluidic technology and capability to sequentially add new components. These dsGUVs are easily observable with optical microscopy over long time periods. They offer a convenient platform as cell-sized compartments within which interactions between different adhesion-associated proteins can be systematically analyzed by means of a high-throughput screening.

This is due to the complex binding process of talin to the integrin β-tail. Binding is mediated by the lipid phosphatidylinositol 4,5-bisphosphate (PIP2), which alters the conformation of talin to expose its binding site for integrin.[438, 439] Here, QCM-D in combination with either the integrin-liposome model system presented in this work, or with SLB containing reconstituted integrin[88, 394, 397] could be used to determine optimal conditions. The results could than be transferred to the dsGUV compartment system containing integrin as well as actin fillaments.

As it will take time to adapt the adhesion model system for talin to function as a linker between integrin and actin, an intermediate solution has been found in designed ankyrin repeat proteins (DARPins).[440–442] DARPins are genetically engineered antibody mimetic proteins. They are derivatives of the natural ankyrin proteins, a protein class that mediates high-affinity protein-protein interactions in

nature.[443] By genetic fusion multi-specific DARPins constructs can be created. Recently, a project was started to fabricate a DARPin that specifically binds to the β-tail of integrin $\alpha_{IIb}\beta_3$ and actin filaments. A DARPin construct anchoring actin filaments to the β-tail of integrin is expected to be available in the near future. Implementation of DARPins in SB can be of enormous interest as they will enable scientists to further reduce the biological complexity by restricting the function of a protein to its binding capability.

The dsGUV compartment system has already found adoption in the scientific community. Within the group the compartment system has been used in combination with another transmembrane protein, F_0F_1-ATP synthase and cytoskeletal proteins, actomyosin and tubulin. F_0F_1-ATP synthase in combination with either bacteriorhodopsin,[444] or pH gradients controlled through the oil phase[445] could provide energy in form of adenosine triphosphate could provide energy to processes within the droplets. A sketch of the planned model system is shown in figure 17.1, left inlet. Furthermore, collaborators have build the necessary setups to apply the developed methods in their own experiments, such as. cell polarization. Once the dsGUV system has been presented to a wider scientific audience, its impact should further increase.

A great part of the potential of the model system has yet to be unlocked. Advances microfluidic techniques, such as pico-injectors,[106] and fluorescence-activated droplet sorting,[108, 109] allow automated high throughput manipulation and screening of a large numbers of proto-cells. This would, for example, allow to vary concentrations of multiple reagents dynamically and analyze the effect with minimal user interaction.

Towards the goal of more integrated and more complex microfluidic chips, new design approaches will be required.[418, 446, 447] Today most microfluidic chips are designed with the trial and error method. This usually makes multiple iterations necessary to derive a functioning chip and its important properties, such as electric field strengths or dielectrophoretic forces. FEM simulations could provide a reduction in overall design time and cost, while improve the control over the design function.[417, 448, 449] A good example were this has already been applied is the design of chips using ultrasonic manipulation.[450] The steps taken in this work towards simulation of electric fields will be further investigated. Especially, through the current ongoing work on a fluorescence-activated droplet sorter in the group.

In summary, the new compartment system, the dsGUV, is young but promises to overcome many restriction of its predecessors. This will hopefully not only lead to new developments in modelling cellular adhesion but will also promote progress in the wider SB field.

Appendix

List of Figures

List of Tables

Bibliography

[1] Bruce Alberts, John Wilson, and Tim Hunt. *Molecular biology of the cell*. New York: Garland Science, 2008. ISBN: 9780815341055.

[2] Oscar Ces and Xavier Mulet. "Physical coupling between lipids and proteins: a paradigm for cellular control". English. In: *Signal Transduction* 6.2 (2006), pp. 112–132. DOI: 10.1002/sita.200500079.

[3] Beverly Wendland. "Everything you ever wanted to know about endocytosis". English. In: *Nature Cell Biology* 3.11 (2001), E254–E254. DOI: 10.1038/ncb1101-e254.

[4] Dale Purves et al. "Channels and Transporters". English. In: *Neuroscience*. Sinauer Associates, 2001. ISBN: 0-87893-742-0.

[5] Sietze Reitsma et al. "The endothelial glycocalyx: composition, functions, and visualization". English. In: *Pflügers Archiv - European Journal of Physiology* 454.3 (2007), pp. 345–359. DOI: 10.1007/s00424-007-0212-8.

[6] Ronen Zaidel-Bar et al. "Functional atlas of the integrin adhesome." English. In: *Nature Cell Biology* 9.8 (2007), pp. 858–867. DOI: 10.1038/ncb0807-858.

[7] Daniel Riveline et al. "Focal Contacts as Mechanosensors". English. In: *The Journal of cell biology* 153.6 (2001), pp. 1175–1186. DOI: 10.1083/jcb.153.6.1175.

[8] Yasuhiro Sawada et al. "Force Sensing by Mechanical Extension of the Src Family Kinase Substrate p130Cas". English. In: *Cell* 127.5 (2006), pp. 1015–1026. DOI: 10.1016/j.cell.2006.09.044.

[9] Armando del Rio et al. "Stretching Single Talin Rod Molecules Activates Vinculin Binding". English. In: *Science (New York, N.Y.)* 323.5914 (2009), pp. 638–641. DOI: 10.1126/science.1162912.

[10] Jeff Hardin et al. *Becker's world of the cell*. Boston: Benjamin Cummings, 2012.

[11] Harald Herrmann et al. "Intermediate filaments: from cell architecture to nanomechanics". English. In: *Nature reviews. Molecular cell biology* 8.7 (2007), pp. 562–573. DOI: 10.1038/nrm2197.

[12] J. Howard. *Mechanics of motor proteins and the cytoskeleton*. Macmillan Education, 2001. ISBN: 0-87893-334-4.

[13] Daniel A Fletcher and R Dyche Mullins. "Cell mechanics and the cytoskeleton." English. In: *Nature* 463.7280 (2010), pp. 485–492. DOI: 10.1038/nature08908.

[14] Martin Deibler. "Maintaining integrity : force-induced optimization responses in cells subjected to cyclic tensile strain". PhD thesis. Heidelberg University, 2011.

[15] P Shi and J Zhang. "Extraordinary Diversity of Chemosensory Receptor Gene Repertoires Among Vertebrates". English. In: *Chemosensory Systems in Mammals, Fishes, and Insects*. Berlin, Heidelberg: Springer Berlin Heidelberg, 2009, pp. 57–75. ISBN: 978-3-540-69918-7. DOI: 10.1007/400_2008_4.

[16] Reginald Frederick Chapman. "Mechanoreception". In: *The Insects*. Ed. by Stephen J Simpson et al. Cambridge University Press, 2009, pp. 738–770. ISBN: 9780521113892.

[17] Reginald Frederick Chapman. "Chemoreception". In: *The Insects*. Ed. by Stephen J Simpson et al. Cambridge University Press, 2009, pp. 771–791. ISBN: 9780521113892.

[18] Benjamin Geiger, Joachim P Spatz, and Alexander D Bershadsky. "Environmental sensing through focal adhesions". English. In: *Nature reviews. Molecular cell biology* 10.1 (2009), pp. 21–33. DOI: 10.1038/nrm2593.

[19] Erich Sackmann and Robijn F Bruinsma. "Cell Adhesion as Wetting Transition?" English. In: *Chemphyschem : a European journal of chemical physics and physical chemistry* 3.3 (2002), pp. 262–269. DOI: 10.1002/1439-7641(20020315)3:3<262::AID-CPHC262>3.0.CO;2-U.

[20] R Merkel et al. "Energy landscapes of receptor|[ndash]|ligand bonds explored with dynamic force spectroscopy". English. In: *Nature* 397.6714 (1999), pp. 50–53. DOI: 10.1038/16219.

[21] R Brackenbury, U Rutishauser, and G M Edelman. "Distinct calcium-independent and calcium-dependent adhesion systems of chicken embryo cells." English. In: *Proceedings of the National Academy of Sciences of the United States of America* 78.1 (1981), pp. 387–391.

[22] Christopher S Chen et al. "Cell shape provides global control of focal adhesion assembly". English. In: *Biochemical and biophysical research communications* 307.2 (2003), pp. 355–361.

[23] Ronen Zaidel-Bar and Benjamin Geiger. "The switchable integrin adhesome." English. In: *Journal of cell science* 123.Pt 9 (2010), pp. 1385–1388. DOI: 10.1242/jcs.066183.

[24] Tamar Geiger and Ronen Zaidel-Bar. "Opening the floodgates: proteomics and the integrin adhesome." English. In: *Current opinion in cell biology* 24.5 (2012), pp. 562–568. DOI: 10.1016/j.ceb.2012.05.004.

[25] Ronen Zaidel-Bar. "Job-splitting among integrins." English. In: *Nature Cell Biology* 15.6 (2013), pp. 575–577. DOI: 10.1038/ncb2770.

[26] Edward R Horton et al. "Mechanosensitivity of integrin adhesion complexes: role of the consensus adhesome." English. In: *Experimental cell research* 343.1 (2016), pp. 7–13. DOI: 10.1016/j.yexcr.2015.10.025.

[27] Eli Zamir and Benjamin Geiger. "Molecular complexity and dynamics of cell-matrix adhesions". English. In: *Journal of cell science* 114.20 (2001), pp. 3583–3590.

[28] Eli Zamir. "Integrative systems and synthetic biology of cell-matrix adhesion sites." English. In: *Cell adhesion & migration* (2016), pp. 1–10. DOI: 10.1080/19336918.2016.1148865.

[29] Pakorn Kanchanawong et al. "Nanoscale architecture of integrin-based cell adhesions". English. In: *Nature* 468.7323 (2010), pp. 580–584. DOI: 10.1038/nature09621.

[30] R Zaidel-Bar et al. "Hierarchical assembly of cell–matrix adhesion complexes". English. In: *Biochem Soc Trans* 32.3 (2004), pp. 416–420. DOI: 10.1042/bst0320416.

[31] Paul W Wiseman et al. "Spatial mapping of integrin interactions and dynamics during cell migration by Image Correlation Microscopy". English. In: *Journal of cell science* 117.23 (2004), pp. 5521–5534. DOI: 10.1242/jcs.01416.

[32] Seiji Tadokoro et al. "Talin Binding to Integrin ß Tails: A Final Common Step in Integrin Activation". English. In: *Science (New York, N.Y.)* 302.5642 (2003), pp. 103–106. DOI: 10.1126/science.1086652.

[33] C M Laukaitis et al. "Differential dynamics of alpha 5 integrin, paxillin, and alpha-actinin during formation and disassembly of adhesions in migrating cells." English. In: *The Journal of cell biology* 153.7 (2001), pp. 1427–1440.

[34] Donna J Webb et al. "FAK-Src signalling through paxillin, ERK and MLCK regulates adhesion disassembly". English. In: *Nature Cell Biology* 6.2 (2004), pp. 154–161. DOI: 10.1038/ncb1094.

[35] Zhiqi Sun, Armin Lambacher, and Reinhard Fässler. "Nascent Adhesions: From Fluctuations to a Hierarchical Organization". English. In: *Current Biology* 24.17 (2017), R801–R803. DOI: 10.1016/j.cub.2014.07.061.

[36] Colin K Choi et al. "Actin and α-actinin orchestrate the assembly and maturation of nascent adhesions in a myosin II motor-independent manner". English. In: *Nature Cell Biology* 10.9 (2008), pp. 1039–1050. DOI: 10.1038/ncb1763.

[37] Ho-Sup Lee et al. "Characterization of an Actin-binding Site within the Talin FERM Domain". English. In: *Journal of molecular biology* 343.3 (2004), pp. 771–784. DOI: 10.1016/j.jmb.2004.08.069.

[38] Margaret L Gardel et al. "Mechanical Integration of Actin and Adhesion Dynamics in Cell Migration". English. In: *Annual review of cell and developmental biology* 26.1 (2010), pp. 315–333. DOI: 10.1146/annurev.cellbio.011209.122036.

[39] M Chrzanowska-Wodnicka and K Burridge. "Rho-stimulated contractility drives the formation of stress fibers and focal adhesions." English. In: *The Journal of cell biology* 133.6 (1996), pp. 1403–1415. DOI: 10.1083/jcb.133.6.1403.

[40] Nathalie Q Balaban et al. "Force and focal adhesion assembly: a close relationship studied using elastic micropatterned substrates". English. In: *Nature Cell Biology* 3.5 (2001), pp. 466–472. DOI: 10.1038/35074532.

[41] Tom Shemesh et al. "Focal adhesions as mechanosensors: A physical mechanism". English. In: *Proceedings of the National Academy of Sciences of the United States of America* 102.35 (2005), pp. 12383–12388. DOI: 10.1073/pnas.0500254102.

[42] Antonina Y Alexandrova et al. "Comparative Dynamics of Retrograde Actin Flow and Focal Adhesions: Formation of Nascent Adhesions Triggers Transition from Fast to Slow Flow". English. In: *PloS one* 3.9 (2008), e3234. DOI: 10.1371/journal.pone.0003234.

[43] Viola Vogel and Michael Sheetz. "Local force and geometry sensing regulate cell functions". English. In: *Nature reviews. Molecular cell biology* 7.4 (2006), pp. 265–275. DOI: 10.1038/nrm1890.

[44] Colin P Johnson et al. "Forced Unfolding of Proteins Within Cells". English. In: *Science (New York, N.Y.)* 317.5838 (2007), pp. 663–666. DOI: 10.1126/science.1139857.

[45] Jianghai Zhu et al. "Structure of a Complete Integrin Ectodomain in a Physiologic Resting State and Activation and Deactivation by Applied Forces". English. In: *Molecular cell* 32.6 (2008), pp. 849–861. DOI: 10.1016/j.molcel.2008.11.018.

[46] Richard O Hynes. "Integrins: Bidirectional, Allosteric Signaling Machines". English. In: *Cell* 110.6 (2002), pp. 673–687. DOI: 10.1016/S0092-8674(02)00971-6.

[47] David S Harburger and David A Calderwood. "Integrin signalling at a glance". English. In: *Journal of cell science* 122.2 (2009), pp. 159–163. DOI: 10.1242/jcs.018093.

[48] Akira Katsumi et al. "Integrins in mechanotransduction." English. In: *The Journal of biological chemistry* 279.13 (2004), pp. 12001–12004. DOI: 10.1074/jbc.R300038200.

[49] Martin Alexander Schwartz. "Integrins and Extracellular Matrix in Mechanotransduction". English. In: *Cold Spring Harbor Perspectives in Biology* 2.12 (2010), a005066–a005066. DOI: 10.1101/cshperspect.a005066.

[50] Sanford J Shattil. "Function and regulation of the beta 3 integrins in hemostasis and vascular biology". In: *Thrombosis and haemostasis* 74.1 (1995), pp. 149–155.

[51] Brian D Adair and Mark Yeager. "Three-dimensional model of the human platelet integrin alpha IIbbeta 3 based on electron cryomicroscopy and x-ray crystallography." English. In: *Proceedings of the National Academy of Sciences of the United States of America* 99.22 (2002), pp. 14059–14064. DOI: 10.1073/pnas.212498199.

[52] J D Humphries. "Integrin ligands at a glance". English. In: *Journal of cell science* 119.19 (2006), pp. 3901–3903. DOI: 10.1242/jcs.03098.

[53] M Pfaff et al. "Selective recognition of cyclic RGD peptides of NMR defined conformation by alpha IIb beta 3, alpha V beta 3, and alpha 5 beta 1 integrins." English. In: *The Journal of biological chemistry* 269.32 (1994), pp. 20233–20238.

[54] JOEL S BENNETT. "Platelet-Fibrinogen Interactions". English. In: *Annals of the New York Academy of Sciences* 936.1 (2001), pp. 340–354. DOI: 10.1111/j.1749-6632.2001.tb03521.x.

[55] Barry S Coller and Sanford J Shattil. "The GPIIb/IIIa (integrin αIIbβ3) odyssey: a technology-driven saga of a receptor with twists, turns, and even a bend". English. In: *Blood* 112.8 (2008), pp. 3011–3025. DOI: 10.1182/blood-2008-06-077891.

[56] Juan J Calvete. "On the Structure and Function of Platelet Integrin αIIbβ3, the Fibrinogen Receptor". English. In: *Experimental Biology and Medicine* 208.4 (1995), pp. 346–360. DOI: 10.3181/00379727-208-43863A.

[57] Christian Eberhard. "Development of a Model System to Study Cell Adhesion and Cell Mechanics". PhD thesis. Heidelberg: Heidelberg University, 2012.

[58] Edward T Eng et al. "Intact alphaIIbbeta3 integrin is extended after activation as measured by solution X-ray scattering and electron microscopy." English. In: *The Journal of biological chemistry* 286.40 (2011), pp. 35218–35226. DOI: 10.1074/jbc.M111.275107.

[59] Kenji Iwasaki et al. "Electron tomography reveals diverse conformations of integrin αIIbβ3 in the active state". English. In: *Journal of Structural Biology* 150.3 (2005), pp. 259–267. DOI: 10.1016/j.jsb.2005.03.005.

[60] Chungho Kim, Feng Ye, and Mark H Ginsberg. "Regulation of integrin activation." English. In: *Annual review of cell and developmental biology* 27.1 (2011), pp. 321–345. DOI: 10.1146/annurev-cellbio-100109-104104.

[61] Aurora Nogales et al. "Three-dimensional model of human platelet integrin alphaIIb beta3 in solution obtained by small angle neutron scattering." English. In: *The Journal of biological chemistry* 285.2 (2010), pp. 1023–1031. DOI: 10.1074/jbc.M109.050039.

[62] Timothy A Springer and Michael L Dustin. "Integrin inside-out signaling and the immunological synapse." English. In: *Current opinion in cell biology* 24.1 (2012), pp. 107–115. DOI: 10.1016/j.ceb.2011.10.004.

[63] Brian D Adair and Mark Yeager. "Electron Microscopy of Integrins". In: *Integrins*. Elsevier, 2007, pp. 337–373. ISBN: 9780123739247. DOI: 10.1016/S0076-6879(07)26015-X.

[64] X Du et al. "Long range propagation of conformational changes in integrin alpha IIb beta 3." English. In: *The Journal of biological chemistry* 268.31 (1993), pp. 23087–23092.

[65] J W Weisel et al. "Examination of the platelet membrane glycoprotein IIb-IIIa complex and its interaction with fibrinogen and other ligands by electron microscopy." English. In: *The Journal of biological chemistry* 267.23 (1992), pp. 16637–16643.

[66] Jian-Ping Xiong, Simon L Goodman, and M Amin Arnaout. "Purification, analysis, and crystal structure of integrins." English. In: *Methods in enzymology* 426 (2007), pp. 307–336. DOI: 10.1016/S0076-6879(07)26014-8.

[67] Xianliang Rui et al. "The α-subunit regulates stability of the metal ion at the ligand-associated metal ion-binding site in β3 integrins." English. In: *The Journal of biological chemistry* 289.33 (2014), pp. 23256–23263. DOI: 10.1074/jbc.M114.581470.

[68] Jieqing Zhu et al. "Tests of the extension and deadbolt models of integrin activation." English. In: *The Journal of biological chemistry* 282.16 (2007), pp. 11914–11920. DOI: 10.1074/jbc.M700249200.

[69] Jian-Ping Xiong et al. "New insights into the structural basis of integrin activation". English. In: *Blood* 102.4 (2003), pp. 1155–1159. DOI: 10.1182/blood-2003-01-0334.

[70] Feng Ye et al. "Integrin αIIbβ3 in a Membrane Environment Remains the Same Height after Mn2+ Activation when Observed by Cryoelectron Tomography". English. In: *Journal of molecular biology* 378.5 (2008), pp. 976–986. DOI: 10.1016/j.jmb.2008.03.014.

[71] Hiroaki Takagi et al. "Functional Analysis of Spontaneous Cell Movement under Different Physiological Conditions". English. In: *PloS one* 3.7 (2008), pp. 1–7. DOI: 10.1371/journal.pone.0002648.

[72] Ernesto Andrianantoandro et al. "Synthetic biology: new engineering rules for an emerging discipline". English. In: *Mol Syst Biol* 2.1 (2006), p. 2006.0028. DOI: 10.1038/msb4100073.

[73] Ahmad S Khalil and James J Collins. "Synthetic biology: applications come of age". English. In: *Nature Reviews Genetics* 11.5 (2010), pp. 367–379. DOI: 10.1038/nrg2775.

[74] Drew Endy. "Foundations for engineering biology". English. In: *Nature* 438.7067 (2005), pp. 449–453. DOI: 10.1038/nature04342.

[75] Steven A Benner and A Michael Sismour. "Synthetic biology". English. In: *Nature Reviews Genetics* 6.7 (2005), pp. 533–543. DOI: 10.1038/nrg1637.

[76] Shankar Mukherji and Alexander van Oudenaarden. "Synthetic biology: understanding biological design from synthetic circuits". English. In: *Nature Reviews Genetics* 10.12 (2009), pp. 859–871. DOI: 10.1038/nrg2697.

[77] Jay D Keasling. "Synthetic Biology for Synthetic Chemistry". English. In: *ACS chemical biology* 3.1 (2008), pp. 64–76. DOI: 10.1021/cb7002434.

[78] Daniel T Chiu, Robert M Lorenz, and Gavin D M Jeffries. "Droplets for Ultrasmall-Volume Analysis". English. In: *Analytical Chemistry* 81.13 (2009), pp. 5111–5118. DOI: 10.1021/ac900306q.

[79] Susanne F Fenz and Kheya Sengupta. "Giant vesicles as cell models". English. In: *Integrative Biology* 4.9 (2012), pp. 982–995. DOI: 10.1039/C2IB00188H.

[80] Bohdana M Discher et al. "Polymersomes: Tough Vesicles Made from Diblock Copolymers". English. In: *Science (New York, N.Y.)* 284.5417 (1999), pp. 1143–1146. DOI: 10.1126/science.284.5417.1143.

[81] C LoPresti et al. "Polymersomes: nature inspired nanometer sized compartments". In: *Journal of Materials ...* (2009). DOI: 10.1039/B818869F.

[82] Madhavan Nallani et al. "Sorting Catalytically Active Polymersome Nanoreactors by Flow Cytometry". English. In: *Small* 5.10 (2009), pp. 1138–1143. DOI: 10.1002/smll.200801204.

[83] Alexandra Graff et al. "Virus-assisted loading of polymer nanocontainer." English. In: *Proceedings of the National Academy of Sciences of the United States of America* 99.8 (2002), pp. 5064–5068. DOI: 10.1073/pnas.062654499.

[84] L Mathivet, S Cribier, and P F Devaux. "Shape change and physical properties of giant phospholipid vesicles prepared in the presence of an AC electric field." English. In: *Biophysical Journal* 70.3 (1996), pp. 1112–1121. DOI: 10.1016/S0006-3495(96)79693-5.

[85] Chiara Martino et al. "Protein Expression, Aggregation, and Triggered Release from Polymersomes as Artificial Cell-like Structures". English. In: *Angewandte Chemie (International ed. in English)* 51.26 (2012), pp. 6416–6420. DOI: 10.1002/anie.201201443.

[86] M B Elowitz and S Leibler. "A synthetic oscillatory network of transcriptional regulators." English. In: *Nature* 403.6767 (2000), pp. 335–338. DOI: 10.1038/35002125.

[87] T S Gardner, C R Cantor, and J.J. Collins. "Construction of a genetic toggle switch in Escherichia coli." English. In: *Nature* 403.6767 (2000), pp. 339–342. DOI: 10.1038/35002131.

[88] Erich Sackmann and Ana-Sunčana Smith. "Physics of cell adhesion: some lessons from cell-mimetic systems". English. In: *Soft Matter* 10.11 (2014), pp. 1644–1659. DOI: 10.1039/C3SM51910D.

[89] Ana-Sunčana Smith and Erich Sackmann. "Progress in Mimetic Studies of Cell Adhesion and the Mechanosensing". English. In: *Chemphyschem : a European journal of chemical physics and physical chemistry* 10.1 (2009), pp. 66–78. DOI: 10.1002/cphc.200800683.

[90] Pasquale Stano. "Minimal cells: Relevance and interplay of physical and biochemical factors". English. In: *Biotechnology Journal* 6.7 (2011), pp. 850–859. DOI: 10.1002/biot.201100079.

[91] John A Rogers and Ralph G Nuzzo. "Recent progress in soft lithography". English. In: *Materials Today* 8.2 (2005), pp. 50–56. DOI: 10.1016/S1369-7021(05)00702-9.

[92] Adam C Siegel et al. "Cofabrication: a strategy for building multicomponent microsystems." English. In: *Accounts of chemical research* 43.4 (2010), pp. 518–528. DOI: 10.1021/ar900178k.

[93] Alexander K Price and Brian M Paegel. "Discovery in Droplets". English. In: *Analytical Chemistry* 88.1 (2016), pp. 339–353. DOI: 10.1021/acs.analchem.5b04139.

[94] Michael J Heller. "DNA microarray technology: devices, systems, and applications." English. In: *Annual review of biomedical engineering* 4.1 (2002), pp. 129–153. DOI: 10.1146/annurev.bioeng.4.020702.153438.

[95] Thomas M Pearce and Justin C Williams. "Microtechnology: Meet neurobiology". English. In: *Lab on a chip* 7.1 (2007), pp. 30–40. DOI: 10.1039/B612856B.

[96] Amy C Rowat et al. "Tracking lineages of single cells in lines using a microfluidic device." English. In: *Proc Natl Acad Sci USA* 106.43 (2009), pp. 18149–18154. DOI: 10.1073/pnas.0903163106.

[97] Mais J Jebrail, Michael S Bartsch, and Kamlesh D Patel. "Digital microfluidics: a versatile tool for applications in chemistry, biology and medicine". English. In: *Lab on a chip* 12.14 (2012), pp. 2452–2463. DOI: 10.1039/C2LC40318H.

[98] Andrew J deMello and Robert C R Wootton. "Miniaturization: Chemistry at the crossroads". English. In: *Nature Chemistry* 1.1 (2009), pp. 28–29. DOI: 10.1038/nchem.156.

[99] L H Hung and A P Lee. "Microfluidic devices for the synthesis of nanoparticles and biomaterials". In: *Journal of Medical and Biological Engineering* (2007).

[100] Adrian S Ishkanian et al. "A tiling resolution DNA microarray with complete coverage of the human genome". English. In: *Nature Genetics* 36.3 (2004), pp. 299–303. DOI: 10.1038/ng1307.

[101] Yu Huang et al. "Microfluidics-based devices: New tools for studying cancer and cancer stem cell migration". English. In: *Biomicrofluidics* 5.1 (2011), p. 013412. DOI: 10.1063/1.3555195.

[102] George M Whitesides. "The origins and the future of microfluidics". English. In: *Nature* 442.7101 (2006), pp. 368–373. DOI: 10.1038/nature05058.

[103] Curtis D Chin et al. "Microfluidics-based diagnostics of infectious diseases in the developing world". In: *Nature medicine* 17.8 (2011), pp. 1015–1019. DOI: 10.1038/nm.2408.

[104] George Whitesides. "Solving problems." English. In: *Lab on a chip* 10.18 (2010), pp. 2317–2318. DOI: 10.1039/c0lc90036b.

[105] Marc A Unger et al. "Monolithic Microfabricated Valves and Pumps by Multilayer Soft Lithography". English. In: *Science (New York, N.Y.)* 288.5463 (2000), pp. 113–116. DOI: 10.1126/science.288.5463.113.

[106] Adam R Abate et al. "High-throughput injection with microfluidics using picoinjectors". English. In: *Proceedings of the National Academy of Sciences of the United States of America* 107.45 (2010), pp. 19163–19166. DOI: 10.1073/pnas.1006888107.

[107] Adam Sciambi and Adam R Abate. "Generating electric fields in PDMS microfluidic devices with salt water electrodes." English. In: *Lab on a chip* (2014). DOI: 10.1039/c4lc00078a.

[108] Jean-Christophe Baret et al. "Fluorescence-activated droplet sorting (FADS): efficient microfluidic cell sorting based on enzymatic activity." English. In: *Lab on a chip* 9.13 (2009), pp. 1850–1858. DOI: 10.1039/b902504a.

[109] Shaun W Lim and Adam R Abate. "Ultrahigh-throughput sorting of microfluidic drops with flow cytometry." English. In: *Lab on a chip* 13.23 (2013), pp. 4563–4572. DOI: 10.1039/c3lc50736j.

[110] Ralf Seemann et al. "Droplet based microfluidics". English. In: *Reports on Progress in Physics* 75.1 (2011), pp. 016601–42. DOI: 10.1088/0034-4885/75/1/016601.

[111] Frederick K Balagaddé et al. "Long-Term Monitoring of Bacteria Undergoing Programmed Population Control in a Microchemostat". English. In: *Science (New York, N.Y.)* 309.5731 (2005), pp. 137–140. DOI: 10.1126/science.1109173.

[112] George Gabriel Stokes. *On the effect of the internal friction of fluids on the motion of pendulums*. 1851.

[113] O Reynolds. "An experimental investigation of the circumstances which determine whether the motion of water shall be direct or sinuous, and of the law of resistance in parallel ..." In: *Proceedings of the royal society of ...* 1883, pp. 935–982.

[114] N Rott. "Note on the history of the Reynolds number". In: *Annual review of fluid mechanics* (1990). DOI: 10.1146/annurev.fl.22.010190.000245.

[115] Howard A Stone. "Introduction to Fluid Dynamics for Microfluidic Flows". English. In: *CMOS Biotechnology*. Boston, MA: Springer US, 2007, pp. 5–30. ISBN: 978-0-387-36836-8. DOI: 10.1007/978-0-387-68913-5_2.

[116] Christie Geankoplis. *Transport processes and separation process principles (includes unit operations) fourth edition*. Prentice Hall Press, 2003. ISBN: 013101367X.

[117] Sangtae Kim and Seppo J Karrila. *Microhydrodynamics: principles and selected applications*. Mineola, 2013. ISBN: 0486317676.

[118] Brian Kirby. *Micro- and nanoscale fluid mechanics : transport in microfluidic devices*. 1st ed. Cambridge University Press, 2013. ISBN: 978-1107617209.

[119] Börn Meier et al. "Chemotactic cell trapping in controlled alternating gradient fields". English. In: *Proceedings of the National Academy of Sciences* 108.28 (2011), pp. 11417–11422. DOI: 10.1073/pnas.1014853108.

[120] Adam R Abate and David A Weitz. "Faster multiple emulsification with drop splitting." English. In: *Lab on a chip* 11.11 (2011), pp. 1911–1915. DOI: 10.1039/c0lc00706d.

[121] Saurabh Vyawahare, Andrew D Griffiths, and Christoph A Merten. "Miniaturization and parallelization of biological and chemical assays in microfluidic devices." English. In: *Chemistry & biology* 17.10 (2010), pp. 1052–1065. DOI: 10.1016/j.chembiol.2010.09.007.

[122] J Lederberg. "A simple method for isolating individual microbes." English. In: *Journal of bacteriology* 68.2 (1954), pp. 258–259.

[123] P B Umbanhowar, V Prasad, and D A Weitz. "Monodisperse Emulsion Generation via Drop Break Off in a Coflowing Stream". English. In: *Langmuir* 16.2 (2000), pp. 347–351. DOI: 10.1021/la990101e.

[124] Guilhem Velve-Casquillas et al. "Microfluidic tools for cell biological research." English. In: *Nano today* 5.1 (2010), pp. 28–47. DOI: 10.1016/j.nantod.2009.12.001.

[125] Shelley L Anna, Nathalie Bontoux, and Howard A Stone. "Formation of dispersions using "flow focusing" in microchannels". English. In: *Applied Physics Letters* 82.3 (2003), pp. 364–366. DOI: 10.1063/1.1537519.

[126] T Thorsen et al. "Dynamic pattern formation in a vesicle-generating microfluidic device." English. In: *Physical review letters* 86.18 (2001), pp. 4163–4166. DOI: 10.1103/PhysRevLett.86.4163.

[127] G F Christopher and S L Anna. "Microfluidic methods for generating continuous droplet streams". English. In: *Journal of Physics D: Applied Physics* 40.19 (2007), R319–R336. DOI: 10.1088/0022-3727/40/19/R01.

[128] Helen Song and Rustem F Ismagilov. "Millisecond kinetics on a microfluidic chip using nanoliters of reagents." English. In: *Journal of the American Chemical Society* 125.47 (2003), pp. 14613–14619. DOI: 10.1021/ja0354566.

[129] Lingling Shui, Jan C T Eijkel, and Albert van den Berg. "Multiphase flow in microfluidic systems –control and applications of droplets and interfaces." English. In: *Advances in Colloid and Interface Science* 133.1 (2007), pp. 35–49. DOI: 10.1016/j.cis.2007.03.001.

[130] Wynter J Duncanson et al. "Microfluidic synthesis of advanced microparticles for encapsulation and controlled release." English. In: *Lab on a chip* 12.12 (2012), pp. 2135–2145. DOI: 10.1039/c2lc21164e.

[131] Tae Yong Lee et al. "Microfluidic production of multiple emulsions and functional microcapsules". English. In: *Lab on a chip* (2016), pp. 1–26. DOI: 10.1039/C6LC00809G.

[132] Lorenzo Capretto et al. "Micromixing Within Microfluidic Devices". English. In: *Microfluidics*. Springer Berlin Heidelberg, 2011, pp. 27–68. DOI: 10.1007/1282011150.

[133] Ashleigh B Theberge et al. "Microdroplets in Microfluidics: An Evolving Platform for Discoveries in Chemistry and Biology". English. In: *Angewandte Chemie (International ed. in English)* 49.34 (2010), pp. 5846–5868. DOI: 10.1002/anie.200906653.

[134] Johannes Patrick Frohnmayer et al. "Droplet-Supported Giant Vesicles as Cell-Like Compartments for Synthetic Biology". In: *The Giant Vesicle Book*. Ed. by R Dimova and R Lipowski. CRC Taylor & Francis, 2017.

[135] Yung-Chieh Tan and Abraham Phillip Lee. "Microfluidic separation of satellite droplets as the basis of a monodispersed micron and submicron emulsification system." English. In: *Lab on a chip* 5.10 (2005), pp. 1178–1183. DOI: 10.1039/b504497a.

[136] Keith J Morton et al. "Hydrodynamic metamaterials: microfabricated arrays to steer, refract, and focus streams of biomaterials." English. In: *Proc Natl Acad Sci USA* 105.21 (2008), pp. 7434–7438. DOI: 10.1073/pnas.0712398105.

[137] Nivedita Nivedita and Ian Papautsky. "Continuous separation of blood cells in spiral microfluidic devices." English. In: *Biomicrofluidics* 7.5 (2013), p. 54101. DOI: 10.1063/1.4819275.

[138] Majid Ebrahimi Warkiani et al. "Slanted spiral microfluidics for the ultra-fast, label-free isolation of circulating tumor cells." English. In: *Lab on a chip* 14.1 (2014), pp. 128–137. DOI: 10.1039/c3lc50617g.

[139] Xize Niu et al. "Real-time detection, control, and sorting of microfluidic droplets." English. In: *Biomicrofluidics* 1.4 (2007), p. 44101. DOI: 10.1063/1.2795392.

[140] Kwang W Oh and Chong H Ahn. "A review of microvalves". English. In: *Journal of Micromechanics and Microengineering* 16.5 (2006), R13–R39. DOI: 10.1088/0960-1317/16/5/R01.

[141] Jeremy J Agresti et al. "Ultrahigh-throughput screening in drop-based microfluidics for directed evolution". English. In: *Proc Natl Acad Sci USA* 107.9 (2010), pp. 4004–4009. DOI: 10.1073/pnas.0910781107.

[142] Todd M Squires and Stephen R Quake. "Microfluidics: Fluid physics at the nanoliter scale". In: *Reviews of modern physics* 77.3 (2005), pp. 977–1026. DOI: 10.1103/RevModPhys.77.977.

[143] Evelien W M Kemna et al. "High-yield cell ordering and deterministic cell-in-droplet encapsulation using Dean flow in a curved microchannel". English. In: *Lab on a chip* 12.16 (2012), pp. 2881–7. DOI: 10.1039/c2lc00013j.

[144] D R Link et al. "Geometrically mediated breakup of drops in microfluidic devices". In: *Physical review letters* (2004). DOI: 10.1103/PhysRevLett.92.054503.

[145] Michele Zagnoni and Jonathan M Cooper. "On-chip electrocoalescence of microdroplets as a function of voltage, frequency and droplet size". English. In: *Lab on a chip* 9.18 (2009), pp. 2652–2658. DOI: 10.1039/B906298J.

[146] Linas Mazutis et al. "Multi-step microfluidic droplet processing: kinetic analysis of an in vitro translated enzyme." English. In: *Lab on a chip* 9.20 (2009), pp. 2902–2908. DOI: 10.1039/b907753g.

[147] John William Strutt. "On The Instability Of Jets". English. In: *Proceedings of the London Mathematical Society* s1-10.1 (1878), pp. 4–13.

[148] H J Kull. "Theory of the Rayleigh-Taylor instability". English. In: *Physics Reports* 206.5 (1991), pp. 197–325. DOI: 10.1016/0370-1573(91)90153-D.

[149] Pierre-Gilles de Gennes, Françoise Brochard-Wyart, and David Quéré. *Capillarity and wetting phenomena : drops, bubbles, pearls, waves*. New York: Springer, 2004.

[150] G Mason. "An experimental determination of the stable length of cylindrical liquid bubbles". English. In: *Journal of Colloid and Interface Science* 32.1 (1970), pp. 172–176. DOI: 10.1016/0021-9797(70)90116-5.

[151] J M Rallison. "The deformation of small viscous drops and bubbles in shear flows". In: *Annual review of fluid mechanics* (1984). DOI: 10.1146/annurev.fl.16.010184.000401.

[152] Howard A Stone. "Dynamics of drop deformation and breakup in viscous fluids". In: *Annual review of fluid mechanics* 26 (1994), pp. 65–102. DOI: 10.1146/annurev.fl.26.010194.000433.

[153] Shelly Gulati et al. "Microdroplet formation in rounded flow-focusing junctions". English. In: *Microfluidics and Nanofluidics* 20.1 (2015), pp. 1–9. DOI: 10.1007/s10404-015-1680-3.

[154] Zhihong Nie et al. "Emulsification in a microfluidic flow-focusing device: effect of the viscosities of the liquids". English. In: *Microfluidics and Nanofluidics* 5.5 (2008), pp. 585–594. DOI: 10.1007/s10404-008-0271-y.

[155] Taotao Fu et al. "Droplet formation and breakup dynamics in microfluidic flow-focusing devices: From dripping to jetting". English. In: *Chemical Engineering Science* 84 IS - (2012), pp. 207–217. DOI: 10.1016/j.ces.2012.08.039.

[156] Thomas Ward et al. "Microfluidic flow focusing: Drop size and scaling in pressure versus flow-rate-driven pumping". English. In: *ELECTROPHORESIS* 26.19 (2005), pp. 3716–3724. DOI: 10.1002/elps.200500173.

[157] J Tan et al. "Drop dispenser in a cross-junction microfluidic device: Scaling and mechanism of break-up". English. In: *Chemical Engineering Journal* 136.2–3 (2008), pp. 306–311. DOI: 10.1016/j.cej.2007.04.011.

[158] "Droplet formation in microfluidic cross-junctions". English. In: *Physics of Fluids* 23.8 (2011), pp. 082101–13. DOI: 10.1063/1.3615643.

[159] Anupam Gupta and Mauro Sbragaglia. "A lattice Boltzmann study of the effects of viscoelasticity on droplet formation in microfluidic cross-junctions". English. In: *The European Physical Journal E* 39.1 (2016), pp. 2–15. DOI: 10.1140/epje/i2016-16002-1.

[160] C M Dobson et al. "Atmospheric aerosols as prebiotic chemical reactors." English. In: *Proceedings of the National Academy of Sciences of the United States of America* 97.22 (2000), pp. 11864–11868. DOI: 10.1073/pnas.200366897.

[161] Irene A Chen and Peter Walde. "From Self-Assembled Vesicles to Protocells". English. In: *Cold Spring Harbor Perspectives in Biology* 2.7 (2010), a002170–a002170. DOI: 10.1101/cshperspect.a002170.

[162] Robert Shapiro. "A Simpler Origin for Life". English. In: *Scientific American* 296.6 (2007), pp. 46–53. DOI: 10.1038/scientificamerican0607-46.

[163] K Kosswig. "Surfactants". In: *Ullmann's Encyclopedia of Industrial Chemistry* (1994), pp. 487–505. DOI: 10.1002/14356007.a25_747.

[164] A W Adamson and A P Gast. *Physical chemistry of surfaces*. 6th ed. John Wiley & Sons, 1997. ISBN: ISBN: 978-0-471-14873-9.

[165] C Ybert and J M di Meglio. "Ascending air bubbles in solutions of surface-active molecules: Influence of desorption kinetics". English. In: *The European Physical Journal E* 3.2 (2000), pp. 143–148. DOI: 10.1007/s101890070027.

[166] Jung-uk Shim et al. "Ultrarapid Generation of Femtoliter Microfluidic Droplets for Single-Molecule-Counting Immunoassays". English. In: *ACS Nano* 7.7 (2013), pp. 5955–5964. DOI: 10.1021/nn401661d.

[167] Farizal Hakiki, Dara Ayuda Maharsi, and Taufan Marhaendrajana. "Surfactant-Polymer Coreflood Simulation and Uncertainty Analysis Derived from Laboratory Study". English. In: *Journal of Engineering and Technological Sciences; Vol 47, No 6 (2015) KW* - 47.6 (2015), pp. 706–725–725. DOI: 10.5614/j.eng.technol.sci.2015.47.6.9.

[168] Daniel J Holt et al. "Fluorosurfactants for microdroplets: Interfacial tension analysis". English. In: *Journal of Colloid and Interface Science* 350.1 (2010), pp. 205–211. DOI: 10.1016/j.jcis.2010.06.036.

[169] J N Phillips. "The energetics of micelle formation". English. In: *Transactions of the Faraday Society* 51.0 (1955), pp. 561–569. DOI: 10.1039/TF9555100561.

[170] J Bibette Poulin, F Leal Calderon, and P. "Emulsions: basic principles". In: *Reports on Progress in Physics* 62.6 (1999), p. 969.

[171] J Bibette et al. "Stability criteria for emulsions". English. In: *Physical review letters* 69.16 (1992), pp. 2439–2442. DOI: 10.1103/PhysRevLett.69.2439.

[172] L Spencer Roach, Helen Song, and Rustem F Ismagilov. "Controlling Nonspecific Protein Adsorption in a Plug-Based Microfluidic System by Controlling Interfacial Chemistry Using Fluorous-Phase Surfactants". English. In: *Analytical Chemistry* 77.3 (2005), pp. 785–796. DOI: 10.1021/ac049061w.

[173] C Holtze et al. "Biocompatible surfactants for water-in-fluorocarbon emulsions". English. In: *Lab on a chip* 8.10 (2008), pp. 1632–1639. DOI: 10.1039/B806706F.

[174] Ilia Platzman, Jan-Willi Janiesch, and Joachim Pius Spatz. "Synthesis of nanostructured and biofunctionalized water-in-oil droplets as tools for homing T cells." English. In: *Journal of the American Chemical Society* 135.9 (2013), pp. 3339–3342. DOI: 10.1021/ja311588c.

[175] Kozo Shinoda, Masakatsu Hato, and Takao Hayashi. "Physicochemical properties of aqueous solutions of fluorinated surfactants". English. In: *The Journal of Physical Chemistry* 76.6 (1972), pp. 909–914. DOI: 10.1021/j100650a021.

[176] M Pabon and J M Corpart. "Fluorinated surfactants: synthesis, properties, effluent treatment". English. In: *13th European Symposium on Fluorine Chemistry (ESFC-13)* 114.2 (2002), pp. 149–156. DOI: 10.1016/S0022-1139(02)00038-6.

[177] W C Griffin. "Calculation of HLB values of non-ionic surfactants". In: 5 (1955), pp. 249–256.

[178] Jan-Willi Janiesch et al. "Key Factors for Stable Retention of Fluorophores and Labeled Biomolecules in Droplet-Based Microfluidics". English. In: *Analytical Chemistry* 87.4 (2015), pp. 2063–2067. DOI: 10.1021/ac504736e.

[179] Robert A Scherrer and Susan M Howard. "Use of distribution coefficients in quantitative structure-activity relations". English. In: *Journal of Medicinal Chemistry* 20.1 (1977), pp. 53–58. DOI: 10.1021/jm00211a010.

[180] Carol N Manners, David W Payling, and Dennis A Smith. "Distribution coefficient, a convenient term for the relation of predictable physico-chemical properties to metabolic processes". English. In: *Xenobiotica; the fate of foreign compounds in biological systems* 18.3 (1988), pp. 331–350. DOI: 10.3109/00498258809041669.

[181] Cory J Gerdts et al. "Time-Controlled Microfluidic Seeding in nL-Volume Droplets To Separate Nucleation and Growth Stages of Protein Crystallization". English. In: *Angewandte Chemie (International ed. in English)* 45.48 (2006), pp. 8156–8160. DOI: 10.1002/anie.200602946.

[182] Helen Song et al. "On-Chip Titration of an Anticoagulant Argatroban and Determination of the Clotting Time within Whole Blood or Plasma Using a Plug-Based Microfluidic System". English. In: *Analytical Chemistry* 78.14 (2006), pp. 4839–4849. DOI: 10.1021/ac0601718.

[183] Nicolas Bremond, Abdou R Thiam, and Jérôme Bibette. "Decompressing Emulsion Droplets Favors Coalescence". English. In: *Physical review letters* 100.2 (2008), p. 024501. DOI: 10.1103/PhysRevLett.100.024501.

[184] Craig Priest, Stephan Herminghaus, and Ralf Seemann. "Controlled electrocoalescence in microfluidics: Targeting a single lamella". English. In: *Applied Physics Letters* 89.13 (2006), p. 134101. DOI: 10.1063/1.2357039.

[185] Ali Fallah-Araghi et al. "A completely in vitro ultrahigh-throughput droplet-based microfluidic screening system for protein engineering and directed evolution." English. In: *Lab on a chip* 12.5 (2012), pp. 882–891. DOI: 10.1039/c2lc21035e.

[186] Manhee Lee et al. "Synchronized reinjection and coalescence of droplets in microfluidics". English. In: *Lab on a chip* 14.3 (2014), pp. 509–513. DOI: 10.1039/C3LC51214B.

[187] Marie Leman et al. "Droplet-based microfluidics at the femtolitre scale." English. In: *Lab on a chip* 15.3 (2015), pp. 753–765. DOI: 10.1039/c4lc01122h.

[188] S Herminghaus. "Dynamical Instability of Thin Liquid Films Between Conducting Media". English. In: *Physical review letters* 83.12 (1999), pp. 2359–2361. DOI: 10.1103/PhysRevLett.83.2359.

[189] Jan-Willi Janiesch. "Development of droplet-based microfluidics for synthetic biology applications". English. PhD thesis. Heidelberg: Heidelberg University, 2015.

[190] Ee Xien Ng et al. "Low-volume multiplexed proteolytic activity assay and inhibitor analysis through a pico-injector array." English. In: *Lab on a chip* 15.4 (2015), pp. 1153–1159. DOI: 10.1039/c4lc01162g.

[191] Brian O'Donovan, Dennis J Eastburn, and Adam R Abate. "Electrode-free picoinjection of microfluidic drops." English. In: *Lab on a chip* 12.20 (2012), pp. 4029–4032. DOI: 10.1039/c2lc40693d.

[192] "Droplet breakup in microfluidic T-junctions at small capillary numbers". English. In: *Physics of Fluids* 21.7 (2009), p. 072001. DOI: 10.1063/1.3170983.

[193] Laure Ménétrier-Deremble and Patrick Tabeling. "Droplet breakup in microfluidic junctions of arbitrary angles." English. In: *Physical Review E* 74.3 (2006), p. 035303. DOI: 10.1103/PhysRevE.74.035303.

[194] Geoffrey M Cooper. "The Mechanism of Vesicular Transport". In: *The Cell*. Sinauer Associates, 2013, pp. 406–411. ISBN: 978-0878939640.

[195] Markus Sällman Almén et al. "Mapping the human membrane proteome: a majority of the human membrane proteins can be classified according to function and evolutionary origin". English. In: *BMC Biology* 7.1 (2009), p. 1. DOI: 10.1186/1741-7007-7-50.

[196] Derek Marsh. *Handbook of Lipid Bilayers, Second Edition*. 2nd ed. CRC Press, 2013. ISBN: 9781420088328.

[197] A J Hulbert et al. "Acyl composition of muscle membranes varies with body size in birds". English. In: *Journal of Experimental Biology* 205.22 (2002), pp. 3561–3569. DOI: 10.1016/0005-2728(94)90099-X.

[198] A J Hulbert, Tahira Rana, and Patrice Couture. "The acyl composition of mammalian phospholipids: an allometric analysis". English. In: *Comparative Biochemistry and Physiology Part B: Biochemistry and Molecular Biology* 132.3 (2002), pp. 515–527. DOI: 10.1016/S1096-4959(02)00066-0.

[199] Harvey F Lodish et al. *Molecular cell biology*. 7th ed. New York: W.H. Freeman and Co., 2012. ISBN: 978-1464109812.

[200] Thomas Günther Pomorski, Tommy Nylander, and Marité Cárdenas. "Model cell membranes: Discerning lipid and protein contributions in shaping the cell". English. In: *Advances in Colloid and Interface Science* 205.C (2014), pp. 207–220. DOI: 10.1016/j.cis.2013.10.028.

[201] Michael F Brown. "Curvature Forces in Membrane Lipid–Protein Interactions". English. In: *Biochemistry* 51.49 (2012), pp. 9782–9795. DOI: 10.1021/bi301332v.

[202] Daniel Lingwood and Kai Simons. "Lipid rafts as a membrane-organizing principle." English. In: *Science (New York, N.Y.)* 327.5961 (2010), pp. 46–50. DOI: 10.1126/science.1174621.

[203] Sarah L Veatch and Sarah L Keller. "Miscibility Phase Diagrams of Giant Vesicles Containing Sphingomyelin". English. In: *Physical review letters* 94.14 (2005), p. 148101. DOI: 10.1103/PhysRevLett.94.148101.

[204] Anna Åkesson et al. "Composition and structure of mixed phospholipid supported bilayers formed by POPC and DPPC". English. In: *Soft Matter* 8.20 (2012), pp. 5658–5665. DOI: 10.1039/C2SM00013J.

[205] Hanna P Wacklin. "Composition and Asymmetry in Supported Membranes Formed by Vesicle Fusion". English. In: *Langmuir* 27.12 (2011), pp. 7698–7707. DOI: 10.1021/la200683e.

[206] Ralf P Richter, Rémi Bérat, and Alain R Brisson. "Formation of Solid-Supported Lipid Bilayers: An Integrated View". English. In: *Langmuir* 22.8 (2006), pp. 3497–3505. DOI: 10.1021/la052687c.

[207] Ralf Richter, Anneke Mukhopadhyay, and Alain Brisson. "Pathways of Lipid Vesicle Deposition on Solid Surfaces: A Combined QCM-D and AFM Study". English. In: *Biophysical Journal* 85.5 (2003), pp. 3035–3047. DOI: 10.1016/S0006-3495(03)74722-5.

[208] Nam-Joon Cho et al. "Quartz crystal microbalance with dissipation monitoring of supported lipid bilayers on various substrates". English. In: *Nature protocols* 5.6 (2010), pp. 1096–1106. DOI: 10.1038/nprot.2010.65.

[209] Paul S Cremer and Steven G Boxer. "Formation and Spreading of Lipid Bilayers on Planar Glass Supports". English. In: *J. Phys. Chem. B* 103.13 (1999), pp. 2554–2559. DOI: 10.1021/jp983996x.

[210] E T Castellana and P S Cremer. "Solid supported lipid bilayers: From biophysical studies to sensor design". In: *Surface Science Reports* (2006). DOI: 10.1016/j.surfrep.2006.06.001.

[211] C A Keller and B Kasemo. "Surface Specific Kinetics of Lipid Vesicle Adsorption Measured with a Quartz Crystal Microbalance". English. In: *Biophysical journal* 75.3 (1998), pp. 1397–1402. DOI: 10.1016/S0006-3495(98)74057-3.

[212] Pat Plunkett et al. "Simulation of edge facilitated adsorption and critical concentration induced rupture of vesicles at a surface". English. In: *Soft Matter* 9.35 (2013), pp. 8420–8427. DOI: 10.1039/C3SM50443C.

[213] Simon J Attwood, Youngjik Choi, and Zoya Leonenko. "Preparation of DOPC and DPPC Supported Planar Lipid Bilayers for Atomic Force Microscopy and Atomic Force Spectroscopy." English. In: *International journal of molecular sciences* 14.2 (2013), pp. 3514–3539. DOI: 10.3390/ijms14023514.

[214] A D Bangham and R W Horne. "Negative staining of phospholipids and their structural modification by surface-active agents as observed in the electron microscope". English. In: *Journal of molecular biology* 8.5 (1964), 660IN2–668IN10. DOI: 10.1016/S0022-2836(64)80115-7.

[215] D D Lasič. "The mechanism of vesicle formation." English. In: *The Biochemical journal* 256.1 (1988), pp. 1–11.

[216] Nelson F Morales-Penningston et al. "GUV preparation and imaging: Minimizing artifacts". English. In: *Biochimica et Biophysica Acta* 1798.7 (2010), pp. 1324–1332. DOI: 10.1016/j.bbamem.2010.03.011.

[217] H T Jung et al. "The origins of stability of spontaneous vesicles." English. In: *Proceedings of the National Academy of Sciences of the United States of America* 98.4 (2001), pp. 1353–1357. DOI: 10.1073/pnas.041420998.

[218] Gregory Gregoriadis. "The Carrier Potential of Liposomes in Biology and Medicine". English. In: *N Engl J Med* 295.14 (1976), pp. 765–770. DOI: 10.1056/NEJM197609302951406.

[219] Roy van der Meel et al. "Extracellular vesicles as drug delivery systems: Lessons from the liposome field". English. In: *Journal of Controlled Release* 195 (2014), pp. 72–85. DOI: 10.1016/j.jconrel.2014.07.049.

[220] V P Torchilin. "Recent advances with liposomes as pharmaceutical carriers". In: *Nature reviews Drug discovery* 4.2 (2005), pp. 145–160. DOI: 10.1038/nrd1632.

[221] Aditi Jhaveri and Vladimir Torchilin. "Intracellular delivery of nanocarriers and targeting to subcellular organelles". English. In: *Expert Opinion on Drug Delivery* 13.1 (2015), pp. 49–70. DOI: 10.1517/17425247.2015.1086745.

[222] George Rouser. "Phospholipids and Blood Coagulation ". In: *The American Journal of Clinical Nutrition* 6.6 (1958), pp. 681–687.

[223] F Olson et al. "Preparation of liposomes of defined size distribution by extrusion through polycarbonate membranes". English. In: *Biochimica et Biophysica Acta (BBA) - Biomembranes* 557.1 (1979), pp. 9–23. DOI: 10.1016/0005-2736(79)90085-3.

[224] Theresa M Allen et al. "Detergent removal during membrane reconstitution". English. In: *Biochimica et Biophysica Acta (BBA) - Biomembranes* 601 (1980), pp. 328–342. DOI: 10.1016/0005-2736(80)90537-4.

[225] A Das, D M Ivey, and L G Ljungdahl. "Purification and reconstitution into proteoliposomes of the F1F0 ATP synthase from the obligately anaerobic gram-positive bacterium Clostridium thermoautotrophicum." English. In: *Journal of Bacteriology* 179.5 (1997), pp. 1714–1720.

[226] Francis Szoka and Demetrios Papahadjopoulos. "Comparative properties and methods of preparation of lipid vesicles (liposomes)." English. In: *Annual review of biophysics and bioengineering* 9 (1980), pp. 467–508. DOI: 10.1146/annurev.bb.09.060180.002343.

[227] Barbara Mui, Laurie Chow, and Michael J Hope. "Extrusion Technique to Generate Liposomes of Defined Size A2 -". In: *Liposomes, Part B*. Academic Press, 2003, pp. 3–14.

[228] Rolf Schubert. "Liposome Preparation by Detergent Removal A2 -". In: *Liposomes, Part B*. Academic Press, 2003, pp. 46–70.

[229] Jean-Louis Rigaud and Daniel Levy. "Reconstitution of Membrane Proteins into Liposomes A2 -". In: *Liposomes, Part B*. Academic Press, 2003, pp. 65–86.

[230] Manfred H W Milsmann, Reto A Schwendener, and Hans-Georg Weder. "The preparation of large single bilayer liposomes by a fast and controlled dialysis". English. In: *Biochimica et Biophysica Acta (BBA) - Biomembranes* 512.1 (1978), pp. 147–155. DOI: 10.1016/0005-2736(78)90225-0.

[231] Otmar Zumbuehl and Hans-Georg Weder. "Liposomes of controllable size in the range of 40 to 180 nm by defined dialysis of lipid/detergent mixed micelles". English. In: *Biochimica et Biophysica Acta (BBA) - Biomembranes* 640.1 (1981), pp. 252–262. DOI: 10.1016/0005-2736(81)90550-2.

[232] H G Enoch and P Strittmatter. "Formation and properties of 1000-A-diameter, single-bilayer phospholipid vesicles". English. In: *Proceedings of the National Academy of Sciences* 76.1 (1979), pp. 145–149.

[233] Jean-Louis Rigaud et al. "Detergent removal by non-polar polystyrene beads". English. In: *European Biophysics Journal* 27.4 (1998), pp. 305–319. DOI: 10.1007/s002490050138.

[234] F Ross Hallett, J Watton, and P Krygsman. "Vesicle sizing". English. In: *Biophysical journal* 59.2 (2017), pp. 357–362. DOI: 10.1016/S0006-3495(91)82229-9.

[235] G Perevucnik et al. "Size analysis of biological membrane vesicles by gel filtration, dynamic light scattering and electron microscopy". English. In: *Biochimica et Biophysica Acta* 821.1 (1985), pp. 169–173.

[236] Jeremy Pencer and F Ross Hallett. "Effects of Vesicle Size and Shape on Static and Dynamic Light Scattering Measurements". English. In: *Langmuir* 19.18 (2003), pp. 7488–7497. DOI: 10.1021/la0345439.

[237] Olga Wesolowska et al. "Giant unilamellar vesicles - a perfect tool to visualize phase separation and lipid rafts in model systems." English. In: *Acta biochimica Polonica* 56.1 (2009), pp. 33–39.

[238] L Ruth Montes et al. "Giant Unilamellar Vesicles Electroformed from Native Membranes and Organic Lipid Mixtures under Physiological Conditions". English. In: *Biophysical Journal* 93.10 (2007), pp. 3548–3554. DOI: 10.1529/biophysj.107.116228.

[239] Dennis Merkle, Nicoletta Kahya, and Petra Schwille. "Reconstitution and Anchoring of Cytoskeleton inside Giant Unilamellar Vesicles". English. In: *ChemBioChem* 9.16 (2008), pp. 2673–2681. DOI: 10.1002/cbic.200800340.

[240] Magdalena Przybylo et al. "Lipid Diffusion in Giant Unilamellar Vesicles Is More than 2 Times Faster than in Supported Phospholipid Bilayers under Identical Conditions". English. In: *Langmuir* 22.22 (2006), pp. 9096–9099. DOI: 10.1021/la061934p.

[241] John P Reeves and Robert M Dowben. "Formation and properties of thin-walled phospholipid vesicles". English. In: *Journal of Cellular Physiology* 73.1 (1969), pp. 49–60. DOI: 10.1002/jcp.1040730108.

[242] A D Bangham, M M Standish, and J C Watkins. "Diffusion of univalent ions across the lamellae of swollen phospholipids". English. In: *Journal of molecular biology* 13.1 (1965), 238IN26–252IN27. DOI: 10.1016/S0022-2836(65)80093-6.

[243] Walter R Perkins et al. "The captured volume of multilamellar vesicles". English. In: *Biochimica et Biophysica Acta (BBA) - Biomembranes* 943.1 (1988), pp. 103–107. DOI: 10.1016/0005-2736(88)90351-3.

[244] Sol M Gruner et al. "Novel multilayered lipid vesicles: comparison of physical characteristics of multilamellar liposomes and stable plurilamellar vesicles". English. In: *Biochemistry* 24.12 (2002), pp. 2833–2842. DOI: 10.1021/bi00333a004.

[245] I Sakurai and Y Kawamura. "Growth mechanism of myelin figures of phosphatidylcholine". English. In: *Biochimica et Biophysica Acta (BBA) - Biomembranes* 777.2 (1984), pp. 347–351. DOI: 10.1016/0005-2736(84)90439-5.

[246] M Buchanan, J Arrault, and M E Cates. "Swelling and Dissolution of Lamellar Phases: Role of Bilayer Organization". English. In: *Langmuir* 14.26 (1998), pp. 7371–7377. DOI: 10.1021/la980722s.

[247] K Akashi et al. "Preparation of giant liposomes in physiological conditions and their characterization under an optical microscope." English. In: *Biophysical Journal* 71.6 (1996), pp. 3242–3250. DOI: 10.1016/S0006-3495(96)79517-6.

[248] Ken-ichirou Akashi et al. "Formation of Giant Liposomes Promoted by Divalent Cations: Critical Role of Electrostatic Repulsion". English. In: *Biophysical Journal* 74.6 (1998), pp. 2973–2982. DOI: 10.1016/S0006-3495(98)78004-X.

[249] Yuko Yamashita et al. "A new method for the preparation of giant liposomes in high salt concentrations and growth of protein microcrystals in them". English. In: *Biochimica et Biophysica Acta (BBA) - Biomembranes* 1561.2 (2002), pp. 129–134. DOI: 10.1016/S0005-2736(02)00338-3.

[250] Jonathan R Howse et al. "Templated formation of giant polymer vesicles with controlled size distributions". English. In: *Nature Materials* 8.6 (2009), pp. 507–511. DOI: 10.1038/nmat2446.

[251] M Hishida et al. "Hydration process of multi-stacked phospholipid bilayers to form giant vesicles". English. In: *Chemical Physics Letters* 455.4–6 (2008), pp. 297–302. DOI: 10.1016/j.cplett.2008.02.065.

[252] Miglena I Angelova and Dimiter S Dimitrov. "Liposome electroformation". English. In: *Faraday Discussions of the Chemical Society* 81.0 (1986), pp. 303–311. DOI: 10.1039/DC9868100303.

[253] Miglena I Angelova. "Liposome Electroformation". English. In: *Perspectives in Supramolecular Chemistry*. Chichester, UK: John Wiley & Sons, Ltd., 2007, pp. 26–36. ISBN: 9780470511534. DOI: 10.1002/9780470511534.ch3.

[254] Toshinori Shimanouchi, Hiroshi Umakoshi, and Ryoichi Kuboi. "Kinetic Study on Giant Vesicle Formation with Electroformation Method". English. In: *Langmuir* 25.9 (2009), pp. 4835–4840. DOI: 10.1021/la8040488.

[255] Miglena I Angelova and Dimiter S Dimitrov. "A mechanism of liposome electroformation". English. In: *Trends in Colloid and Interface Science II*. Ed. by V Degiorgio. Darmstadt: Steinkopff, 1988, pp. 59–67. ISBN: 978-3-7985-0777-7. DOI: 10.1007/BFb0114171.

[256] Yukihisa Okumura et al. "Electroformation of Giant Vesicles on a Non-Electroconductive Substrate". English. In: *Journal of the American Chemical Society* 129.6 (2007), pp. 1490–1491. DOI: 10.1021/ja068127x.

[257] L Ruth Montes et al. "Electroformation of Giant Unilamellar Vesicles from Native Membranes and Organic Lipid Mixtures for the Study of Lipid Domains under Physiological Ionic-Strength Conditions". In: *Liposomes*. Ed. by Volkmar Weissig. Totowa, NJ: Humana Press, 2010, pp. 105–114. ISBN: 978-1-60761-447-0. DOI: 10.1007/978-1-60761-447-0_9.

[258] Tanja Pott, Hélène Bouvrais, and Philippe Méléard. "Giant unilamellar vesicle formation under physiologically relevant conditions". English. In: *Chemistry and physics of lipids* 154.2 (2008), pp. 115–119. DOI: 10.1016/j.chemphyslip.2008.03.008.

[259] Pietro Taylor et al. "A novel technique for preparation of monodisperse giant liposomes". English. In: *Chem. Commun. VL* - 1.14 (2003), pp. 1732–1733. DOI: 10.1039/B304059C.

[260] Maël Le Berre et al. "Electroformation of Giant Phospholipid Vesicles on a Silicon Substrate: Advantages of Controllable Surface Properties". English. In: *Langmuir* 24.6 (2008), pp. 2643–2649. DOI: 10.1021/la703391q.

[261] Daniel J Estes and Michael Mayer. "Electroformation of giant liposomes from spin-coated films of lipids". English. In: *Colloids and Surfaces B: Biointerfaces* 42.2 (2005), pp. 115–123. DOI: 10.1016/j.colsurfb.2005.01.016.

[262] Nicolas Rodriguez, Frédéric Pincet, and Sophie Cribier. "Giant vesicles formed by gentle hydration and electroformation: A comparison by fluorescence microscopy". English. In: *Colloids and Surfaces B: Biointerfaces* 42.2 (2005), pp. 125–130. DOI: 10.1016/j.colsurfb.2005.01.010.

[263] Philippe Girard et al. "A New Method for the Reconstitution of Membrane Proteins into Giant Unilamellar Vesicles". English. In: *Biophysical Journal* 87.1 (2004), pp. 419–429. DOI: 10.1529/biophysj.104.040360.

[264] Daniel J Estes and Michael Mayer. "Giant liposomes in physiological buffer using electroformation in a flow chamber". English. In: *Biochimica et Biophysica Acta* 1712.2 (2005), pp. 152–160. DOI: 10.1016/j.bbamem.2005.03.012.

[265] K Kuribayashi et al. "Electroformation of giant liposomes in microfluidic channels". English. In: *Measurement Science and Technology* 17.12 (2006), pp. 3121–3126. DOI: 10.1088/0957-0233/17/12/S01.

[266] Primoz Peterlin and Vesna Arrigler. "Electroformation in a flow chamber with solution exchange as a means of preparation of flaccid giant vesicles". English. In: *Colloids and surfaces. B, Biointerfaces* 64.1 (2008), pp. 77–87. DOI: 10.1016/j.colsurfb.2008.01.004.

[267] Veronika Kralj-Iglič et al. "Myelin-like protrusions of giant phospholipid vesicles prepared by electroformation". English. In: *Colloids and Surfaces A: Physicochemical and Engineering Aspects* 181.1–3 (2001), pp. 315–318. DOI: 10.1016/S0927-7757(00)00802-5.

[268] Lisa M Dominak and Christine D Keating. "Macromolecular Crowding Improves Polymer Encapsulation within Giant Lipid Vesicles". English. In: *Langmuir* 24.23 (2008), pp. 13565–13571. DOI: 10.1021/la8028403.

[269] Roger Wick et al. "Microinjection into giant vesicles and light microscopy investigation of enzyme-mediated vesicle transformations". English. In: *Chemistry & Biology* 3.2 (2017), pp. 105–111. DOI: 10.1016/S1074-5521(96)90286-0.

[270] Roger Wick and Pier Luigi Luisi. "Enzyme-containing liposomes can endogenously produce membrane-constituting lipids". English. In: *Chemistry & biology* 3.4 (2017), pp. 277–285. DOI: 10.1016/S1074-5521(96)90107-6.

[271] Patricia Bucher et al. "Giant Vesicles as Biochemical Compartments: The Use of Microinjection Techniques". English. In: *Langmuir* 14.10 (1998), pp. 2712–2721. DOI: 10.1021/la971318g.

[272] Kim S Horger et al. "Films of Agarose Enable Rapid Formation of Giant Liposomes in Solutions of Physiologic Ionic Strength". English. In: *Journal of the American Chemical Society* 131.5 (2009), pp. 1810–1819. DOI: 10.1021/ja805625u.

[273] Feng-Ching Tsai et al. "Chapter Six - Biomimetic Liposome Model Systems to Study Cell Shape Control by the Cytoskeleton". In: *Advances in Planar Lipid Bilayers and Liposomes*. Ed. by Aleš Iglič Kulkarni and Chandrashekhar V. Academic Press, 2014, 139–173 T2 –.

[274] Andreas Weinberger et al. "Gel-assisted formation of giant unilamellar vesicles." English. In: *Biophysical Journal* 105.1 (2013), pp. 154–164. DOI: 10.1016/j.bpj.2013.05.024.

[275] Néstor López Mora et al. "Preparation of size tunable giant vesicles from cross-linked dextran(ethylene glycol) hydrogels". English. In: *Chem. Commun. VL* - 50.16 (2014), pp. 1953–1955. DOI: 10.1039/C3CC49144G.

[276] Rafael B Lira, Rumiana Dimova, and Karin A Riske. "Giant Unilamellar Vesicles Formed by Hybrid Films of Agarose and Lipids Display Altered Mechanical Properties". English. In: *Biophysical journal* 107.7 (2014), pp. 1609–1619. DOI: 10.1016/j.bpj.2014.08.009.

[277] Bram van Hoof et al. "Molecular Simulation of Protein Encapsulation in Vesicle Formation". English. In: *J. Phys. Chem. B* 118.12 (2014), pp. 3346–3354. DOI: 10.1021/jp410612k.

[278] Laura R Arriaga et al. "Ultrathin Shell Double Emulsion Templated Giant Unilamellar Lipid Vesicles with Controlled Microdomain Formation". English. In: *Small* 10.5 (2014), pp. 950–956. DOI: 10.1002/smll.201301904.

[279] Clément Campillo et al. "Unexpected membrane dynamics unveiled by membrane nanotube extrusion." English. In: *Biophysical Journal* 104.6 (2013), pp. 1248–1256. DOI: 10.1016/j.bpj.2013.01.051.

[280] Sophie Pautot, Barbara J Frisken, and D A Weitz. "Production of Unilamellar Vesicles Using an Inverted Emulsion". English. In: *Langmuir* 19.7 (2003), pp. 2870–2879. DOI: 10.1021/la026100v.

[281] Kazuya Nishimura et al. "Size control of giant unilamellar vesicles prepared from inverted emulsion droplets." English. In: *Journal of Colloid and Interface Science* 376.1 (2012), pp. 119–125. DOI: 10.1016/j.jcis.2012.02.029.

[282] Tsutomu Hamada et al. "Construction of Asymmetric Cell-Sized Lipid Vesicles from Lipid-Coated Water-in-Oil Microdroplets". English. In: *J. Phys. Chem. B* 112.47 (2008), pp. 14678–14681. DOI: 10.1021/jp807784j.

[283] Léa-Laetitia Pontani et al. "Reconstitution of an actin cortex inside a liposome." English. In: *Biophysical Journal* 96.1 (2009), pp. 192–198. DOI: 10.1016/j.bpj.2008.09.029.

[284] Frederick A Heberle et al. "Subnanometer Structure of an Asymmetric Model Membrane: Interleaflet Coupling Influences Domain Properties". English. In: *Langmuir* 32.20 (2016), pp. 5195–5200. DOI: 10.1021/acs.langmuir.5b04562.

[285] Yuval Elani et al. "Measurements of the effect of membrane asymmetry on the mechanical properties of lipid bilayers". English. In: *Chemical Communications* 51.32 (2015), pp. 6976–6979. DOI: 10.1039/C5CC00712G.

[286] Koki Kamiya et al. "Cell-sized asymmetric lipid vesicles facilitate the investigation of asymmetric membranes". English. In: *Nature Chemistry* 8.9 (2016), pp. 881–889. DOI: 10.1038/nchem.2537.

[287] Peichi C Hu, Su Li, and Noah Malmstadt. "Microfluidic Fabrication of Asymmetric Giant Lipid Vesicles". English. In: *ACS Appl. Mater. Interfaces* 3.5 (2011), pp. 1434–1440. DOI: 10.1021/am101191d.

[288] Elise Lorenceau et al. "Generation of Polymerosomes from Double-Emulsions". English. In: *Langmuir* 21.20 (2005), pp. 9183–9186. DOI: 10.1021/la050797d.

[289] Ho Cheung Shum et al. "Double Emulsion Templated Monodisperse Phospholipid Vesicles". English. In: *Langmuir* 24.15 (2008), pp. 7651–7653. DOI: 10.1021/la801833a.

[290] Ho Cheung Shum, Jin-Woong Kim, and David A Weitz. "Microfluidic Fabrication of Monodisperse Biocompatible and Biodegradable Polymersomes with Controlled Permeability". English. In: *J. Am. Chem. Soc.* 130.29 (2008), pp. 9543–9549. DOI: 10.1021/ja802157y.

[291] Chun Xia Zhao et al. "Stable Ultrathin-Shell Double Emulsions for Controlled Release". English. In: *Chemphyschem : a European journal of chemical physics and physical chemistry* 17.11 (2016), pp. 1553–1556. DOI: 10.1002/cphc.201600142.

[292] Sandro Matosevic and Brian M Paegel. "Stepwise synthesis of giant unilamellar vesicles on a microfluidic assembly line." English. In: *Journal of the American Chemical Society* 133.9 (2011), pp. 2798–2800. DOI: 10.1021/ja109137s.

[293] Jeanne C Stachowiak et al. "Unilamellar vesicle formation and encapsulation by microfluidic jetting." English. In: *Proc Natl Acad Sci USA* 105.12 (2008), pp. 4697–4702. DOI: 10.1073/pnas.0710875105.

[294] Jan Wilschut et al. "Studies on the mechanism of membrane fusion: kinetics of calcium ion induced fusion of phosphatidylserine vesicles followed by a new assay for mixing of aqueous vesicle contents". English. In: *Biochemistry* 19.26 (1980), pp. 6011–6021. DOI: 10.1021/bi00567a011.

[295] Austin L Bailey and Pieter R Cullis. "Membrane Fusion with Cationic Liposomes: Effects of Target Membrane Lipid Composition". English. In: *Biochemistry* 36.7 (1997), pp. 1628–1634. DOI: 10.1021/bi961173x.

[296] Shinpei Ohki and Klaus Arnold. "A mechanism for ion-induced lipid vesicle fusion". English. In: *Colloids and surfaces. B, Biointerfaces* 18.2 (2000), pp. 83–97. DOI: 10.1016/S0927-7765(99)00131-9.

[297] Christopher K Haluska et al. "Time scales of membrane fusion revealed by direct imaging of vesicle fusion with high temporal resolution". English. In: *Proceedings of the National Academy of Sciences of the United States of America* 103.43 (2006), pp. 15841–15846. DOI: 10.1073/pnas.0602766103.

[298] A Darszon et al. "Reassembly of protein-lipid complexes into large bilayer vesicles: perspectives for membrane reconstitution." English. In: *Proceedings of the National Academy of Sciences of the United States of America* 77.1 (1980), pp. 239–243.

[299] Manuel Criado and Bernhard U Keller. "A membrane fusion strategy for single-channel recordings of membranes usually non-accessible to patch-clamp pipette electrodes". English. In: *FEBS Letters* 224.1 (1987), pp. 172–176. DOI: 10.1016/0014-5793(87)80442-8.

[300] Catherine Berrier et al. "A patch-clamp study of ion channels of inner and outer membranes and of contact zones of E. coli, fused into giant liposomes". English. In: *FEBS Letters* 259.1 (1989), pp. 27–32. DOI: 10.1016/0014-5793(89)81486-3.

[301] J B Manneville et al. "Activity of Transmembrane Proteins Induces Magnification of Shape Fluctuations of Lipid Membranes". English. In: *Physical review letters* 82.21 (1999), pp. 4356–4359. DOI: 10.1103/PhysRevLett.82.4356.

[302] Mahinda Y Abeywardena, Theresa M Allen, and John S Charnock. "Lipid-protein interactions of reconstituted membrane-associated adenosinetriphosphatases. Use of a gel-filtration procedure to examine phospholipid-activity relationships". English. In: *Biochimica et Biophysica Acta (BBA) - Biomembranes* 729.1 (1983), pp. 62–74.

[303] Daniel Levy et al. "A systematic study of liposome and proteoliposome reconstitution involving Bio-Bead-mediated Triton X-100 removal". English. In: *Biochimica et Biophysica Acta (BBA) - Biomembranes* 1025.2 (1990), pp. 179–190. DOI: 10.1016/0005-2736(90)90096-7.

[304] Daniel Levy et al. "Reconstitution of the sarcoplasmic reticulum Ca2+-ATPase: mechanisms of membrane protein insertion into liposomes during reconstitution procedures involving the use of detergents". English. In: *Biochimica et Biophysica Acta (BBA) - Biomembranes* 1107.2 (1992), pp. 283–298. DOI: 10.1016/0005-2736(92)90415-I.

[305] Marie Therese Paternostre, Michel Roux, and Jean-Louis Rigaud. "Mechanisms of membrane protein insertion into liposomes during reconstitution procedures involving the use of detergents. 1. Solubilization of large unilamellar liposomes (prepared by reverse-phase evaporation) by Triton X-100, octyl glucoside, and sodium cholate". English. In: *Biochemistry* 27.8 (1988), pp. 2668–2677. DOI: 10.1021/bi00408a006.

[306] Jean-Louis Rigaud, Marie Therese Paternostre, and Aline Bluzat. "Mechanisms of membrane protein insertion into liposomes during reconstitution procedures involving the use of detergents. 2. Incorporation of the light-driven proton pump bacteriorhodopsin". English. In: *Biochemistry* 27.8 (1988), pp. 2677–2688. DOI: 10.1021/bi00408a007.

[307] Kirsten Bacia et al. "SNAREs prefer liquid-disordered over "raft" (liquid-ordered) domains when reconstituted into giant unilamellar vesicles." English. In: *The Journal of biological chemistry* 279.36 (2004), pp. 37951–37955. DOI: 10.1074/jbc.M407020200.

[308] Sophie Aimon et al. "Functional Reconstitution of a Voltage-Gated Potassium Channel in Giant Unilamellar Vesicles". English. In: *PloS one* 6.10 (2011), e25529. DOI: 10.1371/journal.pone.0025529.

[309] Vanessa Ruta et al. "Functional analysis of an archaebacterial voltage-dependent K+ channel." English. In: *Nature* 422.6928 (2003), pp. 180–185. DOI: 10.1038/nature01473.

[310] Paige M Shaklee et al. "Protein incorporation in giant lipid vesicles under physiological conditions." English. In: *ChemBioChem* 11.2 (2010), pp. 175–179. DOI: 10.1002/cbic.200900669.

[311] Mohamed Kreir et al. "Rapid screening of membrane protein activity: electrophysiological analysis of OmpF reconstituted in proteoliposomes". English. In: *Lab on a chip* 8.4 (2008), pp. 587–595. DOI: 10.1039/B713982A.

[312] Andrew R Battle et al. "Rapid and improved reconstitution of bacterial mechanosensitive ion channel proteins MscS and MscL into liposomes using a modified sucrose method." English. In: *FEBS Letters* 583.2 (2009), pp. 407–412. DOI: 10.1016/j.febslet.2008.12.033.

[313] Nicoletta Kahya et al. "Reconstitution of Membrane Proteins into Giant Unilamellar Vesicles via Peptide-Induced Fusion". In: *Biophysical Journal* 81.3 (2001), pp. 1464–1474. DOI: 10.1016/S0006-3495(01)75801-8.

[314] Armelle Varnier et al. "A Simple Method for the Reconstitution of Membrane Proteins into Giant Unilamellar Vesicles". English. In: *Journal of Membrane Biology* 233.1 (2010), pp. 85–92. DOI: 10.1007/s00232-010-9227-8.

[315] Olivier Biner et al. "Delivery of membrane proteins into small and giant unilamellar vesicles by charge-mediated fusion." English. In: *FEBS Letters* 590.14 (2016), pp. 2051–2062. DOI: 10.1002/1873-3468.12233.

[316] Isaac Newton, Joseph Streater, and Royal Society Great Britain. *Philosophiae naturalis principia mathematica*. Londini: Jussu Societatis Regiae ac typis Iosephi Streater : Prostat apud plures bibliopolas, 1687.

[317] Aleksander Hinek. "Nature and the Multiple Functions of the 67-kD Elastin-/Laminin Binding Protein". English. In: *Cell Communication & Adhesion* (2009). DOI: 10.1080/icac20.v002.i03;wgroup:string:Publication.

[318] Sue Goo Rhee and Hyun Ae Woo. "Multiple Functions of Peroxiredoxins: Peroxidases, Sensors and Regulators of the Intracellular Messenger H2O2, and Protein Chaperones". English. In: *Antioxidants & Redox Signaling* 15.3 (2010), pp. 781–794. DOI: 10.1089/ars.2010.3393.

[319] Donald Voet and Judith G Voet. *Biochemistry*. Hoboken, NJ: John Wiley & Sons, 2011.

[320] Jeremy Mark Berg et al. *Biochemistry*. 8th ed. Basingstoke: W.H. Freeman, 2002. ISBN: 978-1464126109.

[321] Harald Tschesche. *Methods in protein biochemistry*. Berlin: De Gruyter, 2011. ISBN: 978-3-11-025233-0.

[322] Kai Lars Peter. "Isolation und Charakterisierung des Zellrezeptors Integrin αIIbβ3". PhD thesis. Technical University Munich, 1999. ISBN: 3-89675-497-1.

[323] Priya Ramsamooj, George J Doellgast, and Roy R Hantgan. "Inhibition of fibrin(ogen) binding to stimulated platelets by a monoclonal antibody specific for a conformational determinant of GPIIIa". English. In: *Thrombosis Research* 58.6 (1990), pp. 577–592. DOI: 10.1016/0049-3848(90)90304-U.

[324] Pietro Speziale et al. "Purification of human plasma fibronectin using immobilized gelatin and Arg affinity chromatography". English. In: *Nature Protocols* 3.3 (2008), pp. 525–533. DOI: 10.1038/nprot.2008.12.

[325] Eva-Maria Erb and Jürgen Engel. "Reconstitution of Functional Integrin into Phospholipid Vesicles and Planar Lipid Bilayers". In: *Extracellular Matrix Protocols*. New Jersey: Humana Press, 2000, pp. 71–82. ISBN: 1-59259-063-2. DOI: 10.1385/1-59259-063-2:71.

[326] Eva-Maria Erb et al. "Integrin αIIbβ3 Reconstituted into Lipid Bilayers Is Nonclustered in Its Activated State but Clusters after Fibrinogen Binding†". English. In: *Biochemistry* 36.24 (1997), pp. 7395–7402. DOI: 10.1021/bi9702187.

[327] Erik Reimhult, Fredrik Hook, and Bengt Kasemo. "Intact Vesicle Adsorption and Supported Biomembrane Formation from Vesicles in Solution: Influence of Surface Chemistry, Vesicle Size, Temperature, and Osmotic Pressure". English. In: *Langmuir* 19.5 (2003), pp. 1681–1691. DOI: 10.1021/la0263920.

[328] Eike Lüthgens et al. "Adhesion of liposomes: a quartz crystal microbalance study". English. In: *Measurement Science and Technology* 14.11 (2003), p. 1865. DOI: 10.1088/0957-0233/14/11/003.

[329] Thi Huong Vu et al. "Immobilization of intact liposomes on solid surfaces: a quartz crystal microbalance study." English. In: *Journal of Colloid and Interface Science* 336.2 (2009), pp. 902–907. DOI: 10.1016/j.jcis.2009.04.048.

[330] Kristian Dimitrievski and Bengt Kasemo. "Influence of Lipid Vesicle Composition and Surface Charge Density on Vesicle Adsorption Events: A Kinetic Phase Diagram". English. In: *Langmuir* 25.16 (2009), pp. 8865–8869. DOI: 10.1021/la9025409.

[331] A P Serro et al. "Formation of an intact liposome layer adsorbed on oxidized gold confirmed by three complementary techniques: QCM-D, AFM and confocal fluorescence microscopy". English. In: *Surface and Interface Analysis* 44.4 (2011), pp. 426–433. DOI: 10.1002/sia.3820.

[332] Kathryn Melzak, Achilleas Tsortos, and Electra Gizeli. "Chapter 2 - Use of Acoustic Sensors to Probe the Mechanical Properties of Liposomes A2 -". English. In: *Methods in Enzymology*. Vancouver: Academic Press, 2009, pp. 21–41. ISBN: 9780123813794. DOI: 10.1016/S0076-6879(09)65002-3.

[333] C A Keller et al. "Formation of Supported Membranes from Vesicles". English. In: *Physical review letters* 84.23 (2000), pp. 5443–5446. DOI: 10.1103/PhysRevLett.84.5443.

[334] Reimhult, E, Höök, F, and Kasemo, B. "Vesicle adsorption on SiO2 and TiO2: Dependence on vesicle size". English. In: *The Journal of Chemical Physics* 117.16 (2002), pp. 7401–7404. DOI: 10.1063/1.1515320.

[335] E Reimhult, F Höök, and B Kasemo. "Temperature dependence of formation of a supported phospholipid bilayer from vesicles on SiO2". English. In: *Physical review letters* 66.5 (2002), pp. 051905–4. DOI: 10.1103/PhysRevE.66.051905.

[336] Nicole Hain, Marta Gallego, and Ilya Reviakine. "Unraveling Supported Lipid Bilayer Formation Kinetics: Osmotic Effects". English. In: *Langmuir* 29.7 (2013), pp. 2282–2288. DOI: 10.1021/la304197m.

[337] Ralf P Richter and Alain R Brisson. "Following the formation of supported lipid bilayers on mica: a study combining AFM, QCM-D, and ellipsometry." English. In: *Biophysical Journal* 88.5 (2005), pp. 3422–3433. DOI: 10.1529/biophysj.104.053728.

[338] Günter Sauerbrey. "Verwendung von Schwingquarzen zur Wägung dünner Schichten und zur Mikrowägung". German. In: *Zeitschrift für Physik* 155.2 (1959), pp. 206–222. DOI: 10.1007/BF01337937.

[339] M V Voinova et al. "Viscoelastic Acoustic Response of Layered Polymer Films at Fluid-Solid Interfaces: Continuum Mechanics Approach". English. In: *Physica Scripta* 59.5 (1999), pp. 391–396. DOI: 10.1238/Physica.Regular.059a00391.

[340] János Vörös. "The Density and Refractive Index of Adsorbing Protein Layers". English. In: *Biophysical Journal* 87.1 (2004), pp. 553–561. DOI: 10.1529/biophysj.103.030072.

[341] Irving Langmuir. "The adsorption of gases on plane surfaces of glass, mica and platinum". English. In: *J. Am. Chem. Soc.* 40.9 (1918), pp. 1361–1403. DOI: 10.1021/ja02242a004.

[342] Johannes Patrick Frohnmayer et al. "Minimal synthetic cells to study integrin-mediated adhesion." English. In: *Angewandte Chemie (International ed. in English)* 54.42 (2015), pp. 12472–12478. DOI: 10.1002/anie.201503184.

[343] Thomas C Scanlon, Sarah M Dostal, and Karl E Griswold. "A high-throughput screen for antibiotic drug discovery". English. In: *Biotechnology and Bioengineering* 111.2 (2014), pp. 232–243. DOI: 10.1002/bit.25019.

[344] Assaf Rotem et al. "Single-cell ChIP-seq reveals cell subpopulations defined by chromatin state." English. In: *Nature biotechnology* 33.11 (2015), pp. 1165–1172. DOI: 10.1038/nbt.3383.

[345] Jean-Christophe Baret. " Surfactants in droplet-based microfluidics". English. In: *Lab on a chip* 12.3 (2012), pp. 422–433. DOI: 10.1039/C1LC20582J.

[346] Nadya Anscombe. "Direct laser writing". English. In: *Nature Photonics* 4.1 (2010), pp. 22–23. DOI: 10.1038/nphoton.2009.250.

[347] Martin Hermatschweiler. "3D-Druck erobert die Mikroskala". English. In: *Laser Technik Journal* 10.4 (2013), pp. 55–57. DOI: 10.1002/latj.201300001.

[348] Matthias Eibauer et al. "Unraveling the structure of membrane proteins in situ by transfer function corrected cryo-electron tomography". English. In: *Journal of Structural Biology* 180.3 (2012), pp. 488–496. DOI: 10.1016/j.jsb.2012.09.008.

[349] Melanie Bokstad et al. "Reconstructing adhesion structures in tissues by cryo-electron tomography of vitrified frozen sections". English. In: *Journal of Structural Biology* 178.2 (2012), pp. 76–83. DOI: 10.1016/j.jsb.2011.10.013.

[350] J F Nagle and S Tristram-Nagle. "Structure of lipid bilayers." English. In: 1469.3 (2000), pp. 159–195.

[351] Sybille Rex. "Pore formation induced by the peptide melittin in different lipid vesicle membranes". English. In: *Electro-Opto '94* 58.1 (1996), pp. 75–85. DOI: 10.1016/0301-4622(95)00087-9.

[352] Joseph M Johnson et al. "Early Steps of Supported Bilayer Formation Probed by Single Vesicle Fluorescence Assays". English. In: *Biophysical journal* 83.6 (2017), pp. 3371–3379. DOI: 10.1016/S0006-3495(02)75337-X.

[353] Christoph Herold et al. "Efficient Electroformation of Supergiant Unilamellar Vesicles Containing Cationic Lipids on ITO-Coated Electrodes". English. In: *Langmuir* 28.13 (2012), pp. 5518–5521. DOI: 10.1021/la3005807.

[354] Michel Le Bellac, Fabrice Mortessagne, and G George Batrouni. *Equilibrium and Non-Equilibrium Statistical Thermodynamics*. Cambridge: Cambridge University Press, 2009. ISBN: 9780511606571. DOI: 10.1017/CBO9780511606571.

[355] N G van Kampen. *Stochastic Processes in Physics and Chemistry*. English. 3rd ed. North Holland, 2007. ISBN: 978-0444529657.

[356] Michael Cross and Henry Greenside. *Pattern Formation and Dynamics in Nonequilibrium Systems*. Cambridge: Cambridge University Press, 2009. ISBN: 9780511627200. DOI: 10.1017/CBO9780511627200.

[357] Radek Machán and Martin Hof. "Lipid diffusion in planar membranes investigated by fluorescence correlation spectroscopy". English. In: *Biochimica et Biophysica Acta* 1798.7 (2010), pp. 1377–1391. DOI: 10.1016/j.bbamem.2010.02.014.

[358] D Axelrod et al. "Lateral motion of fluorescently labeled acetylcholine receptors in membranes of developing muscle fibers." English. In: *Proceedings of the National Academy of Sciences of the United States of America* 73.12 (1976), pp. 4594–4598.

[359] D M Soumpasis. "Theoretical analysis of fluorescence photobleaching recovery experiments." English. In: *Biophysical Journal* 41.1 (1983), pp. 95–97. DOI: 10.1016/S0006-3495(83)84410-5.

[360] Minchul Kang et al. "A generalization of theory for two-dimensional fluorescence recovery after photobleaching applicable to confocal laser scanning microscopes." English. In: *Biophysical Journal* 97.5 (2009), pp. 1501–1511. DOI: 10.1016/j.bpj.2009.06.017.

[361] Minchul Kang et al. "Simplified Equation to Extract Diffusion Coefficients from Confocal FRAP Data". English. In: *Traffic* 13.12 (2012), pp. 1589–1600. DOI: 10.1111/tra.12008.

[362] Minchul Kang, Manuel Andreani, and Anne K Kenworthy. "Validation of Normalizations, Scaling, and Photofading Corrections for FRAP Data Analysis." English. In: *PloS one* 10.5 (2015), e0127966. DOI: 10.1371/journal.pone.0127966.

[363] Venkatachalam Chokkalingam et al. "An electro-coalescence chip for effective emulsion breaking in droplet microfluidics". English. In: *Lab on a chip* 14.14 (2014), pp. 2398–2402. DOI: 10.1039/C4LC00365A.

[364] Michele Zagnoni, Guillaume Le Lain, and Jonathan M Cooper. "Electrocoalescence Mechanisms of Microdroplets Using Localized Electric Fields in Microfluidic Channels". English. In: *Langmuir* 26.18 (2010), pp. 14443–14449. DOI: 10.1021/la101517t.

[365] Osami Kuroda et al. "Liposome Deformation by Imbalance of pH and Ionic Strength Across the Membrane". English. In: *Trends in Colloid and Interface Science XXIV*. Berlin, Heidelberg: Springer, Berlin, Heidelberg, 2011, pp. 49–53. ISBN: 978-3-642-19038-4. DOI: 10.1007/978-3-642-19038-4_9.

[366] Sayed Ul Alam Shibly et al. "Experimental Estimation of Membrane Tension Induced by Osmotic Pressure". English. In: *Biophysical journal* 111.10 (2016), pp. 2190–2201. DOI: 10.1016/j.bpj.2016.09.043.

[367] James C S Ho et al. "Mixing Water, Transducing Energy, and Shaping Membranes: Autonomously Self-Regulating Giant Vesicles". English. In: *Langmuir* 32.9 (2016), pp. 2151–2163. DOI: 10.1021/acs.langmuir.5b04470.

[368] Xize Niu et al. "Pillar-induced droplet merging in microfluidic circuits." English. In: *Lab on a chip* 8.11 (2008), pp. 1837–1841. DOI: 10.1039/b813325e.

[369] B C Lin and Y C Su. "On-demand liquid-in-liquid droplet metering and fusion utilizing pneumatically actuated membrane valves". In: *Journal of Micromechanics and ...* (2008). DOI: 10.1088/0960-1317/18/11/115005.

[370] Xize Niu et al. "Electro-Coalescence of Digitally Controlled Droplets". English. In: *Analytical Chemistry* 81.17 (2009), pp. 7321–7325. DOI: 10.1021/ac901188n.

[371] Melinda G Simon et al. "A Laplace pressure based microfluidic trap for passive droplet trapping and controlled release." English. In: *Biomicrofluidics* 6.1 (2012), pp. 14110–1411013. DOI: 10.1063/1.3687400.

[372] Hans-Jürgen Butt, Karlheinz Graf, and Michael Kappl. *Physics and Chemistry of Interfaces*. Weinheim, FRG: Wiley-VCH Verlag GmbH & Co. KGaA, 2003. ISBN: 3527404139. DOI: 10.1002/3527602313.

[373] Pierre-Gilles de Gennes, Françoise Brochard-Wyart, and David Quéré. *Capillarity and Wetting Phenomena*. Drops, Bubbles, Pearls, Waves. New York: Springer Science+Business Media, 2010. ISBN: 978-0-387-21656-0.

[374] Sophie Raffy and Justin Teissié. "Control of Lipid Membrane Stability by Cholesterol Content". English. In: *Biophysical journal* 76.4 (1999), pp. 2072–2080. DOI: 10.1016/S0006-3495(99)77363-7.

[375] Frédérick de Meyer and Berend Smit. "Effect of cholesterol on the structure of a phospholipid bilayer". English. In: *Proceedings of the National Academy of Sciences* 106.10 (2009), pp. 3654–3658. DOI: 10.1073/pnas.0809959106.

[376] Iris van Uitert, Séverine Le Gac, and Albert van den Berg. "The influence of different membrane components on the electrical stability of bilayer lipid membranes". English. In: *Biochimica et Biophysica Acta* 1798.1 (2010), pp. 21–31. DOI: 10.1016/j.bbamem.2009.10.003.

[377] James C Weaver et al. "A brief overview of electroporation pulse strength-duration space: A region where additional intracellular effects are expected". English. In: *International Symposium on Bioelectrochemistry and Bioenergetics, 21st BES 2011* 87 IS - (2012), pp. 236–243. DOI: 10.1016/j.bioelechem.2012.02.007.

[378] Pelin Kubra Isgor et al. "Microfluidic droplet content detection using integrated capacitive sensors". English. In: *Sensors and Actuators B: Chemical* 210 (2015), pp. 669–675. DOI: 10.1016/j.snb.2015.01.018.

[379] M Demori et al. "A microfluidic capacitance sensor for fluid discrimination and characterization". English. In: *Eurosensors XXIV, Linz, Austria, 5-8 September 2010* 172.1 (2011), pp. 212–219. DOI: 10.1016/j.sna.2011.07.013.

[380] Yihong Zhan et al. "Electroporation of Cells in Microfluidic Droplets". English. In: *Analytical Chemistry* 81.5 (2009), pp. 2027–2031. DOI: 10.1021/ac9001172.

[381] Jenifer Clausell-Tormos et al. "Droplet-Based Microfluidic Platforms for the Encapsulation and Screening of Mammalian Cells and Multicellular Organisms". English. In: *Chemistry & biology* 15.5 (2008), pp. 427–437. DOI: 10.1016/j.chembiol.2008.04.004.

[382] R Hain et al. "Uptake, integration, expression and genetic transmission of a selectable chimaeric gene by plant protoplasts". English. In: *Molecular and General Genetics MGG* 199.2 (1985), pp. 161–168. DOI: 10.1007/BF00330254.

[383] Irena Barbulovic-Nad, Sam H Au, and Aaron R Wheeler. "A microfluidic platform for complete mammalian cell culture." English. In: *Lab on a chip* 10.12 (2010), pp. 1536–1542. DOI: 10.1039/c002147d.

[384] Kristina Woodruff and Sebastian J Maerkl. "A High-Throughput Microfluidic Platform for Mammalian Cell Transfection and Culturing". English. In: *Scientific reports* 6 (2016), pp. 23937–23941. DOI: 10.1038/srep23937.

[385] Koji Asami, Tetsuya Hanai, and Naokazu Koizumi. "Dielectric properties of yeast cells". English. In: *The Journal of Membrane Biology* 28.1 (1976), pp. 169–180. DOI: 10.1007/BF01869695.

[386] Gerard H Markx and Christopher L Davey. "The dielectric properties of biological cells at radiofrequencies: applications in biotechnology". English. In: *Enzyme and Microbial Technology* 25.3–5 (1999), pp. 161–171. DOI: 10.1016/S0141-0229(99)00008-3.

[387] Emil Prodan, Camelia Prodan, and John H Miller Jr. "The Dielectric Response of Spherical Live Cells in Suspension: An Analytic Solution". English. In: *Biophysical journal* 95.9 (2008), pp. 4174–4182. DOI: 10.1529/biophysj.108.137042.

[388] P Corley and H C Loughrey. "Binding of biotinated-liposomes to streptavidin is influenced by liposome composition". English. In: *Biochimica et Biophysica Acta* 1195.1 (1994), pp. 149–156.

[389] Constantinos M Paleos, Zili Sideratou, and Dimitris Tsiourvas. "Molecular Recognition of Complementary Liposomes in Modeling Cell–Cell Recognition". English. In: *ChemBioChem* 2.5 (2001), pp. 305–310. DOI: 10.1002/1439-7633(20010504)2:5<305::AID-CBIC305>3.0.CO;2-9.

[390] Joshua A Jackman et al. "Vesicle Adhesion and Rupture on Silicon Oxide: Influence of Freeze–Thaw Pretreatment". English. In: *Langmuir* 30.8 (2014), pp. 2152–2160. DOI: 10.1021/la404582n.

[391] Jacques Blümmel et al. "Protein repellent properties of covalently attached PEG coatings on nanostructured SiO2-based interfaces". English. In: *Biomaterials* 28.32 (2007), pp. 4739–4747. DOI: 10.1016/j.biomaterials.2007.07.038.

[392] Matthew A Cooper and Victoria T Singleton. "A survey of the 2001 to 2005 quartz crystal microbalance biosensor literature: applications of acoustic physics to the analysis of biomolecular interactions". English. In: *Journal of Molecular Recognition* 20.3 (2007), pp. 154–184. DOI: 10.1002/jmr.826.

[393] Edurne Tellechea et al. "Model-Independent Analysis of QCM Data on Colloidal Particle Adsorption". English. In: *Langmuir* 25.9 (2009), pp. 5177–5184. DOI: 10.1021/la803912p.

[394] Stefanie Goennenwein et al. "Functional Incorporation of Integrins into Solid Supported Membranes on Ultrathin Films of Cellulose: Impact on Adhesion". English. In: *Biophysical journal* 85.1 (2003), pp. 646–655. DOI: 10.1016/S0006-3495(03)74508-1.

[395] Motomu Tanaka and Erich Sackmann. "Polymer-supported membranes as models of the cell surface". English. In: *Nature* 437.7059 (2005), pp. 656–663. DOI: 10.1038/nature04164.

[396] Patrick Müller et al. "Morphogen transport". English. In: *Development* 140.8 (2013), pp. 1621–1638. DOI: 10.1242/dev.083519.

[397] Ana-Sunčana Smith et al. "Force-induced growth of adhesion domains is controlled by receptor mobility." English. In: *Proc Natl Acad Sci USA* 105.19 (2008), pp. 6906–6911. DOI: 10.1073/pnas.0801706105.

[398] Kenneth A Johnson and Roger S Goody. "The Original Michaelis Constant: Translation of the 1913 Michaelis-Menten Paper". English. In: *Biochemistry* 50.39 (2011), pp. 8264–8269. DOI: 10.1021/bi201284u.

[399] Seiichi Morita, Miho Nukui, and Ryoichi Kuboi. "Immobilization of liposomes onto quartz crystal microbalance to detect interaction between liposomes and proteins". English. In: *Journal of Colloid and Interface Science* 298.2 (2006), pp. 672–678. DOI: 10.1016/j.jcis.2005.12.043.

[400] Jack W Szostak, David P Bartel, and P Luigi Luisi. "Synthesizing life". English. In: *Nature* 409.6818 (2001), pp. 387–390. DOI: 10.1038/35053176.

[401] Dan S Tawfik and Andrew D Griffiths. "Man-made cell-like compartments for molecular evolution". English. In: 16.7 (1998), pp. 652–656. DOI: 10.1038/nbt0798-652.

[402] Gábor Csúcs and Jeremy J Ramsden. "Interaction of phospholipid vesicles with smooth metal-oxide surfaces". English. In: *Biochimica et Biophysica Acta* 1369.1 (1998), pp. 61–70. DOI: 10.1016/S0005-2736(97)00209-5.

[403] Bastien Seantier and Bengt Kasemo. "Influence of Mono- And Divalent Ions on the Formation of Supported Phospholipid Bilayers via Vesicle Adsorption". English. In: *Langmuir* 25.10 (2009), pp. 5767–5772. DOI: 10.1021/la804172f.

[404] Tripta Bhatia et al. "Fluid domain patterns in free-standing membranes captured on a solid support". English. In: *Biochimica et Biophysica Acta (BBA) - Biomembranes* 1838.10 (2014), pp. 2503–2510. DOI: 10.1016/j.bbamem.2014.05.016.

[405] John T Edward. "Molecular volumes and the Stokes-Einstein equation". English. In: *J. Chem. Educ.* 47.4 (1970), p. 261. DOI: 10.1021/ed047p261.

[406] Sivaramakrishnan Ramadurai et al. "Lateral Diffusion of Membrane Proteins". English. In: *J. Am. Chem. Soc.* 131.35 (2009), pp. 12650–12656. DOI: 10.1021/ja902853g.

[407] Kurt Kremer and Gary S Grest. "Dynamics of entangled linear polymer melts: A molecular-dynamics simulation". English. In: *The Journal of Chemical Physics* 92.8 (1990), pp. 5057–5086. DOI: 10.1063/1.458541.

[408] Timothy P Lodge. "Reconciliation of the Molecular Weight Dependence of Diffusion and Viscosity in Entangled Polymers". English. In: *Physical review letters* 83.16 (1999), pp. 3218–3221. DOI: 10.1103/PhysRevLett.83.3218.

[409] S J Singer and Garth L Nicolson. "The Fluid Mosaic Model of the Structure of Cell Membranes". English. In: *Science (New York, N.Y.)* 175.4023 (1972), pp. 720–731. DOI: 10.1126/science.175.4023.720.

[410] William S Trimble and Sergio Grinstein. "Barriers to the free diffusion of proteins and lipids in the plasma membrane". English. In: *The Journal of cell biology* 208.3 (2015), pp. 259–271. DOI: 10.1083/jcb.201410071.

[411] Fabian Itel et al. "Molecular Organization and Dynamics in Polymersome Membranes: A Lateral Diffusion Study". English. In: *Macromolecules* 47.21 (2014), pp. 7588–7596. DOI: 10.1021/ma5015403.

[412] Rainer A Böckmann et al. "Effect of Sodium Chloride on a Lipid Bilayer". English. In: *Biophysical journal* 85.3 (2003), pp. 1647–1655. DOI: 10.1016/S0006-3495(03)74594-9.

[413] Rainer A Böckmann and Helmut Grubmüller. "Multistep binding of divalent cations to phospholipid bilayers: a molecular dynamics study." English. In: *Angewandte Chemie (International ed. in English)* 43.8 (2004), pp. 1021–1024. DOI: 10.1002/anie.200352784.

[414] Cornelia G Sinn, Markus Antonietti, and Rumiana Dimova. "Binding of calcium to phosphatidylcholine–phosphatidylserine membranes". English. In: *A Collection of Papers in Honor of Professor Ivan B. Ivanov (Laboratory of Chemical Physics and Engineering, University of Sofia) Celebrating his Contributions to Colloid and Surface Science on the Occasion of his 70th Birthday* 282–283 IS - (2006), pp. 410–419. DOI: 10.1016/j.colsurfa.2005.10.014.

[415] Sylvio May, Daniel Harries, and Avinoam Ben-Shaul. "Lipid Demixing and Protein-Protein Interactions in the Adsorption of Charged Proteins on Mixed Membranes". English. In: *Biophysical journal* 79.4 (2000), pp. 1747–1760. DOI: 10.1016/S0006-3495(00)76427-7.

[416] Joshua B Edel et al. "High Spatial Resolution Observation of Single-Molecule Dynamics in Living Cell Membranes". English. In: *Biophysical journal* 88.6 (2005), pp. L43–L45. DOI: 10.1529/biophysj.105.061937.

[417] Junfeng Zhang. "Lattice Boltzmann method for microfluidics: models and applications". English. In: *Microfluidics and Nanofluidics* 10.1 (2011), pp. 1–28. DOI: 10.1007/s10404-010-0624-1.

[418] David Erickson. "Towards numerical prototyping of labs-on-chip: modeling for integrated microfluidic devices". English. In: *Microfluidics and Nanofluidics* 1.4 (2005), pp. 301–318. DOI: 10.1007/s10404-005-0041-z.

[419] Rania Leventis et al. "Divalent Cation Induced Fusion and Lipid Lateral Segregation in Phosphatidylcholine-Phosphatidic Acid Vesicles". English. In: *Biochemistry* 25.22 (1986), pp. 6978–6987. DOI: 10.1021/bi00370a600.

[420] Naoto Oku et al. "Low pH induced membrane fusion of lipid vesicles containing proton-sensitive polymer". English. In: *Biochemistry* 26.25 (1987), pp. 8145–8150. DOI: 10.1021/bi00399a019.

[421] Yolanda Schaerli et al. "Continuous-Flow Polymerase Chain Reaction of Single-Copy DNA in Microfluidic Microdroplets". English. In: *Analytical Chemistry* 81.1 (2009), pp. 302–306. DOI: 10.1021/ac802038c.

[422] A Huebner et al. "Quantitative detection of protein expression in single cells using droplet microfluidics". English. In: *Chemical Communications* 0.12 (2007), pp. 1218–1220. DOI: 10.1039/B618570C.

[423] Erich Sackmann and Motomu Tanaka. "Supported membranes on soft polymer cushions: fabrication, characterization and applications". English. In: *Trends in biotechnology* 18.2 (2000), pp. 58–64. DOI: 10.1016/S0167-7799(99)01412-2.

[424] Joachim Rädler and Erich Sackmann. "Imaging optical thicknesses and separation distances of phospholipid vesicles at solid surfaces". English. In: *Journal de Physique II* 3.5 (1993), pp. 727–748. DOI: 10.1051/jp2:1993163.

[425] Enas Abu Shah and Kinneret Keren. "Symmetry breaking in reconstituted actin cortices." English. In: *eLife* 3 (2014), e01433. DOI: 10.7554/eLife.01433.

[426] Makito Miyazaki et al. "Cell-sized spherical confinement induces the spontaneous formation of contractile actomyosin rings in vitro". In: *Nature Cell Biology* 17.4 (2015), pp. 480–489. DOI: 10.1038/ncb3142.

[427] S Kaufmann et al. "Talin binds to actin and promotes filament nucleation". English. In: *FEBS Letters* 284.2 (1991), pp. 187–191. DOI: 10.1016/0014-5793(91)80681-R.

[428] S Kaufmann et al. "Talin anchors and nucleates actin filaments at lipid membranes A direct demonstration". English. In: *FEBS Letters* 314.2 (1992), pp. 203–205. DOI: 10.1016/0014-5793(92)80975-M.

[429] W H Goldmann, J Käs, and G Isenberg. "Talin decreases the bending elasticity of actin filaments". English. In: *Biochemical Society Transactions* 22.1 (1994), 46S–46S. DOI: 10.1042/bst022046s.

[430] D R Critchley and A R Gingras. "Talin at a glance". English. In: *Journal of cell science* 121.9 (2008), pp. 1345–1347. DOI: 10.1242/jcs.018085.

[431] Dorothea Brüggemann, Johannes Patrick Frohnmayer, and Joachim P Spatz. "Model systems for studying cell adhesion and biomimetic actin networks." English. In: *Beilstein journal of nanotechnology* 5.1 (2014), pp. 1193–1202. DOI: 10.3762/bjnano.5.131.

[432] Sanford J Shattil, Chungho Kim, and Mark H Ginsberg. "The final steps of integrin activation: the end game". English. In: *Nature reviews. Molecular cell biology* 11.4 (2010), pp. 288–300. DOI: 10.1038/nrm2871.

[433] Jia-huai Wang. "Pull and push: talin activation for integrin signaling." English. In: *Cell research* 22.11 (2012), pp. 1512–1514. DOI: 10.1038/cr.2012.103.

[434] Jacob R Haling et al. "Talin-dependent integrin activation is required for fibrin clot retraction by platelets". English. In: *Blood* 117.5 (2011), pp. 1719–1722. DOI: 10.1182/blood-2010-09-305433.

[435] C Brakebusch. "NEW EMBO MEMBER'S REVIEW: The integrin-actin connection, an eternal love affair". In: *The EMBO Journal* 22.10 (2003), pp. 2324–2333. DOI: 10.1093/emboj/cdg245.

[436] N C Collier and K Wang. "Purification and properties of human platelet P235. A high molecular weight protein substrate of endogenous calcium-activated protease(s)." English. In: *The Journal of biological chemistry* 257.12 (1982), pp. 6937–6943.

[437] H Heise et al. "Human platelet P-235, a talin-like actin binding protein, binds selectively to mixed lipid bilayers". English. In: *Biochimica et Biophysica Acta* 1061.2 (1991), pp. 121–131. DOI: 10.1016/0005-2736(91)90276-E.

[438] Jun Yang et al. "Conformational activation of talin by RIAM triggers integrin-mediated cell adhesion." English. In: *Nature communications* 5 (2014), p. 5880. DOI: 10.1038/ncomms6880.

[439] Xin Ye, Mark A McLean, and Stephen G Sligar. "Phosphatidylinositol 4,5-Bisphosphate Modulates the Affinity of Talin-1 for Phospholipid Bilayers and Activates Its Autoinhibited Form". English. In: *Biochemistry* 55.36 (2016), pp. 5038–5048. DOI: 10.1021/acs.biochem.6b00497.

[440] Ykelien L Boersma and Andreas Plückthun. "DARPins and other repeat protein scaffolds: advances in engineering and applications". English. In: *Current Opinion in Biotechnology* 22.6 (2011), pp. 849–857. DOI: 10.1016/j.copbio.2011.06.004.

[441] Michael T Stumpp, H Kaspar Binz, and Patrick Amstutz. "DARPins: A new generation of protein therapeutics". English. In: *Drug Discovery Today* 13.15–16 (2008), pp. 695–701. DOI: 10.1016/j.drudis.2008.04.013.

[442] Michael T Stumpp and Patrick Amstutz. "DARPins: a true alternative to antibodies". In: *Current opinion in drug discovery & development* 10.2 (2007), pp. 153–159.

[443] Andreas Plückthun. "Designed ankyrin repeat proteins (DARPins): binding proteins for research, diagnostics, and therapy." English. In: *Annual review of pharmacology and toxicology* 55.1 (2015), pp. 489–511. DOI: 10.1146/annurev-pharmtox-010611-134654.

[444] E Alfinito and L Reggiani. "Modeling Current-Voltage Charateristics of Proteorhodopsin and Bacteriorhodopsin: Towards an Optoelectronics Based on Proteins". English. In: *IEEE transactions on nanobioscience* 15.7 (2016), pp. 775–780. DOI: 10.1109/TNB.2016.2617678.

[445] Samaneh Mashaghi and Antoine M van Oijen. "External control of reactions in microdroplets". English. In: *Scientific reports* 5 (2015), pp. 11837–11837. DOI: 10.1038/srep11837.

[446] Vittorio Cristini and Yung-Chieh Tan. "Theory and numerical simulation of droplet dynamics in complex flows–a review." English. In: *Lab on a chip* 4.4 (2004), pp. 257–264. DOI: 10.1039/b403226h.

[447] Shazia Bashir, Julia M Rees, and William B Zimmerman. "Simulations of microfluidic droplet formation using the two-phase level set method". English. In: *Chemical Engineering Science* 66.20 (2011), pp. 4733–4741. DOI: 10.1016/j.ces.2011.06.034.

[448] Martin Wörner. "Numerical modeling of multiphase flows in microfluidics and micro process engineering: a review of methods and applications". English. In: *Microfluidics and Nanofluidics* 12.6 (2012), pp. 841–886. DOI: 10.1007/s10404-012-0940-8.

[449] Krishnendu Chakrabarty and Jun Zeng. *Design automation methods and tools for microfluidics-based biochips*. Ed. by Krishnendu Chakrabarty and Jun Zeng. Springer, 2006. ISBN: 978-1-4020-5122-7.

[450] Adrian Neild, Stefano Oberti, and Jürg Dual. "Design, modeling and characterization of microfluidic devices for ultrasonic manipulation". English. In: *Sensors and Actuators B: Chemical* 121.2 (2007), pp. 452–461. DOI: 10.1016/j.snb.2006.04.065.

Supplementary Materials

I. Matlab Code

I.1. FRAP Recovery Evaluation Script

```
%%%%%%%%%%%%%%%%%%%%%%%%%%%%%%%%%%%%%%%%%%%%%%%
%% FRAP evaluation
% version 5 20161010
% Matlab-script for the evaluation of FRAP data. This script is designed to to evaluate '.csv' files exported
% using the Leica Microscopy Software. For correct evaluation the files should contain
% three columns, first the intensity values form the bleaching spot, second a reference spot
% and a thrid a larger area containing the bleaching spot. The data sets can differ in time steps and total
% number of datapoints. The script will output the computed diffusion coefficient for each dataset as well
% the average diffusion coefficient and it's corresponding standard error. Optionally the script will draw
% graphs of each evaluation step.

%%%%%%%%%%%%%%%%%%%%%%%%%%%%%%%%%%%%%%%%%%%%%%%
%% A set of parameters that control the evaluation of the results
% Plotting switch. If value is true all intermediary results are plotted into
% pdf files. This slows down script drastically
plotall = true;
% Radius of the bleached spot in µm. Important for the evaluation of the
% diffusion coefficient
w = 2.5;
% For good results its important, to correct the collected data points for background.
bg=0;
% The calculation is on standard done according to protocols published by Axelrod et al. (1976) and Soumpasis (1983).
% Alternatively a model proposed by Kang et al. (2012) can be used, correcting for diffusion during the bleaching.
% To derive the prefactor the script 'Frap radius evaluation.m' can be used.
pf=0.32;

%%%%%%%%%%%%%%%%%%%%%%%%%%%%%%%%%%%%%%%%%%%%%%%
%% Main body of code
%%%%%%%%%%%%%%%%%%%%%%%%%%%%%%%%%%%%%%%%%%%%%%%

%%%%%%%%%%%%%%%%%%%%%%%%%%%%%%%%%%%%%%%%%%%%%%%
%% Importing the data and removing rows with empty cells
files = dir('*.csv');
for i=1:length(files)
    data=importdata(files(i).name);
    J=all(~isnan(data.data),2);
    A{i}=data.data(J,:);
    clear data J
end

%%%%%%%%%%%%%%%%%%%%%%%%%%%%%%%%%%%%%%%%%%%%%%%
%% Plotting of raw data
if plotall == true
for i=1:length(files)
   figure('vis', 'off');
    plot1=plot(A{i}(:,1),A{i}(:,2:4),'LineStyle','none');
    set(plot1(1),'Marker','o','DisplayName','ROI1');
    set(plot1(2),'Marker','.','DisplayName','ROI2');
    set(plot1(3),'Marker','x','DisplayName','ROI3');
    xlabel('time [s]');
    ylabel('intensity');
    title(files(i).name)
    print(sprintf('raw%02d',i) ,'-dpdf')
end
end

%%%%%%%%%%%%%%%%%%%%%%%%%%%%%%%%%%%%%%%%%%%%%%%
%% Data correction and normalization
% Each dataset is corrected for background, normalized by the prebleaching value
% and corrected for photofading in this step
for i=1:length(files)
    B{i}=zeros(length(A{i}),2);
```

```
    %% Mean intensity of focus point before bleach
    Ipre=mean(A{i}(1:10,2));
    %% Mean intensity of the total cell before bleach
    Tpre=mean(A{i}(1:10,4));
    %% Calculating normalized values (without background substration)
    B{i}(:,1)=A{i}(:,1);
    B{i}(:,2)=(A{i}(:,2)-bg)./(Ipre-bg) * (Tpre-bg) ./ (A{i}(:,4)-bg);
end

clear i j A Ipre Tpre bg

%%%%%%%%%%%%%%%%%%%%%%%%%%%%%%%%%%%%%%%%%%%%%%%
%% Plotting normalized graphs
if plotall == true
for i=1:length(files)
   figure('vis', 'off');
    plot(B{i}(:,1),B{i}(:,2),'Marker','o','LineStyle','none','DisplayName','B(:,1.6)');
    xlabel('time [s]');
    ylabel('intensity');
    title(files(i).name)
    print(sprintf('normalized%02d',i) ,'-dpdf')
end
clear i
end

%%%%%%%%%%%%%%%%%%%%%%%%%%%%%%%%%%%%%%%%%%%%%%%
%% Initialization of the fitting model
% As fitting function an exponential recovery curve is chosen. A robust, non-linear least square has proven to
% show good results. The fit outputs information about the fit quality to allow debugging.
    fo = fitoptions('method','NonlinearLeastSquares','Lower',[0 0],'Upper',[1 Inf], 'Display', 'iter', 'Robust','Bisquare');
    st = [1 1]; %starting point
    set(fo,'Startpoint',st);
    ft = fittype('a*(1-exp(-t*b))',...
               'dependent',{'y'},'independent',{'t'},...
               'coefficients',{'a','b'});

%%%%%%%%%%%%%%%%%%%%%%%%%%%%%%%%%%%%%%%%%%%%%%%
%% The normalized data is fitted to the previously initialized fitting model. The results are directly plotted.
C=zeros(2,length(files));
for i=1:length(files)
    [cf,gof] = fit(B{i}(11:length(B{i}),1)-B{i}(11,1),B{i}(11:length(B{i}),2)-B{i}(11,2),ft,fo);
    C(:,i) =  transpose(coeffvalues(cf));
    if plotall == true
        figure('vis', 'off')
        hold on
        ylim([-0.2 0.8])
        plot(B{i}(:,1)-B{i}(11,1),B{i}(:,2)-B{i}(11,2),'Marker','o','LineStyle','none','DisplayName','B(:,1.6)');
        plot(cf);
        xlabel('time [sec]','FontSize',20)
        ylabel('normalized fluorescence Intensity','FontSize',20)
        title(files(i).name)
        print(sprintf('fitted%02d',i) ,'-dpdf')
    end
    clear cf gof
end

clear i st fo ft plotall B

%%%%%%%%%%%%%%%%%%%%%%%%%%%%%%%%%%%%%%%%%%%%%%%
%% Calculation of diffusion coefficients
% The values are computed from the fitting results and the size of the bleaching spot. They are
% first calculated for each dataset seperately and then the average and standard error is computed.
% The calculation is on standard done according to protocols published by Axelrod et al. (1976) and Soumpasis (1983).
% Alternatively a model proposed by Kang et al. (2012) can be used, correcting for diffusion during the bleaching
tauh=-log(0.5)./C(2,:);
C(3,:) = pf*w^2./tauh;
D = [mean(C(3,:)), std(C(3,:))/sqrt(length(C(3,:)))];

%%%%%%%%%%%%%%%%%%%%%%%%%%%%%%%%%%%%%%%%%%%%%%%
%% Saving the results
save coefficients.txt C -ASCII
fid = fopen('diffusion_coefficient.txt', 'w');
fprintf(fid, 'diffusion_coefficient std_error [µM^2/s]\n');
fprintf(fid, '%f    %f',D);
close

clear files w fid tauh
```

I.2. FRAP Bleaching Spot Evaluation Script

```
%%%%%%%%%%%%%%%%%%%%%%%%%%%%%%%%%%%%%%%%%%%%%%%%
%% FRAP radius evaluation
% version 2 20161010
% Script fitting the effective radius of a bleaching spots from FRAP data. Prior to running this script, extract
% fluorescence intensity line profiles cutting the center of the bleaching spot from the first post bleach image
% and save them as '.txt' files, e.g. using ImageJ/Fiji. The Script will evaluate all '.txt' file in the active directory.
% The output of this script is the prefactor 'pf' needed to calculate the diffusion coefficient D=pf*r_n^2/tau_0.5
% according to Kang et al. (2012).

%%%%%%%%%%%%%%%%%%%%%%%%%%%%%%%%%%%%%%%%%%%%%%%%
%% A set of parameters that control the evaluation of the results
% Plotting switch. If value is set to true (plotall==true) all intermediary results are plotted into
% pdf files. Slows down script drastically.
plotall = true;
% Radius of the bleached spot in µm. Important for the evaluation of the
% diffusion coefficient.
w = 2.5;

%%%%%%%%%%%%%%%%%%%%%%%%%%%%%%%%%%%%%%%%%%%%%%%%
%% Main body of code
%%%%%%%%%%%%%%%%%%%%%%%%%%%%%%%%%%%%%%%%%%%%%%%%

%%%%%%%%%%%%%%%%%%%%%%%%%%%%%%%%%%%%%%%%%%%%%%%%
%% Importing the data
files = dir('*.txt');
for i=1:length(files)
    data=importdata(files(i).name);
    A{i}=data.data;
    clear data
end

%%%%%%%%%%%%%%%%%%%%%%%%%%%%%%%%%%%%%%%%%%%%%%%%
%% Initialization of the fitting model
% As fitting function a Gaussian distribution is chosen. A robust, non-linear least square has proven to
% show good results. The fit outputs information about the fit quality to allow debugging.
    fo = fitoptions('method','NonlinearLeastSquares','Lower',[0 0 w 0],'Upper',[Inf Inf 100 Inf], 'Display', 'iter',
     ↪    'Robust','Bisquare');
    st = [20 15 5 6]; %starting point
    set(fo,'Startpoint',st);
    ft = fittype('a*(1-b*exp((-2* (x-d)^2)/c^2))',...
              'dependent',{'y'},'independent',{'x'},...
              'coefficients',{'a','b','c', 'd'});
B=zeros(4,length(files));

%%%%%%%%%%%%%%%%%%%%%%%%%%%%%%%%%%%%%%%%%%%%%%%%
%% The data is fitted to the previously initialized fitting model. The results are directly plotted.
for   i=1:length(files)
      [cf,gof] = fit(A{i}(:,1),A{i}(:,2),ft,fo);
      B(:,i) =  transpose(coeffvalues(cf));
      if plotall == true
          figure('vis', 'off')
          hold on
          plot(A{i}(:,1),A{i}(:,2),'Marker','o','LineStyle','none','DisplayName','B(:,1.6)');
          plot(cf);
          xlabel('position [µm]','FontSize',20)
          ylabel('fluorescence Intensity','FontSize',20)
          title(files(i).name)
          print(sprintf('fitted%02d',i) ,'-dpdf')
          clear cf gof
      end
end

%%%%%%%%%%%%%%%%%%%%%%%%%%%%%%%%%%%%%%%%%%%%%%%%
%% Outputof the results the results
C = (1+(B(3,:)./w)^2)/8;
D = [mean(C), std(B(3,:))*mean(B(3,:))/(w^2*4)];

%%%%%%%%%%%%%%%%%%%%%%%%%%%%%%%%%%%%%%%%%%%%%%%%
%% Saving the results
save prefactor.txt C -ASCII
fid = fopen('prefactor.txt', 'w');
fprintf(fid, 'prefactor std_deviation \n');
fprintf(fid, '%f    %f',D);
close

clear i st fo ft plotall files w
```

I.3. Intensity Profile Evaluation Script

```
%%%%%%%%%%%%%%%%%%%%%%%%%%%%%%%%%%%%%%%%%%%%%%%
%% Droplet intensity profile evaluation script
% version 4 20161205
% As there is refraction and defraction on the water oil interface of the droplets,
% it is difficult to compare the fluorescence intensity of GUV and dsGUV. This script
% tries to solve this problem by fitting and integrating the fluorescence
% intensity profile. This script is designed to to evaluate '.csv' files exported
% using the Leica Microscopy Software

%%%%%%%%%%%%%%%%%%%%%%%%%%%%%%%%%%%%%%%%%%%%%%%
%% A set of parameters that control the evaluation of the results
% Plotting switch. If value is true all intermediary results are plotted into
% pdf files. This slows down script drastically
plotall = true;


%%%%%%%%%%%%%%%%%%%%%%%%%%%%%%%%%%%%%%%%%%%%%%%
%% Main body of code
%%%%%%%%%%%%%%%%%%%%%%%%%%%%%%%%%%%%%%%%%%%%%%%

%%%%%%%%%%%%%%%%%%%%%%%%%%%%%%%%%%%%%%%%%%%%%%%
%% Importing the data and removing rows with empty cells
files = dir('*.csv');
for i=1:length(files)
    data=importdata(files(i).name);
    J=all(~isnan(data.data),2);
    A{i}=data.data(J,:);
    clear data J
end

%%%%%%%%%%%%%%%%%%%%%%%%%%%%%%%%%%%%%%%%%%%%%%%
%% Plotting of raw data
if plotall == true
  for i=1:length(files)
    figure('vis', 'off');
    hold on
    plot1=plot(A{i}(:,3),A{i}(:,4));
    set(plot1(1),'Marker','o','DisplayName','ROI1');
    xlabel('position [µm]');
    ylabel('intensity');
    title(files(i).name,'FontSize',24)
    print(sprintf('raw%02d',i) ,'-dpdf')
   end
end

%%%%%%%%%%%%%%%%%%%%%%%%%%%%%%%%%%%%%%%%%%%%%%%
%% Fitting of Gaussian functions to the peaks
% The data is split in two arrays around each peak and fitted with Gaussian functions
B=zeros(length(files)*2,2);

%%%%%%%%%%%%%%%%%%%%%%%%%%%%%%%%%%%%%%%%%%%%%%%
%% Finding good starting points
% Searches for the position and values of two intensity peaks of a droplet crossection.
for i=1:length(files)
    j=round(length(A{i})/2);
    [m1 p1]=max(A{i}(1:j,4));
    [m2 p2]=max(A{i}(j:length(A{i}),4));
    B(i*2-1,1)=m1;
    B(i*2,1)=m2;
%%%%%%%%%%%%%%%%%%%%%%%%%%%%%%%%%%%%%%%%%%%%%%%
%% Fitting a Gaussian function to the data via a nonlinear least square to the 'left' peak
% The fit uses the previously derived values as starting points
    fo = fitoptions('method','NonlinearLeastSquares','Lower',[0 0 0 2],'Upper',[100 A{i}(j,3) 1e-4 3], 'Robust','Bisquare');
    st = [m1 A{i}(p1,3) 1e-6 2.2]; %starting point
    set(fo,'Startpoint',st);
    ft = fittype('a1*exp(-((x-b1)/c1)^2) +c3',...
            'dependent',{'y'},'independent',{'x'},'coefficients',{'a1','b1','c1','c3'});
    x=A{i}(1:j,3);
    y=A{i}(1:j,4);
    f1=fit(x,y,ft,fo);
    c=coeffvalues(f1);
    B(i*2-1,2)=c(1)*c(3)*pi^.5;
    clear c
%%%%%%%%%%%%%%%%%%%%%%%%%%%%%%%%%%%%%%%%%%%%%%%
%% Fitting a Gaussian function to the data via a nonlinear least square to the 'right' peak
% The fit uses the previously derived values as starting points
    fo = fitoptions('method','NonlinearLeastSquares','Lower',[0 A{i}(j,3) 1e-10 2],'Upper',[100 A{i}(length(A{i}),3) 1e-4 3],
     ↪    'Robust','Bisquare');
    st = [m2 A{i}(p2+j,3) 1e-6 2.2];
    set(fo,'Startpoint',st);
    x=A{i}(j:length(A{i}),3);
```

```
    y=A{i}(j:length(A{i}),4);
    f2=fit(x,y,ft,fo);
    c=coeffvalues(f2);
    B(i*2,2)=c(1)*c(3)*pi^.5;
    clear c
%%%%%%%%%%%%%%%%%%%%%%%%%%%%%%%%%%%%%%%%%%%%%%%
%% Plotting of data with fitting results
        if plotall == true
          figure('vis', 'off');
          hold on
          plot(A{i}(:,3),A{i}(:,4));
          plot(f1);
          plot(f2);
          xlabel('position [µm]','FontSize',20)
          ylabel('Intensity','FontSize',20)
          title(files(i).name,'FontSize',24)
          print(sprintf('fitted%02d',i) ,'-dpdf')
    end
    clear x y j m1 m2 p1 p2 fo ft f1 f2 i st c
end
%%%%%%%%%%%%%%%%%%%%%%%%%%%%%%%%%%%%%%%%%%%%%%%
%% Calculation of maximal intesity values and integrated intensity
% The columns contain in order: the mean maximal values, the corresponding standard error,
% the integrated intensity, and the corresponding standard error.
C(1,1)=mean(B(:,1));
C(1,2)=std(B(:,1))%/sqrt(length(files));
C(1,3)=mean(B(:,2))*10^6;
C(1,4)=std(B(:,2))*10^6%/sqrt(length(files));

%%%%%%%%%%%%%%%%%%%%%%%%%%%%%%%%%%%%%%%%%%%%%%%
%% Saving the results
fid = fopen('intensitiy_values.txt', 'w');
fprintf(fid, 'max intensity [au] std error [au] integrated intensity [au*µm]  std error [au*µm]\n %f  %f  %f  %f',C);
close

clear plotall files ans plot1 fid
```

II. Gnuplot Scripts

II.1. Basic Frequency, and Dissipation against Time Plotting

```
# Gnuplot Script for plotting QCM-D data

#Setting up the export document (size labels, etc.)
reset
set terminal pdfcairo enhanced font 'Helvetica,10'
set output 'name_of_output_file.pdf'
set size ratio 0.618
set xlabel 'time [hours]'
set ylabel  '{/Symbol D} frequency_7/N [Hz]'
set y2label '{/Symbol D} dissipation_7 [10^{-6}]'
set y2tics
set key out vert right top

# setting up different line styles
set style line 1 lc rgb '#800000' lt 1 lw 1 pt 2 ps 0.5
set style line 2 lc rgb 'red' lt 1 lw 1 pt 5 ps 0.5
set style line 3 lc rgb '#FF8C00' lt 1 lw 1 pt 7 ps 0.5
set style line 4 lc rgb '#0000CD' lt 1 lw 1 pt 9 ps 0.5
set style line 5 lc rgb '#1E90FF' lt 1 lw 1 pt 11 ps 0.5
set style line 6 lc rgb '#32CD32' lt 1 lw 1 pt 13 ps 0.5

# list of variables used in the plots to denoting timepoints
# when a new solution reached the measurement chamber
vl1=0.667
vl2=3.1667
vl3=3.667
vl4=7.667
vl5=11.667
# variable for time shift
timeshift=3.5
# if using a timeshift, offset values for different samples
of1=103
of2=113.1
of3=100

# vertical lines (arrow) marking the timepoints when new solutions reached the analysis chamber
# arrow one defined twice as a workaround for a bug
set arrow 1 from 0,0 to 0,1 nohead
set arrow 1 from vl1, graph 0 to vl1, graph 1 nohead
set arrow 2 from vl2, graph 0 to vl2, graph 1 nohead
set arrow 3 from vl3, graph 0 to vl3, graph 1 nohead
set arrow 4 from vl4, graph 0 to vl4, graph 1 nohead
set arrow 5 from vl5, graph 0 to vl5, graph 1 nohead
unset arrow 1

# range, statistics and interval of symbols
set xrange [timeshift:12.66]
stats 'S1.txt' u ($1/3600):7 name "A"
interval=floor(A_records/10)

set title 'title_of_current_experiment'
plot         'S1.txt' u ($1/3600):($7-timeshift) axes x1y2 t '{/Symbol D}D S1_sample name' w lp ls 1 pi interval,\
             'S2.txt' u ($1/3600):($7-timeshift) axes x1y2 t '{/Symbol D}D S2_sample name' w lp ls 2 pi interval,\
             'S3.txt' u ($1/3600):($7-timeshift) axes x1y2 t '{/Symbol D}D S3_sample name' w lp ls 3 pi interval,\
             'S1.txt' u ($1/3600):($6+of1) axes x1y1 t '{/Symbol D}F S2_sample name' w lp ls 4 pi interval,\
             'S2.txt' u ($1/3600):($6+of2) axes x1y1 t '{/Symbol D}F S2_sample name' w lp ls 5 pi interval,\
             'S3.txt' u ($1/3600):($6+of3) axes x1y1 t '{/Symbol D}F S3_sample name' w lp ls 6 pi interval
```

II.2. Script for Plotting Disipation against Frequency

```
# Gnuplot Script for plotting QCM-D data (dissipation against frequency) with fitting

#Setting up the export document (size labels, etc.)
reset
set terminal pdfcairo enhanced font 'Helvetica,10'
set output 'name_of_output_file.pdf'set grid
set xlabel  '{/Symbol D} frequency_7/N [Hz]'
set ylabel '{/Symbol D} dissipation_7 [10^{-6}]'
set cblabel 'time [h]'

#variables
var1=2520 #start of protein binding
var2=var1+7200 #end of protein binding
var3=13500 #start of specimen binding
var4=var3+7200#end of specimen binding
fit1=2750
fit2=6000
fb1=-400
fb2=-580

#fitting
f1(x)=a1*x+b1
f2(x)=a2*x+b2


fit f1(x) 'S1.txt' u ($6):($1 >= var3 && $1 <= var3+360 ? $7 : 1/0) via a1, b1
fit f2(x) 'S1.txt' u ($6):($1 >= var3+720 && $1 <= var4 ? $7 : 1/0) via a2, b2
plot         'S1.txt' u ($6):($1 >= var3 && $1 <= var4 ? $7 : 1/0):($1/3600) pt 7 ps 1 palette t '',\
               x >= -1300  ? f1(x) : 1/0 lw 2 title sprintf('f(x)=%.3f * x + c', a1),\
               x <= -1350 ? f2(x) : 1/0 lw 2 title sprintf('f(x)=%.3f * x + c', a2)
var3=13500+720
plot         'S1.txt' u ($6):($1 >= var3 && $1 <= var4 ? $7 : 1/0):($1/3600) pt 7 ps 1 palette t '',\
               x <= -1425 ? f2(x) : 1/0 lw 2 title sprintf('f(x)=%.3f * x + c', a2)

var3=13500 #start of specimen binding
var4=27000
fit f1(x) 'S1.txt' u ($6):($1 >= var3 && $1 <= var4 ? $7 : 1/0) via a1, b1
plot         'S1.txt' u ($6):($1 >= var3 && $1 <= var4 ? $7 : 1/0):($1/3600) pt 7 ps 1 palette t '',\
               f1(x) lw 2 title sprintf('f(x)=%.3f * x + %.3f', a1, b1)
var3=13150
fit f1(x) 'S1.txt' u ($6):($1 >= var3 && $1 <= var3+150 ? $7 : 1/0) via a1, b1
fit f2(x) 'S1.txt' u ($6):($1 >= var3+350 && $1 <= var4 ? $7 : 1/0) via a2, b2
plot         'S1.txt' u ($6):($1 >= var3 && $1 <= var4 ? $7 : 1/0):($1/3600) pt 7 ps 1 palette t '',\
               x >= -150  ? f1(x) : 1/0 lw 2 title sprintf('f(x)=%.3f * x + c', a1),\
               x <= -190 ? f2(x) : 1/0 lw 2 title sprintf('f(x)=%.3f * x + c', a2)
```

II.3. Script for Computing and Plotting the First Derivative of Frequency, and Dissipation

```
# Gnuplot Script for plotting the first derivative of QCM-D data

#Setting up the export document (size labels, etc.)
reset
set terminal pdfcairo enhanced font 'Helvetica,10'
set output 'name_of_output_file.pdf'
set size ratio 0.618
set xlabel 'time [hours]'
set ylabel  '{/Symbol D} frequency_7/N [Hz]'
set y2label '{/Symbol D} dissipation_7 [10^{-6}]'
set y2tics
set key out vert right top

# setting up different line styles
set style line 1 lc rgb '#800000' lt 1 lw 1 pt 2 ps 0.5
set style line 2 lc rgb 'red' lt 1 lw 1 pt 5 ps 0.5
set style line 3 lc rgb '#FF8C00' lt 1 lw 1 pt 7 ps 0.5
set style line 4 lc rgb '#0000CD' lt 1 lw 1 pt 9 ps 0.5
set style line 5 lc rgb '#1E90FF' lt 1 lw 1 pt 11 ps 0.5
set style line 6 lc rgb '#32CD32' lt 1 lw 1 pt 13 ps 0.5

# list of variables used in the plots to denoting timepoints
# when a new solution reached the measurement chamber
vl1=0.667
vl2=3.1667
vl3=3.667
vl4=7.667
vl5=11.667

# variable for time shift
timeshift=3.5
# if using a timeshift, offset values for different samples
of1=103
of2=113.1
of3=100



# vertical lines (arrow) marking the timepoints when new solutions reached the analysis chamber
# arrow one defined twice as a workaround for a bug
set arrow 1 from 0,0 to 0,1 nohead
set arrow 1 from vl1, graph 0 to vl1, graph 1 nohead
set arrow 2 from vl2, graph 0 to vl2, graph 1 nohead
set arrow 3 from vl3, graph 0 to vl3, graph 1 nohead
set arrow 4 from vl4, graph 0 to vl4, graph 1 nohead
set arrow 5 from vl5, graph 0 to vl5, graph 1 nohead
unset arrow 1
unset arrow 2
unset arrow 3
unset arrow 4
unset arrow 5


set xrange[timeshift:8.4]

# derivative functions
d = d1 = d2 = d3 = d4 = d5 = d6 = d7 = d8 = d9 = 0
x1 = y1 = 0

d(x,y) = ($0 < 4) ? (x2 = x1, x1 = x, y2 = y1, y1 = y, d4 = d3, d3 = d2, d2 = d1, d1 = d, d = (y1-y2)/(x1-x2), 1/0) : (x2 = x1, x1 = x, y2 = y1, y1 = y, d4 = d3, d3 = d2, d2 = d1, d1 = d, d = (y1-y2)/(x1-x2), (d+d1+d2+d3+d4)/5)
d2(x,y) = ($0 < 9) ? (x2 = x1, x1 = x, y2 = y1, y1 = y, d9 = d8, d8 = d7, d7 = d6, d6 = d5, d5 = d4, d4 = d3, d3 = d2, d2 = d1, d1 = d, d = (y1-y2)/(x1-x2), 1/0) : (x2 = x1, x1 = x, y2 = y1, y1 = y, d9 = d8, d8 = d7, d7 = d6, d6 = d5, d5 = d4, d4 = d3, d3 = d2, d2 = d1, d1 = d, d = (y1-y2)/(x1-x2), (d+d1+d2+d3+d4+d5+d6+d7+d8+d9)/10)

set ylabel '{/Symbol d}_{t} {/Symbol D} frequency [Hz/s]'
set y2label '{/Symbol d}_{t}{/Symbol D} dissipation [10^{-6}/s]'

set title "derivative of integrin-liposomes \nwith 5 data point averaging"

plot         'S1.txt' u ($1/3600):(d($1,$7-timeshift)) axes x1y2 t '{/Symbol D}D nsample_name'  w lp ls 1 pi interval,\
             'S2xt' u ($1/3600):(d($1,$7*-timeshift)) axes x1y2 t '{/Symbol D}D sample_name'  w lp ls 2 pi interval,\
             'S3.txt' u ($1/3600):(d($1,$7*-timeshift)) axes x1y2 t '{/Symbol D}D sample_name'  w lp ls 3 pi interval,\
             'S1.txt' u ($1/3600):(d($1,$6+of1)) axes x1y1 t '{/Symbol D}F sample_name'  w lp ls 4 pi interval,\
             'S2.txt' u ($1/3600):(d($1,$6+of2)) axes x1y1 t '{/Symbol D}F sample_name'  w lp ls 5 pi interval,\
             'S3.txt' u ($1/3600):(d($1,$6+of3)) axes x1y1 t '{/Symbol D}F sample_name'  w lp ls 6 pi interval

set title "derivative of sample_name \nwith 10 data point averaging"
```

```
76
77  plot         'S1.txt' u ($1/3600):(d2($1,$7-timeshift)) axes x1y2 t '{/Symbol D}D sample_name'  w lp ls 1 pi interval,\
78                  'S2.txt' u ($1/3600):(d2($1,$7-timeshift)) axes x1y2 t '{/Symbol D}D sample_name'  w lp ls 2 pi interval,\
79                  'S3.txt' u ($1/3600):(d2($1,$7-timeshift)) axes x1y2 t '{/Symbol D}D sample_name'  w lp ls 3 pi interval,\
80                  'S1.txt' u ($1/3600):(d2($1,$6+of1)) axes x1y1 t '{/Symbol D}F sample_name'  w lp ls 4 pi interval,\
81                  'S2.txt' u ($1/3600):(d2($1,$6+of2)) axes x1y1 t '{/Symbol D}F sample_name'  w lp ls 5 pi interval,\
82                  'S3.txt' u ($1/3600):(d2($1,$6+of3)) axes x1y1 t '{/Symbol D}F sample_name'  w lp ls 6 pi interval
```

III. Estimation of the Electric Field in a Picoinjection Device

The following calculation will give a rough estimate of the electric fields, created in a pico-injection device. By showing the amount of simplifications necessary to derive an analytical solution, the use of the FEM can be motivated.
To calculate the strength of the electric field, the charge distribution in the wires has to be calculated first. Therefore, the capacitance of the wires close to the channel is approximated. Note, this ansatz will ignore part of the electric field. The total capacitance of the wires could also be experimentally measured. However this method would be ignorant to their distribution.

III.1. Capacity

The geometry of the electrodes is quite complex and its impossible to calculate it's capacitance analytically. As any field within a conductor, immediately causes charges to align on it's surface in such a manner, that the field is cancelled. Hence it can be assumed assumed, that the charges is mostly concentrated at the opposing surfaces of the electrodes. Therefore, the geometry is simplified to a plate capacitor. The capacity of a plate capacitor is approximated as

$$C \approx \varepsilon_0 \varepsilon \frac{A}{d} = \frac{Q}{U}. \tag{S1}$$

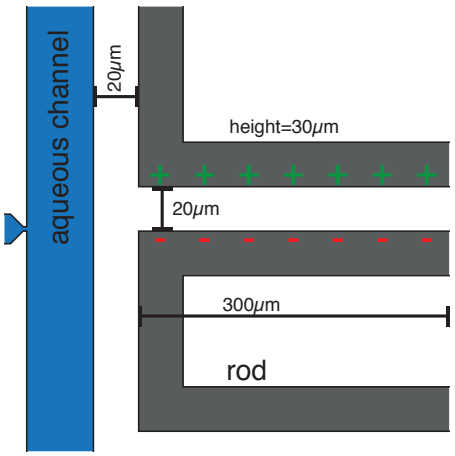

Figure 1.: Sketch of the wires and the charge distribution.

Where A is the surface area of the opposing interfaces of the wires and d is the

distance in between. Q is the total charge of the capacitor in relation to the applied voltage U. Equation S1 can be rearranged as follows,

$$Q = \varepsilon_0 \varepsilon \frac{AU}{d}. \tag{S2}$$

As the charge is approximately equally spread over the wire, we can assume the charge density as

$$\rho = Q/l, \tag{S3}$$

where l is the length of the rod. Note, that the charge distribution is reduced by one dimension, as it is not important in our later calculation.

III.2. Vectorial Electric Field

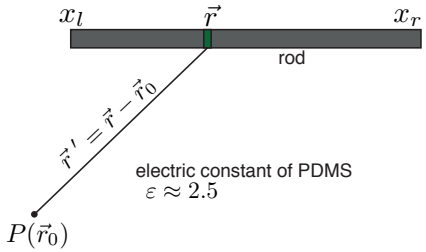

Figure 2.: Sketch of the geometry used to compute the field strength.

The calculation starts by considering the field created by one rod at a point P at the coordinates $\mathbf{r}_0$,

$$\mathbf{E} = \frac{1}{4\pi\varepsilon_0\varepsilon} \int \frac{Q(\mathbf{r})}{(\mathbf{r})^2} d\mathbf{r}, \tag{S4}$$

with $\mathbf{r} = \mathbf{r}\,' - \mathbf{r}_0$. Where $d\mathbf{r}$ is defined as

$$d\mathbf{r} = \mathbf{e}_r dr = \frac{\mathbf{r}}{|\mathbf{r}|} dr. \tag{S5}$$

Here charge can be written as

$$Q(\mathbf{r}) = \rho \left(\Theta(x_l) - \Theta(x_r)\right) \delta(y_{rod}), \tag{S6}$$

where ρ is defined in equation S3. Combining equation S4 and S6 gives

$$\begin{aligned}\mathbf{E} = & \frac{\rho}{4\pi\varepsilon_0\varepsilon} \int \frac{\delta(y_{rod})}{\mathbf{r}^{\,2}} \frac{\mathbf{r}}{|\mathbf{r}|} dr \\ = & \frac{\rho}{4\pi\varepsilon_0\varepsilon} \int\int_{x_l}^{x_r} \frac{\delta(y_{rod})}{(x-x_p)^2+(y-y_p)^2} \frac{(x-x_p)\mathbf{e}_x + (y-y_p)\mathbf{e}_y}{\sqrt{(x-x_p)^2+(y-y_p)^2}}\, dx\, dy \\ = & \frac{\rho}{4\pi\varepsilon_0\varepsilon} \int\int_{x_l}^{x_r} \frac{1}{(x-x_p)^2+(y_{rod}-y_p)^2} \frac{(x-x_p)\mathbf{e}_x + (y_{rod}-y_p)\mathbf{e}_y}{\sqrt{(x-x_p)^2+(y_{rod}-y_p)^2}}\, dx.\end{aligned} \tag{S7}$$

Which can be split in the electric field in the direction of vector $\mathbf{e}_x$ and $\mathbf{e}_y$ part,

$$E_x = \frac{\rho}{4\pi\varepsilon_0\varepsilon} \int_{x_l}^{x_r} \frac{1}{(x-x_p)^2+(y_{rod}-y_p)^2} \frac{x-x_p}{\sqrt{(x-x_p)^2+(y_{rod}-y_p)^2}} dx, \tag{S8}$$

and

$$E_y = \frac{\rho}{4\pi\varepsilon_0\varepsilon} \int_{x_l}^{x_r} \frac{1}{(x-x_p)^2+(y_{rod}-y_p)^2} \frac{y_{rod}-y_p}{\sqrt{(x-x_p)^2+(y_{rod}-y_p)^2}} dx. \tag{S9}$$

Integration of equations S8 and S9 yields

$$\begin{aligned}E_x = & \frac{\rho}{4\pi\varepsilon_0\varepsilon} \left[\frac{-1}{\sqrt{y'^2+x'^2}} \right]_{x_l-x_p}^{x_r-x_p} \\ = & \frac{\rho}{4\pi\varepsilon_0\varepsilon} \left(\frac{1}{\sqrt{y'^2+(x_l-x_p)^2}} - \frac{1}{\sqrt{y'^2+(x_r-x_p)^2}} \right),\end{aligned} \tag{S10}$$

and

$$\begin{aligned}E_y = & \frac{\rho}{4\pi\varepsilon_0\varepsilon} \left[\frac{x'}{y'\sqrt{y'^2+x'^2}} \right]_{x_l-x_p}^{x_r-x_p} \\ = & \frac{\rho}{4\pi\varepsilon_0\varepsilon} \left(\frac{x_r-x_p}{y'\sqrt{y'^2+(x_r-x_p)^2}} - \frac{x_l-x_p}{y'\sqrt{y'^2+(x_l-x_p)^2}} \right),\end{aligned} \tag{S11}$$

respectively. To calculate the total field strength, the fields from both rods have to be added. Note, that the charges of anode and cathode are of opposite charge.

III.3. Matlab Script Implementing the Field Calculation

```
%% Picoinjection electric field calculator

%% device properties
% sturcture height [µm]
height = 70;
% length were wires are parallel [µm]
length = 300;
% distance of wire [µm]
distance = 20;
% electric constant (PDMS =2.5)
epsilon = 2.5;
% voltage [V]
U = 250;
%position wire top left [µm]
xleft = 20;
yleft = 10;

%% area to be calculated
%x-area [µm]
xmin = -40;
xmax = 10;
%y-area [µm]
ymin = -40;
ymax = 40;
stepsize = 5;

%% calculating the charge for an assumed plate capacitor
Q = pccalc(length,height,distance,epsilon,U);

%% grid
xgrid = xmin:stepsize:xmax;
ygrid = ymin:stepsize:ymax;
clear stepsize

%% field calculator
[Ex,Ey, Eabsolute] = fieldcalc( xgrid , ygrid , Q, length, epsilon, distance, xleft, yleft );

%gnuplot=zeros(numel(ygrid)*numel(xgrid),3);
%limit = 500;
%for i=1:numel(ygrid);
%    for j=1:numel(xgrid);
%        if Eabsolute(i,j)> limit
%            gnuplot((i-1)*numel(xgrid)+j,:) = [xgrid(j),ygrid(i),500];
%        else
%            gnuplot((i-1)*numel(xgrid)+j,:) = [xgrid(j),ygrid(i),Eabsolute(i,j)];
%        end
%    end
%end
%save('gnuplot.txt','gnuplot','-ascii')

figure(1)
surf(xgrid,ygrid,Eabsolute/100);
title('Field distribution');
axis([xmin xmax ymin ymax 0 0.5]);
caxis([0 0.5]);
xlabel('x-axis [µm]');
ylabel('y-axis [µm]');
zlabel('electric field [kV/cm]');


figure(2)
contour(xgrid,ygrid,Eabsolute/100,40);
title('Field distribution');
axis([xmin xmax ymin ymax]);
caxis([0 0.5]);
colorbar
xlabel('x-axis [µm]');
ylabel('y-axis [µm]');

figure(3)
quiver(xgrid,ygrid,Ex,Ey);
hold on
contour(xgrid,ygrid,Eabsolute/100,20);
hold off
title('Field distribution');
axis([xmin xmax ymin ymax]);
caxis([0 0.5]);
colorbar
xlabel('x-axis [µm]');
ylabel('y-axis [µm]');

```

```
clear distance epsilon height length U xleft yleft i j limit xmin xmax ymin ymax
```

```
function [ Ex , Ey , Eabsolute ] = fieldcalc( xgrid , ygrid , Q , length, epsilon, distance, xl, yrod )
e0=8.854187817e-12;
rho = Q/length*10e6;
C = rho/(4*pi*e0*epsilon);
Ex = zeros(numel(ygrid),numel(xgrid));
Ey = zeros(numel(ygrid),numel(xgrid));
for i=1:numel(ygrid);
    for j=1:numel(xgrid)
        Ex(i,j) = C*(((yrod-ygrid(i))^2 + (xl - xgrid(j))^2)^-0.5-((yrod-ygrid(i))^2 + (xl + length - xgrid(j))^2)^-0.5-((yrod -
          ↪    distance - ygrid(i))^2 + (xl - xgrid(j))^2)^-0.5+((yrod -distance-ygrid(i))^2 + (xl + length -
          ↪    xgrid(j))^2)^-0.5);
        if ygrid(i) == yrod;
            Ey(i,j)= C*((xl+length-xgrid(j))/(distance*sqrt(distance^2+(xl+length-xgrid(j))^2)) -
              ↪    (xl-xgrid(j))/(distance*sqrt(distance^2+(xl-xgrid(j))^2)));
        elseif ygrid(i) == yrod - distance
            Ey(i,j)= C*((xl+length-xgrid(j))/(distance*sqrt(distance^2+(xl+length-xgrid(j))^2)) -
              ↪    (xl-xgrid(j))/(distance*sqrt(distance^2+(xl-xgrid(j))^2)));
        else
            Ey(i,j)= C*((xl+length-xgrid(j))/((yrod-ygrid(i))*sqrt((yrod-ygrid(i))^2+(xl+length-xgrid(j))^2)) -
              ↪    (xl-xgrid(j))/((yrod-ygrid(i))*sqrt((yrod-ygrid(i))^2 + (xl-xgrid(j))^2)) - (xl+length-xgrid(j)) /
              ↪    ((yrod-distance-ygrid(i))*sqrt((yrod-distance-ygrid(i))^2 + (xl+length-xgrid(j))^2)) + (xl-xgrid(j)) /
              ↪    ((yrod-distance-ygrid(i))*sqrt((yrod-distance-ygrid(i))^2 + (xl-xgrid(j))^2)));
        end
    end
end
Eabsolute =sqrt(Ex.^2+Ey.^2);
end
```

```
function [ Q ] = pccalc( x,y,d,epsilon,U )
%
e0=8.854187817e-12;
Q=e0*epsilon*U*x*y/d*1e-6;
end
```

List of Publications

Published

[1] **J. P. Frohnmayer**[*], D. Brüggemann[*], C. Eberhard, S. Neubauer, C. Mollenhauer, H. Boehm, H. Kessler, B. Geiger, and J. P. Spatz, "Minimal,synthetic cells to study integrin-mediated adhesion," Angew. Chem. Int. Ed. Engl., vol. 54, no. 42, pp. 12472–12478, Oct. 2015.

J. P. Frohnmayer[*], D. Brüggemann[*], C. Eberhard, S. Neubauer, C. Mollenhauer, H. Boehm, H. Kessler, B. Geiger, and J. P. Spatz, "Synthetische Adhäsion von Integrin-Liposomen als minimales Zellmodell, "Angewandte Chemie, vol. 127, no. 42, pp. 12649–12655, Oct. 2015.

[2] D. Brüggemann, **J. P. Frohnmayer**, and J. P. Spatz, "Model systems for studying cell adhesion and biomimetic actin networks," Beilstein J Nanotechnol, vol. 5, no. 1, pp. 1193–1202, 2014.

Accepted

[3] **J. P. Frohnmayer**[*], M. Weiss[*], B. Haller, J.-W. Janiesch, L. T. Benk, R. B. Lira, R. Dimova, I. Platzman, and J. P. Spatz, "Droplet-Supported Giant Vesicles as Cell-Like Compartments for Synthetic Biology," in The Giant Vesicle Book, R. Dimova and R. Lipowski, Eds. CRC Taylor & Francis, 2017.

Submitted

[4] M. Weiss[*], **J. P. Frohnmayer**[*], L. T. Benk, B. Haller, J.-W. Janiesch, T. Heitkamp, M. Börsch, R. Dimova, R. Lipowsky, E. Bodenschatz, J.-C. Baret, I. Platzman, and J. P. Spatz, Sequential Bottom-up Assembly of Cell-like Compartments, Nature Materials.

[*]These authors contributed equally to this work.

JOHN WILEY AND SONS LICENSE TERMS AND CONDITIONS

Jan 05, 2017

This Agreement between Johannes P. Frohnmayer ("You") and John Wiley and Sons ("John Wiley and Sons") consists of your license details and the terms and conditions provided by John Wiley and Sons and Copyright Clearance Center.

License Number	4022660285977
License date	Jan 05, 2017
Licensed Content Publisher	John Wiley and Sons
Licensed Content Publication	Angewandte Chemie International Edition
Licensed Content Title	Minimal Synthetic Cells to Study Integrin-Mediated Adhesion
Licensed Content Author	Johannes P. Frohnmayer,Dorothea Brüggemann,Christian Eberhard,Stefanie Neubauer,Christine Mollenhauer,Heike Boehm,Horst Kessler,Benjamin Geiger,Joachim P. Spatz
Licensed Content Date	Aug 7, 2015
Licensed Content Pages	7
Type of Use	Dissertation/Thesis
Requestor type	Author of this Wiley article
Format	Print and electronic
Portion	Full article
Will you be translating?	No
Title of your thesis / dissertation	Bottom-Up Assembly of Synthetic Model Systems for Cellular Adhesion
Expected completion date	Feb 2017
Expected size (number of pages)	220
Requestor Location	Johannes P. Frohnmayer Heisenbergstr. 3 MPI for Intelligent Systems Stuttgart, BW 70569 Germany Attn: Johannes P. Frohnmayer
Publisher Tax ID	EU826007151
Billing Type	Invoice
Billing Address	Johannes P. Frohnmayer Heisenbergstr. 3 MPI for Intelligent Systems Stuttgart, Germany 70569 Attn: Johannes P. Frohnmayer
Total	**0.00 EUR**
Terms and Conditions	

TERMS AND CONDITIONS

This copyrighted material is owned by or exclusively licensed to John Wiley & Sons, Inc. or one of its group companies (each a"Wiley Company") or handled on behalf of a society with which a Wiley Company has exclusive publishing rights in relation to a particular work (collectively "WILEY"). By clicking "accept" in connection with completing this licensing transaction, you agree that the following terms and conditions apply to this transaction (along with the billing

ROYAL SOCIETY OF CHEMISTRY LICENSE TERMS AND CONDITIONS

Jan 05, 2017

This Agreement between Johannes P. Frohnmayer ("You") and Royal Society of Chemistry ("Royal Society of Chemistry") consists of your license details and the terms and conditions provided by Royal Society of Chemistry and Copyright Clearance Center.

License Number	4022691146292
License date	Jan 05, 2017
Licensed Content Publisher	Royal Society of Chemistry
Licensed Content Publication	Lab on a Chip
Licensed Content Title	High-yield cell ordering and deterministic cell-in-droplet encapsulation using Dean flow in a curved microchannel
Licensed Content Author	Evelien W. M. Kemna,Rogier M. Schoeman,Floor Wolbers,Istvan Vermes,David A. Weitz,Albert van den Berg
Licensed Content Date	Apr 26, 2012
Licensed Content Volume Number	12
Licensed Content Issue Number	16
Type of Use	Thesis/Dissertation
Requestor type	academic/educational
Portion	figures/tables/images
Number of figures/tables /images	1
Format	print and electronic
Distribution quantity	10
Will you be translating?	no
Order reference number	
Title of the thesis/dissertation	Bottom-Up Assembly of Synthetic Model Systems for Cellular Adhesion
Expected completion date	Feb 2017
Estimated size	220
Requestor Location	Johannes P. Frohnmayer Heisenbergstr. 3 MPI for Intelligent Systems Stuttgart, BW 70569 Germany Attn: Johannes P. Frohnmayer
Billing Type	Invoice
Billing Address	Johannes P. Frohnmayer Heisenbergstr. 3 MPI for Intelligent Systems

ELSEVIER LICENSE
TERMS AND CONDITIONS

Jan 05, 2017

This Agreement between Johannes P. Frohnmayer ("You") and Elsevier ("Elsevier") consists of your license details and the terms and conditions provided by Elsevier and Copyright Clearance Center.

License Number	4022680060821
License date	Jan 05, 2017
Licensed Content Publisher	Elsevier
Licensed Content Publication	Current Opinion in Cell Biology
Licensed Content Title	Integrin inside-out signaling and the immunological synapse
Licensed Content Author	Timothy A Springer,Michael L Dustin
Licensed Content Date	February 2012
Licensed Content Volume Number	24
Licensed Content Issue Number	1
Licensed Content Pages	9
Start Page	107
End Page	115
Type of Use	reuse in a thesis/dissertation
Intended publisher of new work	other
Portion	figures/tables/illustrations
Number of figures/tables /illustrations	2
Format	both print and electronic
Are you the author of this Elsevier article?	No
Will you be translating?	No
Order reference number	
Original figure numbers	figures 1, 2
Title of your thesis/dissertation	Bottom-Up Assembly of Synthetic Model Systems for Cellular Adhesion
Expected completion date	Feb 2017
Estimated size (number of pages)	220
Elsevier VAT number	GB 494 6272 12
Requestor Location	Johannes P. Frohnmayer Heisenbergstr. 3 MPI for Intelligent Systems

NATURE PUBLISHING GROUP LICENSE
TERMS AND CONDITIONS

Jan 05, 2017

This Agreement between Johannes P. Frohnmayer ("You") and Nature Publishing Group ("Nature Publishing Group") consists of your license details and the terms and conditions provided by Nature Publishing Group and Copyright Clearance Center.

License Number	4022661048833
License date	Jan 05, 2017
Licensed Content Publisher	Nature Publishing Group
Licensed Content Publication	Nature
Licensed Content Title	Nanoscale architecture of integrin-based cell adhesions
Licensed Content Author	Pakorn Kanchanawong, Gleb Shtengel, Ana M. Pasapera, Ericka B. Ramko, Michael W. Davidson, Harald F. Hess
Licensed Content Date	Nov 24, 2010
Licensed Content Volume Number	468
Licensed Content Issue Number	7323
Type of Use	reuse in a dissertation / thesis
Requestor type	academic/educational
Format	print and electronic
Portion	figures/tables/illustrations
Number of figures/tables /illustrations	1
High-res required	no
Figures	Figure 4d
Author of this NPG article	no
Your reference number	
Title of your thesis / dissertation	Bottom-Up Assembly of Synthetic Model Systems for Cellular Adhesion
Expected completion date	Feb 2017
Estimated size (number of pages)	220
Requestor Location	Johannes P. Frohnmayer Heisenbergstr. 3 MPI for Intelligent Systems Stuttgart, BW 70569 Germany Attn: Johannes P. Frohnmayer
Billing Type	Invoice

THE AMERICAN ASSOCIATION FOR THE ADVANCEMENT OF SCIENCE LICENSE TERMS AND CONDITIONS

Jan 05, 2017

This Agreement between Johannes P. Frohnmayer ("You") and The American Association for the Advancement of Science ("The American Association for the Advancement of Science") consists of your license details and the terms and conditions provided by The American Association for the Advancement of Science and Copyright Clearance Center.

License Number	4022680414599
License date	Jan 05, 2017
Licensed Content Publisher	The American Association for the Advancement of Science
Licensed Content Publication	Science
Licensed Content Title	Long-Term Monitoring of Bacteria Undergoing Programmed Population Control in a Microchemostat
Licensed Content Author	Frederick K. Balagaddé,Lingchong You,Carl L. Hansen,Frances H. Arnold,Stephen R. Quake
Licensed Content Date	Jul 1, 2005
Licensed Content Volume Number	309
Licensed Content Issue Number	5731
Volume number	309
Issue number	5731
Type of Use	Thesis / Dissertation
Requestor type	Scientist/individual at a research institution
Format	Print and electronic
Portion	Figure
Number of figures/tables	1
Order reference number	
Title of your thesis / dissertation	Bottom-Up Assembly of Synthetic Model Systems for Cellular Adhesion
Expected completion date	Feb 2017
Estimated size(pages)	220
Requestor Location	Johannes P. Frohnmayer Heisenbergstr. 3 MPI for Intelligent Systems Stuttgart, BW 70569 Germany Attn: Johannes P. Frohnmayer
Billing Type	Invoice
Billing Address	Johannes P. Frohnmayer Heisenbergstr. 3 MPI for Intelligent Systems

Garland Science - Books LICENSE
TERMS AND CONDITIONS

Jan 09, 2017

This is a License Agreement between Johannes P. Frohnmayer ("You") and Garland Science - Books ("Garland Science - Books") provided by Copyright Clearance Center ("CCC"). The license consists of your order details, the terms and conditions provided by Garland Science - Books, and the payment terms and conditions.

All payments must be made in full to CCC. For payment instructions, please see information listed at the bottom of this form.

License Number	4024890600312
License date	Jan 06, 2017
Licensed content publisher	Garland Science - Books
Licensed content title	Molecular biology of the cell
Licensed content date	Jan 1, 2007
Type of Use	Thesis/Dissertation
Requestor type	Academic institution
Format	Print, Electronic
Portion	chart/graph/table/figure
Number of charts/graphs /tables/figures	2
Title or numeric reference of the portion(s)	Figure 1-30 (overview eucariotic cell), Figure 19-2 (types of cell junctions)
Title of the article or chapter the portion is from	N/A
Editor of portion(s)	ALBERTS ET. AL
Author of portion(s)	ALBERTS ET. AL
Volume of serial or monograph.	N/A
Page range of the portion	N/A
Publication date of portion	2007
Rights for	Main product
Duration of use	Life of current and all future editions
Creation of copies for the disabled	no
With minor editing privileges	no
For distribution to	Worldwide
In the following language(s)	Original language of publication
With incidental promotional use	no

ELSEVIER LICENSE
TERMS AND CONDITIONS

Jan 31, 2017

This Agreement between Johannes P. Frohnmayer ("You") and Elsevier ("Elsevier") consists of your license details and the terms and conditions provided by Elsevier and Copyright Clearance Center.

License Number	4039480610892
License date	Jan 31, 2017
Licensed Content Publisher	Elsevier
Licensed Content Publication	Journal of Structural Biology
Licensed Content Title	Electron tomography reveals diverse conformations of integrin αIIbβ3 in the active state
Licensed Content Author	Kenji Iwasaki,Kaoru Mitsuoka,Yoshinori Fujiyoshi,Yukio Fujisawa,Masakazu Kikuchi,Kiyotoshi Sekiguchi,Takao Yamada
Licensed Content Date	June 2005
Licensed Content Volume Number	150
Licensed Content Issue Number	3
Licensed Content Pages	9
Start Page	259
End Page	267
Type of Use	reuse in a thesis/dissertation
Intended publisher of new work	other
Portion	figures/tables/illustrations
Number of figures/tables /illustrations	1
Format	both print and electronic
Are you the author of this Elsevier article?	No
Will you be translating?	No
Order reference number	
Original figure numbers	figure 8
Title of your thesis/dissertation	Bottom-Up Assembly of Synthetic Model Systems for Cellular Adhesion
Expected completion date	Feb 2017
Estimated size (number of pages)	220
Elsevier VAT number	GB 494 6272 12

The Road Not Taken

Two roads diverged in a yellow wood,
And sorry I could not travel both
And be one traveler, long I stood
And looked down one as far as I could
To where it bent in the undergrowth;

Then took the other, as just as fair,
And having perhaps the better claim,
Because it was grassy and wanted wear;
Though as for that the passing there
Had worn them really about the same,

And both that morning equally lay
In leaves no step had trodden black.
Oh, I kept the first for another day!
Yet knowing how way leads on to way,
I doubted if I should ever come back.

I shall be telling this with a sigh
Somewhere ages and ages hence:
Two roads diverged in a wood, and I–
I took the one less traveled by,
And that has made all the difference.

Robert Frost

Acknowledgements

Firstly, I would like to express my sincere gratitude to my advisor Prof. Joachim Spatz for providing me the chance to work on such a fascinating project. Without his advice and continued support throughout my Ph.D would never have seen so much progress. I can't thank enough for the opportunities and freedom I was given to explore the merry world of science. Moreover, I am very grateful for the understanding I was shown for a young father's troubles.

I would like to thank Prof. Ulrich Schwarz for kindly accepting to review my thesis.

As Prof. Benjamin Geiger once quoted Winnie the Pooh to me, I also want to return a quote by A. A. Milne: "Piglet noticed that even though he had a very small heart, it could hold a rather large amount of gratitude." Not only do I have to thank for guidance and proteins you provide, much more I would like to inviting me to your wonderful country. I am looking forward to visiting Israel again. Maybe I get the chance to listen to more of your adventures.

Next, I want to thank another great storyteller, Professor Horst Kessler. The peptides he and his postdoc, Dr. Stefanie Neubauer, supplied, were essential to my first first-author publication. I greatly enjoyed the shared time at castle Ringberg.

As this Ph.D thesis was written as a servant of two masters, my gratitude goes to both of them. Dr. Dorothea Brüggemann, thank you for starting this Ph.D. with me. Although, our roads diverged after some time, I'm thankful for the help and advice you gave me. I wish you all the best and success with your very own Emmy Nöther group.

But every end is also a beginning. Therefore, I have to thank Dr. (Y)Ilia Pla(t)zman* who picked up supervision during my microfluidic research. Ilia always had scientific advice or knew where to find it. He is a specialist at removing obstacles. Moreover, he is a kind and caring group leader. I am grateful, that you helped making the best out of my Ph.D.

*After over three years of working together, I am still confused about the different spellings of your name.

Acknowledgements

You are tall when you stand on a giants shoulder. As my predecessor on the synthetic adhesion Dr. Christian Eberhard walked a rocky road, to laid the solid foundation, I could build my research on. Thank you for being a mentor and a friend. I owe you a lot.

Christian's wasn't the only shoulder I could stand on. I will never forget Christine Mollenhauer, the head of the biochemistry lab and the good heart of the Spatz department. Without Christine's deep insight into protein biochemistry I would have gone lost. I also want to thank your, for always having an open ear when needed.

When my research took a new direction after the first year, Dr. Jan-Willi Janiesch was there to help me get a microfluidics lab up and running. Jan's drive and attitude were always refreshing and the beer (after) work mandatory. Additionally, I have to thank Jan and Gerri Kannenberg for the constant supply with microfluidic surfactants.

Soon after the new lab was set up the microfluidic group started to grow. And new members Marian Weiss, Lucia Benk and soon after Barbara Haller joined. Lucia, my longest co-worker, I want to thank for the nice working atmosphere and the time spend together. I want to thank Marian for the good collaboration and productive joined work. I am convinced we achieved something together, that I could not have done alone.

As a researcher I am grateful that my work won't pass in obscurity, but that the torch will be carried on by a group of talented people. I want to thank Dr. Eli Zamir who knows much more about cellular adhesion than I will ever know, for his advice. I want to thank Christoph Frey for carrying on many of my burdens, such as the cleanroom and the microscope maintenance. Additionally, I want to thank Dr. Rongcong luo, Silvia Antona and Stojan Perisic.

I also thank all the members of the whole Spatz department in Heidelberg and Stuttgart. My Ph.D was an eventful time of my life – I got married and saw the birth of my son. I want to thank all of you who shared this special time with me. Moreover, I really appreciated the working atmosphere, the many valuable discussions and all the help I received.

Moreover, I want to thank my two longest office mates, Dr. Christine Belz and Dr. Mohammad Raoufi. As a long time member of the group Chrissy helped me to get a successful start in the group. I want to thank Mohammadfor the good time we had together and the Persian food he shared every now and then.

Finally, I want to thank the two most important persons in my life – my wife, Dr. Sieglinde Frohnmayer, and our son Samuel. As I had to work a lot to finish this thesis, they had to manage a lot of time without me. Thank you for your patience and understanding. It was always a joy and a source of strength to be with my loved ones.

Parts of the research leading to this thesis have received funding from the European Research Council/ ERC Grant Agreement no. 294852, SynAd. This work is also part of the MaxSynBio consortium, which is jointly funded by the Federal Ministry of Education and Research of Germany and the Max Planck Society. The Max Planck Society is appreciated for its general support in all aspects of our research.